UNIVERSIDAD NACIONAL DE COLOMBIA

Synthesis and application of supported metallic and multi-metallic oxides nanoparticles for *in-situ* upgrading and inhibition of formation damage

Camilo Andrés Franco Ariza

Universidad Nacional de Colombia
Facultad de Minas, Escuela de Procesos y Energía
Medellín, Colombia
2015

Synthesis and application of supported metallic and multi-metallic oxides nanoparticles for *in-situ* upgrading and inhibition of formation damage

Camilo Andrés Franco Ariza

Tesis o trabajo de investigación presentada(o) como requisito parcial para optar al título de:
Doctor en Ingeniería – Sistemas Energéticos

Director:
Ph.D., M.Sc., Ingeniero Químico, Farid Bernardo Cortés Correa

Línea de Investigación:
Mejoramiento in-situ de curos pesados y extra pesados. Daño de formación
Grupo de Investigación:
Grupo de Investigación en Fenómenos de Superficie "Michael Polanyi"

Universidad Nacional de Colombia
Facultad de Minas, Escuela de Procesos y Energía
Medellín, Colombia
2015

A Dios y la Santísima Virgen María por fortalecerme y darme luz en el camino. A mi mamá que siempre ha creído en mí y me ha brindado su apoyo y amor incondicional. A Pepe y Mimi que también se han encargado de apoyarme sin condición. A Stefanía Betancur que me ha respaldado tanto sentimental como laboralmente. A mi tío y padrino que se ha encargado de brindarme apoyo durante toda mi vida. A Nana, Pablo Andrés y Nataly por su compañía y hacer parte de mi vida. A Lolo por todas su oraciones y cariño. A mi director y amigo Farid B. Cortés. A todos y cada uno de mis compañeros del grupo de investigación Grupo de Investigación en Fenómenos de Superficie “Michael Polanyi” y aquellos involucrados en el proyecto de Colciencias. A todos mis amigos, que siempre me han brindado su respaldo.

Acknowledgments

Special thanks to my supervisor Farid Bernardo Cortés Correa for his valuable support, advice, guidance and patience.

Also, special acknowledgments to the members of the research group in surface phenomena "Michael Polanyi", the research group in hydrocarbon reservoirs and the petrophysics lab for their support and valuable advices in the development of the experimental work.

My sincere thanks to Dr. Nashaat N. Nassar for his valuable opinions, recommendations and his hospitality at the An-Najah National University in Nablus city, Palestine. Additionally, thanks to all people at the An-Najah National University and Dr. Nassar students.

Special thanks to Dr. Francisco José Maldonado-Hódar and Dr. Francisco Carrasco-Marin for your guidance and hospitality at the Universidad de Granada in Granada, Spain. To each one of the members of the Adsorption and Catalysis laboratory at the UGR.

I also want to acknowledge Dr. Pedro Pereira-Almao from University of Calgary and Dr. Sócrates Acevedo from Universidad Central de Venezuela for sharing their expertise and their valuable contributions.

Special acknowledge to COLCIENCIAS and ECOPETROL for the support provided in the agreement 264 of 2013. I also acknowledge Universidad Nacional de Colombia for logistical and financial support.

To each and every one of the contributors to the successful development of this thesis work.

Resumen

Debido a la creciente demanda energética a nivel global y el decrecimiento en las fuentes convencionales de petróleo, la industria energética ha optado por explotar otras fuentes de crudo no convencionales tales como los crudos pesados y extra pesados y contribuir de esta manera al suplemento de la demanda energética. Sin embargo, los crudos pesados pueden acarrear diferentes tipos de problemas en todo el sistema de producción, generando costos y operaciones adicionales en procesos de recobro o mejoramiento de la calidad del crudo, además del empleo de grandes cantidades de agua que directamente generan un impacto ambiental negativo. Adicionalmente, la vida productora de un yacimiento puede verse afectada por componentes de alto peso molecular como los asfaltenos. Los asfaltenos pueden generar problemas operacionales en la producción y procesamiento del crudo tanto a nivel de yacimiento, pozo o superficie. La nanotecnología se presenta como una solución viable para mejorar la calidad de crudos pesados y extra pesados, mitigar/inhibir problemas relacionados con los asfaltenos y aumentar el recobro de petróleo mediante su aplicación a nivel de yacimiento. En este orden de ideas, esta tesis tiene como objetivo principal la síntesis y aplicación de nanopartículas soportadas con óxidos metálicos o multimetálicos de NiO y/o PdO que tengan una alta selectividad actividad catalítica hacia la adsorción y posterior descomposición de asfaltenos. Mediante este estudio se pretende generar un mejor panorama acerca de la influencia del proceso de adsorción de asfaltenos en la actividad catalítica de nanopartículas funcionalizadas y dar un mejor entendimiento acerca del uso de la nanotecnología para mejoramiento *in-situ* de crudos pesados y extra-pesados y la inhibición del daño de formación por asfaltenos.

Palabras clave: Nanopartículas, Daño de Formación, Crudos Pesados, Asfaltenos, Adsorción, Catálisis.

Abstract

With the increasing world energy demand and the subsequent decrease in the world's easy-access oil supplies, conventional oil, the energy industry is increasingly turning to unconventional resources to recover oil, such as heavy and extra heavy oil and meet the world energy demand. However, in the current context, upgrading and recovery of heavy oil are highly energy and water intensive that requires a substantial capital and operating cost and consequently results in environmental footprints. In addition, asphaltenes are one of the most difficult problems to overcome in oil production and processing. The presence of asphaltenes in crude oil, and consequently, the adsorption and deposition of asphaltenes on the rock surfaces, affects the rock properties, such as porosity, permeability, and wettability. An alternative to the current upgrading, mitigate/inhibit asphaltene-related problems and enhance recovery processes is the potential employment of nanoparticle technology at reservoir conditions. This thesis aims at synthesize and apply metallic and/or multi-metallic oxides (e.g, Ni, and Pd) supported nanoparticles that have high adsorption selectivity and catalytic activity towards heavy hydrocarbons like asphaltenes. This study should provide a better insight on the influence of the adsorption process on the catalytic activity of the nanoparticles and give a better understanding about the use of nanotechnology for *in-situ* upgrading of heavy and extra-heavy oils and inhibition of formation damage.

Keywords: Nanoparticles, Formation Damage, Heavy Oil, Asphaltenes, Adsorption, Catalysis.

Content

List of Figures

List of tables

Introduction

The available conventional energy supplies have become an area of global concern as these supplies are decreasing due to several factors,[1] such as worldwide population growth, competing demands from a variety of users, increasing industrialization and motorization of the world, increasing technical development and living standard, etc. Accordingly, energy industries strive for finding alternative energy supplies that can be produced from natural resources that would be available and suitable for use. The utilization of fossil fuels, like unconventional crude oil, has now become an important source of alternative energy resources.[2 3-5] According to the International Energy Agency (IEA), by the year of 2035 the demand for fossil fuels will increase about one-third.[3, 6] However, with the gradual depletion of conventional resources as light and medium crude oil, the rise of unconventional oil is changing the way we understand the distribution of the world's energy resources.[6] Accordingly, the oil and gas industries have recently paid special attention to unconventional resources such as tight gas,[7, 8] gas/oil shale and oil sands,[9] coal-bed methane (CBM),[10, 11] gas from hydrates,[12, 13] heavy oil (HO) and extra-heavy oil (EHO).[3, 9, 14, 15] Deposits of HO and EHO are approximately of the same order than those of conventional crude oil according to the International Energy Agency.[16, 17] In fact, in the scenario 2014-2035 about the 9% of the cumulative investment upstream is necessary for developing heavy and extra heavy oil resources.[18]

Actually, Venezuela, Canada and Russia represent about the 87% of the future recovery and 81% of the future production of HO and EHO.[16] Other key players are Cuba, Peru, Mexico and Brazil in Latin America and China with the greatest resource in the eastern hemisphere.[9] It is expected that the growth of production in the next years in Colombia and Brazil will increase the overall regional production. In Colombia, the resources of HO and EHO represent the fourth market with more potential for the exploration and production.[19] The 45% of the current oil production in Colombia is related to HO and EHO and is expected that for 2018 this percentage will increase to 60%.[20] However, in the current context, the production of HO and EHO is complex as it involves higher costs than conventional resources and requires improved technology not just in production, but also in the evaluation, exploration, transportation and processing.[9, 21] These kinds of crude oils have large amount of heavy hydrocarbon compounds like asphaltenes that reduce the American Petroleum Institute gravity (°API) and increase drastically the oil viscosity. Some problems associated with asphaltenes are reduction of oil mobility at reservoir conditions, changes in the reservoir wettability and deposition on refining equipment.[22]

Asphaltenes typically are defined as the heaviest, most aromatic and surface-active fraction of the crude oil, being insoluble in light paraffins like *n*-pentane, *n*-hexane and *n*-heptane, but soluble in light aromatics like benzene, toluene or pyridine.[22-24] Although, the structure of asphaltenes is complex, a general description is that they have a nucleus composed by one or more cross-linked poly aromatic hydrocarbons (PAH's).[23-25] Asphaltenes have heteroatoms like N, S and O, and metals such as V, Fe and Ni.[26] Thus, the presence of functional groups such as carboxyl, ketones, aldehydes, benzothiophenes, dibenzothiophenes, naftenobenzotiophenes, alkyl sulfides, aryl alkyl sulfides and

aryl sulfides is likely to be in asphaltene structure.[23, 27, 28] Several hypothesis on asphaltenes chemical structures are proposed in literature; including island, archipelago, continental or rosary-type.[24, 25, 29, 30] The island architecture is composed by seven fused rings and one PAH while the archipelago architecture is composed by more than one PAH per asphaltene molecule connected by alkyl chains.[24, 30] The continental architecture is composed also by one or two PAH's but with a larger number of fused rings than seven.[29, 30] The rosary-type asphaltenes are very flexible and are composed by two or more PAH's joined by flexible aliphatic chains. However, owing to its complex chemical structure, asphaltene architectures get updated with time. The most accepted model that describes the asphaltenes colloidal and molecular structure is known as the Yen-Mullis model.[23, 24, 31-34] This model considers that island-type architecture is the dominant molecular architecture of asphaltenes with an average of seven fused rings in the PAH core and with an asphaltene molecular weight of ~750 Da. As the asphaltenes concentration increases, its self-associative nature leads to form nanoaggregates with an average size of 2 nm. Further increase in asphaltene concentration, higher concentration, the nanoaggregates form clusters, with an average size of 5 nm and aggregation numbers < 10.[24] This aggregation behavior of asphaltenes is also highly dependent on the chemical nature of the crude oil, temperature, compositions and the true vertical depth of the well that is directly associated with the reservoir pressure.[35] For instance, the asphaltenes in condensate oils with an average gas–oil–ratio (GOR) of 350 m^3/m^3 behave as molecules with a size of 1.5 nm based on the Yen–Mullins model.[24, 31] In black oils with a GOR of 90–180 m^3/m^3, asphaltenes behave as aggregates with an approximate size of 2 nm; however, for low GOR oils, such as heavy and extra heavy crude oils, asphaltenes may behave like clusters with a minimum size of 5 nm.[35] Asphaltenes self-association and further formation of large asphaltic flocs that also increase the HO viscosity.[36-38] In addition, asphaltenes that contain high content of sulfur form strong C-S and C=S bonds and subsequently increase drastically the crude oil viscosity.[39, 40] Further, presence of large amounts of N and S in the asphaltene structure leads to production of SO*x*, NO*x* and H_2S during processing. These characteristics of asphaltenes and their high content in HO and EHO make it difficult for production, transportation and processing.

Injection of naphtha or CO_2 for viscosity reduction are proven techniques for improving the production of HO and EHO. However, these techniques could lead to serious problems due to the possibility of modifying the flow and phase behaviour of the oil at reservoir conditions, leading to asphaltenes precipitation and deposition in the porous media and through the production system.[37, 41-43] For sub-surface application, if asphaltene precipitation and deposition occur in the reservoir rock it could reduce both porosity and permeability, and affecting negatively the reservoir wettability from a water-wet system to an oil-wet system that together with the high HO viscosities result in the reduction of the crude oil mobility.[37, 43] For on surface application, if asphaltene precipitation occurs throughout the production system, it could have a negative impact on pumps, pipelines and surface facilities due to flow blocking and corrosion.[39] In both cases these adverse effects result in reducing production and hence the energy return on investment (EROI), and in the worst scenario it could cause the abandonment of the operation.[42] Besides the role of asphaltenes in increasing crude oil viscosity and reducing its mobility in the reservoir, these asphaltenic compounds have significant effect on catalytic processes in refinery such as hydrocracking, hydrodesulfurization, hydrodenitrogenation and hydrodemetallisation, as they are considered the precursors of heteroatoms and high coke yield that lead to inefficient catalysis and reduce the distillable fraction of crude oil.[38, 44, 45] Modern techniques for in situ upgrading and recovery of crude oil consist in fractionating the chemical structure of the heaviest compounds present in the crude oil through in situ combustion,[46-48] pyrolysis,[49, 50] aquathermolysis [50-52] and oxidation at low temperatures.[53] More recently the steam assisted gravity drainage (SAGD) process appears as promising alternative to enhance the oil recovery.[54-56] However, all the aforementioned techniques have an average recovery

of 20-25% of the oil in place and up to 50% for SAGD procces.[20, 57] Besides the low EROI, during HO and EHO production and processing other problems like high greenhouse gases (GHG) emissions, disposal of wastewater and disposal of by-product carbon and sulfur have to be taken into account.[9]

Further, modern techniques for in situ upgrading and damage inhibition involve destabilization and deposition of asphaltenes or fractionating the chemical structure of the heaviest compounds present in the crude oil, leading to low energy return on investment (EROI) and a higher emission of greenhouse gas.[22]

Consequently, nanoparticles have recently become an area of interest for the oil and gas industries. Nanoparticle technology (i.e., the technology related to the preparation and/or applications of materials at nanoscale, 1–100 nm) has emerged as an area of interest for many applications;[58] including energy storage, production and conversion,[59-61] agricultural productivity enhancement and food processing,[62-66] water treatment and remediation,[67-72] medicine,[73-78] air pollution and remediation,[79-81] construction,[82, 83] pest detention and control, and so forth.[84, 85] In the oil industry, nanoparticles have potential to be used in several applications like enhancing the upgrading and recovery of bitumen,[56, 86-89] improving the efficiency of drilling fluids[90-94] and drilling bit,[95, 96] fines migration control [97-99] and oil removal from produced wastewater.[67, 68, 72] Further, because of their unique and exceptional properties, such as large surface area and size-and shape-dependent catalytic properties, nanoparticles can also be employed as adsorbents and/or catalysts for removal of heavy waste polar hydrocarbons from crude oil, like asphaltenes.[100-114] Nanoparticles have the flexibility for in-situ (in place) application, where the particles can travel smoothly with good degree of dispersion through the porous media without risk of pore blocking. [115] One would anticipate that by in-situ sequestration of the asphaltene molecules from the crude oil would enhance the in situ upgrading and inhibit asphaltene damage. This consequently leads to a lighter crude oil with an improved mobility through the reservoir, easier production and transporting processes, with a higher distillable fraction and higher EROI.

Although some published research works have focused on the role of nanoparticles as catalysts in crude oil upgrading and as inhibitors of the asphaltene damage, there is still a lack of understanding on the mechanism of interactions between the asphaltene molecules and nanoparticle surface. Accordingly, a depth and extensive investigation on different key variables, such as nanoparticle functionality and the presence of co-existing molecules will provide an insight on the mechanism and behavior of the nanoparticles efficiency as catalysts and inhibitors, resulting in an enhanced oil recovery and improving its quality. Hence, the main objective of this study is to synthesize and apply metallic and/or multi-metallic oxides (e.g, Ni, and Pd) supported nanoparticles that have high adsorption selectivity and catalytic activity towards heavy hydrocarbons like asphaltenes. Further, the specific objectives are:

I. Synthesize and characterize the supported and unsupported nanomaterials.

II. Evaluate the chemical nature of asphaltenes and the synthetized nanoparticles in adsorption and subsequent thermo-oxidative decomposition of adsorbed asphaltenes.

III. Develop a model that describes and captures the kinetic behavior of asphaltene aggregation in oil matrix in presence and absence of nanomaterials.

IV. Perform displacement tests in porous media to corroborate the effect of the nanomaterials in enhancing the crude oil mobility and the increase of the oil recovery using an in-house designed displacement setup.
V. Determine the catalytic activity of the synthesized nanomaterials towards asphaltenes thermo-oxidative decomposition by estimating the effective activation energy using the isoconversional method of Ozawa-Flyn-Wall.

VI. Propose different reaction mechanisms for the thermo-oxidative decomposition of asphaltenes in the presence and absence of nanomaterials.

VII. Develop a correlation between the adsorption affinity, the degree of asphaltene aggregation and the effective activation energy for asphaltene adsorption and subsequent thermal decomposition.

Hence, this document is divided in six main chapters that include: 1) Synthesis and characterization of nanoparticles, 2) Adsorption and subsequent catalytic thermal decomposition of *n*-C_7 asphaltenes, 3) Influence of *n*-C_7 asphaltene aggregation on their adsorption and catalytic behavior of nanoparticles, 4) Effect of Resin I on n-C7 asphaltene adsorption onto nanoparticles, 5) Influence of shear and nanoparticles on the aggregation and fragmentation of asphaltene aggregates and 6) Heavy oil upgrading and enhance recovery in a continuous steam injection process assisted by nanoparticulated catalysts.

References

1. Gill, S. S.; Tsolakis, A.; Dearn, K. D.; Rodríguez-Fernández, J., Combustion characteristics and emissions of Fischer-Tropsch diesel fuels in IC engines. *Progress in Energy and Combustion Science* **2011,** 37, (4), 503-523.
2. Berkowitz, N.; Speight, J. G., The oil sands of Alberta. *Fuel* **1975,** 54, (3), 138-149.
3. Shah, A.; Fishwick, R.; Wood, J.; Leeke, G.; Rigby, S.; Greaves, M., A review of novel techniques for heavy oil and bitumen extraction and upgrading. *Energy & Environmental Science* **2010,** 3, (6), 700-714.
4. Castaneda, L. C.; Munoz, J. A.; Ancheyta, J., Current situation of emerging technologies for upgrading of heavy oils. *Catalysis Today* **2014,** 220, 248-273.
5. Fan, C.; Zan, C.; Zhang, Q.; Ma, D.; Chu, Y.; Jiang, H.; Shi, L.; Wei, F., The oxidation of heavy oil: Thermogravimetric analysis and non-isothermal kinetics using the distributed activation energy model. *Fuel Processing Technology* **2014,** 119, 146-150.
6. Agency, I. E., *World Energy Outlook 2013*. Internationl Energy Agency: 2013.
7. Holditch, S. A., Tight gas sands. *Journal of Petroleum Technology* **2006,** 58, (6), 86-93.
8. Dong, Z.; Ayers, W. B.; Holditch, S. In *Probabilistic Evaluation of Global Technically Recoverable Tight Gas Resources*, SPE Eastern Regional Meeting, 2013; Society of Petroleum Engineers: 2013.
9. Chew, K. J., The future of oil: unconventional fossil fuels. *Philosophical Transactions of the Royal Society A: Mathematical, Physical and Engineering Sciences* **2014,** 372, (2006), 20120324.

10. Lv, Y.; Tang, D.; Xu, H.; Luo, H., Production characteristics and the key factors in high-rank coalbed methane fields: A case study on the Fanzhuang Block, Southern Qinshui Basin, China. *International Journal of Coal Geology* **2012,** 96, 93-108.
11. Gale, J.; Freund, P., Coal-Bed Methane Enhancement with CO2 Sequestration Worldwide Potential. *Environmental Geosciences* **2001,** 8, (3), 210-217.
12. Collett, T. S. In *Gas Hydrate Reservoir Properties*, Unconventional Resources Technology Conference, 2013; Society of Petroleum Engineers: 2013.
13. Kvenvolden, K. A.; Lorenson, T. D. In *Global occurrences of gas hydrate*, 1 th International Offshore and Polar Engineering Conference Stavanger, Stavanger, 2001; 2001; pp 462-467.
14. Rana, M. S.; Sámano, V.; Ancheyta, J.; Diaz, J., A review of recent advances on process technologies for upgrading of heavy oils and residua. *Fuel* **2007,** 86, (9), 1216-1231.
15. Meyer, R. F.; Attanasi, E. D., Heavy oil and natural bitumen-strategic petroleum resources. *World* **2003,** 434, 650.7.
16. Tedeschi, M. n. In *[13] RESERVES AND PRODUCTION OF HEAVY CRUDE OIL AND NATURAL BITUMEN*, 13th World Petroleum Congress, 1991; World Petroleum Congress: 1991.
17. IEA, Resources to reserves 2013. **2013**.
18. IEA, World Energy Investment Outlook. **2014**.
19. Beraud, S. S. L. In *Latin America Crude Oil Market Short Term Outlook*, Instituto Petroquimico Argentino, Buenos Aires, 2014; Buenos Aires, 2014.
20. Crudos pesados, la gran apuesta del sector. *Colombia Energía* 2013.
21. Haskett, W. J.; Brown, P. J. In *Evaluation of unconventional resource plays*, SPE Annual Technical Conference and Exhibition, 2005; Society of Petroleum Engineers: 2005.
22. Adams, J. J., Asphaltene Adsorption, a Literature Review. *Energy & Fuels* **2014**.
23. Mullins, O. C., The asphaltenes. *Annual Review of Analytical Chemistry* **2011,** 4, 393-418.
24. Mullins, O. C.; Sabbah, H.; Eyssautier, J. l.; Pomerantz, A. E.; Barré, L.; Andrews, A. B.; Ruiz-Morales, Y.; Mostowfi, F.; McFarlane, R.; Goual, L., Advances in asphaltene science and the Yen–Mullins model. *Energy & Fuels* **2012,** 26, (7), 3986-4003.
25. Acevedo, S.; Castro, A.; Negrin, J. G.; Fernández, A.; Escobar, G.; Piscitelli, V.; Delolme, F.; Dessalces, G., Relations between asphaltene structures and their physical and chemical properties: The rosary-type structure. *Energy & fuels* **2007,** 21, (4), 2165-2175.
26. Groenzin, H.; Mullins, O. C., *J. Phys. Chem. A* **1999,** 103, 11237.
27. Groenzin, H.; Mullins, O. C., Asphaltene molecular size and structure. *The Journal of Physical Chemistry A* **1999,** 103, (50), 11237-11245.
28. Speight, J. G., *The chemistry and technology of petroleum*. CRC press: 2014.
29. Durand, E.; Clemancey, M.; Lancelin, J.-M.; Verstraete, J.; Espinat, D.; Quoineaud, A.-A., Effect of chemical composition on asphaltenes aggregation. *Energy & Fuels* **2010,** 24, (2), 1051-1062.
30. Murgich, J., Molecular simulation and the aggregation of the heavy fractions in crude oils. *Molecular Simulation* **2003,** 29, (6-7), 451-461.
31. Mullins, O. C., The Modified Yen Model†. *Energy & Fuels* **2010,** 24, (4), 2179-2207.
32. Sabbah, H.; Morrow, A. L.; Pomerantz, A. E.; Zare, R. N., Evidence for island structures as the dominant architecture of asphaltenes. *Energy & Fuels* **2011,** 25, (4), 1597-1604.
33. Ruiz-Morales, Y., Aromaticity in pericondensed cyclopenta-fused polycyclic aromatic hydrocarbons determined by density functional theory nucleus-independent chemical shifts and the Y-rule-Implications in oil asphaltene stability. *Canadian Journal of Chemistry* **2009,** 87, (10), 1280-1295.
34. Yen, T. F.; Erdman, J. G.; Pollack, S. S., Investigation of the structure of petroleum asphaltenes by X-ray diffraction. *Analytical Chemistry* **1961,** 33, (11), 1587-1594.
35. Mullins, O. C.; Pomerantz, A. E.; Zuo, J. Y.; Dong, C., Downhole Fluid Analysis and Asphaltene Science for Petroleum Reservoir Evaluation. *Annual review of chemical and biomolecular engineering* **2014**, (0).

36. Ghanavati, M.; Shojaei, M.-J.; S. A, A. R., Effects of Asphaltene Content and Temperature on Viscosity of Iranian Heavy Crude Oil: Experimental and Modeling Study. *Energy & Fuels* **2013,** 27, (12), 7217-7232.
37. Leontaritis, K.; Amaefule, J.; Charles, R., A systematic approach for the prevention and treatment of formation damage caused by asphaltene deposition. *SPE Production & Facilities* **1994,** 9, (03), 157-164.
38. Chianelli, R. R.; Siadati, M.; Mehta, A.; Pople, J.; Ortega, L. C.; Chiang, L. Y., Self-assembly of asphaltene aggregates: Synchrotron, simulation and chemical modeling techniques applied to problems in the structure and reactivity of asphaltenes. In *Asphaltenes, Heavy Oils, and Petroleomics*, Springer: 2007; pp 375-400.
39. Chavan, S.; Kini, H.; Ghosal, R., Process for Sulfur Reduction from High Viscosity Petroleum Oils.
40. WU, C.; LEI, G.-L.; YAO, C.-j.; SUN, K.-j.; Gai, P.-y.; CAO, Y.-b., Mechanism for reducing the viscosity of extra-heavy oil by aquathermolysis with an amphiphilic catalyst. *Journal of Fuel Chemistry and Technology* **2010,** 38, (6), 684-690.
41. Oskui, G. R. P.; Jumaa, M. A.; Folad, E. G.; Rashed, A.; Patil, S. In *Systematic Approach for Prevention and Remediation of Asphaltene Problems During CO2/Hydrocarbon Injection Project*, The Twenty-first International Offshore and Polar Engineering Conference, 2011; International Society of Offshore and Polar Engineers: 2011.
42. Gharfeh, S.; Yen, A.; Asomaning, S.; Blumer, D., Asphaltene flocculation onset determinations for heavy crude oil and its implications. *Petroleum science and technology* **2004,** 22, (7-8), 1055-1072.
43. Al-Maamari, R. S.; Buckley, J. S., Asphaltene precipitation and alteration of wetting: the potential for wettability changes during oil production. *SPE Reservoir Evaluation & Engineering* **2003,** 6, (04), 210-214.
44. Benito, A. M.; Callejas, M. A.; Martínez, M. T., Kinetics of asphaltene hydroconversion: 2. Catalytic hydrocracking of a coal residue. *Fuel* **1997,** 76, (10), 907-911.
45. Alshareef, A. H.; Scherer, A.; Tan, X.; Azyat, K.; Stryker, J. M.; Tykwinski, R. R.; Gray, M. R., Formation of archipelago structures during thermal cracking implicates a chemical mechanism for the formation of petroleum asphaltenes. *Energy & Fuels* **2011,** 25, (5), 2130-2136.
46. Shu, W. R., In-situ combustion method for recovery of heavy oil utilizing oxygen and carbon dioxide as initial oxidant. In Google Patents: 1983.
47. Cavallaro, A.; Galliano, G.; Moore, R.; Mehta, S.; Ursenbach, M.; Zalewski, E.; Pereira, P., In situ upgrading of Llancanelo heavy oil using in situ combustion and a downhole catalyst bed. *Journal of Canadian Petroleum Technology* **2008,** 47, (9), 23-31.
48. Moore, R.; Laureshen, C.; Mehta, S.; Ursenbach, M.; Belgrave, J.; Weissman, J.; Kessler, R., A downhole catalytic upgrading process for heavy oil using in situ combustion. *Journal of Canadian Petroleum Technology* **1999,** 38, (13).
49. Johnson, A. R.; Narayanan, S.; Woebcke, H. N., Integrated heavy oil pyrolysis process. In Google Patents: 1986.
50. Ambalae, A.; Mahinpey, N.; Freitag, N., Thermogravimetric studies on pyrolysis and combustion behavior of a heavy oil and its asphaltenes. *Energy & fuels* **2006,** 20, (2), 560-565.
51. Clark, P.; Hyne, J., Steam-oil chemical reactions: mechanisms for the aquathermolysis of heavy oil. *Aostra J Res* **1984,** 1, (1), 15-20.
52. Li, W.; Zhu, J.-H.; Qi, J.-H., Application of nano-nickel catalyst in the viscosity reduction of Liaohe extra-heavy oil by aqua-thermolysis. *Journal of Fuel Chemistry and Technology* **2007,** 35, (2), 176-180.
53. Wichert, G.; Okazawa, N.; Moore, R.; Belgrave, J. In *In-situ upgrading of heavy oils by low-temperature oxidation in the presence of caustic additives*, International heavy oil symposium, 1995; 1995; pp 529-536.
54. Butler, R., SAGD comes of age! *Journal of Canadian Petroleum Technology* **1998,** 37, (07).

55. Nasr, T.; Beaulieu, G.; Golbeck, H.; Heck, G., Novel expanding solvent-SAGD process ES-SAGD. *Journal of Canadian Petroleum Technology* **2003,** 42, (1), 13-16.
56. Hashemi, R.; Nassar, N. N.; Pereira Almao, P., Enhanced heavy oil recovery by in situ prepared ultradispersed multimetallic nanoparticles: A study of hot fluid flooding for Athabasca bitumen recovery. *Energy & Fuels* **2013,** 27, (4), 2194-2201.
57. Birn, K.; Khanna, P. In *A discussion paper on the oil sands: challenges and opportunities*, World Energy Congress, 2010; 2010.
58. Salamanca-Buentello, F.; Persad, D. L.; Martin, D. K.; Daar, A. S.; Singer, P. A., Nanotechnology and the developing world. *PLoS Medicine* **2005,** 2, (5), e97.
59. Liu, C.; Fan, Y.; Liu, M.; Cong, H.; Cheng, H.; Dresselhaus, M. S., Hydrogen storage in single-walled carbon nanotubes at room temperature. *Science* **1999,** 286, (5442), 1127-1129.
60. Leschkies, K. S.; Divakar, R.; Basu, J.; Enache-Pommer, E.; Boercker, J. E.; Carter, C. B.; Kortshagen, U. R.; Norris, D. J.; Aydil, E. S., Photosensitization of ZnO nanowires with CdSe quantum dots for photovoltaic devices. *Nano Letters* **2007,** 7, (6), 1793-1798.
61. Rowell, M. W.; Topinka, M. A.; McGehee, M. D.; Prall, H.-J.; Dennler, G.; Sariciftci, N. S.; Hu, L.; Gruner, G., Organic solar cells with carbon nanotube network electrodes. *Applied Physics Letters* **2006,** 88, (23), 233506.
62. Ramesh, K.; Biswas, A. K.; Somasundaram, J.; Subba Rao, A., Nanoporous zeolites in farming: current status and issues ahead. *Current Science (00113891)* **2010,** 99, (6).
63. Pérez-de-Luque, A.; Rubiales, D., Nanotechnology for parasitic plant control. *Pest management science* **2009,** 65, (5), 540-545.
64. Grillo, R.; dos Santos, N. Z. P.; Maruyama, C. R.; Rosa, A. H.; de Lima, R.; Fraceto, L. F., Poly (ε-caprolactone) nanocapsules as carrier systems for herbicides: Physico-chemical characterization and genotoxicity evaluation. *Journal of hazardous materials* **2012,** 231, 1-9.
65. Avella, M.; De Vlieger, J. J.; Errico, M. E.; Fischer, S.; Vacca, P.; Volpe, M. G., Biodegradable starch/clay nanocomposite films for food packaging applications. *Food chemistry* **2005,** 93, (3), 467-474.
66. Sorrentino, A.; Gorrasi, G.; Vittoria, V., Potential perspectives of bio-nanocomposites for food packaging applications. *Trends in Food Science & Technology* **2007,** 18, (2), 84-95.
67. Franco, C. A.; Cortés, F. B.; Nassar, N. N., Adsorptive Removal of Oil Spill From Oil-in-Fresh Water Emulsions by Hydrophobic Alumina Nanoparticles Functionalized with Petroleum Vacuum Residue. *Journal of Colloid and Interface Science* **2014**.
68. MARTÍNEZ AGUILAR, M.; BERNARDO CORTÉS, F.; ANDRÉS FRANCO ARIZA, C., Tratamiento de agua basado en la adsorción de crudo en nanopartículas polares y no polares. *Informador Técnico* **2013,** 77, (1).
69. Anbia, M.; Amirmahmoodi, S., Adsorption of phenolic compounds from aqueous solutions using functionalized SBA-15 as a nano-sorbent. *Scientia Iranica* **2011,** 18, (3), 446-452.
70. Nassar, N. N.; Ringsred, A., Rapid adsorption of methylene blue from aqueous solutions by goethite nanoadsorbents. *Environmental Engineering Science* **2012,** 29, (8), 790-797.
71. Nassar, N. N., Kinetics, equilibrium and thermodynamic studies on the adsorptive removal of nickel, cadmium and cobalt from wastewater by superparamagnetic iron oxide nanoadsorbents. *The Canadian Journal of Chemical Engineering* **2012,** 90, (5), 1231-1238.
72. Franco, C. A.; Nassar, N. N.; Cortés, F. B., Removal of oil from oil-in-saltwater emulsions by adsorption onto nano-alumina functionalized with petroleum vacuum residue. *Journal of colloid and interface science* **2014,** 433, 58-67.
73. Nie, S.; Xing, Y.; Kim, G. J.; Simons, J. W., Nanotechnology applications in cancer. *Annu. Rev. Biomed. Eng.* **2007,** 9, 257-288.
74. Gupta, U.; Jain, N. K., Non-polymeric nano-carriers in HIV/AIDS drug delivery and targeting. *Advanced drug delivery reviews* **2010,** 62, (4), 478-490.

75. du Toit, L. C.; Pillay, V.; Choonara, Y. E., Nano-microbicides: Challenges in drug delivery, patient ethics and intellectual property in the war against HIV/AIDS. *Advanced drug delivery reviews* **2010,** 62, (4), 532-546.
76. Sumer, B.; Gao, J., Theranostic nanomedicine for cancer. **2008**.
77. Moghimi, S. M.; Hunter, A. C.; Murray, J. C., Nanomedicine: current status and future prospects. *The FASEB Journal* **2005,** 19, (3), 311-330.
78. Wagner, V.; Dullaart, A.; Bock, A.-K.; Zweck, A., The emerging nanomedicine landscape. *Nature biotechnology* **2006,** 24, (10), 1211-1218.
79. Nel, A.; Xia, T.; Mädler, L.; Li, N., Toxic potential of materials at the nanolevel. *Science* **2006,** 311, (5761), 622-627.
80. Cheng, Y. T.; Rodak, D.; Wong, C.; Hayden, C., Effects of micro-and nano-structures on the self-cleaning behaviour of lotus leaves. *Nanotechnology* **2006,** 17, (5), 1359.
81. Nakajima, A.; Hashimoto, K.; Watanabe, T.; Takai, K.; Yamauchi, G.; Fujishima, A., Transparent superhydrophobic thin films with self-cleaning properties. *Langmuir* **2000,** 16, (17), 7044-7047.
82. Zhu, W.; Bartos, P.; Porro, A., Application of nanotechnology in construction. *Materials and Structures* **2004,** 37, (9), 649-658.
83. Makar, J.; Beaudoin, J., Carbon nanotubes and their application in the construction industry. *SPECIAL PUBLICATION-ROYAL SOCIETY OF CHEMISTRY* **2004,** 292, 331-342.
84. Bhattacharyya, A.; Bhaumik, A.; Rani, P. U.; Mandal, S.; Epidi, T. T., Nano-particles-A recent approach to insect pest control. *African Journal of Biotechnology* **2010,** 9, (24), 3489-3493.
85. Yang, F.-L.; Li, X.-G.; Zhu, F.; Lei, C.-L., Structural characterization of nanoparticles loaded with garlic essential oil and their insecticidal activity against Tribolium castaneum (Herbst)(Coleoptera: Tenebrionidae). *Journal of agricultural and food chemistry* **2009,** 57, (21), 10156-10162.
86. Hashemi, R.; Nassar, N. N.; Pereira Almao, P., In Situ Upgrading of Athabasca Bitumen Using Multimetallic Ultradispersed Nanocatalysts in an Oil Sands Packed-Bed Column: Part 2. Solid Analysis and Gaseous Product Distribution. *Energy & Fuels* **2014,** 28, (2), 1351-1361.
87. Hashemi, R.; Nassar, N. N.; Pereira Almao, P., In Situ Upgrading of Athabasca Bitumen Using Multimetallic Ultradispersed Nanocatalysts in an Oil Sands Packed-Bed Column: Part 1. Produced Liquid Quality Enhancement. *Energy & Fuels* **2014,** 28, (2), 1338-1350.
88. Franco, C. A.; Nassar, N. N.; Ruiz, M. A.; Pereira-Almao, P. R.; Cortés, F. B., Nanoparticles for Inhibition of Asphaltenes Damage: Adsorption Study and Displacement Test on Porous Media. *Energy & Fuels* **2013,** 27, 2899−2907.
89. Hashemi, R.; Nassar, N. N.; Pereira-Almao, P., Transport Behavior of Multimetallic Ultradispersed Nanoparticles in an Oil-Sands-Packed Bed Column at a High Temperature and Pressure. *Energy & Fuels* **2012,** 26, (3), 1645-1655.
90. Jimenez, M. A.; Genolet, L. C.; Chavez, J. C.; Espin, D., Method for treating drilling fluid using nanoparticles. In Google Patents: 2003.
91. Sensoy, T.; Chenevert, M. E.; Sharma, M. M. In *Minimizing water invasion in shales using nanoparticles*, SPE Annual Technical Conference and Exhibition, 2009; Society of Petroleum Engineers: 2009.
92. Zakaria, M.; Husein, M. M.; Harland, G. In *Novel nanoparticle-based drilling fluid with improved characteristics*, SPE International Oilfield Nanotechnology Conference and Exhibition, 2012; Society of Petroleum Engineers: 2012.
93. Srivatsa, J. T.; Ziaja, M. B. In *An Experimental Investigation on Use of Nanoparticles as Fluid Loss Additives in a Surfactant-Polymer Based Drilling Fluids*, International Petroleum Technology Conference, 2011; International Petroleum Technology Conference: 2011.
94. Hareland, G.; Wu, A.; Lei, L.; Husein, M. M.; Zakaria, M. F. In *Innovative Nanoparticle Drilling Fluid and Its Benefits to Horizontal or Extended Reach Drilling*, SPE Canadian Unconventional Resources Conference, 2012; Society of Petroleum Engineers: 2012.

95. Sengupta, S.; Kumar, A. In *Nano-Ceramic Coatings-A Means of Enhancing Bit Life and Reducing Drill String Trips*, IPTC 2013: International Petroleum Technology Conference, 2013; 2013.
96. Chakraborty, S.; Agrawal, G.; DiGiovanni, A.; Scott, D. E. In *The Trick Is The Surface-Functionalized Nanodiamond PDC Technology*, SPE International Oilfield Nanotechnology Conference and Exhibition, 2012; Society of Petroleum Engineers: 2012.
97. Huang, T.; Evans, B. A.; Crews, J. B.; Belcher, C. K. In *Field case study on formation fines control with nanoparticles in offshore applications*, SPE Annual Technical Conference and Exhibition, 2010; Society of Petroleum Engineers: 2010.
98. Huang, T.; Crews, J. B.; Willingham, J. R. In *Nanoparticles for formation fines fixation and improving performance of surfactant structure fluids*, International Petroleum Technology Conference, 2008; International Petroleum Technology Conference: 2008.
99. Habibi, A.; Pourafshari, P.; Ahmadi, M.; Ayatollahi, S. In *Reduction of Fine Migration by Nanofluids Injection An Experimental Study*, SPE European Formation Damage Conference, 2011; Society of Petroleum Engineers: 2011.
100. Franco, C.; Patiño, E.; Benjumea, P.; Ruiz, M. A.; Cortés, F. B., Kinetic and thermodynamic equilibrium of asphaltenes sorption onto nanoparticles of nickel oxide supported on nanoparticulated alumina. *Fuel* **2013,** 105, 408-414.
101. Giraldo, J.; Nassar, N. N.; Benjumea, P.; Pereira-Almao, P.; Cortés, F. B., Modeling and Prediction of Asphaltene Adsorption Isotherms Using Polanyi's Modified Theory. *Energy & Fuels* **2013,** 27, 2908−2914.
102. Nassar, N. N.; Hassan, A.; Luna, G.; Pereira-Almao, P., Kinetics of the catalytic thermo-oxidation of asphaltenes at isothermal conditions on different metal oxide nanoparticle surfaces. *Catalysis Today* **2013,** 207, (0), 127-132.
103. Hassan, A.; Lopez-Linares, F.; Nassar, N. N.; Carbognani-Arambarri, L.; Pereira-Almao, P., Development of a support for a NiO catalyst for selective adsorption and post-adsorption catalytic steam gasification of thermally converted asphaltenes. *Catalysis Today* **2013,** 207, (0), 112-118.
104. Franco, C. A.; Montoya, T.; Nassar, N. N.; Pereira-Almao, P.; Cortés, F. B., Adsorption and Subsequent Oxidation of Colombian Asphaltenes onto Nickel and/or Palladium Oxide Supported on Fumed Silica Nanoparticles. *Energy & Fuels* **2013,** 27, (12), 7336-7347.
105. Nassar, N. N.; Hassan, A.; Carbognani, L.; Lopez-Linares, F.; Pereira-Almao, P., Iron oxide nanoparticles for rapid adsorption and enhanced catalytic oxidation of thermally cracked asphaltenes. *Fuel* **2012,** 95, 257–262.
106. Nassar, N.; Hassan, A.; Pereira-Almao, P., Thermogravimetric studies on catalytic effect of metal oxide nanoparticles on asphaltene pyrolysis under inert conditions. *Journal of Thermal Analysis and Calorimetry* **2012,** 110, (3), 1327-1332.
107. Nassar, N. N.; Hassan, A.; Pereira-Almao, P., Effect of the Particle Size on Asphaltene Adsorption and Catalytic Oxidation onto Alumina Particles. *Energy & Fuels* **2011,** 25, (9), 3961-3965.
108. Nassar, N. N.; Hassan, A.; Pereira-Almao, P., Comparative oxidation of adsorbed asphaltenes onto transition metal oxide nanoparticles. *Colloids and Surfaces A: Physicochemical and Engineering Aspects* **2011,** 384, (1-3), 145-149.
109. Nassar, N. N.; Hassan, A.; Pereira-Almao, P., Effect of surface acidity and basicity of aluminas on asphaltene adsorption and oxidation. *Journal of Colloid and Interface Science* **2011,** 360 233–238.
110. Nassar, N. N.; Hassan, A.; Pereira-Almao, P., Application of Nanotechnology for Heavy Oil Upgrading: Catalytic Steam Gasification/Cracking of Asphaltenes. *Energy & Fuels* **2011,** 25, (4), 1566-1570.
111. Nassar, N. N.; Hassan, A.; Pereira-Almao, P., Metal Oxide Nanoparticles for Asphaltene Adsorption and Oxidation. *Energy & Fuels* **2011,** 25, (3), 1017-1023.

112. Montoya, T.; Coral, D.; Franco, C. A.; Nassar, N. N.; Cortés, F. B., A Novel Solid–Liquid Equilibrium Model for Describing the Adsorption of Associating Asphaltene Molecules onto Solid Surfaces Based on the "Chemical Theory". *Energy & Fuels* **2014,** 28, (8), 4963-4975.
113. Nassar, N. N.; Tatiana Montoya, T.; Franco, C. A.; Cortés, F. B.; Pereira-Almao, P. R., A New Model for Describing the Adsorption of Asphaltenes on Porous Media at a High Pressure and Temperature under Flow Conditions. *Energy & Fuels* **2015**.
114. Cortés, F. B.; Mejía, J. M.; Ruiz, M. A.; Benjumea, P.; Riffel, D. B., Sorption of asphaltenes onto nanoparticles of nickel oxide supported on nanoparticulated silica gel. *Energy & Fuels* **2012,** 26, (3), 1725-1730.
115. Hashemi, R.; Nassar, N. N.; Pereira-Almao, P., *Energy Fuels* **2012,** 26, (3), 1645.

1. Synthesis and characterization of nanoparticles

According to the International Union of Pure and Applied Chemistry (IUPAC), a nanoparticle is defined as a "*Microscopic particle whose size is measured in nanometers, often restricted to so-called nanosized particles (NSPs; <100 nm in aerodynamic diameter), also called ultrafine particles"*.[1] Recently, nanoparticle technology has promised many benefits through nano-enabled applications in multiple sectors, including energy,[2-4] environment,[5-12] medicine[13-18] and agriculture,[19-23] among others.[24] The applications of nanoparticle technology to enhance upgrading and recover of crude oil are well recognized in the oil industry due to their high stability, superior adsorption and catalytic behavior, as well as their excellent dispersion ability.[25, 26] Hence, the characterization of the nanoparticles is of paramount importance in the understanding of the nanoparticles' role in the heavy oil and extra-heavy oil upgrading and inhibition of formation damage. Nanoparticles' size is a key parameter to take into account when considering these materials for an *in-situ* application. It has to be ensured that the material available for injection into the reservoir meets the size constraints to ensure that nanoparticles would not cause a further damage into the reservoir due to pore throat bridging or blockage. According to the one-third to one-seventh arch principles, the particle size could contribute to the bridging/blockage as follows: i) particles larger than 1/3 of pore size are prone to generate pore blocking, ii) particles in the range 1/7 – 1/3 of pore size would generate a bridge in the pore throat that further will generate pore blockage and iii) particles with size lower than 1/7 of pore size are able to pass through the pore throat.[27-29] It is expected that nanoparticles employed for injection into the reservoir would accomplish the third aforementioned scenario. Properties such as surface area and thermal stability of nanoparticles are important in the understanding of the uptake capacity and availability of its use at determined temperature.[30] In this order, this chapter describes the synthesis and characterization of the selected nanoparticles. Silica and carbon sphere nanoparticles were synthesized through the sol-gel and resorcinol-formaldehyde polycondensation methods, respectively. Additionally, a selected support was functionalized with NiO and PdO nanocrystals by the incipient wetness technique followed by calcination in order to obtain the metal oxide dispersed over the support surface. Nanoparticles were characterized trough thermal stability, particle size and surface area measurements.

1.1 Experimental

1.1.1 Materials

In-house prepared silica nanoparticles (SS) and carbon nanospheres (CNS) and commercial nanoparticles of fumed silica (CS), magnetite (CM), titania (CTi), and γ-alumina (CAl) were used as adsorbents along the thesis work. The commercial nanoparticles of fumed silica, titania and γ-alumina were obtained from Sigma-Aldrich (St. Louis, MO) and commercial magnetite nanoparticles from Nanostructured & Amorphous Materials (Houston, TX).

Tetraethyl orthosilicate (TEOS, > 99%), ethanol (99.9%) and NH_4OH (28%) were used to synthesize the silica nanoparticles. Additionally, formaldehyde (37%), resorcinol (99%), hexadecyltrimethyl - ammonium bromide (CTAB, >99%), tert-butanol (99.5%), Cs_2O_3 (99.9%), acetone (>99.5%), deionized water and gaseous N_2 were used for the CNS synthesis. All reactants employed for the SS and CNS synthesis were purchased from Sigma-Aldrich (St. Louis, MO). The nanoparticles' surface was functionalized with Pd and Ni oxides using salt precursors $Ni(NO_3)_2{\cdot}(6H_2O)$ and $Pd(NO_3)_2$ obtained from MercK KGaA, Germany.

1.1.2 Nanoparticles Synthesis

- **Silica nanoparticles**

The SS nanoparticles were synthetized using the sol-gel method following two different basic routes, namely A and B, based on the procedure initially proposed by Stöber et al.[31, 32] The sol-gel method consists in a sol preparation, its further gelation and solvent removal and could be produced from inorganic or organic precursors. Here, silica nanoparticles were obtained by forming a 3-D structure of interconnected siloxane bridges (Si–O–Si) achieved through simultaneous and repeated hydrolysis and polycondensation of determined precursor such as TEOS.[33] NH_4OH and ethanol are used, respectively, as catalyst of the hydrolysis reaction and as mutual solvent between water and TEOS.[31] Route A consisted in stirring the previously mixed reactants at 300 rpm for 4 hours. Then, the solution is centrifuged at 4500 rpm for 30 min using a Hermle Z 306 Universal Centrifuge (Labnet, NJ) and left to stand overnight. Finally, the result is washed with ethanol and deionized water and dried overnight at 120°C. For route A two TEOS:H_2O:NH_4OH:ethanol molar ratios of 1:6:1:0.25 and 1:3:0.5:0.17 were used. For route B the TEOS:H_2O:NH_4OH:ethanol molar ratio was changed to 1:6:1:3 and the initial stirring of the reactants was carried out for 24 h. The following steps of the procedure were the same as for route A. In this document, SS nanoparticles are nomenclated according to the employed route and the H_2O/TEOS molar ratio. For instance, SS nanoparticles obtained through route A using a H_2O/TEOS molar ratio of 6 are labeled as SSA6.

- **Carbon nanospheres**

The CNS were prepared trough resorcinol-formaldehyde polycondensation in water.[34] Cs_2CO_3 was used as catalyst of the polymerization reaction and tert-butanol was employed as surfactant. Figure 1.1 shows the experimental set-up required for the CNS synthesis. Two different CNS were synthesized by varying the resorcinol:Cs_2CO_3 molar ratio in 150:1 and 300:1. First, a solution of CTAB, tert-butanol and water is prepared at a molar ratio of H_2O:CTAB:ter-butanol of 1:323:153 and is preheated at 85°C in the tripple-neck round-bottom flask. At the same time, a resorcinol-formaldehyde solution is prepared at recorcinol:formaldehyde:H_2O molar ratio of 1:0.19:0.006 and the Cs_2CO_3 is added until the desired resorcinol:Cs_2CO_3 molar ratio is reached. Once the H_2O+CTAB+ter-butanol reaches the desired temperature, the resorcinol+formaldehyde+catalyst is carefully added by one of the lateral necks of the round-bottom flask. The system is then closed and maintained under stirring at 250 rpm for 34 hours at the desired temperature. Posteriorly, the solution is recovered and filtered. The product is immersed in acetone for three days and the acetone is replaced each 12 hours in order to prevent the structure collapse during the drying or carbonization steps.[35] After, the product is filtered again and dried at 80°C using a stove. Finally, the material was carbonized in an inert atmosphere using a tubular furnace with a constant N_2 flow of 150 cm^3/min and a heating rate of 1°C/min until 600°C were the sample was left in an isotherm for 2 hours. In this document CNS with resorcinol:Cs_2CO_3 molar ratios of 150:1 and 300:1 are labeled CNS150 and CNS300, respectively.

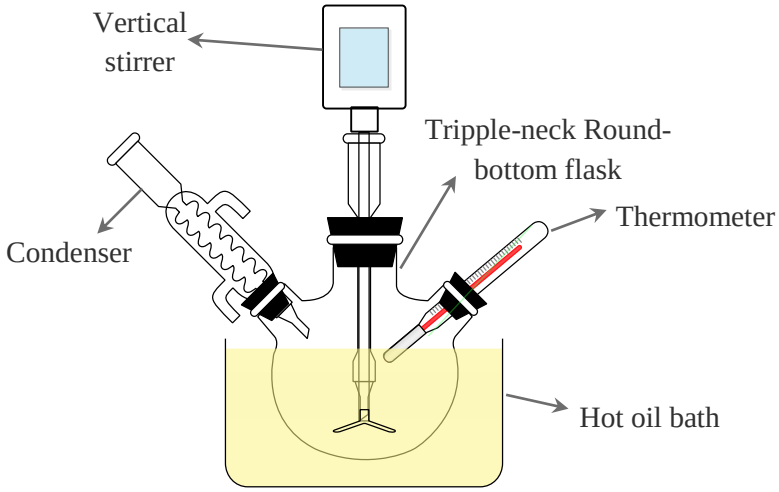

Figure 1.1. Experimental set-up for CNS synthesis.

- **Nanoparticles functionalization**

Nanoparticles were functionalized with NiO and/or PdO in order to provide a higher selectivity and catalytic activity to asphaltenes adsorption and subsequent decomposition. CS was used as support for evaluating the efficiency of the incorporation of the aforementioned metal oxides in the adsorption and decomposition of asphaltenes under oxidation, pyrolysis and gasification catalytic processes. In addition, CTi and CAl nanoparticles were used as support for evaluating the effect of the inorganic oxide support on the asphaltenes adsorption and post catalytic gasification. Then, the following procedure was applied independently of the support employed. In brief, the desired support was firstly dried at 120°C and posteriorly impregnated with an aqueous solutions of nickel nitrate $Ni(NO_3)_2$ and/or $Pd(NO_3)_2$ at the defined mass percentage for 3 h according to a Simplex−centroid mixture design (SCMD). The SCMD was used to determine the optimal mixture of palladium, nickel, and support nanoparticles to minimize the decomposition temperature of the asphaltenes. Normally, SCMD is used to study the relationships between the proportions of different variables and responses.[36] Figure 1.2 shows the SCMD with CS, NiO and PdO. Details of the used SCMD can be found in Appendix A. The impregnated material was then further dried at 120°C for 6 h. The obtained solid was calcined at 450°C for 6 h to obtain the hybrid nanoparticle support. The aqueous solution used for impregnation containing an X wt % of $Pd(NO_3)_2$ and/or Y wt % of $Ni(NO_3)_2$ quantity was used for the synthesis of CSNiYPdX nanoparticles on the silica support with the incipient wetness technique.[37, 38] Should be noted here that the Ni and Pd precursors are hygroscopic salts. These materials become oxides after calcination. The hybrid nanomaterials obtained in this study are called supported hygroscopic salt (SHS) and denoted by the initial letter of the support followed by the symbol of the cation of the resulting metal oxide after calcination and the weight percentage of the aqueous solutions of nickel nitrate $Ni(NO_3)_2$ and/or $Pd(NO_3)_2$ employed for impregnation. For instance, CSNi1Pd1 denotes a SHS synthesized by using commercial silica nanoparticles as support and containing 1 wt % of $Ni(NO_3)_2$ and 1 wt % $Pd(NO_3)_2$, which would produce, after calcination, a nanosilica with NiO and PdO nanoparticles on its surface.

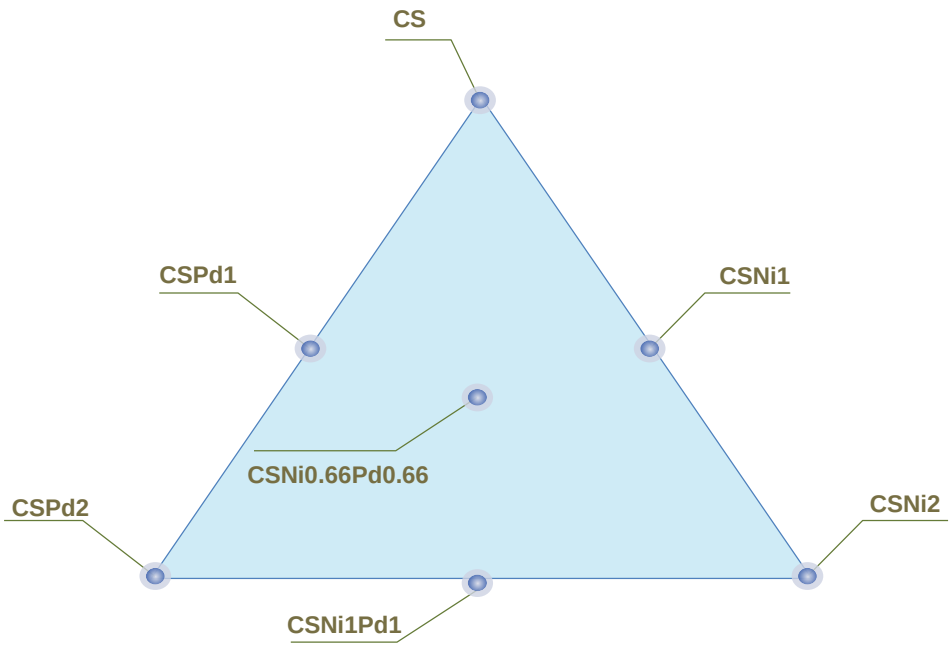

Figure 1.2. Simplex−centroid mixture design with CS, NiO and/or PdO.

1.1.3 Nanoparticles characterization

Commercial, synthesized and functionalized nanoparticles were characterized trough particles size and surface area. Additionally, the thermal stability of the synthesized nanoparticles was evaluated trough thermo-gravimetric analyses (TGA). Particle or crystallite size of nanoparticles was determined using field emission scanning electron microscopy (FESEM) X-ray diffraction (XRD and dynamic light scattering (DLS) measurements. The surface areas (S_{BET}) of the selected nanoparticles were measured following the Brunauer−Emmett−Teller (BET)[39, 40] method and was compared to the geometrical surface area according to the estimated particle size.

- **Thermo-gravimetric analyses (TGA)**

TGA studies are important for understanding the temperature effect on the stability of the different synthesized nanoparticles. The thermogravimetric analyses were carried out with a TGA analyzer (Q50, TA Instruments, Inc., New Castle, DE) by heating the samples in air from 30°C to 700°C at a fixed heating rate of 20°C/min. The sample mass was kept low to circumvent the diffusion limitations (ca. 5 mg). The airflow rate was a constant 100 cm^3/min throughout the experiment. Before the samples were transferred for TGA analysis, they were dried overnight in a vacuum oven. Further, before the TGA experiments, the instrument was calibrated for mass and heat changes as well as temperature readings, using nickel as a reference material. Each run was repeated at least twice to confirm the reproducibility of the experiment, which was achieved successfully.

- **Particle size measurements**

The size of the evaluated nanoparticles (*dp*) was determined by FESEM, DLS and XRD. A JSM-6701F (JEOL, Japan) field emission scanning electron microscope was used to obtain images of the selected materials with their particle size distribution. Sample was prepared by dispersing the material on ethanol in a concentration of 100 mg/L and sonicated for 3 h at room temperature. Then, a drop of the dispersion was carefully placed in a graphite tape previously stuck in the apparatus sampler. Finally, the sample is gold-plated and further introduced to the microscope.

DLS measurements were performed using a nanoplus-3 from Micromeritics (Norcross, ATL) set at room temperature and equipped with a 0.9 mL glass cell.[41-43] The solid sample was dispersed in water in a relation of 0.5 mg/10 mL and sonicated for four hours. Then, an aliquot of the sonicated sample was placed on the glass cell. The scattering angle varies according to the solvent used to optimize the intensity of the flocculation of scattering light. The mean particle diameter (hydrodynamic diameter) is obtained from the Stokes-Einstein equation, as follows: [44]

$$dp = \frac{k_B T}{3\pi\eta D_a} \tag{1.1}$$

where k_B (1.38 x 10^{-23} $m^2kg{\cdot}s^{-2}K^{-1}$) is the Boltzmann constant, T (K) is temperature, η (cP) is the viscosity of the medium, and D_a ($m^2{\cdot}s^{-1}$) is the diffusion coefficient of the particles.

The crystallite size of the nanoparticles was measured by applying the Scherrer equation to the primary XRD peak. XRD patterns were recorded with an X Pert PRO MPD X-ray diffractometer from PANalytical using Cu Ka radiation operating at 60 kV and 40 mA with a θ/2θ goniometer.

- **Surface area estimation**

The S_{BET} of the selected nanoparticles were measured following the BET method.[39, 40] This was achieved by performing nitrogen adsorption−desorption at 196°C, using an Autosorb-1 from Quantacrome. The samples were degassed at 140°C under N_2 flow overnight before analysis. Surface areas were calculated using the BET equation.

Additionally, assuming non-porous spheres with sphericity = 1, the geometrical surface area (*SA*, m^2/g) of the nanoparticles was calculated according to Eq. 1.2: [45, 46]

$$SA = \frac{6000}{dp \cdot \rho} \tag{1.2}$$

where ρ (g/cm^3) is the material true density taken as 2.65, 4.23, 3.95, 4.95 and 1.80 g/cm^3 for SiO_2, TiO_2, Al_2O_3, Fe_3O_4 and CNS, respectively.

1.2 Results

1.2.1 Thermal stability of synthesized nanoparticles

Panels a and b of Figure 1.3 show the mas loss profile of a) SS nanoparticles and b) CNS under an oxidative atmosphere at a fixed heating rate of 20°C/min. From Figure 1.3a it can observed that the mass loss follows the trend SSA6 < SSB6 < SSA3. The mass loss could be due to remaining solvent in the particles structure, adsorbed water or expulsion of silanol groups from the silica structure.[47] When comparing SSA6 and SSB6 nanoparticles, one can infer that, as the only difference in the molar ratios corresponds to ethanol, the higher mass loss for SSB6 than SSA6 nanoparticles could lie in the remaining amount of adsorbed solvent in the material structure. Jal et al.,[47] found that until 360°C the complete removal of entrapped or adsorbed water is achieved, leading then to a phase transition of the nanoparticles. Also, Fyfe et al.[48] reported that vicinal silanol are expelled in the range 200°C – 400°C and germinal and isolated silanols between 400°C and 800°C.[48] Regarding to the CNS, it is observed from Figure 1.3b that about the 10% of the sample mass is oxidized until 560°C for both CNS150 and CNS300. However, the main mass loss occurs around 600°C. This is due at 600°C the CNS were carbonized and is expected that for higher temperatures their thermal stability decreases.

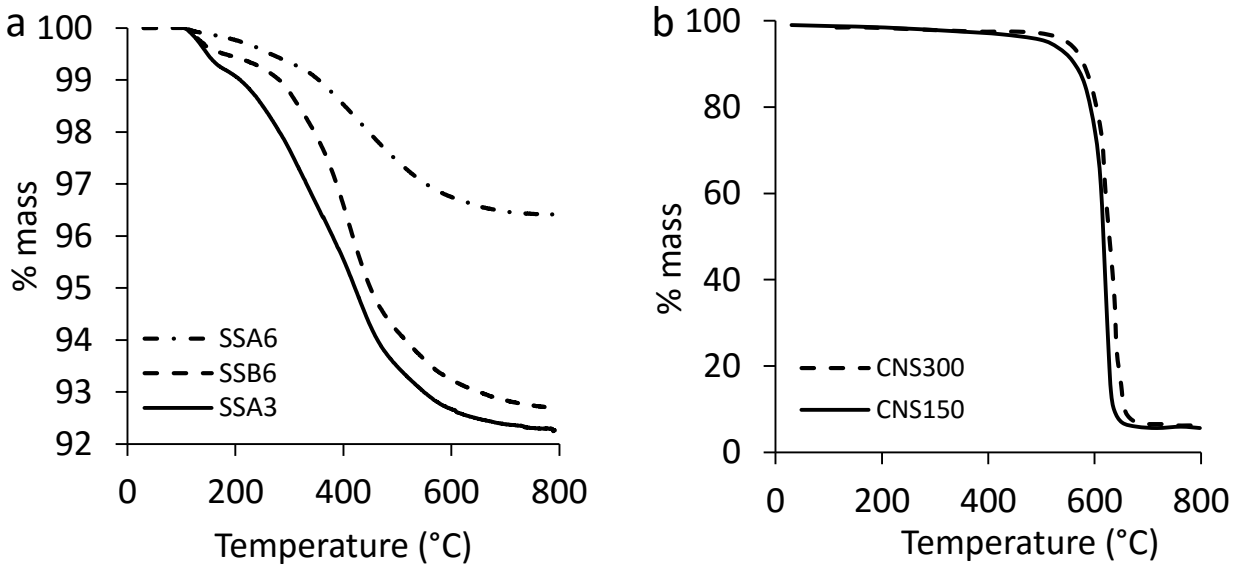

Figure 1.3. Thermal stability of a) SS nanoparticles and b) CNS materials under an oxidative atmosphere. Air flow, 100 cm^3/min; heating rate, 20°C/min.

1.2.2 Particle size

- **Synthesized nanoparticles**

Panels a−f from Figure 1.4 show the FESEM images and the corresponding particle size probability distribution for the synthesized nanoparticles (a and b) SSA3, (c and d) SSA6, (e and f) SSB6, (g

and h) CNS150 and (i and j) CNS 300. Additionally, Table 1.1 shows the estimated values of the mean particle size and surface areas of the selected nanoparticles obtained by the methods previously described. As observed in Figure 1.4 almost all synthesized materials, except CNS150, have a mean particle diameter in the nano-scale according to the definition of nanotechnology. For the SS nanoparticles, it is observed that the mean particle diameter increases in the order SSA3 < SSA6 < SSB6, indicating that by increasing the amount of the silicate precursor, the size of the particle can be reduced. This could be due to as the amount of the water decreases, the rate of hydrolysis reaction is reduced and the addition of a monomer to the network is inhibited, hence reducing the particle size.[49] In addition, as SSB6 have larger mean particle size than SSA6 nanoparticles, it can be also inferred that as the as the amount of catalyst increases, the particle diameter increases due to the increased hydrolysis rate.[47, 49] Results are in excellent agreement with Dabbaghian et al.,[14] who synthesized silica nanoparticles trough the sol-gel method using TEOS as the precursor and NH_4OH as catalyst and found that for molar ratios NH_4OH/H_2O < 2 the particle size increased as the NH_4OH/H_2O molar ratio increased. In Table 1.1 it can be observed that for the SS nanoparticles the crystallite size is much lower than the mean particle size measured by FESEM, indicating that the synthesized materials have polycrystalline structures. Figure 1.5 shows the DLS results for the synthesized nanoparticles. As seen in Figure 1.5a and Table 1.1, the mean particle of SS nanoparticles has the same trend than the one observed trough FESEM and XRD. This could be due to great van der Waals attractive forces between nanoparticles in the aqueous medium because of Brownian motion.[45, 50]

Regarding to the synthesized CNS, it can be observed in Figure 1.4c,d that the mean particle size of CNS300 sample is about 49 nm larger than the one acceptable for classifying them as nanoparticles. However, sample will be considered for asphaltenes adsorption and subsequent oxidation tests due to two main reasons: i) nanoparticles could be sufficiently small for neglecting the possibility of blockage or bridging in a HO reservoir formation[51, 52] and ii) about the 15% of the particles are in the nanoscale range. For example, Pachón[25] evaluated the petrophysic properties of the K1 and K2 units from the Gacheta and Une formations in the Castilla field (HO) placed in the Meta department, central region of Colombia. The author found that for depths between 6417 and 6911 ft the predominant mean pore diameter was about 204 μm. Hence, according to the bridge arch principle, bridging due to particle intrusion in the pore throats would happen for particles with an average size between 29 and 68 μm, values much higher than that of the mean particle size of CNS150. Nevertheless, when the resorcinol:Cs_2CO_3 molar ratio increased from 150:1 to 300:1, the mean particle size decreased. From Figure 1.3 i.j it can be seen that the mean particle size of CNS300 is 95 nm. This increase in the particle size by increasing the amount catalyst could be to the accelerated rate of polymerization reaction. Also, DLS results (Figure 1.5b) showed that the hydrodynamic diameter of the CNS particles is greater than that of $dp_{Crystallite}$ and $dp50_{FESEM}$.

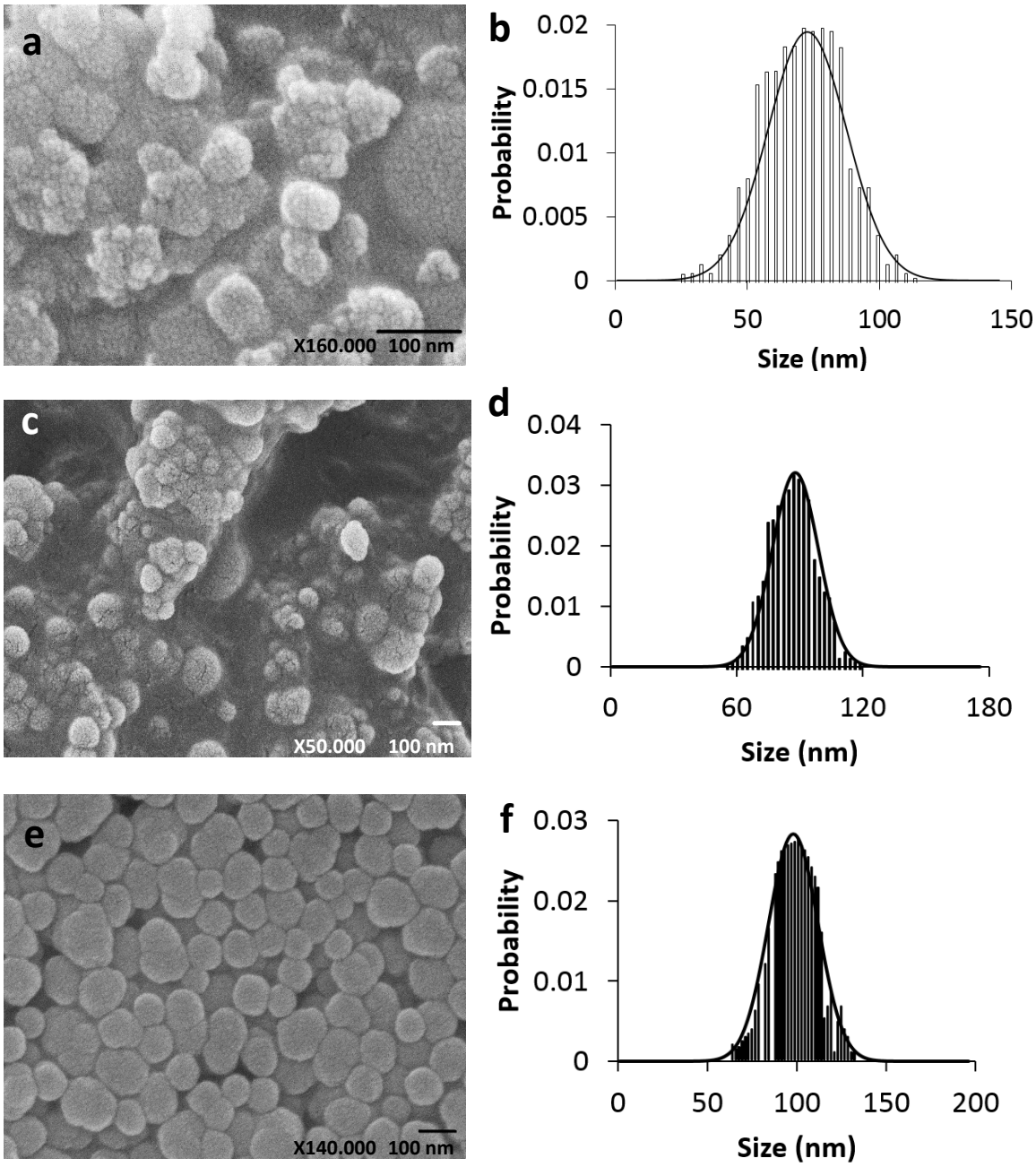
a
X160.000 100 nm
b
Probability
0.02
0.015
0.01
0.005
0
0
50
100
150
Size (nm)
c
X50.000 100 nm
d
Probability
0.04
0.03
0.02
0.01
0
0
60
120
180
Size (nm)
e
X140.000 100 nm
f
Probability
0.03
0.02
0.01
0
0
50
100
150
200
Size (nm)

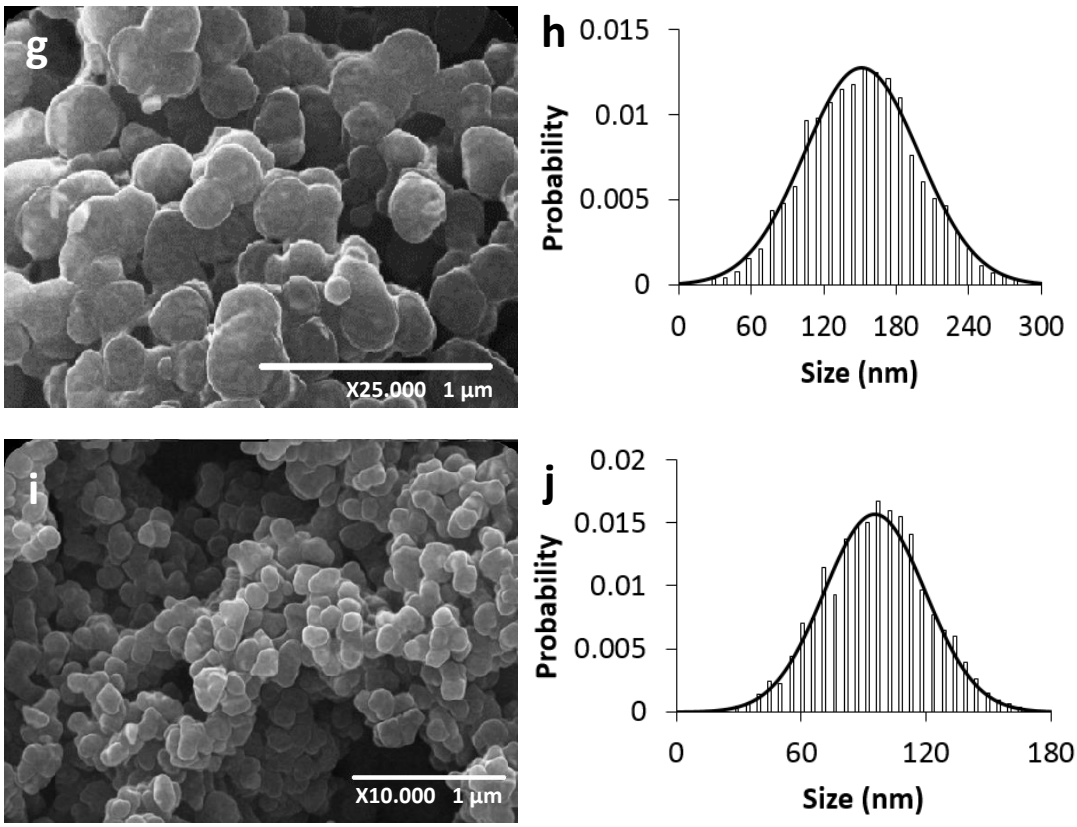

Figure 1.4. FESEM images and the corresponding particle size probability distribution for (a and b) SSA3, (c and d) SSA6, (e and f) SSB6, (g and h) CNS150 and (i and j) CNS 300.

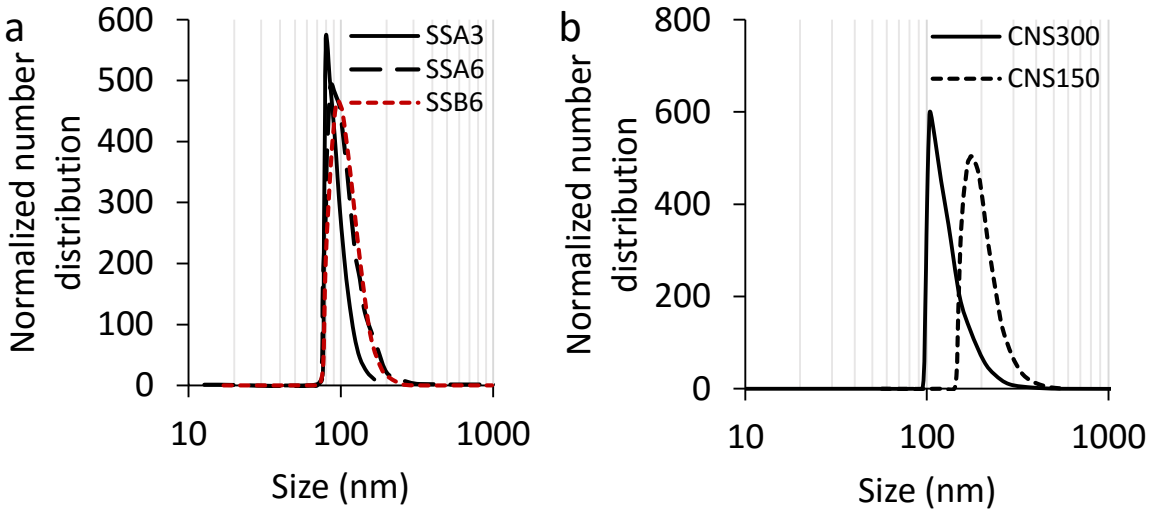

Figure 1.5. Normalized number distribution obtained by DLS for a) SS and b) CNS materials.

- **Commercial nanoparticles**

Panels a−h from Figure 1.6 show the FESEM images and the corresponding particle size probability distribution for the commercial nanoparticles (a and b) CS, (c and d) CAl, (e and f) CTi and (g and

h) CM. As seen, and in agreement with the values obtained for the crystallite size from XRD results (Table 1.1), the trend of the mean particle size is CS < CTi < CAl < CM. Additionally, the size distribution is wider for CM nanoparticles than for CS, CTi and CAl nanoparticles with a mean particle diameter ($dp50_{FESEM}$) of 97, 9, 29 and 52 nm, respectively. When comparing the mean crystallite size from XRD and FESEM, the values from FESEM are greater than those from XRD, indicating that a portion of the size distribution has a polycrystalline structure. Accordingly, the *d48*, *d45*, *d25* and *d46* values from the probability distributions for CS, CAl, CTi and CM nanoparticles would correspond to single-crystallite structures, respectively, i.e. less than the 48, 45, 25 and 46% of the particles are single crystallite structured. Figure 1.7 shows the normalized number distribution obtained for commercial nanoparticles trough DLS technique. As it was observed for SS and CNS materials, for all commercial nanoparticles the hydrodynamic size was higher than that obtained with FESEM and XRD. It can be observed from Figure 1.7 that a higher aggregation occurs for the CM nanoparticles, and is due to the magnetic characteristics of magnetite nanoparticles, they tend to aggregate due to anisotropic dipolar attraction and form clusters.[53]

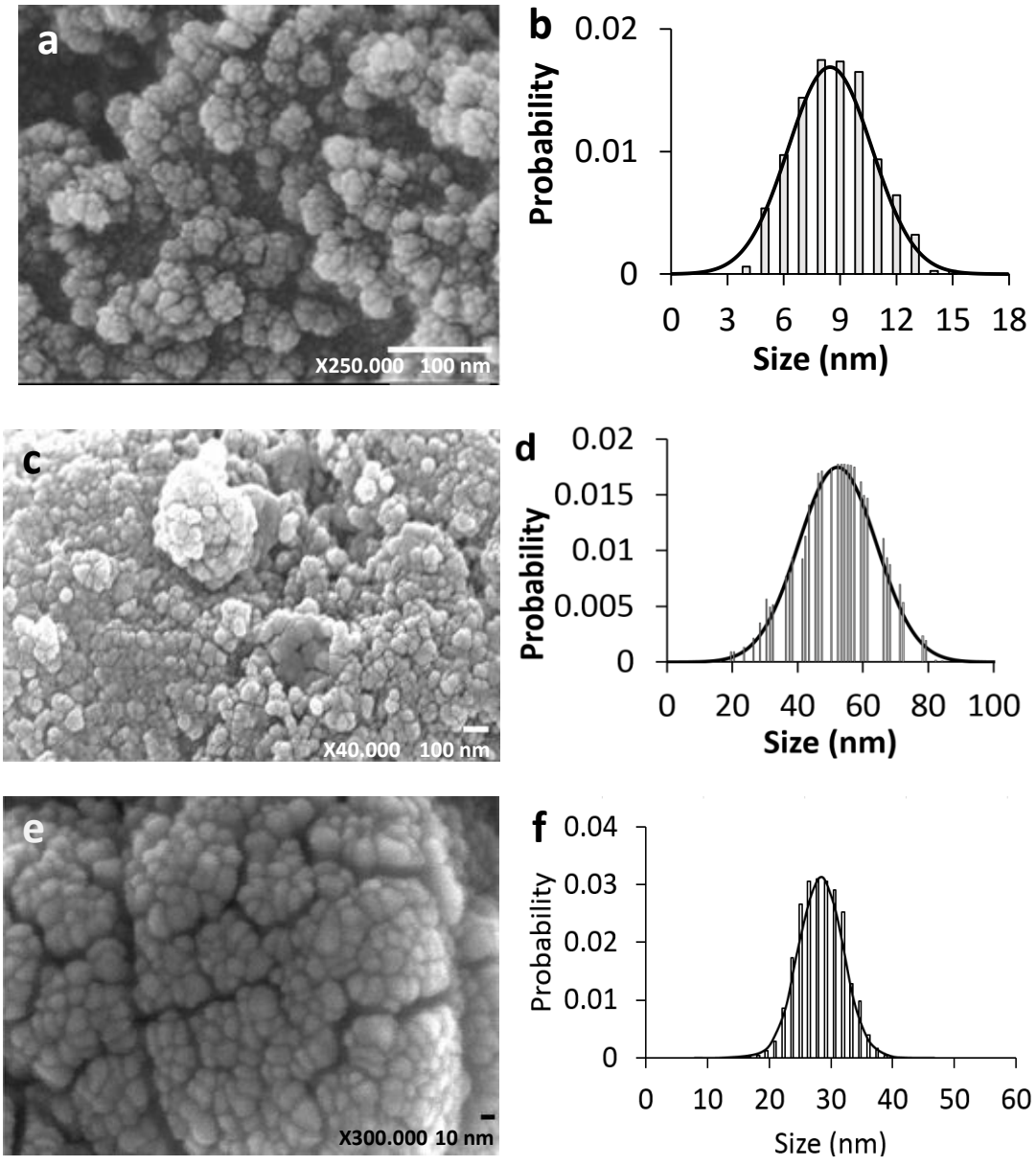

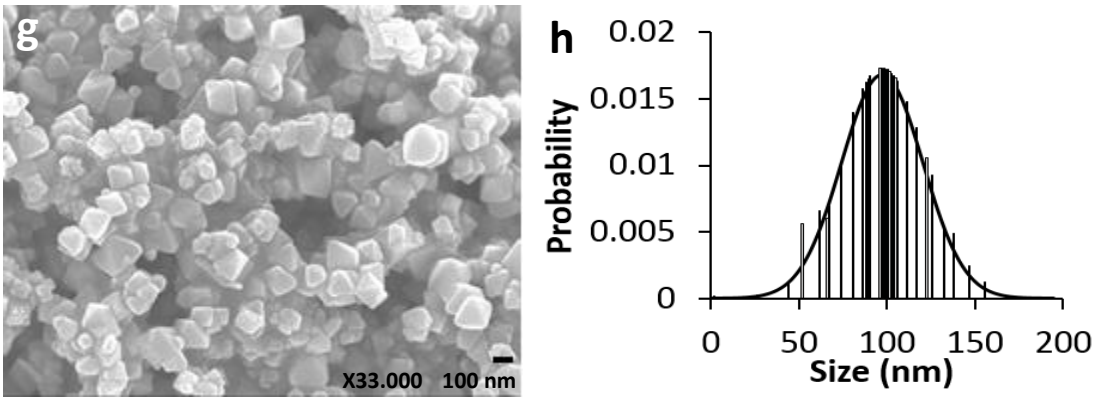

Figure 1.6. FESEM images and the corresponding particle size probability distribution for (a and b) CS, (c and d) CAl, (e and f) CTi and (g and h) CM.

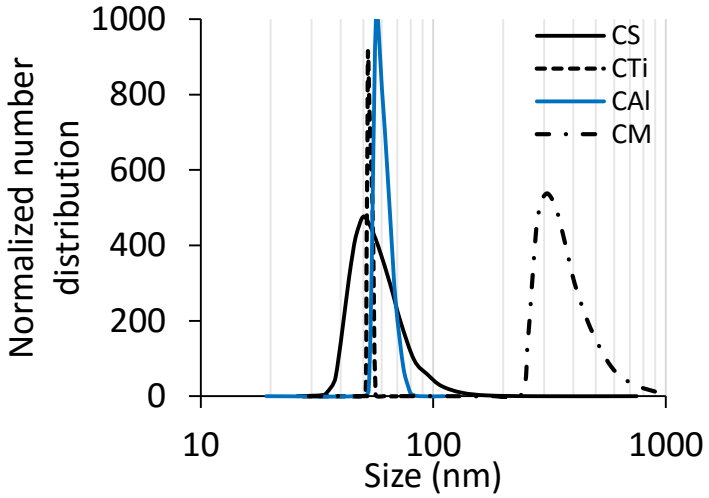

Figure 1.7. Normalized number distribution obtained by DLS for commercial nanoparticles.

Table 1.1 Estimated surface area and particle size of the selected nanoparticles.

Material	Particle size (nm)			Surface Area (m^2/g)	
	$dp_{Crystallite}$	$dp50_{FESEM}$	$dp50_{DLS}$	S_{BET}	SA
SSA3	1.4	72	87	42.6	31.4
SSA6	1.5	87	89	26.9	26.0
SSB6	1.5	97	100	23.6	23.3
CNS150	-	149	173	57.1	22.3
CNS300	-	95	104	89.7	35.1
CS	7.2	9	51	389.1	314.5
CAl	49.7	52	58	223.2	28.5
CTi	26.1	29	52	54.1	78.1
CM	70.2	97	308	102.2	12.5

- **SHS nanoparticles**

The crystallite size of NiO and PdO nanocrystals was determined through XRD measurements. Table 1.2. shows the estimated values of NiO and PdO crystallite size over the support surface. As seen, the $dp_{Crystallite}$ increases as the metal oxide loading on the adsorbent surface increases. For bimetallic SHS nanoparticles, it is observed that the degree of crystal growth is inhibited. For example, if crystal growth inhibition does not occur, the crystal size of NiO and PdO for the sample CSNi0.66Pd0.66 would be 1.3 and 1.6 nm, respectively, indicating a value 31 and 25% higher than the one measured by XRD. Similar observation can be made for CSNi1Pd1 nanoparticles. It is well known that the sintering of metals on the support surface could be alleviated in complex materials by the presence of noble metals[54] and is dependent on many factors in the synthesis step such as temperature, time, atmosphere and metal content.[55] Hence, these results are an indicative of good dispersion and better homogeneity in the coordination of the PdO and NiO over the support surface for bimetallic nanoparticles than for monometallic SHS.

Table 1.2. Estimated values of NiO and PdO crystallite size and surface area of selected nanoparticles.

Material	S_{BET} **(m²/g)**	$dp_{Crystallite,NiO}$ **(nm)**	$dp_{Crystallite,PdO}$ **(nm)**
CSNi1	290.31	1.9	-
CSPd1	265.56	-	2.4
CSNi2	233.63	2.9	-
CSPd2	205.15	-	4.1
CSNi0.66Pd0.66	220.79	0.9	1.2
CSNi1Pd1	201.50	1.3	2.2

1.2.3 Surface area

- **Synthesized and commercial nanoparticles**

Table 1.1 shows the estimated values of the surface areas obtained through the BET method and the geometrical calculation according to the $dp50_{FESEM}$ **.** As observed, except for CTi sample, the surface area estimated geometrically is lower than that obtained through the BET method and could be due to four main reasons: i) geometrical surface area is estimated assuming a mean particle size while the whole sample is represented by a distribution of particles with different sizes, ii) the density employed for calculations could be not the exact density of the material, iii) synthesized nanoparticles have no sphericity = 1 and nanoparticles could have even a small volume of micropores that would alter the surface area calculation. Among the SS nanoparticles, it can be observed that as expected, the surface area increases as the size of the particle decreases. Same trend can be observed for CNS materials. Regarding to the commercial nanoparticles, the trend followed by the surface area is CS > CAl > CM > CTi.

- **SHS nanoparticles**

The S_{BET} of the functionalized nanoparticles was determined through N_2 physisorption at -196°C after the functionalization process. Results of the obtained S_{BET} are shown in Table 1.2. As seen in Table 1.2, the S_{BET} was drastically reduced by including NiO and PdO nanocrystals on the support surface. It is worth to mention that the inclusion of the metal oxide on the nanoparticles surface could alter significantly the surface area of the materials. As seen in Table 1.2, the estimated crystallite size of the PdO is about one third than for the fumed silica support and by their deposition on the surface, a percentage of the possibly existing micropores can be blocked. Also, the heat treatment at 450°C for the metal oxides obtaining could lead to the support sintering and hence in the reduction of the surface area. Additionally, the cubic special model (see appendix A) described in an excellent way the experimental results for the obtained S_{BET} with and R^2 = 1.0. Table 1.3 lists the cubic special model parameters that describes the behavior of the S_{BET} and Figure 1.8 shows the contour lines according to the stablished SCMD. It can be seen from Figure 1.8 that the contour lines shift to lower values of as the amount of PdO on the sample increases and could be due to PdO nanocrystals are larger than that of NiO.

Table 1.3. Calculated Parameters of the Special Cubic Model for the S_{BET}.

β_1	β_2	β_3	β_{12}	β_{13}	β_{23}	β_{123}
389.00	233.63	205.15	-84.02	-126.06	-71.56	-643.882

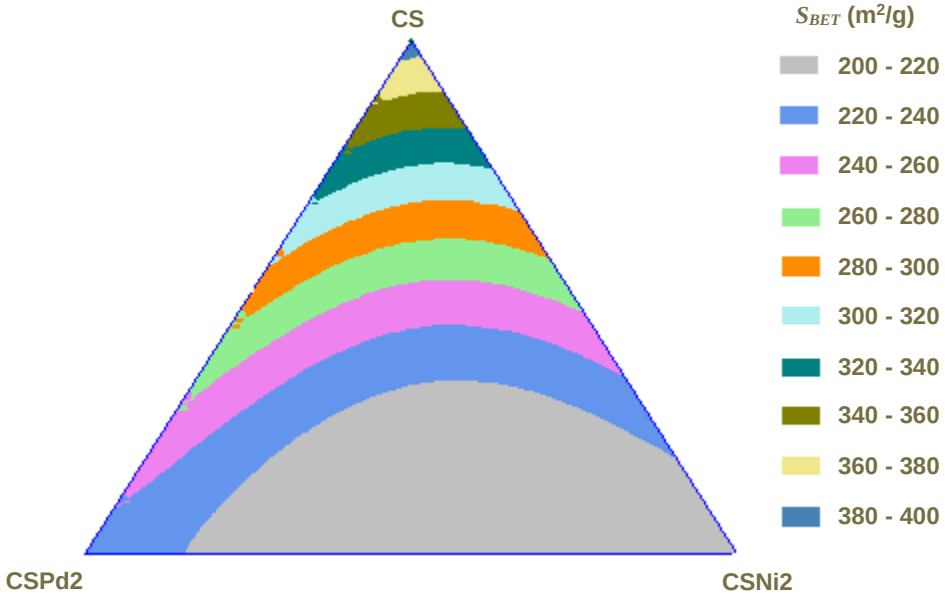

Figure 1.8. Response surface for the S_{BET} according to the cubic special model of the SCMD.

1.3 Partial conclusions

Silica and carbon spheres nanoparticles were successfully synthesized through the sol-gel method and polycondensation of resorcinol-formaldehyde, respectively. Obtained materials were characterized by thermal stability, particle size and surface area. SS nanoparticles resulted in mean particle diameters in the nanoscale and with a decreasing trend as the amount of precursor increased. In the case of CNS, nano-spheres with a higher R:C molar ratio resulted in particles with lower mean diameter. Also, commercial nanoparticles were characterized by particle size and surface area. The trend followed by the surface area of the commercial nanoparticles was CS > CAl > CM > CTi. In addition, the crystallite size of NiO and PdO nano-crystals over the support surface was estimated trough XRD measurements. Surface are determination of functionalized nanoparticles was successfully described by the special cubic model according to the postulated SCMD.

1.4 References

1. Duffus, J. H.; Nordberg, M.; Templeton, D. M., Glossary of terms used in toxicology, (IUPAC recommendations 2007). *Pure and Applied Chemistry* **2007,** 79, (7), 1153-1344.
2. Liu, C.; Fan, Y.; Liu, M.; Cong, H.; Cheng, H.; Dresselhaus, M. S., Hydrogen storage in single-walled carbon nanotubes at room temperature. *Science* **1999,** 286, (5442), 1127-1129.
3. Leschkies, K. S.; Divakar, R.; Basu, J.; Enache-Pommer, E.; Boercker, J. E.; Carter, C. B.; Kortshagen, U. R.; Norris, D. J.; Aydil, E. S., Photosensitization of ZnO nanowires with CdSe quantum dots for photovoltaic devices. *Nano Letters* **2007,** 7, (6), 1793-1798.
4. Rowell, M. W.; Topinka, M. A.; McGehee, M. D.; Prall, H.-J.; Dennler, G.; Sariciftci, N. S.; Hu, L.; Gruner, G., Organic solar cells with carbon nanotube network electrodes. *Applied Physics Letters* **2006,** 88, (23), 233506.
5. Franco, C. A.; Cortés, F. B.; Nassar, N. N., Adsorptive Removal of Oil Spill From Oil-in-Fresh Water Emulsions by Hydrophobic Alumina Nanoparticles Functionalized with Petroleum Vacuum Residue. *Journal of Colloid and Interface Science* **2014**.
6. MARTÍNEZ AGUILAR, M.; BERNARDO CORTÉS, F.; ANDRÉS FRANCO ARIZA, C., Tratamiento de agua basado en la adsorción de crudo en nanopartículas polares y no polares. *Informador Técnico* **2013,** 77, (1).
7. Anbia, M.; Amirmahmoodi, S., Adsorption of phenolic compounds from aqueous solutions using functionalized SBA-15 as a nano-sorbent. *Scientia Iranica* **2011,** 18, (3), 446-452.
8. Nassar, N. N.; Ringsred, A., Rapid adsorption of methylene blue from aqueous solutions by goethite nanoadsorbents. *Environmental Engineering Science* **2012,** 29, (8), 790-797.
9. Nassar, N. N., Kinetics, equilibrium and thermodynamic studies on the adsorptive removal of nickel, cadmium and cobalt from wastewater by superparamagnetic iron oxide nanoadsorbents. *The Canadian Journal of Chemical Engineering* **2012,** 90, (5), 1231-1238.
10. Nel, A.; Xia, T.; Mädler, L.; Li, N., Toxic potential of materials at the nanolevel. *Science* **2006,** 311, (5761), 622-627.
11. Cheng, Y. T.; Rodak, D.; Wong, C.; Hayden, C., Effects of micro-and nano-structures on the self-cleaning behaviour of lotus leaves. *Nanotechnology* **2006,** 17, (5), 1359.
12. Nakajima, A.; Hashimoto, K.; Watanabe, T.; Takai, K.; Yamauchi, G.; Fujishima, A., Transparent superhydrophobic thin films with self-cleaning properties. *Langmuir* **2000,** 16, (17), 7044-7047.
13. Nie, S.; Xing, Y.; Kim, G. J.; Simons, J. W., Nanotechnology applications in cancer. *Annu. Rev. Biomed. Eng.* **2007,** 9, 257-288.

14. Gupta, U.; Jain, N. K., Non-polymeric nano-carriers in HIV/AIDS drug delivery and targeting. *Advanced drug delivery reviews* **2010,** 62, (4), 478-490.
15. du Toit, L. C.; Pillay, V.; Choonara, Y. E., Nano-microbicides: Challenges in drug delivery, patient ethics and intellectual property in the war against HIV/AIDS. *Advanced drug delivery reviews* **2010,** 62, (4), 532-546.
16. Sumer, B.; Gao, J., Theranostic nanomedicine for cancer. **2008**.
17. Moghimi, S. M.; Hunter, A. C.; Murray, J. C., Nanomedicine: current status and future prospects. *The FASEB Journal* **2005,** 19, (3), 311-330.
18. Wagner, V.; Dullaart, A.; Bock, A.-K.; Zweck, A., The emerging nanomedicine landscape. *Nature biotechnology* **2006,** 24, (10), 1211-1218.
19. Ramesh, K.; Biswas, A. K.; Somasundaram, J.; Subba Rao, A., Nanoporous zeolites in farming: current status and issues ahead. *Current Science (00113891)* **2010,** 99, (6).
20. Pérez-de-Luque, A.; Rubiales, D., Nanotechnology for parasitic plant control. *Pest management science* **2009,** 65, (5), 540-545.
21. Grillo, R.; dos Santos, N. Z. P.; Maruyama, C. R.; Rosa, A. H.; de Lima, R.; Fraceto, L. F., Poly (ε-caprolactone) nanocapsules as carrier systems for herbicides: Physico-chemical characterization and genotoxicity evaluation. *Journal of hazardous materials* **2012,** 231, 1-9.
22. Avella, M.; De Vlieger, J. J.; Errico, M. E.; Fischer, S.; Vacca, P.; Volpe, M. G., Biodegradable starch/clay nanocomposite films for food packaging applications. *Food chemistry* **2005,** 93, (3), 467-474.
23. Sorrentino, A.; Gorrasi, G.; Vittoria, V., Potential perspectives of bio-nanocomposites for food packaging applications. *Trends in Food Science & Technology* **2007,** 18, (2), 84-95.
24. Salamanca-Buentello, F.; Persad, D. L.; Martin, D. K.; Daar, A. S.; Singer, P. A., Nanotechnology and the developing world. *PLoS Medicine* **2005,** 2, (5), e97.
25. Hashemi, R.; Nassar, N. N.; Pereira-Almao, P., Transport behavior of multimetallic ultradispersed nanoparticles in an oil-sands-packed bed column at a high temperature and pressure. *Energy & Fuels* **2012,** 26, (3), 1645-1655.
26. Hashemi, R.; Nassar, N. N.; Almao, P. P., Nanoparticle technology for heavy oil in-situ upgrading and recovery enhancement: Opportunities and challenges. *Applied Energy* **2014,** 133, 374-387.
27. Bedrikovetsky, P.; Monteiro, P.; Neto, A.; Riente, A. In *Fractional flow theory for suspension flow in petroleum reservoirs*, SPE 121822 presented at 2009 SPE Latin American and Caribbean Petroleum Engineering Conference held in Cartagena, Colombia, 2009; 2009.
28. Bratli, R. K.; Risnes, R., Stability and failure of sand arches. *Society of Petroleum Engineers Journal* **1981,** 21, (02), 236-248.
29. Yu, C.; Jingen, D.; Xianmin, G.; Qian, J., Analysis of Gravel-Sizing Optimization Method for High-Pressure Gravel-Packing Sand Control. *Petroleum Science and Technology* **2011,** 29, (12), 1257-1263.
30. Nassar, N. N.; Hassan, A.; Pereira-Almao, P., Effect of the particle size on asphaltene adsorption and catalytic oxidation onto alumina particles. *Energy & Fuels* **2011,** 25, (9), 3961-3965.
31. Brinker, C. J.; Scherer, G. W., *Sol-gel science: the physics and chemistry of sol-gel processing*. Academic press: 2013.
32. Stöber, W.; Fink, A.; Bohn, E., Controlled growth of monodisperse silica spheres in the micron size range. *Journal of colloid and interface science* **1968,** 26, (1), 62-69.
33. Rahman, I. A.; Padavettan, V., Synthesis of silica nanoparticles by sol-gel: size-dependent properties, surface modification, and applications in silica-polymer nanocomposites—a review. *Journal of Nanomaterials* **2012,** 2012, 8.
34. Pekala, R., Organic aerogels from the polycondensation of resorcinol with formaldehyde. *Journal of Materials Science* **1989,** 24, (9), 3221-3227.

35. Bailon-Garcia, E.; Carrasco-Marin, F.; Perez-Cadenas, A.; Maldonado-Hodar, F., Microspheres of carbon xerogel: An alternative Pt-support for the selective hydrogenation of citral. *Applied Catalysis A: General* **2014,** 482, 318-326.
36. Scheffe, H., The simplex-centroid design for experiments with mixtures. *Journal of the Royal Statistical Society. Series B (Methodological)* **1963**, 235-263.
37. Cortés, F. B.; Mejía, J. M.; Ruiz, M. A.; Benjumea, P.; Riffel, D. B., Sorption of asphaltenes onto nanoparticles of nickel oxide supported on nanoparticulated silica gel. *Energy & Fuels* **2012,** 26, (3), 1725-1730.
38. Franco, C.; Patiño, E.; Benjumea, P.; Ruiz, M. A.; Cortés, F. B., Kinetic and thermodynamic equilibrium of asphaltenes sorption onto nanoparticles of nickel oxide supported on nanoparticulated alumina. *Fuel* **2013,** 105, 408-414.
39. Rouquerol, J.; Rouquerol, F.; Llewellyn, P.; Maurin, G.; Sing, K. S., *Adsorption by powders and porous solids: principles, methodology and applications*. Academic press: 2013.
40. Brunauer, S.; Emmett, P. H.; Teller, E., Adsorption of gases in multimolecular layers. *Journal of the American chemical society* **1938,** 60, (2), 309-319.
41. Ramalho, J. B. V.; Lechuga, F. C.; Lucas, E. F., Effect of the structure of commercial poly (ethylene oxide-b-propylene oxide) demulsifier bases on the demulsification of water-in-crude oil emulsions: elucidation of the demulsification mechanism. *Química Nova* **2010,** 33, (8), 1664-1670.
42. Yudin, I. K.; Anisimov, M. A., Dynamic light scattering monitoring of asphaltene aggregation in crude oils and hydrocarbon solutions. In *Asphaltenes, Heavy Oils, and Petroleomics*, Springer: 2007; pp 439-468.
43. Rane, J. P.; Harbottle, D.; Pauchard, V.; Couzis, A.; Banerjee, S., Adsorption kinetics of asphaltenes at the oil–water interface and nanoaggregation in the bulk. *Langmuir* **2012,** 28, (26), 9986-9995.
44. Bern, B.; Pecora, R., Dynamic Light scattering with Applications to Chemistry. *Biology and Physics (Wiley, New York, 1976). JJ Fisz et al./Two-photon-excitation fluorescence depolarization in solutions* 207.
45. Bowen, P., Particle size distribution measurement from millimeters to nanometers and from rods to platelets. *Journal of Dispersion Science and Technology* **2002,** 23, (5), 631-662.
46. Nassar, N. N.; Hassan, A.; Vitale, G., Comparing kinetics and mechanism of adsorption and thermo-oxidative decomposition of Athabasca asphaltenes onto TiO 2, ZrO 2, and CeO 2 nanoparticles. *Applied Catalysis A: General* **2014,** 484, 161-171.
47. Jal, P.; Sudarshan, M.; Saha, A.; Patel, S.; Mishra, B., Synthesis and characterization of nanosilica prepared by precipitation method. *Colloids and Surfaces A: Physicochemical and Engineering Aspects* **2004,** 240, (1), 173-178.
48. Fyfe, C.; Gobbi, G.; Putnis, A., Elucidation of the mechanism and kinetics of the Si, Al ordering process in synthetic magnesium cordierite by 29Si magic angle spinning NMR spectroscopy. *Journal of the American Chemical Society* **1986,** 108, (12), 3218-3223.
49. Dabbaghian, M.; Babalou, A.; Hadi, P.; Jannatdoust, E., A Parametric Study of the Synthesis of Silica Nanoparticles via Sol-Gel Precipitation Method. *International Journal of Nanoscience and Nanotechnology* **2010,** 6, (2), 104-113.
50. Akbari, B.; Tavandashti, M. P.; Zandrahimi, M., Particle Size Characterization of Nanoparticles–A Practicalapproach. *Iranian Journal of Materials Science and Engineering* **2011,** 8, (2), 48-56.
51. Chopra, S.; Lines, L. R.; Schmitt, D. R.; Batzle, M. L., *Heavy oils: reservoir characterization and production monitoring*. Society of Exploration Geophysicists Tulsa, OK: 2010.
52. Pachón, Z. Determinación de las propiedades petrofísicas de rocas de yacimientos petrolíferos colombianos por métodos de relajación de resonancia magnética nuclear Universidad Industrial de Santander, 2005.

53. Lu, Y.; Yin, Y.; Mayers, B. T.; Xia, Y., Modifying the surface properties of superparamagnetic iron oxide nanoparticles through a sol-gel approach. *Nano letters* **2002,** 2, (3), 183-186.
54. Guo, Y.; Zhou, L.; Kameyama, H., Steam reforming reactions over a metal-monolithic anodic alumina-supported Ni catalyst with trace amounts of noble metal. *international journal of hydrogen energy* **2011,** 36, (9), 5321-5333.
55. Contreras, J. L.; Fuentes, G. A., Sintering of Supported Metal Catalysts. *ChemInform* **2013,** 44, (41).

2. Adsorption and subsequent catalytic thermal decomposition of *n*-C_7 asphaltenes

Because of their unique and exceptional properties, such as large surface area and size-and shape-dependent catalytic properties, nanoparticles can also be employed as adsorbents and/or catalysts for removal of heavy waste polar hydrocarbons from crude oil, like asphaltenes.[1-10] Nanoparticles have the flexibility for *in-situ* (in place) application, where the particles can travel smoothly with good degree of dispersion through the porous media without risk of pore blocking.[11] One would anticipate that by in-situ sequestration of the asphaltene molecules from the crude oil would enhance the *in-situ* upgrading and inhibit asphaltene damage. This consequently leads to a lighter crude oil with an improved mobility through the reservoir, easier production and transporting processes, with a higher distillable fraction and higher EROI.

Asphaltene adsorption onto solid surfaces has been widely studied.[12-22] Although asphaltene adsorption onto different solid surfaces of nanoparticles has been reported in literature, there is still lack of understanding of the mechanisms of interaction between the asphaltenes and nanoparticle surface and how the chemical nature of both affects adsorption and catalytic processes. The adsorption and subsequent catalytic thermal decomposition of asphaltenes onto different surfaces of nanoparticles was first introduced by Nassar and coworkers.[2, 4-9, 23, 24]. In his earlier study,[24] Nassar investigated the kinetics and thermodynamic of the asphaltene adsorption on γ-Al_2O_3 nanoparticles. The author reported that adsorption was fast as adsorption equilibrium was achieved in less than 2 h. This was attributed to the non-porous character of the material, where the external adsorption is dominated. Adsorption was influenced by the temperature, *n*-heptane/toluene ratio, and water content. As the temperature increased the amount adsorbed of asphaltenes decreased, indicating that asphaltene adsorption onto the surface of nanoparticles is an exothermic process. Further, Nassar[24] found that the asphaltene adsorption in presence of a precipitating agent like *n*-heptane is enhanced, this because of asphaltene self-association and the subsequent formation of colloidal aggregates. In other studies, Nassar et al.[7] evaluated the asphaltene adsorption and subsequent oxidation in presence of alumina with different surface acidity and different particle size. The authors found that for same acidic surfaces and different particle sizes, and on surface area basis, the adsorption capacity of asphaltenes onto nanoalumina is higher than that of microalumina, while the microalumina has a higher catalytic activity than that of nanoalumina, revealing that the textural properties are more important than the particle size during the catalytic oxidation of asphaltenes. For different surface acidity, and on surface area basis, acidic alumina has the highest adsorption of asphaltenes, and basic alumina has the highest catalytic activity toward asphaltene oxidation. Nassar et al.[6, 8-10] have also tested other nanoparticles on asphaltene adsorption and oxidation (i.e., NiO, Co_3O_4, Fe_3O_4, TiO_2, and CaO). During the adsorption process, the authors observed a monolayer adsorption isotherm with good fitting to the Langmuir model. The adsorption capacity followed the trend CaO > Co_3O_4 > Fe_3O_4 > MgO > NiO > TiO_2. After the adsorption process, the authors evaluated the catalytic

activity of the nanoparticles; the oxidation temperature of asphaltene decreased by 140, 136 and 100°C relative to the non-catalytic oxidation of virgin asphaltenes in the presence of NiO, Co_3O_4, and Fe_3O_4 nanoparticles, respectively. Further, the nanoparticles significantly decreased the activation energy, confirming their catalytic activity toward asphaltene decomposition. The authors confirmed that the asphaltene adsorption/oxidation is metal oxide specific. Similar results were observed by the same authors for asphaltenes steam gasification/cracking and thermal decomposition under inert conditions.[8] For these two processes the catalytic activity also followed the same trend $NiO > Co_3O_4 > Fe_3O_4$. A correlation between the adsorption affinity and the catalytic activity of the metal oxide nanoparticles was reported, indicating that the higher the adsorption affinity the better the catalytic activity of the nanoparticles.[8, 25] A similar study, but for Iranian *n*-C_7 asphaltenes, were reported by Hosseinpour et al.[26, 27] The authors used metal oxide nanoparticles similar to the ones reported by Nassar et al[9] for adsorption and subsequent oxidation and pyrolysis of Iranian asphaltenes and also found that the outcome gases in the process are particle-type dependent,[27] confirming the catalytic role of the selected metal oxide nanoparticles.

More recently, Cortés et al.[28] and Franco et al. [37] has developed several studies on the adsorption of *n*-C_7 asphaltenes extracted from Colombian crude oils using NiO nanoparticles supported onto nanoparticles of silica and alumina,[29-31] respectively. Authors found that the selected nanoparticles have high adsorptive capacities and the adsorption equilibrium time was very short (i.e., about two minutes).[30] Also found that these kinds of materials do not allow the formation of multilayers adsorption, hence facilitating later processes of asphaltenes such catalytic thermal cracking and inhibition of formation damage.[29-31] It is worth noting here that all the reported studies have confirmed that nanoparticles are effective adsorbents and catalysts for adsorption and thermal decomposition of heavy hydrocarbons and enhancing heavy oil upgrading and recovery as well. Owing to the complex structure of HO, heavy hydrocarbon species like asphaltenes can be adsorbed onto the nanoparticle surfaces as colloidal aggregates, micelles, or single molecules, depending on their concentration and experimental conditions. Hence, the changes in the colloidal state of the asphaltenes can impact the catalytic activity of the nanoparticle surfaces.

However, none of the aforementioned study correlates the self-association of asphaltenes with the adsorption affinity or catalytic activity of the nanoparticle surfaces. Although some authors reported multilayer adsorption according to the adsorption isotherms they obtained, there was no evidence about the effect of the size of the asphaltene aggregate on the catalytic activity of nanoparticle surface. Thus, it is very important to have an estimation of the asphaltene aggregate on the catalyst surface as larger aggregates could result in reducing the catalytic activity of the catalyst, even up to a point where there is no catalytic effect of the nanoparticle on asphaltene decomposition. Further, until now the evaluation of metallic and/or multi-metallic oxides supported and unsupported nanoparticles on asphaltenes adsorption and subsequent thermal decomposition processes for enhancing HO and EHO upgrading and inhibition of asphaltene formation damage is not yet fully understood. Therefore, there is a need to study and evaluate the effect of the chemical nature of the interaction of asphaltene-nanoparticle to obtain a better understanding of the mechanisms of the aforementioned processes. Hence, this chapter is aimed at synthesizing and applying different types of supported and unsupported nanoparticles for adsorption and subsequent catalytic thermal decomposition of the adsorbed asphaltenes under different atmospheres. In addition, a correlation between adsorption affinity, extent of asphaltene aggregation and catalytic activity is for the first time established using the solid-liquid equilibrium adsorption model (SLE model) and the OFW isoconversional method.

2.1 Experimental

Synthesized SS nanoparticles, CNS and commercial nanoparticles were employed for the adsorption and subsequent oxidation of *n*-C_7 asphaltenes extracted from three different crude oils. Further, CS nanoparticles functionalized with NiO and/or PdO were used for the evaluation of the enhancement of the adsorption capacity and catalytic active towards asphaltenes thermal decomposition under different atmospheres. Also, CAl and CTi nanoparticles were evaluated as an alternative ceramic support for the NiO and PdO nanocrystals. Adsorption experiments were carried out trough batch-mode adsorption experiments and catalytic activity of nanoparticles was evaluated trough TGA/DSC analyses. SLE model and OFW method were employed for adsorption isotherms modeling and estimation of effective activation energies of *n*-C_7 asphaltenes decompositions, respectively.

2.1.1 Materials

Detailed information about employed nanoparticles can be found in Chapter 1. Two different crude oils AK9 and AK18 from the Akacías field and one from Capella field (Capella HO) were used as source of *n*-C_7 asphaltenes. The Akacías and Capella fields are located in the Meta and Puntumayo departments in center and south regions of Colombia, respectively. Table 2.1 shows some properties of the selected crude oils. *n*-heptane (99%, Sigma-Aldrich, St. Louis, MO) was used for *n*-C_7 asphaltene isolation. After *n*-C_7 asphaltenes extraction, *n*-C_7 asphaltenes were dissolved in toluene (99.5%, Merk KGaA, Germany) for preparing a stock solution of 2000 mg/L.

Table 2.1. Properties of selected crude oil samples and their extracted *n*-C_7 asphaltenes at 25°C.

Crude Oil	API gravity (degrees)	Viscosity (cP)	Asphaltenes content (wt%)
AK9	7.2	5.6×10^6	13.1
AK18	7.9	2.5×10^5	11.9
Capella	10.9	4.8×10^5	9.0

2.1.2 Methods

- **Batch-mode adsorption experiments**

Batch- mode adsorption experiments were carried out in a set of 10 mL vials by mixing 100 mg nanoparticles with 10 mL of the prepared heavy oil solution containing a known concentration of asphaltenes at different temperatures between 25 and 55°C. Subsequently, the mixtures were agitated at 200 rpm by placing the vials in a temperature-controlled incubator and were allowed to equilibrate for 24 h because that was the amount of time needed to ensure equilibrium. The mixture was separated by allowing the nanoparticles containing the adsorbed asphaltenes to precipitate and by decanting the supernatant. The residual asphaltene concentration in the supernatant was measured

using UV−vis spectrophotometry[37] with a Genesys 10S (Thermo Scientific, Waltham, MA) spectrophotometer at a defined wavelength according to the *n*-C_7 asphaltene in evaluation. A calibration curve of the UV−vis absorbance at the respective wavelength against the *n*-C_7 asphaltene concentration was established using standard laboratory-made model solutions with known concentrations. For high asphaltene concentrations (>250 mg/L), the solutions were diluted with toluene to the desired absorbance value, and the actual concentration was estimated by multiplying the obtained concentration by the dilution factor. Accordingly, the amount adsorbed (q) of asphaltenes per surface area of nanoparticles is estimated with a simple mass balance as described by Eq. 2.1:

$$q = \frac{C_0 - C_E}{A} V \tag{2.1}$$

where, C_0 and C_E both in units of mg/L are the initial and equilibrium concentrations of asphaltenes in solution, respectively; V is the solution volume in liters and A is the dry surface area of nanoparticles in m^2.

- **Thermogravimetric analyses of *n*-C_7 asphaltenes**

The thermogravimetric analyses were carried out with a thermos gravimetric TGA Q50 analyzer and a differential scanning calorimeter DSC Q20 analyzer from TA Instruments, Inc. (New Castle, DE) by heating the virgin *n*-C_7 asphaltenes and *n*-C_7 asphaltenes in presence of nanoparticles under the desired atmosphere from 30 °C to 800°C at three rates (5, 10, and 20°C/min). Air, Ar, and Ar saturated with and $H_2O_{(g)}$ were used in the oxidation, pyrolysis and gasification processes, respectively. The sample mass was kept low the diffusion limitations (ca. 5 mg).[9] The gas flow rate was fixed at 100 cm^3/min throughout the experiment. In the case of gasification process, to allow the steam to be present above the sample in excess, the $H_2O_{(g)}$ was introduced into the system using a saturator filled with distilled water at a desired temperature controlled with a thermostatic bath. Before the samples were transferred for TGA analysis, they were dried overnight in a vacuum oven. The nanoparticles selected for TGA analysis have the same amount of asphaltenes/surface area (ca. 0.2 mg/m^2). Details of apparatus calibration can be found in Chapter 1, Section 1.1.3. The produced gases were analyzed using a coupled FTIR spectrophotometer IRAffinity-1 (Shimadzu, Japan) operating in transmission mode at a resolution of 2 cm^{-1} with 16 scans per minute in the range of 4000–400 cm^{-1}. This TGA–FTIR assembly has been recently used to investigate the gases produced in catalytic reactions of asphaltenes decomposition in presence of nanoparticles due to their simplicity and flexibility.[27] The FTIR allows the online measurement of the produced gases in real time, avoiding delays in the sampling that could be present in other techniques. The characteristic intensity of the adsorption bands centered at 2143 cm^{-1} for CO and 1304 and 3016 cm^{-1} for CH_4 were used to obtain the gas evolution profiles and were normalized based on the highest signal. The lower limits for CO andCH_4 measurement were sensitive enough for this purpose within 9.4 and 6.9 ppm, respectively. Additionally, the upper limits for the measurement were 3750 ppm for CO and 2750 ppm for CH_4. To estimate the amount of coke formed after gasification was complete, the sample was exposed to an oxidative atmosphere with an airflow of 100 mL/min from 30 to 900°C at a fixed heating rate of 20°C/min.

2.2 Modeling

The solid-liquid equilibrium model (SLE) is used for describing the adsorption isotherms of asphaltenes on nanoparticles and for estimating the thermodynamic properties of adsorption. Corrected Ozawa-Flynn-Wall method (OFW) is employed for estimating the effective activation energies and describing the kinetic mechanism of the catalytic thermal decomposition of *n*-C_7 asphaltenes.

2.2.1 Solid-Liquid equilibrium model (SLE)

The adsorption isotherm of *n*-C_7 asphaltenes onto nanoparticles is described by using the association theory suggested by Talu and Meunier[32] for the adsorption of associating molecules in micropores and further developed by Montoya et al.[33] for describing the adsorption isotherms of self-assemble asphaltenes onto non-porous surfaces. The model is expressed as follows:[33]

$$C_E = \frac{\psi H}{1+K\psi}\exp\left(\frac{\psi}{q_m \cdot A}\right) \tag{2.2}$$

where q_m (mg/m^2) is the maximum adsorption capacity, H is the measured Henry's law constant, which is only a function of temperature, and an indicator of the adsorption affinity (i.e., the strength of interactions for adsorption) of asphaltenes onto nanoparticle surface. The lower the H value (i.e., higher Henry's constant) is the higher the affinity (i.e., the active sites are in locations which are easily accessible by asphaltenes). K is constant and an indicator of rapid association of asphaltenes molecules once the primary sites are occupied. A (m^2/mg) is the measured surface area per mass of nanoparticles and C_E (mg/g) is the equilibrium concentration of asphaltenes. The other parameters are defined as follows:

$$K = \frac{K_T RT}{A} \tag{2.3}$$

$$\psi = \frac{-1+\sqrt{1+4K\xi}}{2K} \tag{2.4}$$

where, ξ is a constant defined as

$$\xi = \left(\frac{q_m \cdot q}{q_m - q}\right)A \tag{2.5}$$

q is the amount adsorbed (mg/m^2) and K_T is the reaction constant for dimer formation. For describing the thermodynamic properties of asphaltene adsorption, a five-parameter-temperature independent SLE model is used. In this case, H and K parameters in Eq. 2.2 are replaced by the following correlations:[33]

$$H = \exp\left(H_o + \frac{H_1}{T}\right) \tag{2.6}$$

$$K = \exp\left(K_o + \frac{K_1}{T} \right) \tag{2.7}$$

where K_0 and K_1 are related to the reaction entropy and reaction enthalpy of asphaltenes adsorption on the nanoparticles surface and T is the absolute temperature. Accordingly, the change in standard entropy (ΔS^o_{ads}) and standard enthalpy (ΔH^o_{ads}) are calculated as follows

$$\Delta S^0_{ads} = K_0 R \tag{2.8}$$

$$\Delta H^0_{ads} = K_1 R \tag{2.9}$$

Using the Gibbs equation,[34] the change in Gibbs free energy can be estimated as follows:

$$\Delta G^o_{ads} = -RT \ln K \tag{2.10}$$

The accuracy of the model was evaluated through the root-mean-square error (RMSE%) using the excel package:[35]

2.2.2 Effective activation energy estimation: The corrected Ozawa-Flynn-Wall Model

The corrected Ozawa-Flynn-Wall Model (OFW) give us an estimate of the effective activation energies assuming that for a constant reaction conversion, the reaction rate (Eq. 2.11) is function of the temperature and the state.[36, 37]

$$\frac{d\alpha}{dt} = A_\alpha \exp\left(-\frac{E_\alpha}{RT} \right) f(\alpha) \tag{2.11}$$

with A_α (1/s) as the pre-exponential factor, E_α (kJ/mol) the effective activation energy for a constant conversion, R (J/mol·K) the ideal gas constant, T (K) the reaction temperature and α the reaction conversion described by Eq. 2.12:

$$\alpha = \frac{m_0 - m_t}{m_0 - m_f} \tag{2.12}$$

where m_0 is the initial mass of the sample; m_f the final mass of the sample and m_t the mass at a given temperature. Defining the heating rate as $\beta = dT / dt$ and integrating, Eq. 2.13 is obtained:

$$g(\alpha) = \int_0^\alpha \frac{d\alpha}{f(\alpha)} = \int_0^T \frac{A_\alpha \exp(-E_\alpha / RT)}{\beta} dT \tag{2.13}$$

The right hand side of Eq. 2.13 is solved by a commonly approach employed for isoconversional methods by defining $x = -E_\alpha / RT$ and applying the Doyle approximation. [38, 39] After arrangement, the effective activation energy at each value of α can by estimated from the slope of the linear fit from the plot of $\ln(\beta)$ against $1/T$ according to Eq. 2.14:[37, 40, 41]

$$\ln(\beta) = \ln\left(\frac{A_\alpha E_\alpha}{205.54R \cdot g(\alpha)}\right) - 1.052\frac{E_\alpha}{RT} \tag{2.14}$$

The error in the estimation of E_α due to Doyle's approximation is corrected using a correction factor as showed in Eq. 2.15:[37, 42, 43]

$$E_{\alpha,corrected} = E_\alpha / F(x_m) \tag{2.15}$$

with,

$$x_m = E_\alpha / RT_m \tag{2.16}$$

$$F(x_m) = 0.94961\left(1 + \frac{7.770439 + x_m}{1 + 4.56092x_m + 0.48843x_m^2}\right) \tag{2.17}$$

where T_m (K) is the mean temperature at determined value of selected α.

- **Estimation of the thermodynamic parameters of the transition state functions**

Thermodynamic parameters of the transition state functions such as changes in the Gibbs free energy ($\Delta G^\ddagger$), enthalpy ($\Delta H^\ddagger$) and entropy ($\Delta S^\ddagger$) of activation are of importance in the understanding of the catalytic role of the SHS's nanoparticles. A conversion of 50% at a fixed heating rate of 5°C/min was used for the estimation of the thermodynamic parameters at the respective temperature T_p (K). Hence, $\Delta G^\ddagger$ can be estimated as shown in Eq. 2.18:

$$\Delta G^\ddagger = \Delta H^\ddagger - T_p \Delta S^\ddagger \tag{2.18}$$

where $\Delta H^\ddagger$ can be approximated to $\Delta H^\ddagger = E^\ddagger - RT_p$, with $E^\ddagger$ as the effective activation energy at the selecte.[45] In addition, after arrangement of the Arrhenius and Eyring equations,[37, 44-46] $\Delta S^\ddagger$ can be estimated as follows:

$$\Delta S^\ddagger = R\ln\left(\frac{A_\alpha h}{eT_p k_B}\right) \tag{2.19}$$

where h (6.6261 x 10^{-34} J·s) is the Planck's constant; e (2.7183) is the Neper number and k_B (1.3806 x 10^{-23} J/K) the Boltzmann's constant. The pre-exponential factor A_α can be estimated from the intercept of the linear plots of $\ln[g(\alpha)]$ against $\ln(\beta)$ according to Eq. 2.14. The *n*-order kinetic

expressions $(1-\alpha)^{-n+1}-1$ and $\frac{1}{n-1}(1-\alpha)^{n}$ were used for the estimation of the best-fit chemical reaction models $g(\alpha)$ and $f(\alpha)$, respectively. n is the mechanism order and was estimated as the value where the slope and the R^2 of the linear plots of $\ln[g(\alpha)]$ against $\ln(\beta)$ are equal to -1.0 and 1.0, respectively.

2.3 Results and discussions

2.3.1 Effect of *n*-C_7 asphaltenes origin on their adsorption and subsequent catalytic oxidation

- **Adsorption of *n*-C_7 asphaltenes from different origin over CS nanoparticles**

A number of factors can influence the adsorption of asphaltenes onto nanoparticles; including adsorbent surface chemistry, heterogeneity of adsorbent surface, particle size, asphaltenes chemical structure, heteroatom content, etc.[47] Figure 2.1 shows the experimental data of adsorption isotherms of Capella, AK9 and AK18 *n*-C_7 asphaltenes onto nanoparticles of CS together with the SLE model fits. As seen, there is excellent agreement between the model and experimental results. The values of the obtained model parameters and their corresponding *RSME%* values are presented in Table 2.2. Further, for all cases, the obtained adsorption isotherms followed Type I behavior according to the International Union of Pure and Applied Chemistry (IUPAC).[148] This is could be due to the strong interaction between the functional groups present on the asphaltene structure and the Si-OH group of the CS nanoparticle surface,[49] in agreement with previous studies on the adsorption of *n*-C_7 asphaltenes over silica nanoparticles.[29, 31] As observed in Figure 2.1, adsorption isotherms are similar for *n*-C_7 asphaltenes extracted from crude oils from the Akacías field and present a higher uptake than that for Capella *n*-C_7 asphaltenes. This results indicate that the asphaltenes origin strongly influences their adsorption over CS nanoparticles. However, for asphaltenes from the same reservoir it could be said that there is a similar uptake. Regarding to the SLE model, from Table 2.2 it can be observed that the *H* parameter follows the order Capella > AK18 > AK9, indicating that the adsorption affinity is highest for AK9 *n*-C_7 asphaltenes. This is in agreement with the shape of the adsorption isotherms that indicates that bigger slopes in the Henry's region (low C_E) are indicative of higher affinity between the adsorbent – adsorbate couple.[31] It is worth to mention that a direct relationship was found between the crude oil API gravity and the *H* parameter (adsorption affinity) of the SLE model: as the API gravity increases, the adsorption affinity decreases.

[1]In general, adsorption isotherms of *n*-C_7 asphaltenes in this work followed a Type I behavior according to the IUPAC. Although other classifications exists, IUPAC scheme is the most used for description of asphaltenes adsorption over nanoparticles. Actually, IUPAC reports six different types of adsorption isotherms. Differences among the different types could be attributed to many factors that are involved in the adsorbate – adsorbate and adsorbate – adsorbent surface interactions.

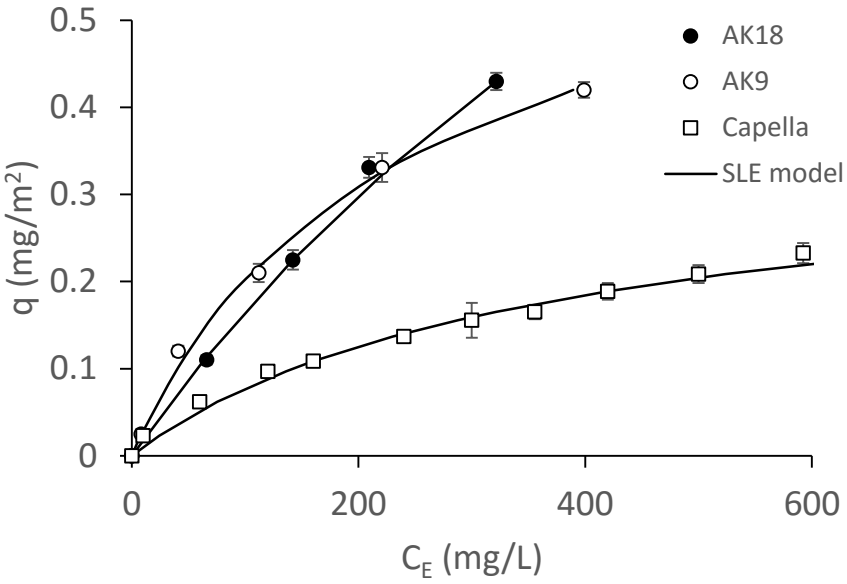

Figure 2.1. Adsorption isotherms of *n*-C_7 asphaltenes from different sources over CS nanoparticles at 25°C.

Thermodynamic studies are important for understanding the temperature effects on the adsorption of asphaltenes on different nanoparticle surfaces. Panels a-c from Figure 2.2 show the adsorption isotherms for Capella, AK9 and AK18 *n*-C_7 asphaltenes onto CS nanoparticles at 25, 50 and 55°C together with the five-parameters SLE model fits. For all systems, the amount of adsorbed asphaltenes decreases as the temperature increases because asphaltene adsorption onto nanoparticle surfaces is an exothermic process, while temperature affects the colloidal state of the asphaltenes.[2] [3, 24, 29, 50, 51] This could be explained as the solubility of *n*-C_7 asphaltenes increases, they tend to stay more in the liquid phase than in the adsorbed phase. Further, the increase in the system temperature can influence the degree of *n*-C_7 asphaltenes self-association and subsequently decrease the size of the asphaltenes aggregates.[25] In addition, the increase of the temperature could result in the reduction of Si−OH groups and, consequently, the number of sites available for adsorption is decreased.[49, 52] The values of the obtained model parameters, their corresponding errors and the estimated thermodynamic parameters are listed in Table 2.3. The negative ΔG^0_{ads} values reveal the feasibility and spontaneity of the adsorption processes; specifically, the adsorption process is spontaneous and thermodynamically favorable. The negative values of the standard enthalpy change (ΔH^0_{ads}) confirmed the exothermic nature of the sorption process. The positive values for the standard entropy change (ΔS^0_{ads}) were caused by the increased randomness at the solid−liquid interface during the sorption process. These findings agree with those reported by Nassar et al.,[24] Cortés et al.,[28] and Franco et al.[37] for the adsorption of different asphaltenes onto different nanoparticle surfaces.

[2] Decrease in the amount adsorbed as system temperature increases is a common behavior in the adsorption phenomena of *n*-C_7 asphaltenes over solid surfaces and was observed for all adsorption isotherms obtained in this document.

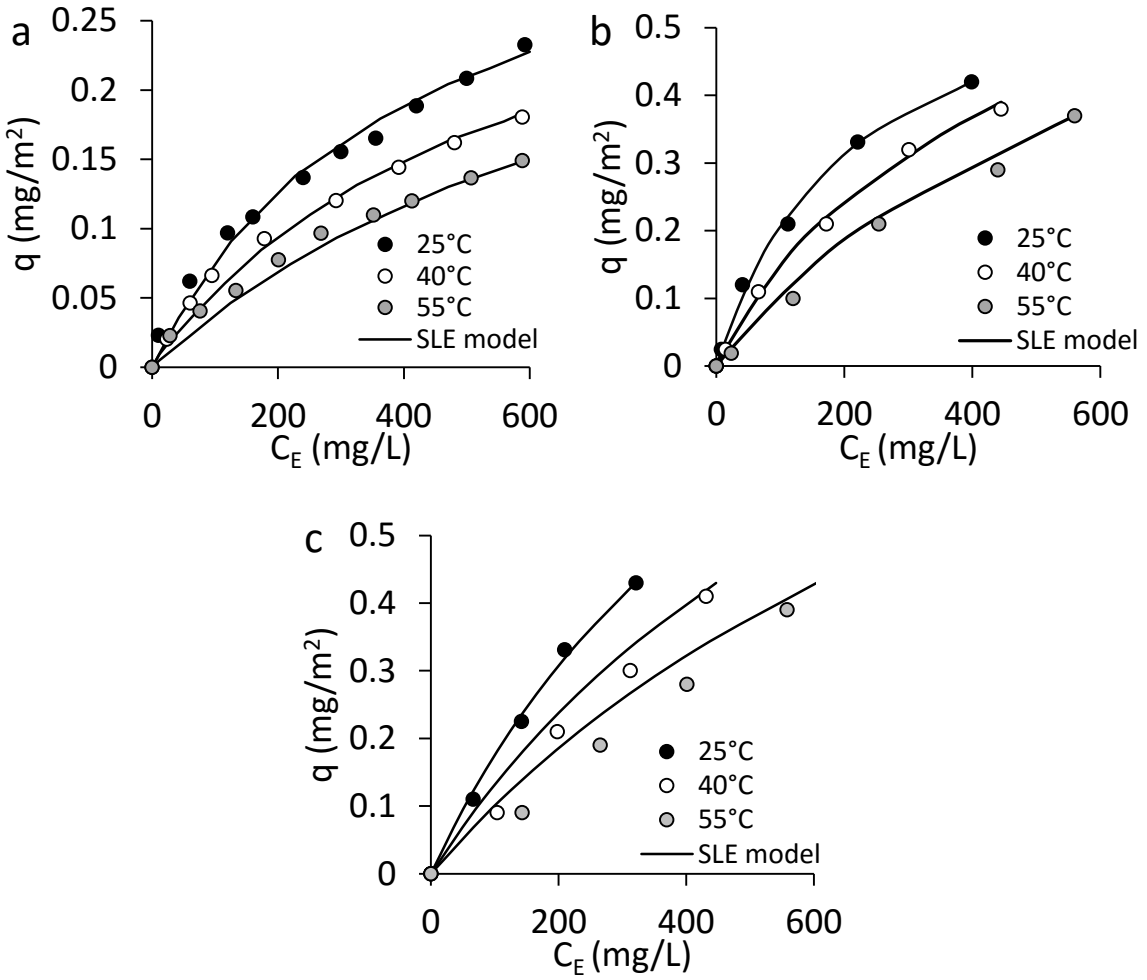

Figure 2.2. Adsorption isotherms of *n*-C_7 asphaltenes extracted from a) Capella, b) AK9 and c) AK18 crude oils over CS nanoparticles at different temperatures.

Table 2.2. Estimated SLE model parameters for *n*-C_7 asphaltenes from different sources adsorption over CS nanoparticles at 25°C.

***n*-C_7 asphaltene**	H **(mg/g)**	K **(g/g) × 10^{-4}**	q_m **(mg/m²)**	R^2	*RSME*%
Capella	2.13	4.39	0.47	0.99	6.69
AK9	0.99	4.46	1.18	0.99	3.93
AK18	2.02	4.51	2.89	0.99	8.72

- **Catalytic thermal oxidation of *n*-C_7 asphaltenes from different origin in absence and presence of CS nanoparticles**

Catalytic thermal oxidation of *n*-C_7 asphaltenes was performed to obtain insight into the effects of the selected nanoparticles under thermogravimetric conditions. The oxidation tests were carried out in an air atmosphere for a specific asphaltene loading in every sample (ca. 0.20 mg/m^2), and each sample had a minimal mass to preclude any mass-transfer limitations. Panels a-d of Figure 2.3 show a) Comparison of rate of mass loss for oxidation of virgin *n*-C_7 asphaltenes extracted from different crude oils and rate of mass loss of *n*-C_7 asphaltenes oxidation in presence of CS nanoparticles for b) Capella, c) AK9 and d) AK18 samples. It can be observed from Figure 2.3a that for the three different *n*-C_7 asphaltenes evaluated, there is no significant mass change in the asphaltenes below 300°C. However, for higher temperatures the asphaltenes underwent thermal cracking, and above 580°C, the oxidation to form gaseous products was complete. These results agree with those of Nassar et al.,[4] who studied the rate of mass loss in asphaltenes obtained from the Athabasca bitumen.

From the rate of mass loss plot, it can be observed that for the three samples there are two main peaks located between 430 and 500°C, indicating that the asphaltene decomposition occurs in different steps, initiating by thermal cracking with low-temperature oxidation followed by complete oxidation to gaseous products. Before 450°C, the mass loss could correspond to the oxidation of the aliphatic moieties of asphaltenes, and for the peaks observed after 450°C may correspond to opening and oxidation of the PAH core.[27] It can also be observed from Figure 2.3a that for *n*-C_7 asphaltenes from the same reservoir the oxidation starts and finishes at approximately the same temperature. The only difference lies in the height of each peak, being the one at lower temperatures smaller for AK9 *n*-C_7 asphaltenes than that of AK18 *n*-C_7 asphaltenes and could be due to the different proportions between the aliphatic and aromatic moieties in both samples. Oxidation of Capella *n*-C_7 asphaltenes occurred later than for *n*-C_7 asphaltenes from Akacías field, possible due to a larger PAH core that results in a more refractory molecule. Regarding to *n*-C_7 asphaltenes catalytic oxidation in presence of CS nanoparticles, it can be clearly seen from Figure 2.3b-d that in all cases the temperature of maximum rate of mass loss was reduced. In comparison with the first peak in the rate of mass loss plots for each asphaltene, the temperature was reduced about a 18, 14 and 15% for Capella, AK9 and AK18 *n*-C_7 asphaltenes, respectively, indicating that the CS nanoparticles catalyze asphaltene oxidation and that the catalytic activity is in a certain way influenced by the *n*-C_7 asphaltenes chemical nature.

It is worth to mention that for all cases of *n*-C_7 asphaltenes decomposition in presence of nanoparticles, noise from mass loss from the support was corrected. Nevertheless, as an example and in order to corroborate that mass loss is occurring due to asphaltenes, in Figure 2.4 is shown the plot of heat flow that describes the heat changes that occurred during oxidation for Capella *n*-C_7 asphaltenes in absence and presence of CS nanoparticles. According to Figure 2.4, the mass loss is not exothermic until 470 °C, when the complete oxidation to gaseous products by the presence of air occurs, as revealed by the similarity between the curves in Figure 2.3b and 2.4 for the virgin *n*-C_7 asphaltenes in this region. However, for the asphaltene oxidation with CS nanoparticles, the oxidation temperature decreased to 355 °C, indicating that the nanoparticles catalyze asphaltene oxidation. Figure 2.4 illustrates an exothermic behavior similar to that of the virgin asphaltenes except that it occurs at a temperature near the oxidation temperature of the asphaltenes with CS, confirming the catalytic role of CS.

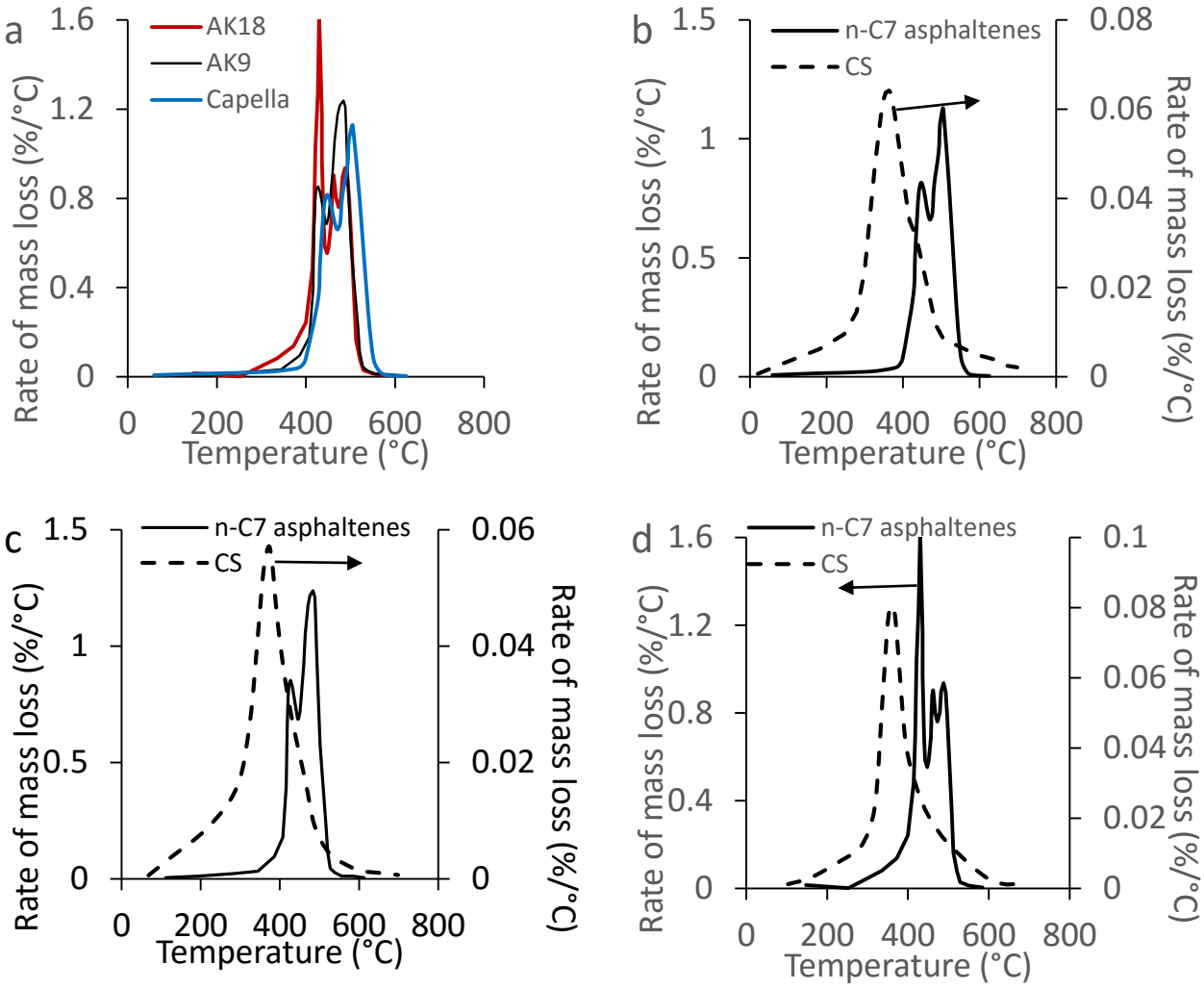

Figure 2.3. a) Comparison of rate of mass loss for oxidation of virgin *n*-C_7 asphaltenes extracted from different crude oils and rate of mass loss of *n*-C_7 asphaltenes oxidation in presence of CS nanoparticles for b) Capella, c) AK9 and d) AK18 samples.

Table 2.3. Estimated parameters of the five-parameter SLE model and thermodynamic properties for *n*-C_7 asphaltenes from different sources adsorption over CS nanoparticles at 25°C.

***n*-C$_7$ asphaltene**	**Temperature (°C)**	H_0	H_1	K_0	K_1	q_m **(g/g)**	$-\Delta G^0_{ads}$ **(kJ/mol)**	$-\Delta H^0_{ads}$ **(kJ/mol)**	$-\Delta S^0_{ads}$ **(J/mol·K)**	R^2	*RSME%*
	25						28.48				
Capella	40	14.19	-4396.97	3.48	-2388.31	0.21	28.93	19.86	28.95	0.99	2.71
	55						29.35				
	25						50.29				
AK9	40	3.79	-915.62	10.16	-3019.93	0.27	51.56	25.10	84.52	0.99	0.86
	55						52.83				
	25						34.58				
AK18	40	6.24	1174.39	7.16	-2025.07	0.83	35.47	16.83	59.54	0.99	6.77
	55						36.36				

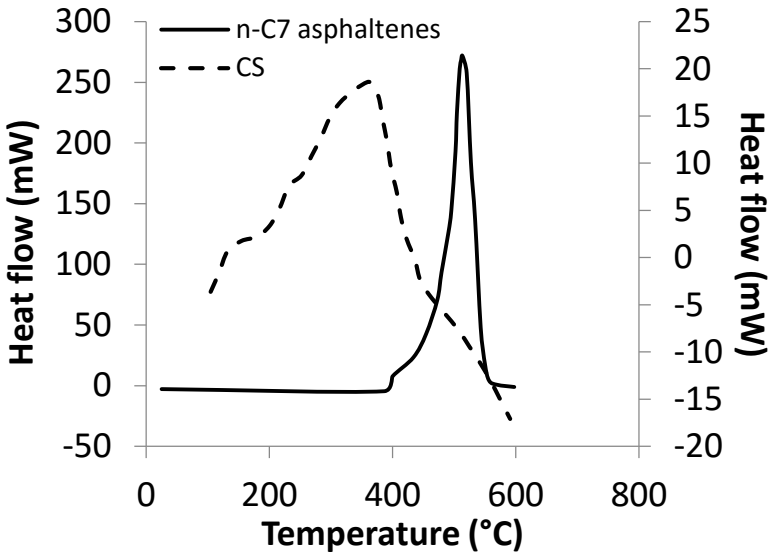

Figure 2.4. DTA-plot heat flow as a function of temperature for Capella *n*-C_7 asphaltenes oxidation in absence and presence of CS nanoparticles.

To further validate the catalytic activity of the nanoparticles, the isoconversional OFW method was used for estimating the effective activation energies using TGA mass loss rate measurements performed at heating rates of 5, 10 and 20°C/min. Panels a-c in Figure 2.5 show plots of conversion for virgin a) Capella, b) AK9 and c) AK18 *n*-C_7 asphaltenes as a function of temperature at three different heating rates. As anticipated, the rate of mass loss changes with the heating rate: at a fixed temperature, a slower heating rate yields a higher conversion[3]. Conversion plots of *n*-C_7 asphaltenes in presence of CS nanoparticles presented the same behavior as function of the heating rate than that of virgin *n*-C_7 asphaltenes.

Panels a-d from Figure 2.6 show the estimated effective activation energies (E_α) by the Ozawa−Flynn−Wall (OFW) method as a function of the conversion for oxidation of a) virgin Capella, AK9 and AK18 *n*-C_7 asphaltenes and b) Capella, c) AK9 and d) AK18 *n*-C_7 asphaltenes in presence of CS nanoparticles. In the case of virgin *n*-C_7 asphaltenes (Figure 2.6a) the E_α decreases with conversion and might occur because the virgin *n*-C_7 asphaltenes undergo thermal cracking in a more "homogeneous" step; there is no discrimination based on the self-association of the asphaltenes. However, the adsorption process onto the CS nanoparticle surfaces from the oil model solution might first adsorb the smaller asphaltene aggregates that reach the nanoparticles via diffusive processes before the larger aggregates are adsorbed in a new layer. Therefore, the catalysts must react with the asphaltenes in the initial layer (i.e., asphaltenes with lower molecular weight) first before interacting with the asphaltenes in other layers. In general, the values of E_α were estimated to be in the range between 200 and 100°C for the minimum and maximum values of conversion, respectively. Figure 2.6b-d indicates that below certain value of conversion, the E_α for *n*-C_7 asphaltenes oxidation lowered dramatically in the presence of CS nanoparticles, favoring the

[3] In this work all conversion curves showed the same trend as function of the employed heating rate and effective activation energies were calculated in the range of conversion were curves do not overlap in order to avoid overestimation of E_α.

catalytic activity. Values of E_α in presence of CS nanoparticles could indicate that due to addition reactions more refractory compounds that need more energy for being cracked could be formed over the catalyst surface, corroborating the influence of the asphaltene origin on the catalytic activity of the nanoparticles. In this sense, from Figure 2.6 it could be said that Capella *n*-C_7 asphaltenes are the *"hardest to crack"* and would need a nanoparticle with higher catalytic activity.

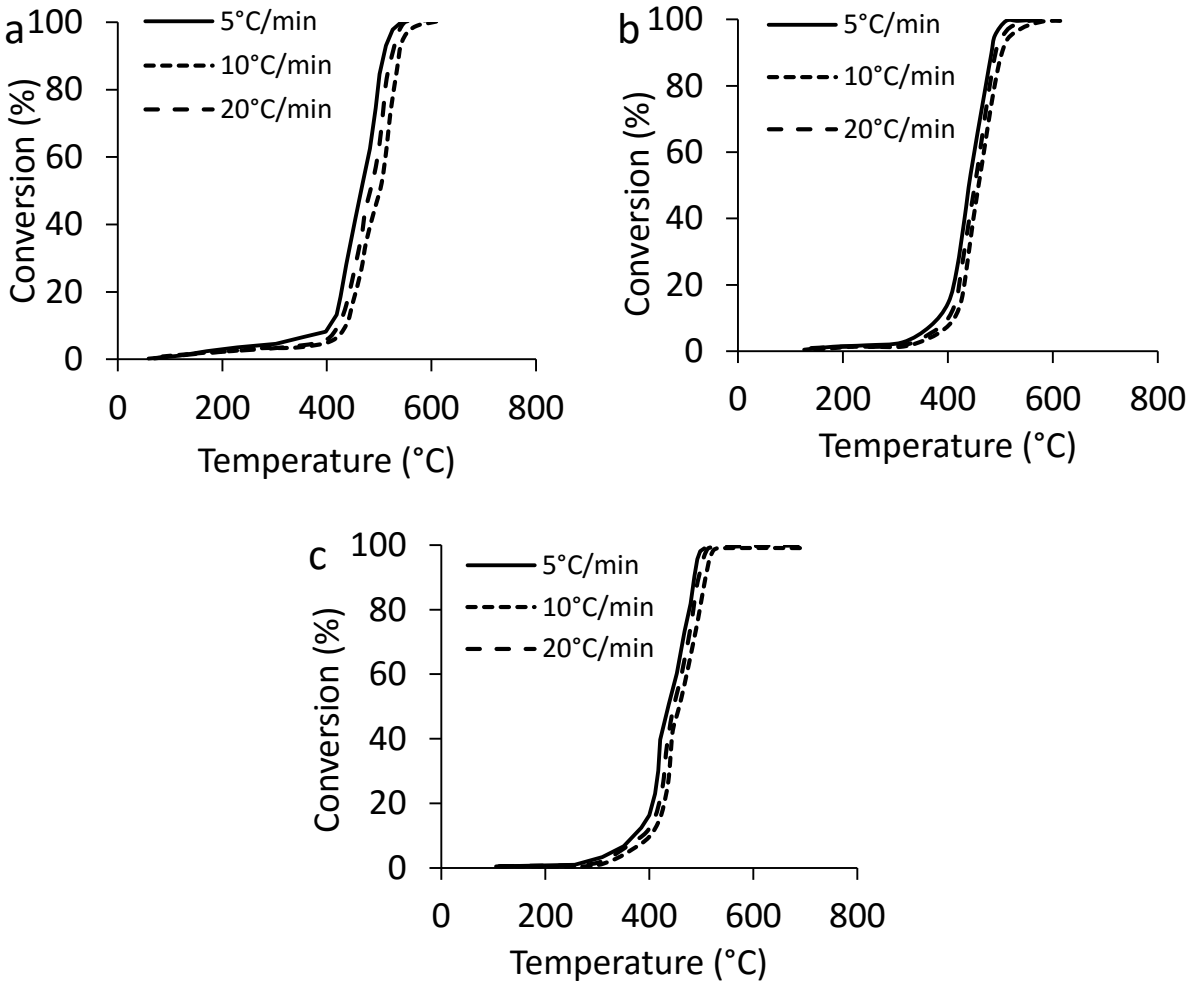

Figure 2.5. Conversion for oxidation of virgin *n*-C_7 asphaltenes extracted from a) Capella, b) AK9 and c) AK18 crude oils.

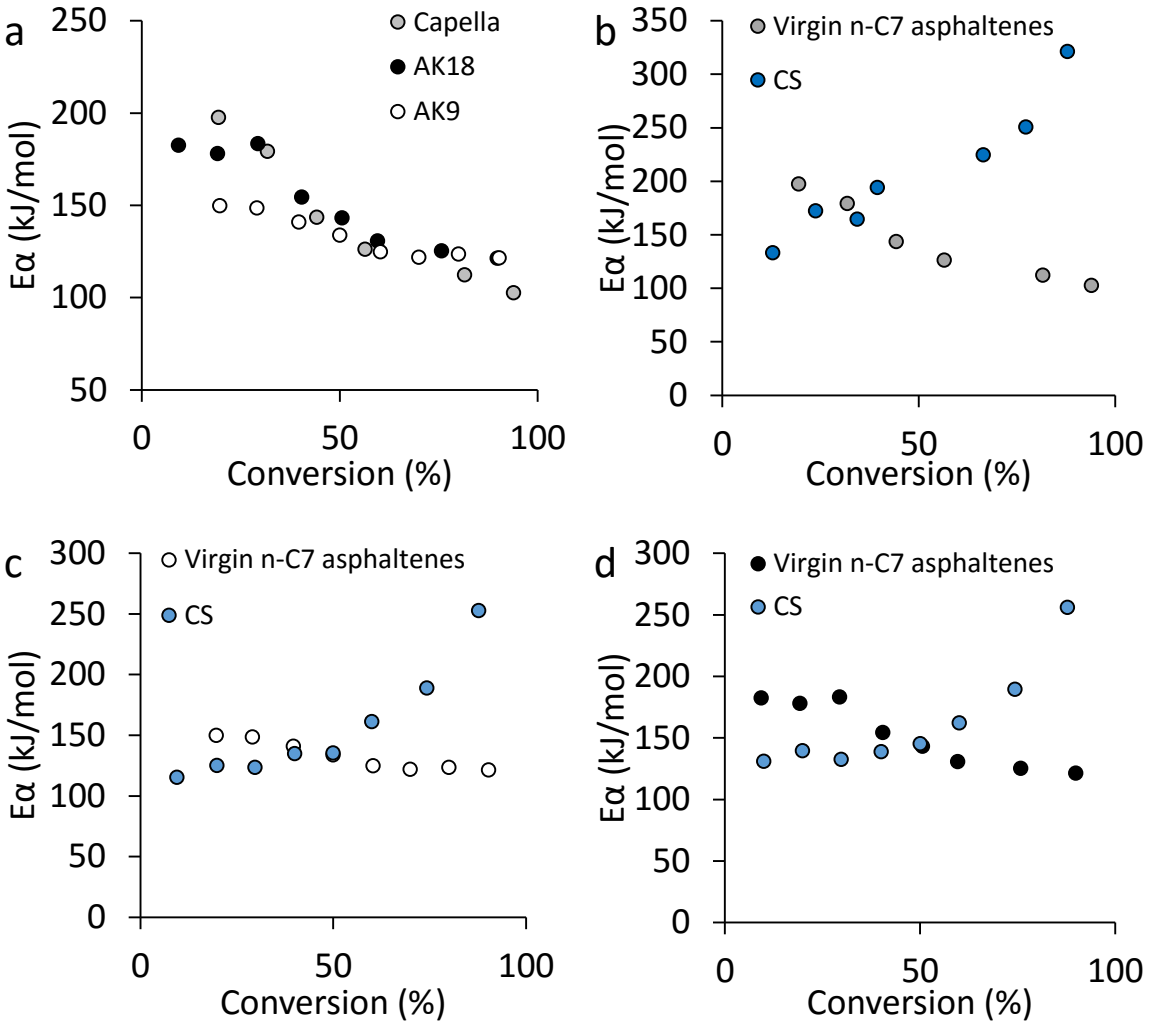

Figure 2.6. Effective activation energies by the Ozawa−Flynn−Wall (OFW) method as a function of the conversion for oxidation of a) virgin Capella, AK9 and AK18 *n*-C_7 asphaltenes and b) Capella, c) AK9 and d) AK18 *n*-C_7 asphaltenes in presence of CS nanoparticles.

2.3.2 *n*-C_7 asphaltenes adsorption and subsequent catalytic oxidation using SS nanoparticles and CNS.

- **Adsorption of *n*-C_7 asphaltenes over SS nanoparticles and CNS**

Adsorption isotherms were constructed for a fixed asphaltene following the procedure described in Section 1.1.2. AK9 *n*-C_7 asphaltenes were selected for adsorption experiments. Panels a,b from Figure 2.7 show the adsorption isotherms of AK9 *n*-C_7 asphaltenes over a) SS nanoparticles and b) CNS at 25°C together with the SLE model fitting. Also, Table 2.4 resumes the estimated SLE model parameters. As observed in Figure 2.7a, all SS nanoparticles showed higher AK9 *n*-C_7 asphaltenes uptake than CS nanoparticles. The trend of AK9 *n*-C_7 asphaltenes uptake and the adsorption affinity is SSB6 > SSA6 > SSA3, indicating that the amount adsorbed increases and the interactions asphaltenes – nanoparticle become greater by increasing the amount of the silicate precursor (see Chapter 1 for full nanoparticles information). Also, it is worth to mention that a higher amount

adsorbed was obtained for smaller materials and could be due to a higher exposition of the functional groups over the adsorbent surface and an enhanced mobility in the bulk phase of the solution. The adsorption process of asphaltenes onto the silica surface occurs mainly due to the Si−OH functional group on the material surface. The theoretical value of the point of zero charge (*pHpzc*) for pure silica corresponds to a pH value of 2.0,[53] and generally for commercial silica the *pHpzc* < 3.5.[54] This indicates that the nature of the adsorbent surface is acidic and would be more prone to attract hydroxyl groups present on the asphaltene molecules.[55]

Regarding to the CNS, it is observed that CNS300 presents a higher amount of adsorbed asphaltenes and higher affinity than CNS150 and could be directly influenced by the lower particle size and higher surface area of CNS300. However, it is observed that the amount adsorbed is an order of magnitude lower than for SS nanoparticles and could be due to the basic nature of the CNS surface.[56] Bailón-García et al.[56] synthesized microspheres of carbon xerogel of 250 nm in diameter and found that the synthesized material had a basic surface with a *pHpzc* = 8.73. Xing et al.[57] reported that the asphaltenes adsorbed onto basic surfaces present higher concentrations of sulfur; however, the total adsorbed amount of the asphaltenes was lower, compared with the adsorbed amount over acid surfaces, which bind more quickly or strongly to lower sulfur-containing species.[57, 58]

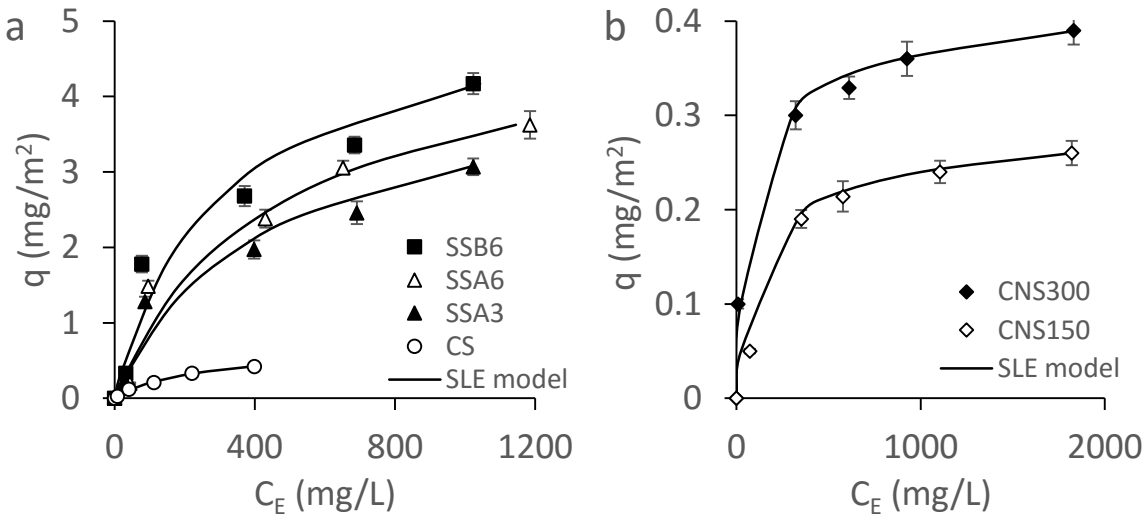

Figure 2.7. Adsorption isotherms of AK9 *n*-C_7 asphaltenes over a) SS nanoparticles and b) CNS at 25°C.

Table 2.4. Estimated SLE model parameters for AK9 *n*-C_7 asphaltenes adsorption over SS nanoparticles and CNS at 25°C.

Material	H **(mg/g)**	K **(g/g) × 10^{-4}**	q_m **(mg/m^2)**	R^2	*RSME*%
SSA3	3.22	4.50	7.25	0.98	7.22
SSA6	2.93	4.57	8.37	0.99	2.92
SSB6	2.51	4.68	8.74	0.98	7.61
CNS150	4.80	4.01	0.40	0.99	2.59
CNS300	2.06	4.04	0.57	0.99	5.70

Table 2.5 lists the obtained thermodynamic parameters and the estimated values of the five-parameter SLE model parameters for all synthesized nanoparticles. As observed, for SS nanoparticles and CNS, the negative values of ΔG^0_{ads} also showed the spontaneity of the adsorption process of *n*-C_7 asphaltenes over the selected materials, being "more spontaneous" for the CNS than for SS nanoparticles. Also, ΔH^0_{ads} and ΔS^0_{ads} followed the same behavior than that observed for CNS nanoparticles.

Table 2.5. Estimated parameters of the five-parameter SLE model and thermodynamic properties for AK9 *n*-C_7 asphaltenes over SS nanoparticles and CNS at 25°C.

Material	**Temperature (°C)**	H_0	H_1	K_0	K_1	q_m **(g/g)**	$-\Delta G^0_{ads}$ **(kJ/mol)**	$-\Delta H^0_{ads}$ **(kJ/mol)**	$-\Delta S^0_{ads}$ **(J/mol·K)**	R^2	*RSME*%
	25						80.20				
SSA3	40	8.48	-2039.13	0.28	-9561.96	0.33	81.22	79.50	2.33	0.98	7.18
	55						82.24				
	25						67.77				
SSA6	40	8.69	-2006.60	12.24	-4503.01	0.41	68.78	37.44	101.77	0.99	1.34
	55						69.80				
	25						42.34				
SSB6	40	4.77	-868.29	9.49	-1046.53	0.42	43.41	86.86	78.90	0.99	0.99
	55						44.45				
	25						154.82				
CNS150	40	14.39	-111.82	52.98	-2832.88	0.22	159.22	23.55	44.50	0.98	6.98
	55						163.33				
	25						108.28				
CNS300	40	1.08	-590.02	11.68	-9542.5	0.85	109.25	79.34	97.11	0.98	6.75
	55						110.22				

- **n-C_7 asphaltenes catalytic oxidation in presence of SS nanoparticles and CNS**

Figure 2.8 shows the rate of mass loss and E_α for oxidation of AK9 n-C_7 asphaltenes in presence of a) and b) SS nanoparticles and c) and d) CNS, respectively. As observed, for all synthesized materials the temperature of n-C_7 asphaltenes decomposition shifted to lower temperatures (Figure 2.8 a and c) in comparison with the virgin AK9 n-C_7 asphaltenes. Regarding to the SS nanoparticles, a one main peak is observed in the rate of mass loss for the three evaluated materials at about 360 ± 2°C, representing a 16% of reduction in the temperature of oxidation of selected asphaltenes. This result indicates that the chemical properties of silica nanoparticles such as particle size, surface area and chemical composition have a more important effect in the adsorption process than in the n-C_7 asphaltenes oxidation and is especially true for nanoparticles obtained from the same synthesis route as observed for SSA materials. Same observations can be made for CNS in Figure 2.8c, were it is observed that the shape of the rate of mass loss curve for CNS150 is similar than that of CNS300.

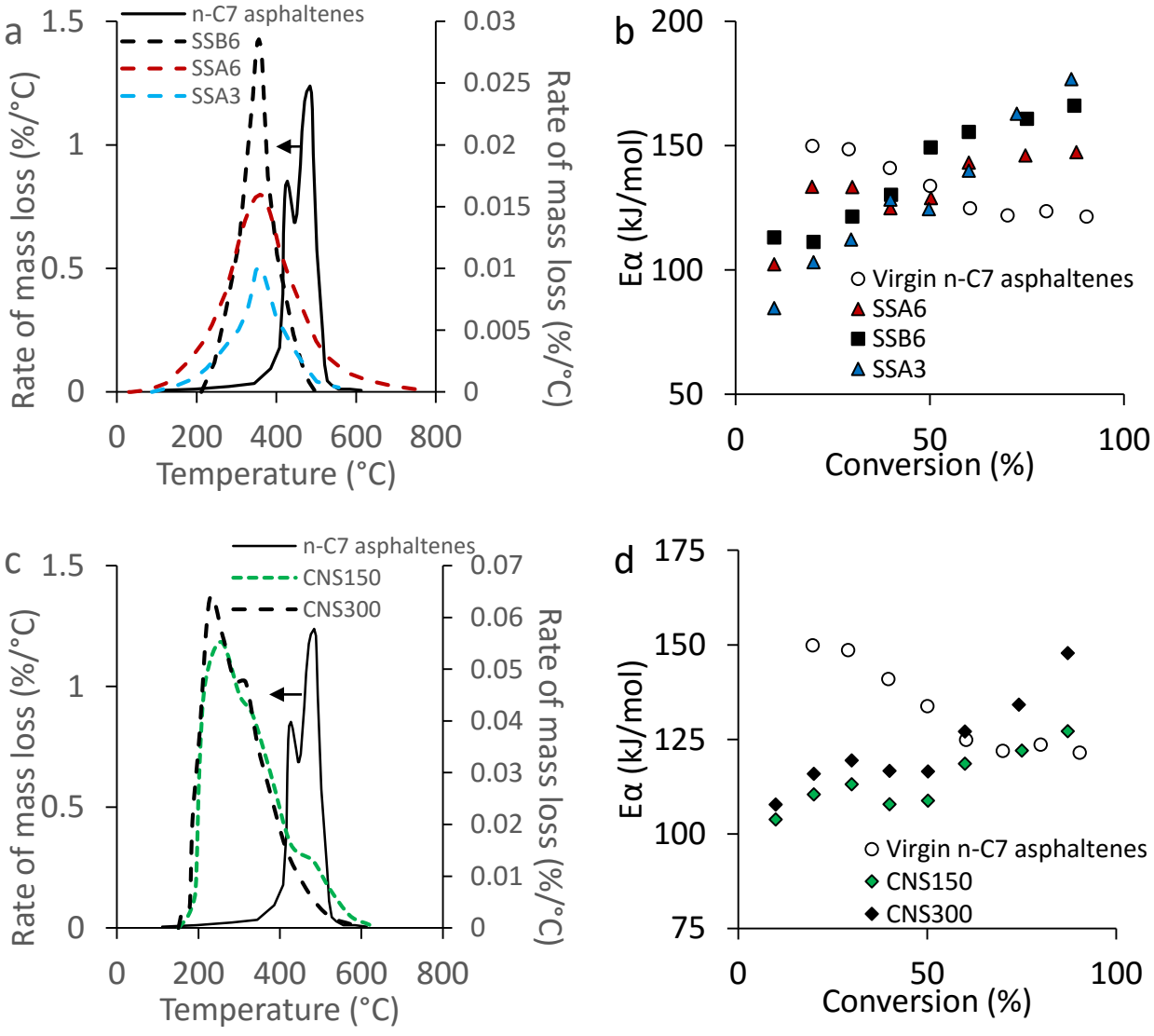

Figure 2.8. Rate of mass loss and effective activation energies by the Ozawa−Flynn−Wall (OFW) method as a function of the conversion for oxidation of AK9 n-C_7 asphaltenes in presence of a) and b) SS nanoparticles and c) and d) CNS, respectively.

However, the maximum of *n*-C_7 asphaltenes oxidation appears 30°C earlier for CNS300 than for CNS150 and could be due to the presence of some Cs from the polymerization catalyst that affected the decomposition of asphaltenes. For all synthesized materials, the trend of E_α for asphaltene gasification in the presence of nanoparticles is opposite of that of virgin *n*-C_7 asphaltenes, showing a markedly lower effective activation energy compared with that of virgin *n*-C_7 asphaltene oxidation. Thus, the trend of effective activation energy is affected by the nanoparticles present due to the occurrence of different reaction mechanisms. In general, the values of E_α for CNS were lower than those for SS nanoparticles. It is also observed that for the asphaltenes adsorbed over CNS, the pathway followed by E_α is similar to an upward shift as the resorcinol:Cs_2CO_3 molar increases, suggesting that the mechanisms involved are similar for the both samples.

2.3.3 SHS nanoparticles for *n*-C_7 asphaltenes adsorption and subsequent catalytic cracking.

Capella *n*-C_7 asphaltenes were selected as adsorbate for the adsorption and oxidation tests in presence of SHS nanoparticles due to, when comparing asphaltenes from different sources, it was the sample with lower amount adsorbed and were "*hardest to crack"* (See Section 2.3.1). SHS nanoparticles are composed by a CS nanoparticulated support functionalized with NiO and/or PdO nanocrystals according to the protocol defined in Chapter 1, Section 1.1.2. Additionally, characterization of SHS nanoparticles can be found in Chapter 1.

- **Adsorption of *n*-C_7 asphaltenes over SHS nanoparticles**

Figure 2.9 shows the experimental data of adsorption isotherms of Capella *n*-C_7 asphaltenes onto selected SHS nanoparticles together with the SLE model fits. SHS's clearly adsorbed more *n*-C_7 asphaltenes than CS across the entire range of asphaltene concentrations; the difference was more noticeable at higher concentrations (C_E > 200 mg/L). The sorption isotherms for every sample revealed an increase in the adsorbed *n*-C_7 asphaltene content as the *n*-C_7 asphaltene concentration increased. In Figure 2.9, the CS and SHS samples evaluated in this study demonstrated a high affinity for asphaltene sorption. At the concentrations at which samples were compared (0−200 mg/L), the asphaltene uptake was higher for CSPd2 and CSNi2 than for CSPd1 and CSNi1; however, the amount adsorbed was the highest on CSNi1Pd1 due to the intermolecular forces between the most polar components of the asphaltenes (mainly functional groups and heteroatoms), the NiO and/or PdO particles present on the silica surface, the high concentration of the metal oxides, and the high dispersion of the NiO/PdO particles across the hybrid nanomaterial surface (Chapter 1, Table 1.2).. However, the synthesized SHS revealed a high affinity for asphaltene sorption. The adsorption capacities for the S and SHS samples were ranked as follows: CSNi1Pd1 > CSPd2 > CSNi2≈CSPd1 > CSNi0.66Pd0.66 > CSNi1 > CS. Further, bimetallic SHS have higher uptake than monometallic SHS. This could be because of the synergistic effect of the compounds that enhances the adsorption due to the multiple selectivity of the adsorbent.[59] In addition, bimetallic compounds have synergistic effects in avoiding sintering processes, which would lead to a less heterogeneous surface.[60] Hence, a heterogeneous adsorbent with multiple selectivity towards *n*-C_7 asphaltenes would be more efficient than that with single selectivity. Table 2.6 shows that the adsorption affinity (i.e., lower H) is higher for the supported nanoparticles, where bimetallic supported on silica showed the highest affinity (lowest *H* value). As for the values of *K* parameter, it followed the order CS > CSNi2 >

CSPd2 > CSNi1Pd1. This suggests that silica supported metal oxide nanoparticles are more prone to inhibit the asphaltenes self-association over its surface than the virgin CS nanoparticles.

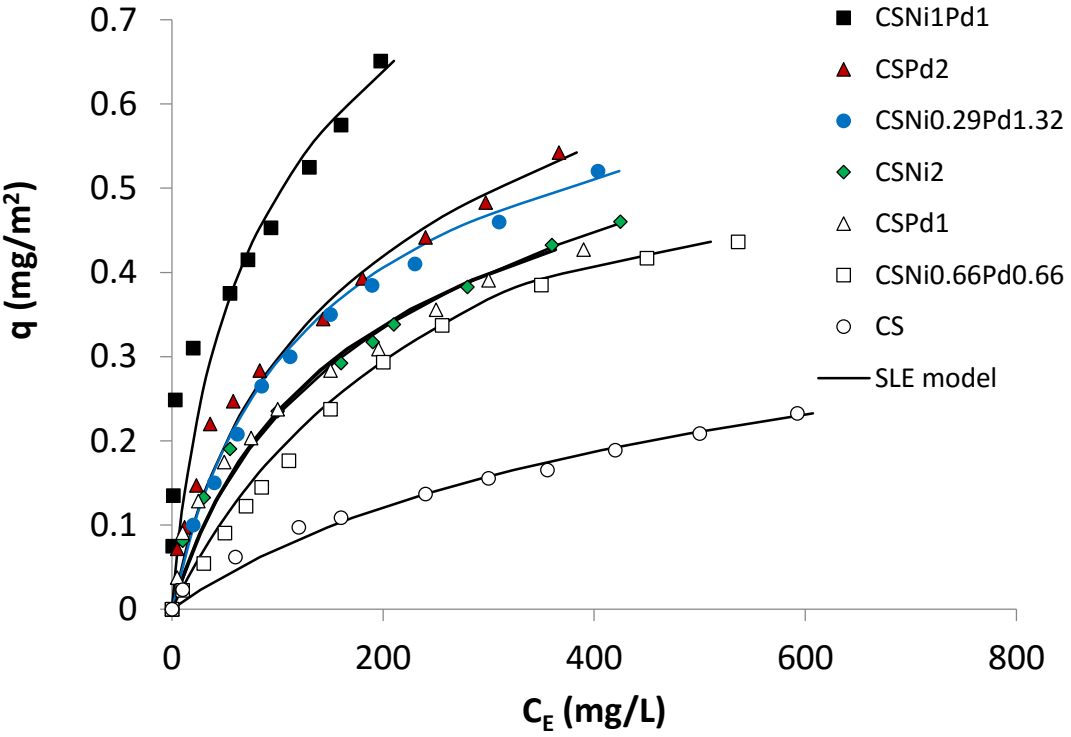

Figure 2.9. Asphaltene adsorption isotherms onto different surfaces of CS supported SHS nanoparticles at 25 °C.

Table 2.6. SLE model parameters for Capella *n*-C_7 asphaltenes adsorption over SHS nanoparticles.

Material	H **(mg/g)**	K **(g/g) × 10^{-4}**	q_m **(mg/m^2)**	R^2	*RSME*%
CSNi1	1.61	4.22	0.91	0.99	2.16
CSNi2	1.31	3.57	1.12	0.99	3.65
CSPd1	1.18	3.32	1.05	0.99	6.42
CSPd2	0.68	2.82	1.07	0.99	2.93
CSNi0.29Pd1.32	0.92	3.41	1.09	0.99	5.49
CSNi0.66Pd0.66	2.03	3.12	1.19	0.99	6.75
CSNi1Pd1	0.29	1.53	1.24	0.98	3.15

Materials on the extreme vertices of the SCMD and the bimetallic SCNi1Pd1 sample were selected for the thermodynamic studies. Again, there is good agreement between the model and the experimental results. The values of the obtained model parameters and their corresponding *RSME%* values are presented in Table 2.7. The estimated thermodynamic parameters are also listed in Table 2.7. ΔG^0_{ads}, ΔH^0_{ads} and ΔS^0_{ads} followed the same behavior than for CNS, SS and CS nanoparticles as presented in previous sections. The trend followed by ΔG^o_{ads} is CS > CSNi2 > CSPd2 > CSNi1Pd1, indicating that bimetallic SHS is more favorable for *n*-C_7 asphaltene adsorption than the monometallic SHS. The values of ΔS^0_{ads} followed the order CSNi1Pd1 > CSPd2 > CSNi2 > CS. This again supports that silica supported metal oxide nanoparticle pose lower degree of asphaltenes self-association onto their surfaces than those of virgin silica nanoparticles.[33]

Table 2.7. Estimated parameters of the five parameters SLE model for adsorption of asphaltenes onto CSNi2, CSPd2 and CSNi1Pd1 nanoparticles.

Material	Temperature (°C)	H_0	H_1	K_0	K_1	q_m (g/g)	$-\Delta G^0_{ads}$ (kJ/mol)	$-\Delta H^0_{ads}$ (kJ/mol)	$-\Delta S^0_{ads}$ (J/mol·K)	R^2	*RSME%*
	25						42.86				
CSNi2	40	9.32	-2642.94	7.82	-2825.72	0.22	43.71	23.49	64.98	0.98	2.48
	55						44.81				
	25						44.24				
CSPd2	40	11.89	-3573.28	8.12	-2901.50	0.24	65.29	24.12	67.52	0.99	4.33
	55						46.27				
	25						49.09				
CSNi1Pd1	40	8.93	-2956.41	8.93	-3244.74	0.25	50.22	26.98	74.21	0.98	5.97
	55						51.32				

- ***n*-C_7 asphaltenes catalytic oxidation in presence of SHS nanoparticles**

n*-C_7 *asphaltenes catalytic oxidation in presence of monometallic SHS: For practical reasons, the full range of temperatures used for the thermogravimetric analysis will be divided into three regions for all SHSs. The first region corresponds to the low-temperature region (LTR) between 200°C and 250°C. The second falls between 251°C and 450°C and is called the midtemperature region (MTR). The last region covers temperatures from 451°C to 800°C and is the high-temperature region (HTR). Because *n*-C_7 asphaltenes are not pure compounds, they exhibit different behaviors during thermal decomposition and oxidation because compounds with lower molecular weight oxidize at lower

temperatures. Figure 2.10a and 2.10b reveals a) a plot of the rate of mass loss relative to temperature and b) the conversion for asphaltenes in the presence of monometallic SHS for a specific amount of adsorbed asphaltene (ca. 0.2 mg/m^2). As observed, the samples containing palladium oxide exhibit a peak in the low temperature range (Figure 2.10a), suggesting that there is a significant change in the sample mass due to *n*-C_7 asphaltene oxidation. *n*-C_7 asphaltene oxidation begins at 244°C and 215°C for CSPd1 and CSPd2, respectively. This temperature reduction reveals that increasing the Pd content on the silica surface enhances the catalytic activity. In the MTR region at approximately 355°C, there is another significant mass loss caused by the oxidation of larger chains. Finally, in the HTR region, the heaviest compounds are oxidized. The functionalization of CS nanoparticles with 2 wt% Pd leads to a higher mass loss in the LTR region, while materials with 1 wt% Pd exhibit the opposite effect. Figure 2.10b displays the conversions for CSPd1 and CSPd2. The asphaltene oxidation is initiated at essentially the same temperature for both samples (220°C), but when the temperature increases, the conversion is higher with CSPd2. For example, at 400°C, the conversions are 43 and 58 wt % for CSPd1 and CSPd2, respectively. Further, the presence of Ni on the silica surface does not generate a peak in the LTR, indicating that CSPd1 and CSPd2 are better catalysts than the nanoparticles functionalized with only nickel oxide. Only two peaks are observed for CSNi1 and CSNi2. The peaks in the MTR region fall at 316°C and 347°C and are the largest mass losses for CSNi1 and CSNi2, respectively. In the HTR, the final asphaltene oxidation step occurs approximately at 480°C in both samples. According to Figure 2.10b, below 300°C (before oxidation begins), the conversions exhibited by both samples functionalized with Ni are quite similar. However, above 300°C, the conversion for CSNi2 is almost 5% higher than that for CSNi1, indicating that, similar to the Pd-loaded nanoparticles, increasing the metal oxide content on the silica surface enhances the catalytic activity. The conversion with CSNi2 is higher than the conversion with SPd2 above 300°C; this result might occur because, between 200°C and 300°C, the SPd2 oxidized fraction of the asphaltenes was adsorbed, while CSNi2 had not yet begin its oxidation process.

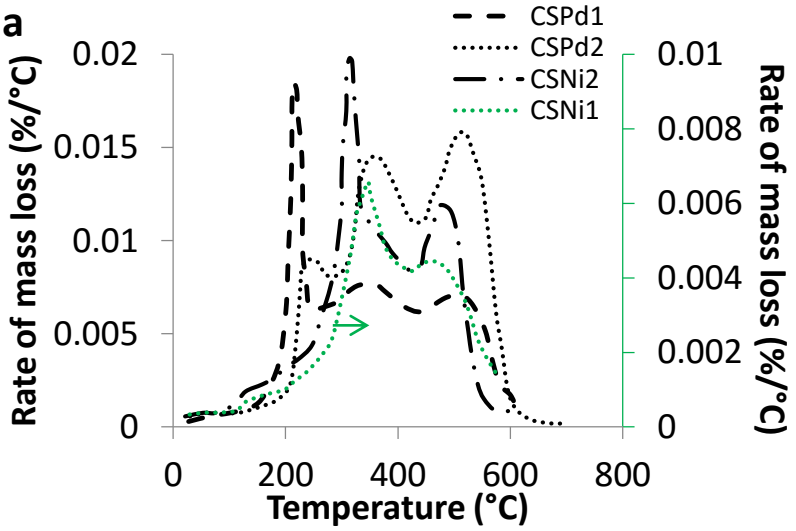

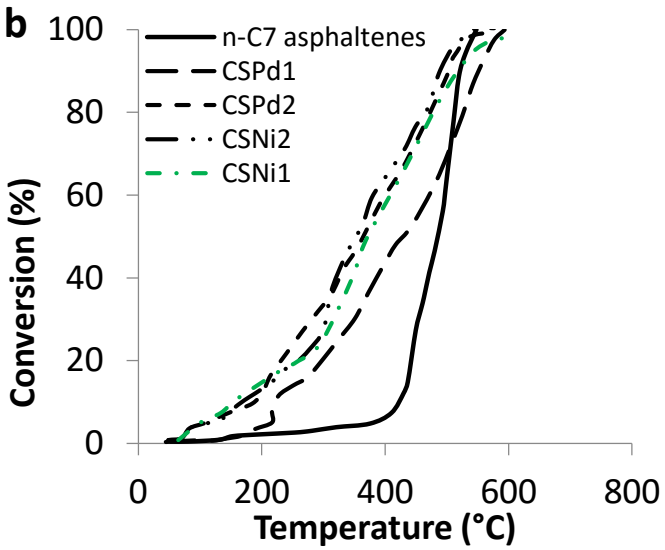

Figure 2.10. a) Plot of rate of mass loss as a function of temperature and b) conversion for *n*-C_7 asphaltenes oxidation in the presence of monometallic SHS.

n*-C_7 *asphaltenes catalytic oxidation in presence of bimetallic SHS: Two bimetallic samples were used to evaluate the effects of using bimetallic catalysts during *n*-C_7 asphaltene oxidation. Figures 2.11a and 2.11b present a) a plot of the rate of mass loss versus temperature and b) the conversion for the *n*-C_7 asphaltene oxidation in presence of bimetallic SHS materials for the same amount of asphaltenes used with the monometallic SHSs. Figure 2.11a reveals that both samples exhibited three peaks, similar to CSPd1 and CSPd2. The difference is that CSNi1Pd1 has one peak in the MTR (255 °C) that is very close to the boundary for the LTR. In addition, the peak in the HTR does not represent as significant of a mass loss as the other two. A similar observation can be noted for the CSNi0.66Pd0.66 samples. Three peaks are observed, with one in each region. The more significant mass losses in this case are revealed at 219°C, 347°C, and 517°C for the LTR, MTR, and HTR, respectively, with the first being the largest. Clearly, the Pd and Ni exert a synergistic effect during *n*-C_7 asphaltene oxidation because having both metals present enhanced the *n*-C_7 asphaltene oxidation in the LTR at the expense of the MTR mass loss. Another indication of the synergistic effects exhibited by the bimetallic SHS is revealed by the conversion analysis. As observed in Figure 2.11b, the conversion under these samples begins near 200°C and is higher with CSNi1Pd1. When making the same comparison as above, at 400°C, the conversion with CSNi0.66Pd0.66 is 4% higher than for CSPd2, while the conversion with CSNi1Pd1 is 94% and therefore 38% higher than for CSPd2. The *n*-C_7 asphaltenes are nonpure components; therefore, NiO and PdO could have different selectivity for different compounds in the *n*-C_7 asphaltenes. When the CS nanoparticles are functionalized with just NiO or just PdO, the catalytic reaction will be based on the compound of preference. However, when the CS nanoparticles are functionalized with both PdO and NiO, the combination of individual constituents enhances the catalytic activity. As reported by Wu et al.[61] hybrid structures with noble metals such as palladium and non-noble metals such as nickel allow better surface electronegativity, leading to more efficient conversion in catalytic processes.

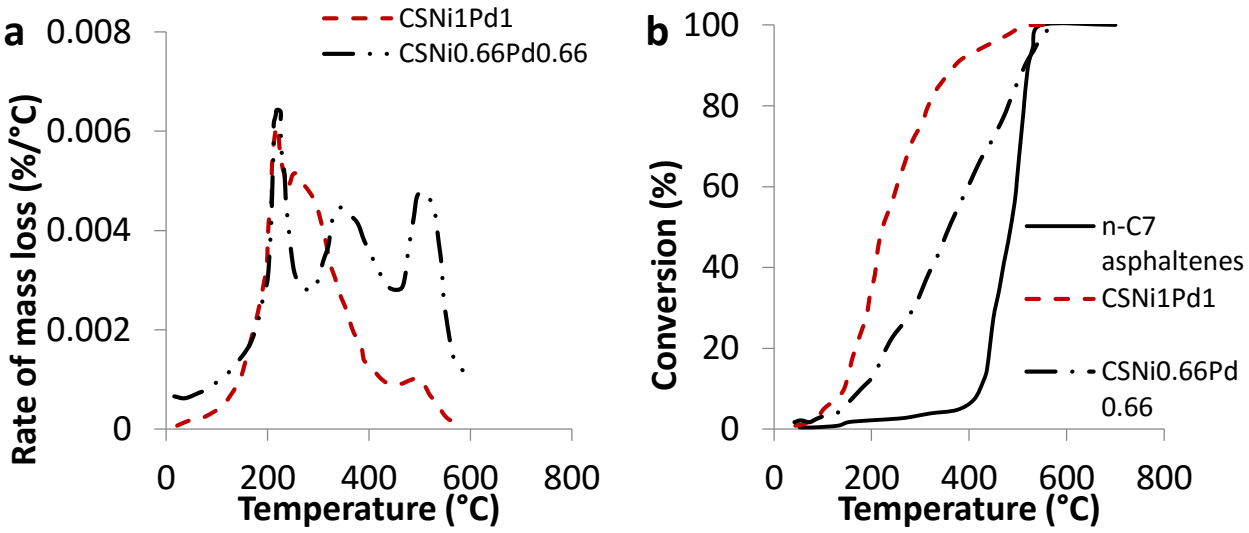

Figure 2.11. a) Plot of rate of mass loss as a function of temperature and b) conversion for *n*-C_7 asphaltenes oxidation in the presence of bimetallic SHS.

Gaseous products from n-C_7 asphaltenes oxidation in absence and presence of SC and SHS nanoparticles: The evolution of gases production was also evaluated using an FTIR device coupled to the TGA analyzer. Panels a-e from Figure 2.12 show the evolution of CO, CO_2, CH_4 and other light hydrocarbons production for oxidation of a) virgin *n*-C_7 asphaltenes and *n*-C_7 asphaltenes in presence of b) CS, c) CSNi2, d) CSPd2 and e) CSNi1Pd1 at a fixed heating rate of 10°C/min. It is worth to mention that the results are normalized based on the signal with highest intensity that corresponds to the CO_2 production. In all cases, it is observed that the major production corresponds to the CO_2. The general trend of effluent production increases in the order CO < CH_4 < Hydrocarbons < CO_2. This could be due to the oxygen chemisorption that occurs at low temperatures in the active sites of the stacked clusters. As the temperature is increased, light hydrocarbons are released and the exposure of the aliphatic moieties in the bulk of the cluster is enhanced, so the oxygen chemisorption is also enhanced.[6] It is observed that in presence of nanoparticles, the gases production starts at earlier temperatures than for virgin *n*-C_7 asphaltenes, corroborating the catalytic effect of the nanoparticulated catalysts.

Minimization of oxidation temperature of n-C_7 asphaltenes from SCMD: The temperature where the oxidation process begins for each sample was used as a reference when performing the minimization. The statistical analysis of the results is generated using the STATGRAPHICS Centurion XVI software. Table 2.8 lists the values of β_i for the cubic special model of the oxidation temperature as a function of the pseudocomponents *S', Pd',* and *Ni'*. The special cubic model validates the experimental data; R^2 = 1.0 and suitably predicts the temperature at which the asphaltene oxidation begins over any amount of S, Ni, and Pd. The optimal concentration of Ni and Pd on the CS surface needed to minimize the asphaltene oxidation temperature is 0.29% Ni and 1.32% Pd (CSNi0.29Pd1.32). Figure 2.9 depicts the sorption isotherm obtained for CSNi0.29Pd1.32 (blue line). Below 50 mg/L, the adsorption capacity of the material exceeds that of CSNi1, CSNi0.66Pd0.66, and CS. However, above 50 mg/L, only CSPd2 and CSNi1Pd1 perform better than the optimized sample. Figure 2.13 presents the conversion and a plot for the rate of mass loss versus temperature for SNi0.29Pd1.32 with an asphaltene loading of 0.2 mg/m^2. Figure 2.13 reveals that the optimized sample also displays three peaks with one in each region, similar to the other bimetallic samples. However, the peak in the MTR falls between the peaks of the other bimetallic SHSs. With regard to conversion, the shape of the curve is similar to that for CSNi0.66Pd0.66. Therefore, when

there is a lower NiO and PdO content on the surface of CS, results can be obtained that are similar to those for CSNi1Pd1.

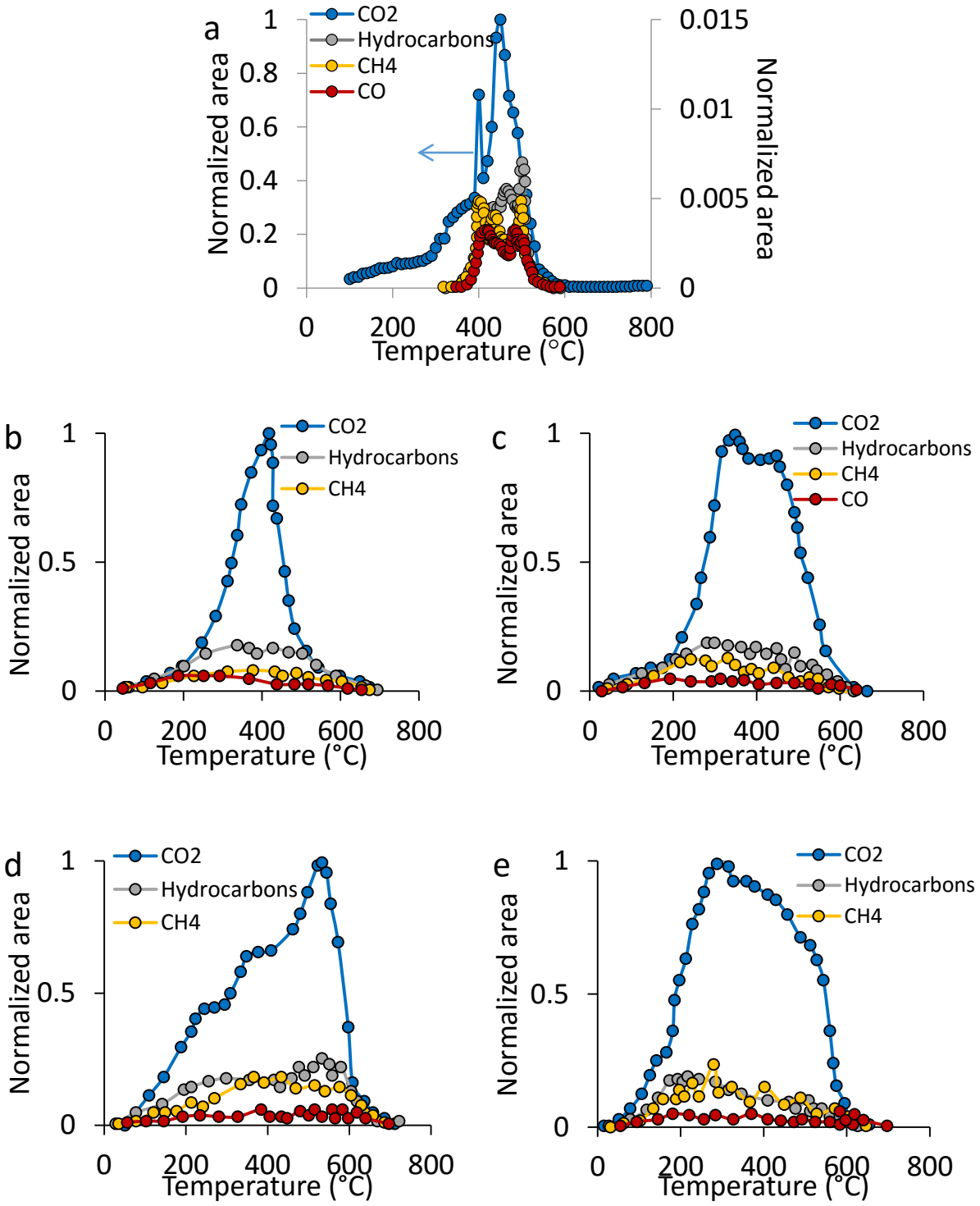

Figure 2.12. Evolution of CO, CO_2, CH_4 and other hydrocarbons production for oxidation of a) virgin *n*-C_7 asphaltenes and *n*-C_7 asphaltenes in presence of b) CS, c) CSNi2, d) CSPd2 and e) CSNi1Pd1.

Table 2.8. Calculated parameters of the special cubic model for the Capella *n*-C_7 asphaltene temperature of oxidation in the presence of CS and SHS.

β_1	β_2	β_3	β_{12}	β_{13}	β_{23}	β_{123}	R^2
354.91	213.73	308.37	-275.88	-60.28	-184.20	-423.41	1.0

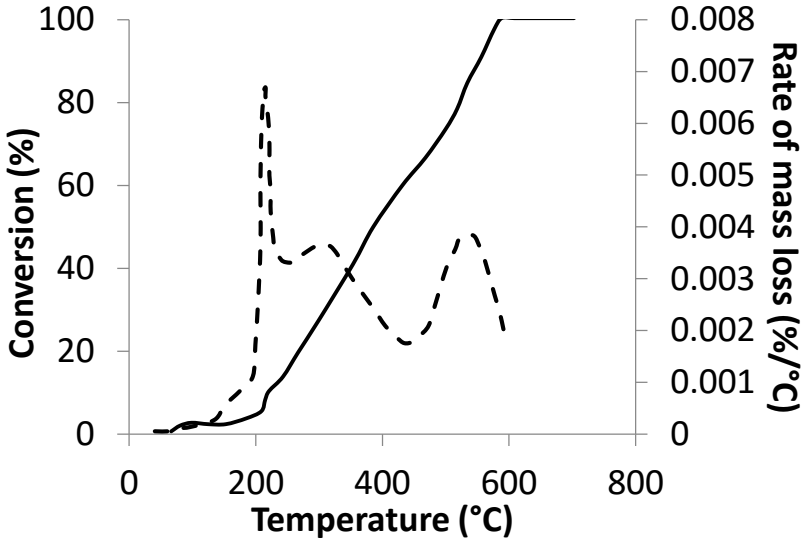

Figure 2.13. Conversion and plot of rate of mass loss as a function of temperature (secondary axis) with an asphaltene loading of 0.2 mg/m^2 onto CSNi0.29Pd1.32.

Effect of asphaltene loading on n-C$_7$ asphaltene oxidation: CSPd2 displays three peaks for asphaltene oxidation (Figure 2.10) when the *n*-C_7 asphaltene loading is 0.2 mg/m^2; this sample was used to study the effect of *n*-C_7 asphaltene loading on the oxidation temperature. Figure 2.14a depicts a plot of the mass loss rate versus temperature for CSPd2 with *n*-C_7 asphaltene loadings of 0.03, 0.05, and 0.20 mg/m^2 and a plot of the enthalpy changes for CSPd2 with 0.2 mg of *n*-C_7 asphaltenes per m^2. The three samples clearly exhibit three peaks, with one at each temperature range. However, as the *n*-C_7 asphaltene loading decreases, the peak in the LTR grows larger while the other two tend to form plateaus, indicating that the oxidation process begins at the LTR and the mass loss remains constant until the oxidation is completed. The plots of the enthalpy changes confirm that, for the 0.2 mg/m^2 sample, there are three exothermic peaks associated with *n*-C_7 asphaltene oxidation, while the 0.03 mg/m^2 sample displays one defined peak in the LTR and a plateau associated with a constant exothermic character. Figure 2.14b displays conversion for *n*-C_7 asphaltenes with CSPd2 at the three tested loadings. As expected, when the amount of *n*-C_7 asphaltenes decreases, the conversion increases because a larger amount of active sites are available for the reaction.[6]

Effective activation energy for the oxidation of n-C$_7$ asphaltenes in the presence and absence of nanoparticles: The E_α required to oxidize the *n*-C_7 asphaltenes in the presence of the S and SHS nanoparticles, were calculated using the thermal analysis data with the OFW method; the results are presented in Figure 2.15. Figure 2.15 indicates that the E_α is lower for the SHS samples than for the

CS nanoparticles. For conversion between 0% and 40%, the activation energy decreased in the following order, confirming the synergetic effect of the bimetallic SHS: CS > CSNi2 > CSPd1 > CSNi0.66Pd0.66 > CSPd2 > CSNi1Pd1. However, after α = 40%, the activation energy of CSNi2 decreases below that for CSPd1 because, before 40% conversion is reached, CSPd1 could oxidize the smaller asphaltene aggregates but afterward required more energy to react with the larger aggregates, while CSNi2 required higher Eα values to start the process; this energy was employed to oxidize both small and medium aggregates. For the optimized sample (CSNi0.29Pd1.32), the activation energy exhibited a trend similar to that of CSPd1, indicating that the amount of PdO dominates the catalytic activity of the sample. However, after 55% conversion, the effective activation energy of the sample falls below that of CSPd1, indicating that the energy employed earlier cracked a greater number of large chains.

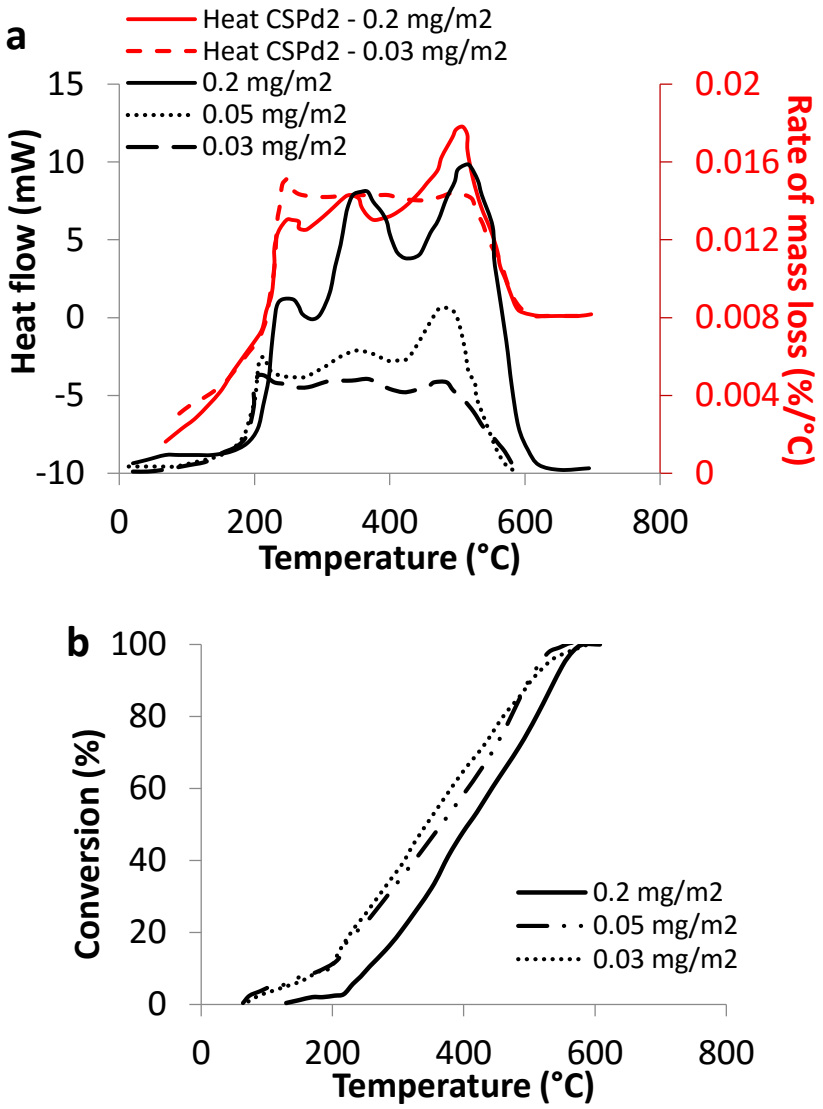

Figure 2.14. a) Plot enthalpy changes for an *n*-C_7 asphaltene loading of 0.2 and 0.03 mg/m^2 and plot of rate of mass loss as a function of temperature with an *n*-C_7 asphaltene loading of 0.2, 0.05, and 0.03 mg/m^2 (red secondary axis) as a function of temperature, and b) conversion for *n*-C_7 asphaltenes in the presence of SPd2 with an *n*-C_7 asphaltene loading of 0.2, 0.05, and 0.03 mg/m^2.

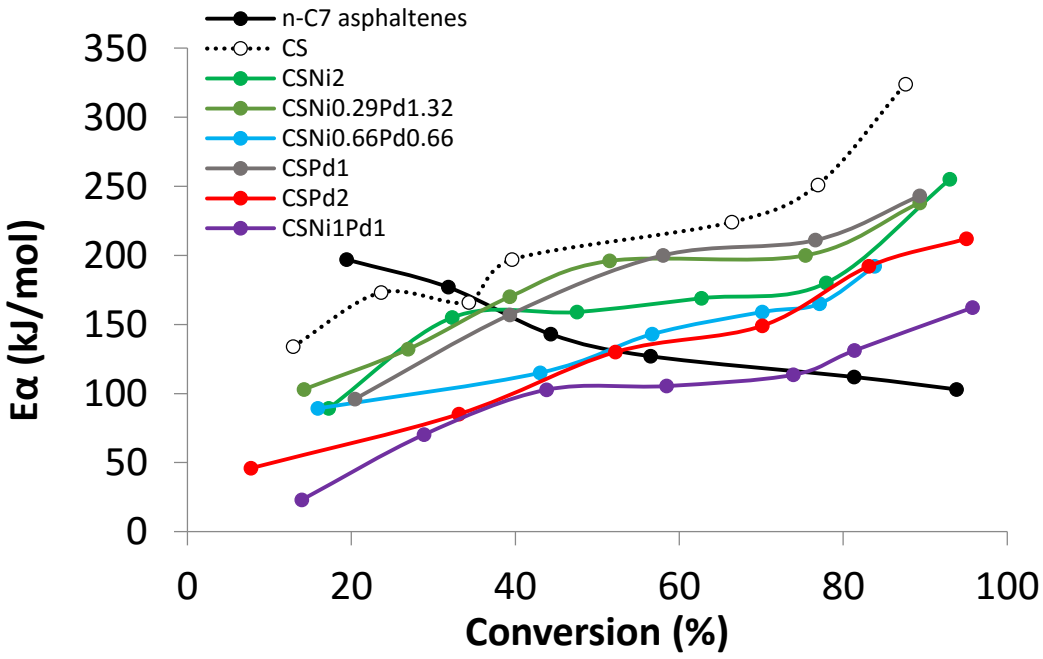

Figure 2.15. Effective activation energies evaluated for oxidation of virgin Capella *n*-C_7 asphaltenes and Capella *n*-C_7 asphaltenes in the presence of CS and SHS by the OFW method.

Clearly, the selected nanoparticles in this study have shown different adsorption affinity, degree of asphaltene self-association and catalytic activity. Accordingly, to have better understanding about the adsorption and catalytic steam gasification and to obtain a good adsorbent/catalyst a correlation between SLE model parameters and effective activation energy estimated by OFW method needs to be addressed. Figure 2.16a shows the effective activation energies as function of *H* parameter related to the adsorption affinity at different degrees of % conversion. As seen, for all % conversion, the E_α decreases as the adsorption affinity increases (represented by lower *H* values). This suggests that good interactions between the adsorbent and the asphaltenes would favor the catalytic steam gasification.[8] These results are in excellent agreements with the findings reported by Nassar et al. for the catalytic steam gasification of Athabasca C_7 asphaltenes onto different surfaces of metal oxide nanoparticles.[8] Figure 2.16b shows the effective activation energy against *K* (refers to asphaltene association on the active primary site) at different degrees of % conversion. As expected, the effective activation energy increases as *K* value increases. This could be due the fact that, at fixed surface of nanoparticles, an increase in *K* value is translated into an increase of the degree of asphaltene aggregation at the primary active site. Hence, a higher *K* value indicates that less active sites are available for reaction and subsequently higher activated energy is expected.

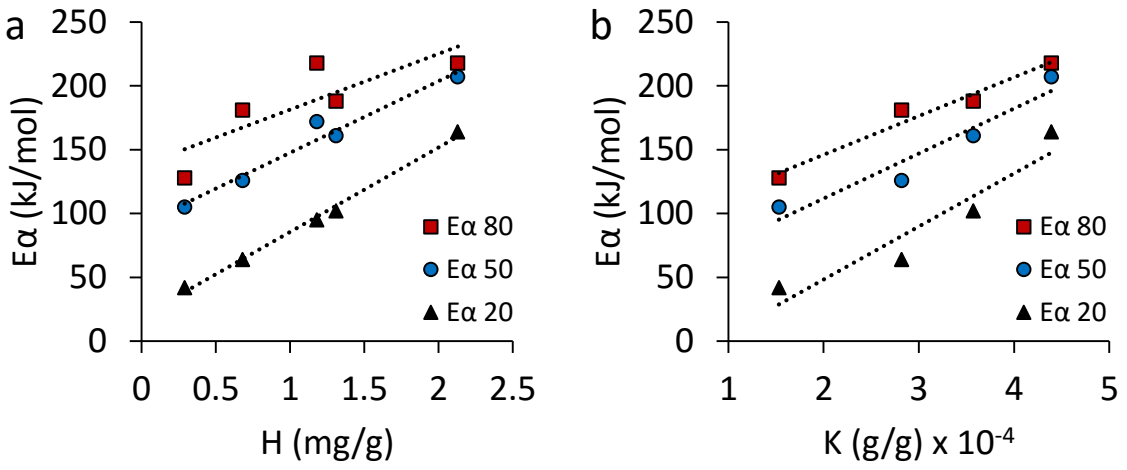

Figure 2.16. Relationship between effective activation energies calculated by the OFW model for catalytic oxidation of *n*-C_7 asphaltenes and the a) *H* parameter and b) *K* constant estimated by the SLE model at different degrees of % conversion: 20% (■), 50% (●) and 80% (▲).

Thermodynamic parameters of the transition state functions: The kinetic parameters and thermodynamic properties of the transition state functions for the oxidation of *n*-C_7 asphaltenes in presence and absence of the selected nanoparticles were estimated following the procedure described in Section 2.2.2 and are presented in Table 2.9. As seen, the values of n ranged from 3 to 12 with values of the slope between -1.07 and -0.97 for R^2 =0.99. However, it is worth to mention that values of n > 4 lack of chemical significance and were only used as fitting parameters for the description of the kinetic equation and the estimation of the thermodynamic properties. This is due as the chemical composition and structure of *n*-C_7 asphaltenes is very complex and could result in a series of unidentified simultaneous reactions. Also, different values of n imply that the thermal oxidation of *n*-C_7 asphaltenes in presence or absence of the selected nanoparticles is not a single-mechanism process and that it is highly dependent on the nanoparticles chemical nature. From Table 2.9 it can be also observed that the trend of the change of the enthalpy of activation follows the order of virgin *n*-C_7 asphaltenes > CS > CSNi2 > CSP2 > CSNi1Pd1, indicating that the highest catalytic effect was obtained for the bimetallic SHS as the reduction in $\Delta H^{\ddagger}$ was highest among the system evaluated; same observations can be made for $\Delta G^{\ddagger}$**.** In addition, according to the negative values of $\Delta S^{\ddagger}$ it can be inferred that the entropy of the activated stated is lower than that of the initial state.[37]

- ***n*-C_7 asphaltenes pyrolysis in presence of SHS nanoparticles**

The bimetallic SCNi1Pd1 sample and materials on the extreme vertices of the SCMD were selected for the studies of *n*-C_7 asphaltenes pyrolysis and gasification. Figure 2.17 shows the rate of mass loss of virgin *n*-C_7 asphaltenes and *n*-C_7 asphaltenes in presence of CS nanoparticles. As seen, virgin asphaltene decomposition starts around 310°C and finishes at about 660°C, with a maximum rate of mass loss at approximately 448°C. These findings are in very close agreement with those reported by Nassar et al.[10] on the pyrolysis of asphaltenes extracted from a vacuum residue from Athabasca EHO and found that the thermal decomposition occurred between 300 and 700°C. The *n*-C_7 asphaltenes thermal decomposition could be fractionated in three steps, beginning with the break of

intermolecular associations, loss of short alkyl chains and weak chemical bonds such as sulfur bridges [62] for temperatures lower than 350°C, followed by the rupture of longer alkyl groups and the opening of the PAH's between 350 and 500°C, and finishing with the coke formation for temperatures higher than 500°C. [10] The catalytic effect of the CS nanoparticles is observed in Figure 2.17. The *n*-C_7 asphaltenes catalytic thermal decomposition of asphaltenes in presence of CS nanoparticles can be divided in two main regions; the first one from 300°C to 500°C and the second one from 500 to 800°C. The first region corresponds to the breaking up of the alkyl sides and the PAH's. In this region, the maximum peak of the rate of mass loss shifts to the left about 40°C, indicating that the reactions involved in this stage occur earlier than for the virgin *n*-C_7 asphaltenes. However, according to the rate of mass loss after 500°C, it seems that some addition reactions happened in the first stage and the decomposition of the resultant compounds is occurring until 800°C, indicating that S nanoparticles could lead to less coke formation in comparison to virgin *n*-C_7 asphaltenes.

Table 2.9. Kinetic parameters and thermodynamic properties of the transition state functions for the oxidation of *n*-C_7 asphaltenes in presence and absence of SHS for a fixed value of α =50%.

Material	n	**slope**	R^2	A **(x10^3 s^{-1})**	**Kinetic equation**	$\Delta S^{\ddagger}$ **(J/mol·K)**	$\Delta H^{\ddagger}$ **(kJ/mol)**	$\Delta G^{\ddagger}$ **(kJ/mol)**
Virgin *n*-C_7 asphaltenes	3	-1.02	0.99	0.34	$\frac{d\alpha}{dt}=\frac{A_\alpha}{3}\exp\left(-\frac{E_\alpha}{RT}\right)(1-\alpha)^4$	-212.10	177.99	153.31
S	12	-0.98	0.99	95.33	$\frac{d\alpha}{dt}=\frac{A_\alpha}{12}\exp\left(-\frac{E_\alpha}{RT}\right)(1-\alpha)^{13}$	-165.57	175.76	124.35
SNi2	9	-1.07	0.99	33.14	$\frac{d\alpha}{dt}=\frac{A_\alpha}{9}\exp\left(-\frac{E_\alpha}{RT}\right)(1-\alpha)^{10}$	-173.46	143.39	117.06
SPd2	11	-0.97	0.99	134.21	$\frac{d\alpha}{dt}=\frac{A_\alpha}{11}\exp\left(-\frac{E_\alpha}{RT}\right)(1-\alpha)^{12}$	-161.37	128.70	102.92
SNi1Pd1	8	-1.06	0.99	22.27	$\frac{d\alpha}{dt}=\frac{A_\alpha}{8}\exp\left(-\frac{E_\alpha}{RT}\right)(1-\alpha)^{9}$	-174.55	100.71	90.17

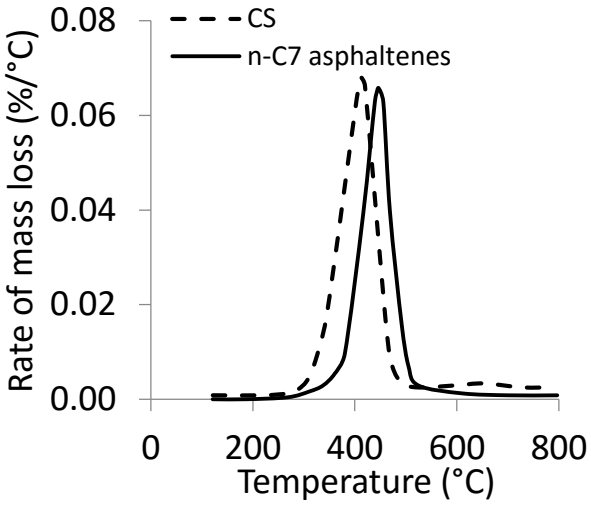

Figure 2.17. Rate of mass loss of *n*-C_7 asphaltenes thermal cracking in presence and absence of fumed silica nanoparticles.

As for the functionalized nanoparticles, Figure 2.18 shows the plot of rate of mass loss for monometallic SHS. As seen, two peaks are observed for CSNi2 and CSPd2 before 660°C. For CSNi2, the first peak is observed near to 300°C and the second one is shifted to the left about 30°C in comparison to the main peak for virgin *n*-C_7 asphaltenes. These results indicated that CSNi2 nanoparticles have a higher catalytic effect towards the *n*-C_7 asphaltene thermal cracking than the support. For CSPd2 nanoparticles, the first peak appeared near to 210°C and the second one in the same position for CSNi2 nanoparticles. It is worth to mention here that the magnitude of the first peak is about one third higher than for the second peak, indicating that a larger amount of components are decomposed in this region. This is in agreement with results obtained for *n*-C_7 asphaltenes oxidation that showed asphaltenes decomposition in presence of CSPd2 at temperatures near to 220°C. For both monometallic SHS, at temperatures higher than 660°C, it is observed that some addition reactions could occur. However, with CSPd2 nanoparticles, just a small peak is observed at 720°C and then the rate of mass loss drop off to zero, indicating that monometallic SHS functionalized with PdO lead to the suppression of coke formation.

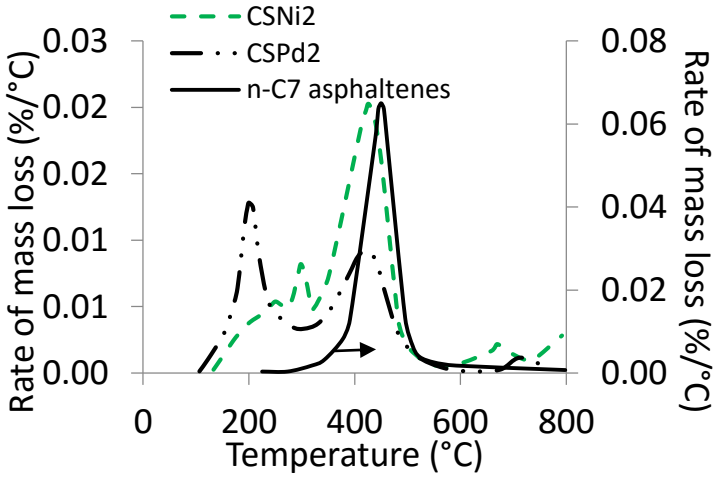

Figure 2.18. Rate of mass loss of virgin *n*-C_7 asphaltenes thermal cracking in presence and absence of monometallic SHS.

Figure 2.19 shows the plot of rate of mass loss for *n*-C_7 asphaltenes in presence of CSNi1Pd1 nanoparticles. The synergistic effect of the NiO and the PdO is clearly observed. Two mean peaks are observed at 220°C and 300°C, showing that the selectivity of NiO and PdO for certain components enhances greatly the catalytic activity. In addition, a third small peak is observed at 530°C that is associated to the decomposition of new compounds due to addition reaction. For temperatures beyond 660°C, no rate of mass loss was observed, indicating that bimetallic nanoparticles are useful for the suppression of coke formation with a better efficiency than CSPd2 nanoparticles.

Sub-products of n-C7 asphaltenes pyrolysis in presence and absence of nanoparticles: *n*-C_7 asphaltenes pyrolysis could lead to different solid and gaseous sub-products in different extent depending on the system evaluated. As temperature increases, radical species may be stabilized to form new lighter compounds such as hydrocarbons with lower molecular weight, CO and CO_2, among others.[27, 63, 64] However, the recombination of free radical species lead to addition reactions that result in changes in the chemical structure of the *n*-C_7 asphaltenes and hence, in heavier and more refractory compounds than the initial *n*-C_7 asphaltenes.[65-67]

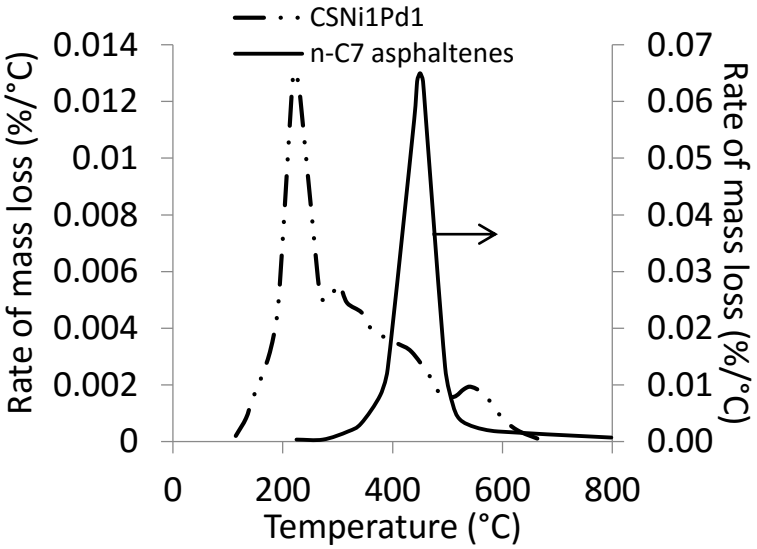

Figure 2.19. Rate of mass loss of virgin *n*-C_7 asphaltenes thermal cracking in presence and absence of bimetallic SHS.

The coke yield after the pyrolysis process was evaluated for the virgin *n*-C_7 asphaltenes and the *n*-C_7 asphaltenes in presence of the evaluated nanoparticles. Reactions such as addition of the free radicals of the olefins [68], cross-linking between aromatic clusters [66] and/or bridging of aromatics by alkyl chains [65] are likely to be responsible for the formation of more refractory compounds. Figure 2.20 shows the results obtained for coke yield of the five samples evaluated. As seen, the presence of nanoparticles reduces significantly the coke formation regarding to the virgin *n*-C_7 asphaltenes. In the presence of CS nanoparticles, the coke yield was reduced by approximately 47% from virgin asphaltenes. However, with the functionalized nanoparticles the inhibition of the coke formation was

greatly enhanced, with reductions higher than 99% for all SHS. It is worth to mention here that the synergistic effect of the bimetallic SHS was also observed, with the 100% inhibition of the coke formation with this material and could be due to the inhibition of *n*-C_7 asphaltenes self-association over the nanoparticles surfaces.

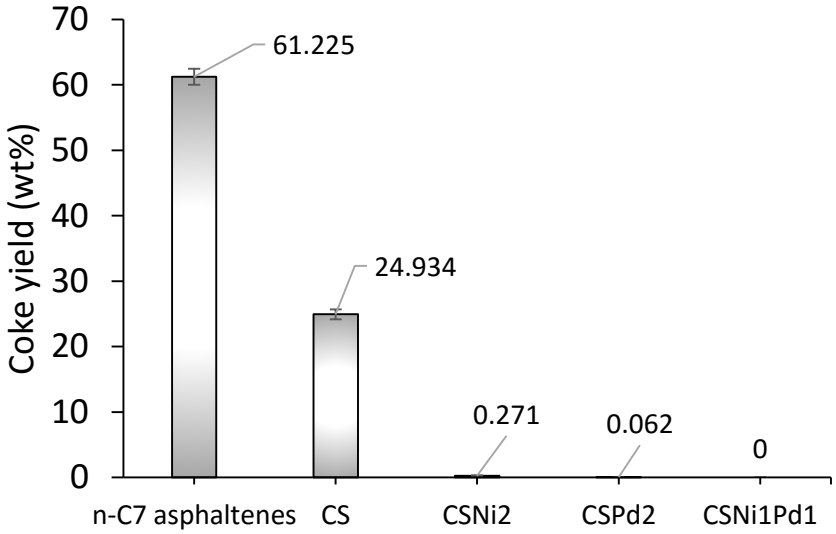

Figure 2.20. Coke yield after the thermal cracking process of *n*-C_7 asphaltenes in presence and absence of the selected nanoparticles.

Virgin *n*-C_7 asphaltenes and *n*-C_7 asphaltenes in presence of CSNi1Pd1 nanoparticles were selected for gaseous products analysis. Figure 2.21 shows the evolution of CO_2, light hydrocarbons and CH_4 during the thermal cracking of *n*-C_7 asphaltenes in a) absence and b) presence of CSNi1Pd1 nanoparticles at a fixed heating rate of 10°C/min. As observed, the gases profile obey in some extent to the shape of the respective rate of mass loss curves for virgin *n*-C_7 asphaltenes and *n*-C_7 asphaltenes with CSNi1Pd1 nanoparticles, confirming the catalytic activity of the bimetallic SHS towards *n*-C_7 asphaltenes thermal decomposition. It is also observed from Figure 2.21 that the amount of CO_2 produced, in both cases, is higher than the production of LHC and CH_4. Results obtained are in agreement with Hosseinpour et al. [27] who evaluated the pyrolysis of *n*-C_7 asphaltenes in presence of NiO and found that the CO_2 production was higher than that of hydrocarbons. The production of CO_2 could be due to two main oxygen sources such as: i) lattice oxygen from the SHS and ii) oxygen content of asphaltenes.[27] Hence, free carbon radicals may react with the oxygen released from O-containing functional groups in the *n*-C_7 asphaltenes structure to form CO and then, CO is chemisorbed in the catalyst surface and after reaction with the surface oxygen is desorbed as CO_2. The oxygen content in the *n*-C_7 asphaltenes structure and the mobility of the lattice oxygen in the adsorbent structure have an important role in the stabilization of free radicals, formation of carbon oxides and hence, suppression of coke formation. Then, as the coke yield was minimized with SHS's, one can infer that the oxygen lattice in the functionalized nanoparticles is more mobile and more prone to react than that of the support.

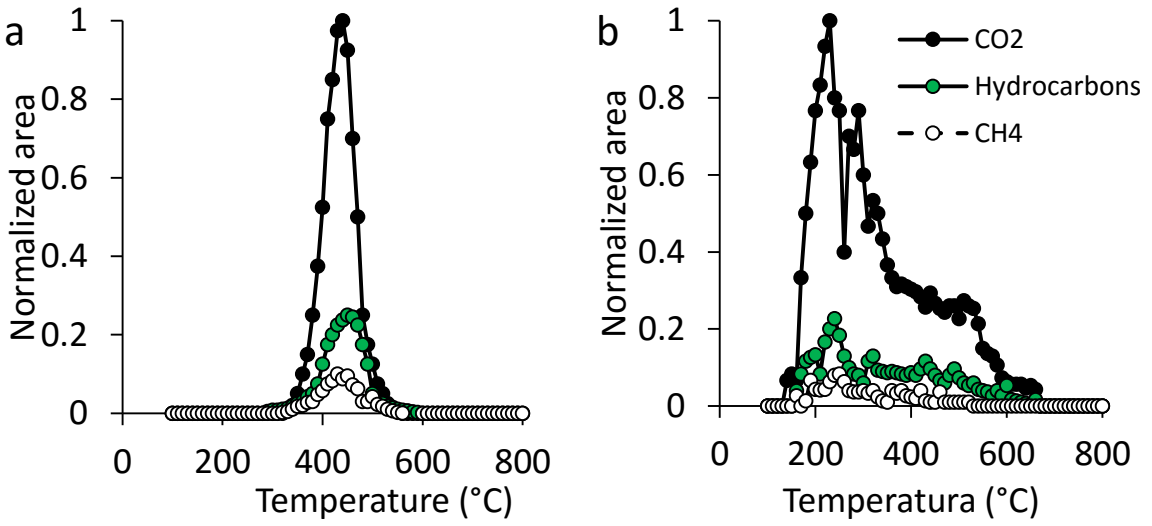

Figure 2.21. Profiles of CO_2, LHC and CH_4 evolution during thermal cracking of a) virgin *n*-C_7 asphaltenes and b) *n*-C_7 asphaltenes in presence of CSNi1Pd1 nanoparticles.

Estimation of the Effective Activation Energies for n-C₇ asphaltenes thermal cracking in absence and presence of CS and SHS nanoparticles: Figure 2.22 shows E_α for the different nanoparticles and the virgin *n*-C_7 asphaltenes as a function of the degree of conversion estimated by OFW. It is observed that E_α is not the same for all conversion degrees, indicating that the *n*-C_7 asphaltenes pyrolysis is not a single-mechanism process,[37] due to different reaction paths that can occur such as aromatization, dealkylation, fragmentation, isomerization and/or rupture of naphthene rings.[69] For virgin *n*-C_7 asphaltenes, the activation energy varied between 117 and 195 kJ/mol while for CSNi1Pd1 the E_α ranged between 55 and 170 kJ/mol. The general trend for the effective activation energy before a conversion percentage of 50% was CSNi1Pd1 ≈ CSPd2 < CSNi2 < CS < virgin *n*-C_7 asphaltenes. However, after 60% of conversion the trend for $E_{\alpha>60\%}$ shift to virgin asphaltenes < CSNi1Pd1 ≈ CSPd2 < CSNi2 ≈ CS. This could be due to the addition reactions mentioned before that lead to decomposition of the new compounds at temperatures higher than that for virgin *n*-C_7 asphaltenes. It is worth to mention that for nanoparticles functionalized with PdO, the values of E_α never reach the highest value of E_α for virgin *n*-C_7 asphaltenes, confirming that with these materials, the addition reactions are suppressed and there is little formation of components of larger molecular weight than virgin *n*-C_7 asphaltenes. For n-C7 asphaltene thermal decomposition in presence of SC and SHS nanoparticles a correlation between the SLE model and was also found. Details of the correlation and thermodynamic parameters of the transition state functions for asphaltenes thermal cracking and gasification can be found in Appendix B.

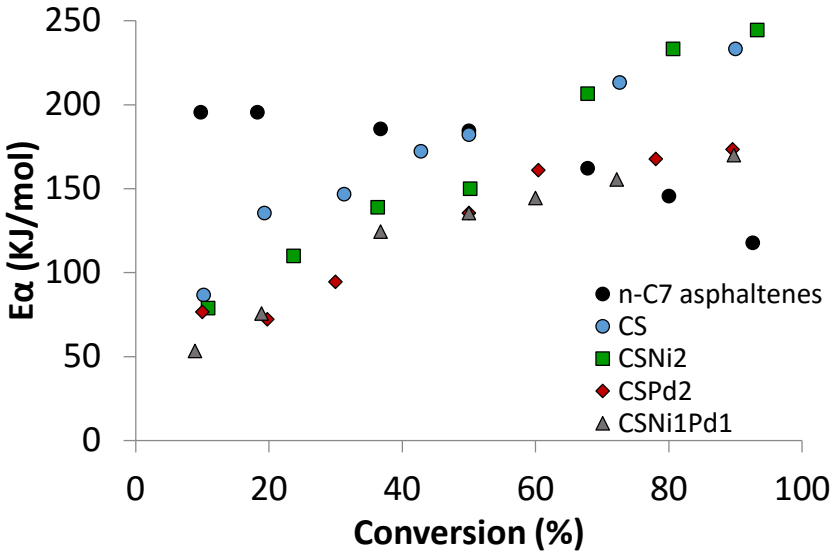

Figure 2.22. Effective activation energies estimated by the OFW method as a function of the conversion for thermal cracking process of *n*-C_7 asphaltenes in presence and absence of the selected nanoparticles.

- ***n*-C_7 asphaltenes catalytic gasification in presence of SHS nanoparticles**

Catalysis to occur, first the asphaltenes have to migrate from the bulk phase to the nanoparticles. The velocity with asphaltenes get adsorbed on the active sites would depend on the adsorption potential of the selected nanoparticles and this is also dependent on their structure and chemical nature. While asphaltenes migrate to the adsorbent surface, a disaggregation of the asphaltenes aggregate could occur. Once asphaltenes get adsorbed, they could be present in the active sites as monomers, dimers, i-mers or aggregates depending on the uptake and the crowding of the available active sites. Then, as temperature increase, the adsorbed species would be cracked and free radicals will react with the H_2 or O_2 from the $H_2O_{(g)}$ that was previously adsorbed and disseminated from the nanoparticle matrix to the active sites. It is expected that the catalytic activity of the nanoparticles would affect the way both asphaltenes and water adsorb on the active sites, leading to a less expensive process in energetic terms. Also, reaction of the asphaltenes with $H_2O_{(g)}$ could occur due to the adsorption of the H_2 or O_2 on the asphaltenes previously adsorbed, reducing then the catalytic effect of the material. The degree asphaltenes self-associate would impact the catalytic activity as bigger aggregates could block some active sites (See Chapter 3).

The virgin CS and SHS nanoparticles were tested in an atmosphere of Ar saturated with $H_2O_{(g)}$ for asphaltenes catalytic steam gasification. Figure 2.23 shows the plot of mass loss rate of Capella *n*-C_7 asphaltenes in presence and absence of CS. As seen, for virgin *n*-C_7 asphaltenes the reaction begins approximately at 300°C, with a maximum peak at 458°C and ceases at 544°C. It is worth noting here that, at the end of the test there was still some remaining hydrocarbons attributed to the coke formation. Figure 2.23 shows that the curve for asphaltenes rate of mass loss in presence of CS nanoparticle shifts to the left, confirming that gasification is occurring at lower temperature probably due to the catalytic activity of the nanoparticles. The maximum peak of mass rate loss was reduced from 458 to 409°C. The catalytic steam gasification of asphaltenes in presence of CS nanoparticles can be divided in two reaction regions, one before 500°C and the other between 500 and 800°C. The first region could correspond to the break-up of alkyl chains, dissociation of S-C and N-C bonds and opening of polycyclic aromatic hydrocarbons.[10, 69, 70] In the second section is observed that there are

still some reactions attributed to the gasification of resultant compounds after addition reactions of free radicals that did not stabilized in the reactions of the first region.

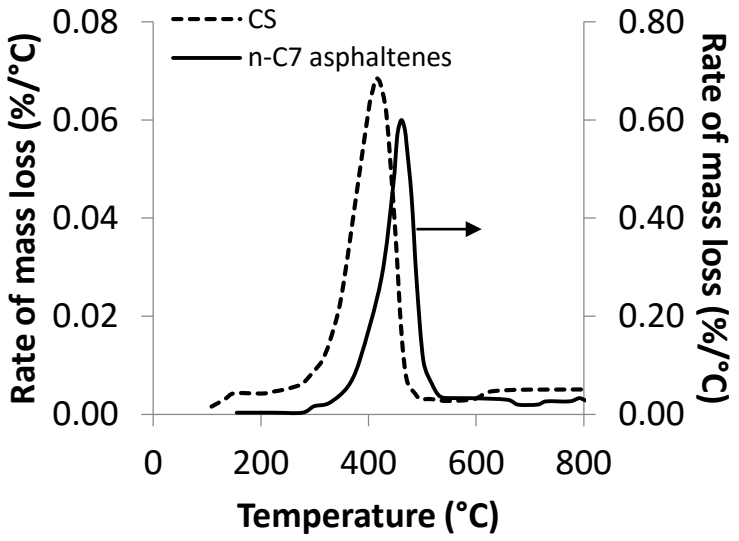

Figure 2.23. Plot of rate of mass loss as a function of temperature for steam gasification of virgin *n*-C_7 asphaltenes and *n*-C_7 asphaltenes in presence of CS nanoparticles.

Figure 2.24 shows the plots of mass loss rate of asphaltenes in presence of CSNi2 and CSPd2 nanoparticles at a fixed amount of adsorbed asphaltenes, 0.2 mg/m^2. It is clear that the inclusion of NiO or PdO reduces the temperature of asphaltene decomposition. For silica supported PdO nanoparticles, two main peaks are observed at 205 and 415°C. The first peak is due to the synergistic effect of PdO with the fumed silica support that allows an early breaking of weakest bonds of asphaltenes. Thus, it could be inferred that the second peak would be due to the decomposition of asphaltenes adsorbed in the fumed silica surface due to the proximity with the peak observed for the asphaltenes in presence of CS nanoparticles (Figure 2.23). Similar situation can be seen for CSNi2 nanoparticles. In this case, two peaks are observed at 311 and 430°C. The first one corresponds to synergistic effect between NiO and CS, and the second one by the effect of CS nanoparticles. The main difference between the monometallic SHS lies in the position of the first peak and the magnitude of the second one. For CSPd2 nanoparticles the magnitude of the first peak is higher than for the second peak, indicating that most of the reactions occur near to that temperature. For CSNi2 nanoparticles the opposite trend is observed. Figure 2.24 shows that for CSNi2 nanoparticles there are reactions corresponding to the decomposition of heavier compounds formed before 600°C, and same situation occurs for CSPd2 nanoparticle regarding to the small third peak observed around 650°C.

The synergistic effect of bimetallic nanoparticles is shown in Figure 2.25. As seen, a big peak is observed at 220°C and a shorter one at 370°C. Clearly, the peaks corresponds to the contributions of PdO and NiO on the support, showing the combined selectivity of the hybrid material. It is also observed that the reaction ceases at approximately 481°C, where not peak corresponding to the CS support could be observed. As it was mentioned before, bimetallic compounds avoid sintering effects

and lead to homogeneous distribution on the surface, resulting in asphaltenes adsorption mainly on the NiO and PdO sites.

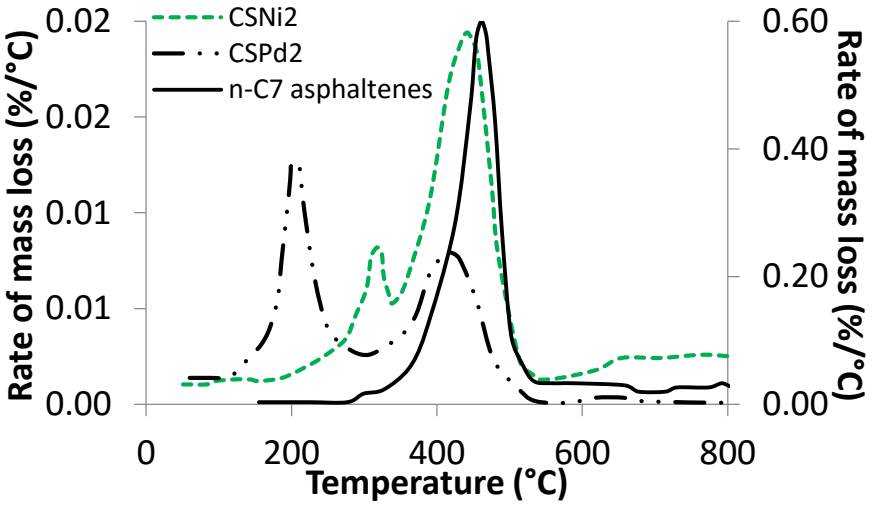

Figure 2.24. Plot of rate of mass loss as a function of temperature for steam gasification of virgin *n*-C_7 asphaltenes and *n*-C_7 asphaltenes in presence of monometallic SHS nanoparticles.

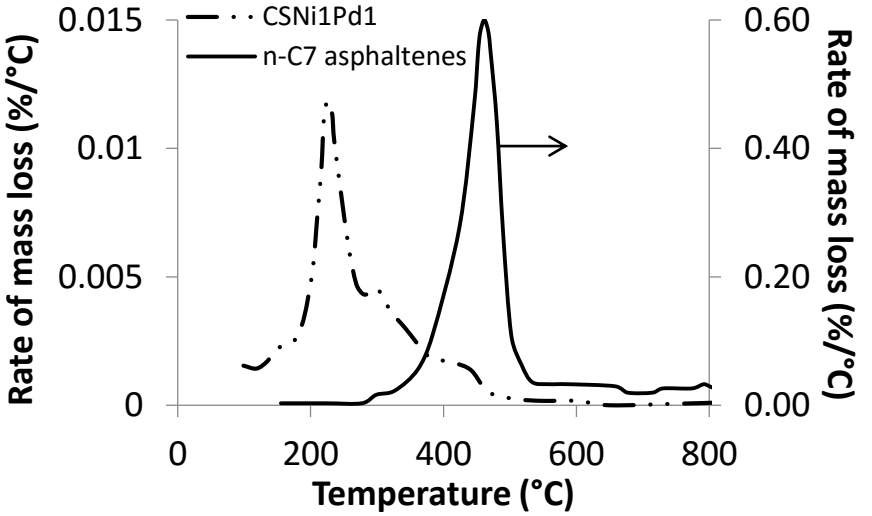

Figure 2.25. Plot of rate of mass loss as a function of temperature for steam gasification of virgin *n*-C_7 asphaltenes and *n*-C_7 asphaltenes in presence of bimetallic SHS nanoparticles.

Sub-products of n-C7 asphaltenes catalytic steam gasification in presence and absence of nanoparticles: A number of gases could be released during the steam gasification process, namely H_2, CO, CH_4, O_2, and CO_2. However, in this study H_2 and O_2 gases were eliminated from analysis as result could be interfered by the water product. Further, CO_2 composition was insignificant and was eliminated from the analysis as well. The product of *n-C7* asphaltenes gasification in presence and absence of nanoparticles were evaluated using the FTIR. Figure 2.26a,b shows the evolution of CH_4 and CO during asphaltenes gasification in the range of experimental temperatures. It is worth

noting here that the band intensity related to the CH_4 in the FTIR spectra was always higher than for CO, and hence the results were normalized based on the CH_4 signal. Figure 2.26a shows the evolution profile of CH_4 for gasification of virgin *n*-C_7 asphaltenes and *n*-C_7 asphaltenes adsorbed onto nanoparticles of CS, CSNi2, CSPd2 and CSNi1Pd1. As seen, to some extent and for all cases, the evolution profile is similar to the mass loss curves presented early. Clearly, the starting and ending temperatures of CH_4 production are strongly influenced by the type of nanoparticles. The starting temperature of CH_4 production as well as the temperature at the maximum peak follows the order virgin asphaltenes > CS > CSNi2 > CSPd2 > CSNi1Pd1. This again, confirms the catalytic activity of the nanoparticles and goes inline with results obtained by the mass loss rate. Similar observations can be seen for the CO evolution profile, but to a less extent. However, worth noting, the ratio between the produced CO and CH_4 is dependent on the type of nanoparticles. It is worth noting here that in steam gasification processes the main reactions for CO production are partial oxidation, water-gas and steam reforming; while for CH_4 it is the methanation reaction.[71] Hence, as seen in Figure 2.26b, the normalized area for the SHS nanoparticles is much higher than that of CS, indicating that the ratio CO/CH_4 is higher. This could be due to that steam-reforming reactions are promoted by the supported nanoparticles, which enhanced the reaction of CH_4 with H_2O to form CO and H_2. This again confirms the catalytic activity of silica-supported metal oxide nanoparticles.

After the asphaltenes gasification has been completed, the remaining coke was evaluated by heating the samples in an oxidative atmosphere at a fixed air flow of 100 cm^3/min and a heating rate of 20°C/min. Results showed that for virgin asphaltenes and asphaltenes in presence of CS the 43 wt% and 2.9 wt% was not gasified, respectively. However, for the three fumed silica supported nanoparticles no significant residue could be observed after gasification, suggesting that the presence of NiO and PdO greatly inhibit the coke formation and hence the catalyst poisoning.

Estimation of the Effective Activation Energies for n-C_7 asphaltenes catalytic steam gasification in absence and presence of CS and SHS nanoparticles: To further validate the catalytic activity of the nanoparticles, the isoconversional OFW method was used for estimating the effective activation energies using TGA mass loss rate measurements performed at heating rates of 5, 10 and 20 °C/min. As mentioned, the amount of coke formed after the gasification process is also dependent on the type of nanoparticles. Hence, the similar values of asphaltene conversion for CSNi2 and CS could be associated to different amounts of coke formed. Figure 2.27 shows the estimated effective activation energies as function of the degree of % conversion. For virgin *n*-C_7 asphaltenes the value of E_α decreases as the conversion increases. On the other hand, the opposite trend for E_α is observed for steam gasification of *n*-C_7 asphaltenes in the presence of nanoparticles and is in agreement with that obtained for oxidation and thermal cracking. It should be noted here that, in all cases for α < 60%, the effective activation energy is lower in presence of nanoparticles than virgin *n*-C_7 asphaltenes. This again, confirms the catalytic activity of the nanoparticles. For α > 60% silica-supported bimetallic nanoparticles showed lowest E_α values, confirming the synergistic effect.

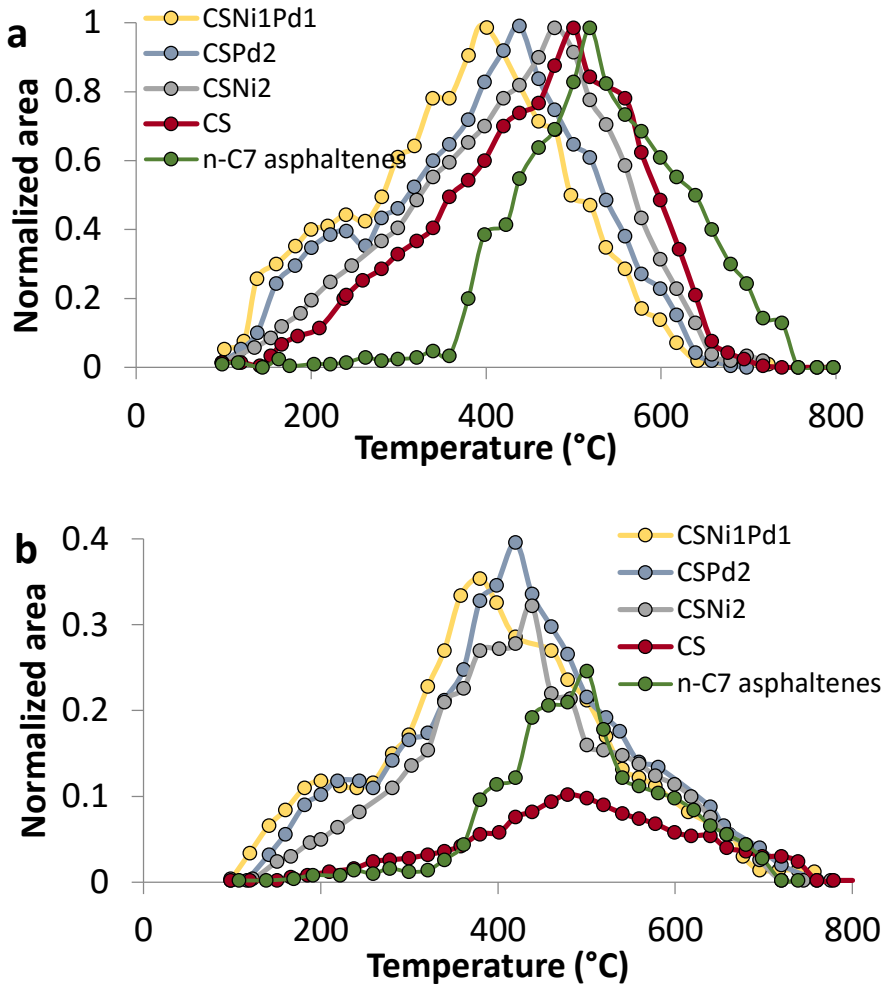

Figure 2.26. Evolution profile of a) CH_4 and b) CO during steam gasification of virgin *n*-C_7 asphaltenes and *n*-C_7 asphaltenes in presence of CS and SHS nanoparticles.

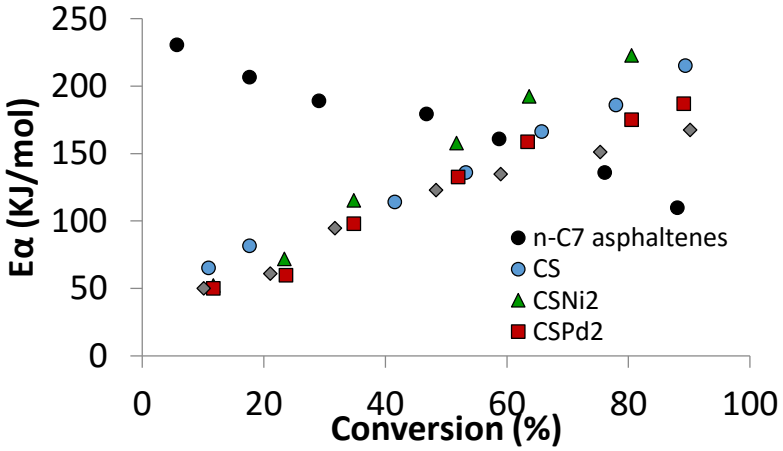

Figure 2.27. Effective activation energies calculated by OFW method as function of the % conversion for steam gasification of *n*-C_7 asphaltenes in the presence and absence of CS and SHS nanoparticles.

- **Effect of the ceramic support on the *n*-C_7 asphaltenes catalytic gasification**

In the same line on using nanoparticles as adsorbents and catalysts for heavy polar hydrocarbons, novel nanomaterials to improve heavy oil quality by adsorptive removal of asphaltenes and subsequent catalytic steam gasification of the adsorbed asphaltenes need to be explored. CTi and CAl nanoparticles were employed as alternative ceramic supports for NiO and/or PdO nanocrystals. Detailed information of the supports can be found in Chapter 1. In addition, Appendix C resumes properties of the obtained SHS using CAl and CTi as supports, results of the obtained adsorption isotherms and the corresponding SLE model parameters. The functionalized nanoparticles have higher adsorptive capacities than the CAl or CTi supports.

Hence, the catalytic activity of the selected nanoparticles was determined by TGA experiments in an Argon atmosphere saturated with $H_2O_{(g)}$. Figure 2.28a shows the rate of mass loss for Capella *n*-C_7 asphaltenes gasification in the presence and absence of CTi and CTi nanoparticles functionalized with 2 wt% of NiO and/or PdO for an asphaltene loading of 0.20 mg/m^2. For simplicity and a practical perspective, the full range of evaluated temperatures for the TGA experiment is divided into three regions: low (LTR), medium (MTR) and high temperature (HTR). The LTR range begins at 200°C and ends at 250°C, the MTR is from 251 to 700°C, and the HTR is from 700 to 800°C. As shown for virgin n-C_7 asphaltenes, the gasification reaction begins at approximately 300°C with a maximum loss at 458°C and ends at 544°C. However, in the HTR region, it can be observed that coke formation leads to residual hydrocarbons that react at high temperatures. The conversion of *n*-C_7 asphaltenes to gaseous products can also be associated with the partial oxidation and pyrolysis of *n*-C_7 asphaltenes.[8] At the beginning of the reaction, the mass loss of *n*-C_7 asphaltenes can be associated with the break-up of alkyl chains and the dissociation of weak bonds of S-C and N-C.[10, 69, 70] By increasing the temperature, addition reactions can occur due to the availability of polycyclic aromatic hydrocarbons (PAH), leading to the formation of heavier compounds and coke. These compounds are larger from the starting species and could be asphaltenes their selves that as temperature increase could change their architecture from the simpler such island architecture, to more complex like continental, archipelago or rosary type until their chemical nature turns into coke. In the HTR region, coke decomposition occurs, and compounds are produced by addition reactions.

For *n*-C_7 asphaltenes in the presence of CTi nanoparticles, two peaks in the profile of the rate of mass loss can be observed in the MTR at 400 and 595°C, indicating that the decomposition of alkyl chains and break-up of N-C and S-C bonds occur at an earlier temperature than with virgin *n*-C_7 asphaltenes. The first peak could correspond to the opening of the PAH of *n*-C_7 asphaltenes, while the second peak corresponds to the decomposition of the heavier products from the addition reactions. As the H_2 and O_2 from the $H_2O_{(g)}$ stabilize radical species in the gasification process, there is also the formation of heavier compounds due to radical recombination in reaction mechanisms of free radical chains.[66, 67] Reactions between aromatics attached by alkyl bridges,[65] additions of the olefins free radicals[68] and/or cross-linking reactions between aromatic clusters[66] can be also explanations of the addition reactions. For *n*-C_7 asphaltenes in the presence of CTiNi2 nanoparticles, a single peak is observed in the rate of mass loss profile at approximately 366°C; this represents a reduction of 6 and 13% in the temperature of *n*-C_7 asphaltenes decomposition compared with the CTi nanoparticles and the virgin *n*-C_7 asphaltenes, respectively. However, because no other peak was observed at higher temperatures, one would anticipate that the incorporation of NiO on the CTi nanoparticles surfaces could lead to the inhibition of addition reactions. For nanoparticles functionalized with PdO, it can be observed from the rate of mass loss profile that three peaks exist. In the LTR region for CTiPd2 and CTiNi1Pd1, the first peak is observed at approximately 207°C for both nanoparticles, indicating that the presence of the PdO reduces the temperature for catalytic gasification of *n*-C_7 asphaltenes significantly. For the CTiPd2 nanoparticles, a second peak is observed at 360°C, which is a reduction of 6 and 14% compared with CTi nanoparticles and virgin

n-C_7 asphaltenes. In addition, a third peak is observed at 643°C and could correspond to the reaction of the heavier compounds produced by the addition reactions or coke.

The synergistic effect of the NiO and PdO is evidenced in the second and third peaks of the rate of mass loss at 321 and 569°C, respectively, which are approximately 39 and 74°C lower than the temperature found for the second and third peak for PdO. The synergistic effect could be due to two principal factors: i) the combined selectivities of Pd and Ni towards different species in the asphaltenes molecule; and ii) avoiding metal sintering on the support surface may have led to increasing the amount of active sites available for the reaction and the enhancement of the resistance for coke formation.[72] It is well known that the sintering of metals on the support surface could be alleviated in complex materials by the presence of noble metals [73] and is dependent on many factors in the synthesis step such as temperature, time, atmosphere and metal content.[60] The effect of the aforementioned factors is beyond the scope of this study and should be addressed in future works.

Figure 2.28b shows the rate of mass loss for the catalytic steam gasification of Capella *n*-C_7 asphaltenes in the presence of CAl, CAlNi2, CAlPd2 and CAlNi1Pd1 nanoparticles. From Figure 2.28b, it is shown that the rate of mass loss of n-C_7 asphaltenes in the presence of CAl nanoparticles shows two peaks in the MTR region at 441 and 510°C, indicating that CAl nanoparticles are able to catalyze the steam gasification of *n*-C_7 asphaltenes. However, the first peak is observed at a temperature 40°C higher than that for CTi, suggesting that the catalytic activity of the CTi nanoparticles on the steam gasification of *n*-C_7 asphaltenes is higher than that for CAl. This could be explained by the fact that TiO_2 has a higher selectivity for nitrogen in the aromatic species in hydrogen addition processes with higher catalytic activity and lower hydrogen consumption than alumina.[74] Additionally, structural changes in the nanoparticles as a function of operating temperatures could lead to a reduction in the catalytic activity of the alumina nanoparticles; thus, nanoparticle sintering could occur, resulting in a decrease of active sites available for the catalytic process.[75] As was observed for CTiNi2 nanoparticles, CAlNi2 nanoparticles showed a peak in the MTR at 427°C. Although for CAlNi2 nanoparticles, the reaction temperature was considerably lower due to the CAl support; the CTiNi2 nanoparticles also showed higher activity, which could be due to the intrinsic activity of the CTi support. In the case of the CAlPd2 nanoparticle, three primary peaks were obtained at 202, 391 and 643°C, indicating that the inclusion of the Pd lead to early reactions on the LTR region. For the bimetallic nanoparticles, a similar behavior to CTiNi1Pd1 is observed. Three peaks are observed in the rate of mass loss at 201, 373 and 615°C, suggesting that the synergistic effect of the PdO and NiO can be obtained with different supports (i.e., silica, alumina and titania). In addition, the first peak is observed at a lower temperature with CAlNi1Pd1 than for CTiN1Pd1; for the other two peaks, the Ti-supported bimetallic nanoparticles showed higher catalytic activity than Al-supported bimetallic nanoparticles. These results could be related to the good dispersion and better homogeneity in the coordination of the Pd and Ni over the Ti surface.[75] Regarding to the effective activation energy is affected by the nanoparticles present due to the occurrence of different reaction mechanisms. In brief, CTiNi1Pd1 displayed the lowest activation energy throughout the process, suggesting that CTiNi1Pd1 is more catalytically active towards *n*-C_7 asphaltene steam gasification, confirming their synergistic effect. This synergistic effect could be explained by the combination of individual selectivities and the hybrid structures of Pd and Ni that lead to better surface electronegativity and hence a more efficient catalytic activity.[61] Similar observations were seen for the effective activation energy trends with CAl support and the functionalized nanoparticles. Details of the estimated effective activation energies can be found in Appendix C.

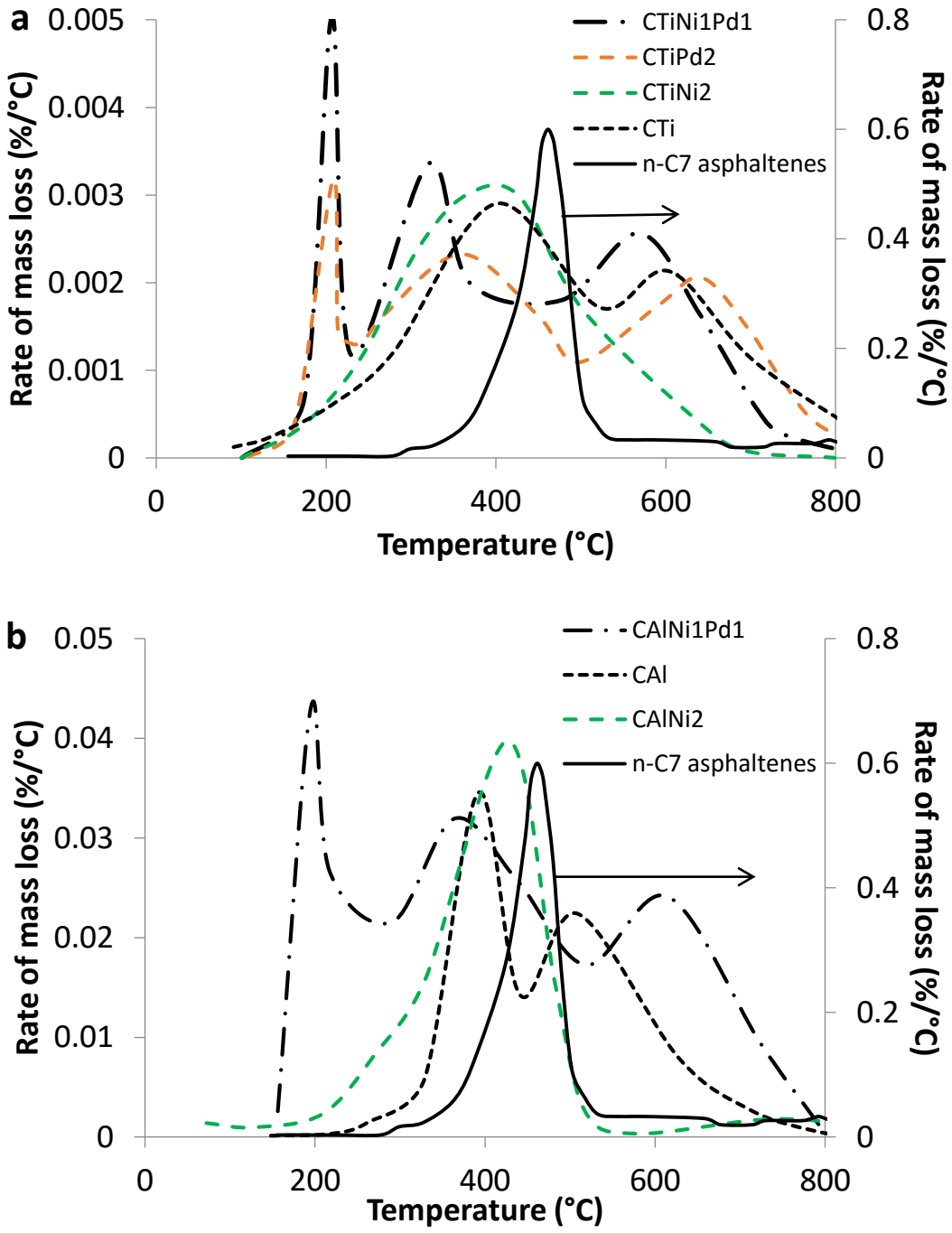

Figure 2.28. Rate of mass loss for *n*-C_7 asphaltenes catalytic steam gasification in the absence and presence of a) CTi supported and b) CAl supported nanoparticles.

Produced gases and estimation of coke formation during steam gasification of Capella n-C_7 asphaltenes using Ti- and Al-supported nanoparticles: Panels a) and b) in Figure 2.29 show the evolution profiles of CH_4 for Capella *n*-C_7 asphaltenes catalytic steam gasification in the presence of a) CTi-supported and b) CAl-supported nanoparticles. It is observed from Figure 2.29 that for both CTi and CAl supports, the gaseous evolution profiles match the rate of mass loss obtained previously,

further indicating that the mass loss observed in Figure 2.28 is associated with asphaltene catalytic steam gasification. In all cases, CH_4 production begins at earlier temperatures in the order of bimetallic < Pd-monometallic < Ni-monometallic < support. This suggests that higher catalytic activities are obtained with bimetallic nanoparticles. Additionally, from Figure 2.29, it is observed that despite the fact that both bimetallic and monometallic nanoparticles functionalized with Pd showed similar profiles, the first peak observed near 200°C is wider and higher for bimetallic nanoparticles than for monometallic nanoparticles; this indicates that by including Ni in the materials, a higher amount of asphaltenes can be catalytically gasified. Similar observations can be seen in the CO evolution.

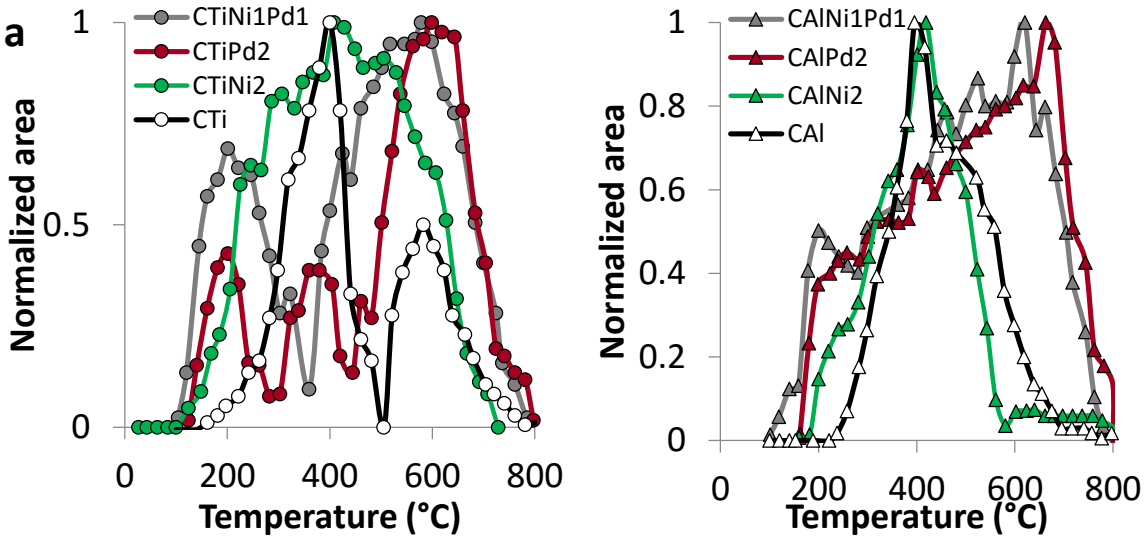

Figure 2.29. Profiles of CH_4 evolution during steam gasification of Capella *n*-C_7 asphaltenes in presence of a) CTi-supported and b) CAl-supported nanoparticles.

Panels a) and b) in Figure 2.30 show the evolution profiles of CO during catalytic steam gasification of Capella *n*-C7 asphaltenes adsorbed on a) CTi-supported and b) CAl-supported nanoparticles. It was also observed that the profile of the produced CO using both supports was similar to the rate of mass loss and that gas production began in the same order of that found for CH_4. Additionally, the amount of CO produced from the catalytic steam gasification of the adsorbed asphaltenes was higher than that for virgin asphaltenes and could be primarily caused by steam reforming reactions that are enhanced by nanoparticles. Results indicate that gas production is highly dependent on the decomposition of the HC precursor and hence, on the type and chemical nature of the nanoparticle.

The coke yield over the nanoparticles was also estimated by heating the samples in an air atmosphere after gasification. Figure 2.31 shows the coke yield after gasification for virgin Capella *n*-C_7 asphaltenes and the *n*-C_7 asphaltenes adsorbed onto the CTi- and CAl-supported nanoparticles. For virgin Capella *n*-C_7 asphaltenes, the coke yield was 43 ± 2 wt%; for n-C_7 asphaltenes in the presence of CTi and Al nanoparticles, the coke yield obtained was 2.3 ± 0.3 and 3.6 ± 0.4 wt%, respectively, indicating that CTi nanoparticles more successfully inhibited coke formation than Al nanoparticles. In addition, for CTiNi2 and CAlNi2 nanoparticles, it was found that coke yields were approximately 0.17 and 0.13 ± 0.02 wt%, indicating that functionalizing the supports with NiO inhibited coke formation more effectively. However, the highest enhancement in coke inhibition was obtained with

the PdO-functionalized nanoparticles, with which no significant residue could be observed after gasification; this could be related to the inhibition of asphaltene self-association on the nanoparticles surface. Results indicate that functionalized nanoparticles were able to inhibit coke formation to different extents and hence prevent catalyst poisoning. In the case of the bimetallic nanoparticles used in this work, the dose of Pd affects Ni regeneration, preventing coke formation over the catalyst.

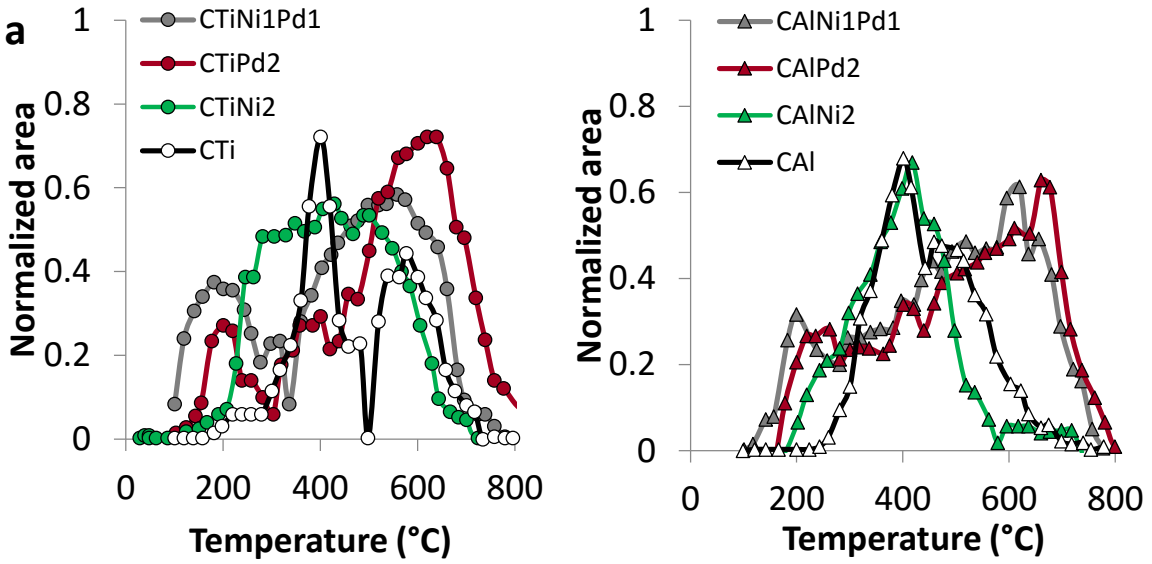

Figure 2.30. Profiles of CO evolution during steam gasification of Capella *n*-C_7 asphaltenes in presence of a) CTi-supported and b) CAl-supported nanoparticles.

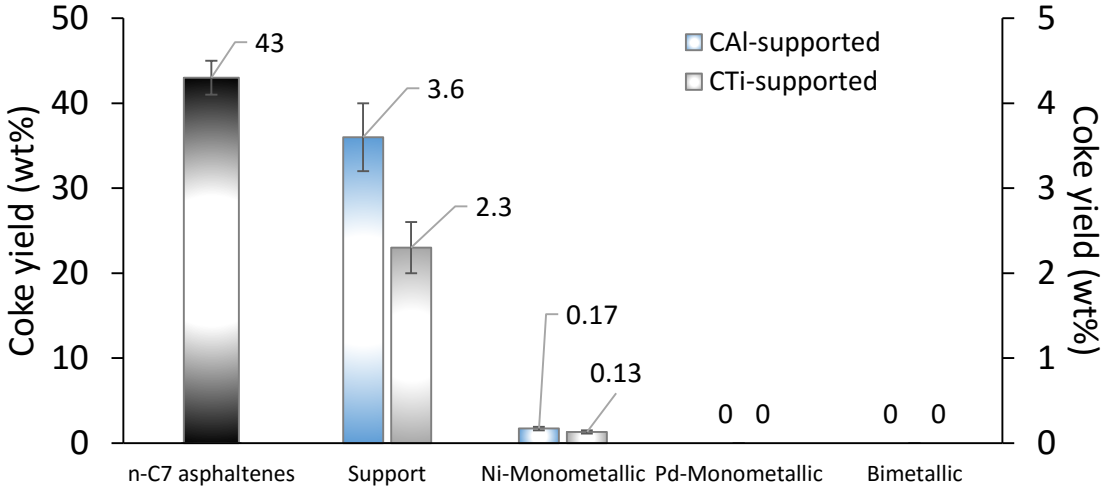

Figure 2.31. Coke yield after the steam gasification of virgin Capella *n*-C_7 asphaltenes and asphaltenes in the presence of the CTi- and CAl-supported nanoparticles.

2.4 Partial conclusions

The advantages of nanotechnology as complementary solution for heavy oils upgrading is clear in this work. Adsorption isotherms of three *n*-C_7 asphaltenes isolated from different crude oils over CS

nanoparticles were determined. Also, *n*-C_7 asphaltenes adsorption isotherms were obtained for the CNS, SS and SHS nanoparticles. In all cases a Type I behavior according to the IUPAC was observed and the SLE model showed good agreement towards the experimental results. Also, the catalytic activity of nanoparticles was studied in presence of different atmospheres. As result, it was found that different pyshicochemical properties of nanoparticles of the same chemical nature play a more important role in the *n*-C_7 asphaltenes adsorption than in the catalytic cracking. In addition, it was observed that asphaltenes form the same reservoir may behave similar in oxidation processes in absence and presence of nanoparticles. In the adsorption process functionalized nanoparticles are prone to reduce the degree of asphaltene self-association and increase the adsorption affinity as observed by the *K* and *H* parameters of the SLE model. Also, the five-parameters SLE model was successfully employed for estimating the thermodynamic properties of adsorption. Nanoparticles also are able to enhance the asphaltene oxidation, thermal cracking and gasification processes by reducing the degree of asphaltene self-association over the catalyst surface, decreasing the temperature of asphaltenes decomposition and by the inhibition of the coke formation and the catalyst poisoning. The temperature of asphaltene decomposition in presence of nanoparticles was greatly reduced with the bimetallic SHS independently of the employed support (CS, CTi or CAl), indicating that the material has a synergistic effect by combining the selectivity of both PdO and NiO. Also, it was observed that in the gasification case, the functionalized nanoparticles are able to reduce the production of CH4 in the process and increase the CO, indicating that steam reforming reactions are occurring and hence the production of H_2 will increase. In addition, a trend between the effective activation energy and the degree of asphaltenes self-association and the adsorption affinity was found. The catalytic effect of the bimetallic SHS was corroborated by the estimated thermodynamic properties of the transition state functions. The kinetic equations for the catalytic decomposition of asphaltenes in presence and absence of the selected nanoparticles were obtained. This works should provide a new insight of the use of nanoparticles for in-situ heavy and extra-heavy oil upgrading and the effect of the adsorption process on the efficiency of the catalytic activity of the nanoparticles.

2.5 References

1. Nassar, N. N.; Hassan, A.; Luna, G.; Pereira-Almao, P., Kinetics of the catalytic thermo-oxidation of asphaltenes at isothermal conditions on different metal oxide nanoparticle surfaces. *Catalysis Today* **2013,** 207, (0), 127-132.
2. Hassan, A.; Lopez-Linares, F.; Nassar, N. N.; Carbognani-Arambarri, L.; Pereira-Almao, P., Development of a support for a NiO catalyst for selective adsorption and post-adsorption catalytic steam gasification of thermally converted asphaltenes. *Catalysis Today* **2013,** 207, (0), 112-118.
3. Giraldo, J.; Nassar, N. N.; Benjumea, P.; Pereira-Almao, P.; Cortés, F. B., Modeling and Prediction of Asphaltene Adsorption Isotherms Using Polanyi's Modified Theory. *Energy & Fuels* **2013,** 27, 2908−2914.
4. Nassar, N. N.; Hassan, A.; Carbognani, L.; Lopez-Linares, F.; Pereira-Almao, P., Iron oxide nanoparticles for rapid adsorption and enhanced catalytic oxidation of thermally cracked asphaltenes. *Fuel* **2012,** 95, 257–262.
5. Nassar, N. N.; Hassan, A.; Pereira-Almao, P., Effect of the Particle Size on Asphaltene Adsorption and Catalytic Oxidation onto Alumina Particles. *Energy & Fuels* **2011,** 25, (9), 3961-3965.
6. Nassar, N. N.; Hassan, A.; Pereira-Almao, P., Comparative oxidation of adsorbed asphaltenes onto transition metal oxide nanoparticles. *Colloids and Surfaces A: Physicochemical and Engineering Aspects* **2011,** 384, (1-3), 145-149.

7. Nassar, N. N.; Hassan, A.; Pereira-Almao, P., Effect of surface acidity and basicity of aluminas on asphaltene adsorption and oxidation. *Journal of Colloid and Interface Science* **2011,** 360 233–238.
8. Nassar, N. N.; Hassan, A.; Pereira-Almao, P., Application of Nanotechnology for Heavy Oil Upgrading: Catalytic Steam Gasification/Cracking of Asphaltenes. *Energy & Fuels* **2011,** 25, (4), 1566-1570.
9. Nassar, N. N.; Hassan, A.; Pereira-Almao, P., Metal Oxide Nanoparticles for Asphaltene Adsorption and Oxidation. *Energy & Fuels* **2011,** 25, (3), 1017-1023.
10. Nassar, N. N.; Hassan, A.; Pereira-Almao, P., Thermogravimetric studies on catalytic effect of metal oxide nanoparticles on asphaltene pyrolysis under inert conditions. *Journal of thermal analysis and calorimetry* **2012,** 110, (3), 1327-1332.
11. Hashemi, R.; Nassar, N. N.; Pereira-Almao, P., *Energy Fuels* **2012,** 26, (3), 1645.
12. Turgman-Cohen, S.; Fischer, D. A.; Kilpatrick, P. K.; Genzer, J., Asphaltene adsorption onto self-assembled monolayers of alkyltrichlorosilanes of varying chain length. *ACS applied materials & interfaces* **2009,** 1, (6), 1347-1357.
13. Turgman-Cohen, S.; Smith, M. B.; Fischer, D. A.; Kilpatrick, P. K.; Genzer, J., Asphaltene adsorption onto self-assembled monolayers of mixed aromatic and aliphatic trichlorosilanes. *Langmuir* **2009,** 25, (11), 6260-6269.
14. Ese, M.-H.; Galet, L.; Clausse, D.; Sjöblom, J., Properties of Langmuir surface and interfacial films built up by asphaltenes and resins: Influence of chemical demulsifiers. *Journal of colloid and interface science* **1999,** 220, (2), 293-301.
15. Rudrake, A.; Karan, K.; Horton, J. H., A combined QCM and XPS investigation of asphaltene adsorption on metal surfaces. *Journal of colloid and interface science* **2009,** 332, (1), 22-31.
16. Abdallah, W.; Taylor, S., Surface characterization of adsorbed asphaltene on a stainless steel surface. *Nuclear Instruments and Methods in Physics Research Section B: Beam Interactions with Materials and Atoms* **2007,** 258, (1), 213-217.
17. Xie, K.; Karan, K., Kinetics and thermodynamics of asphaltene adsorption on metal surfaces: A preliminary study. *Energy & fuels* **2005,** 19, (4), 1252-1260.
18. Mendoza de la Cruz, J. L.; Castellanos-Ramírez, I. V.; Ortiz-Tapia, A.; Buenrostro-González, E.; Durán-Valencia, C. d. l. A.; López-Ramírez, S., Study of monolayer to multilayer adsorption of asphaltenes on reservoir rock minerals. *Colloids and Surfaces A: Physicochemical and Engineering Aspects* **2009,** 340, (1), 149-154.
19. Acevedo, S.; Ranaudo, M. A.; Escobar, G.; Gutiérrez, L.; Ortega, P., Adsorption of asphaltenes and resins on organic and inorganic substrates and their correlation with precipitation problems in production well tubing. *Fuel* **1995,** 74, (4), 595-598.
20. Pernyeszi, T.; Patzko, A.; Berkesi, O.; Dékány, I., Asphaltene adsorption on clays and crude oil reservoir rocks. *Colloids and Surfaces A: Physicochemical and Engineering Aspects* **1998,** 137, (1), 373-384.
21. Dubey, S. T.; Waxman, M. H., *SPE Reservoir Eng.* **1995,** 6, (3), 389.
22. Dudášová, D.; Simon, S.; Hemmingsen, P.; Sjöblom, J., *Colloids Surf., A* **2008,** 317, 1.
23. Nassar, N. N.; Hassan, A.; Pereira-Almao, P., Clarifying the catalytic role of NiO nanoparticles in the oxidation of asphaltenes. *Applied Catalysis A: General* **2013,** 462–463, (0), 116-120.
24. Nassar, N. N., Asphaltene adsorption onto alumina nanoparticles: kinetics and thermodynamic studies. *Energy & Fuels* **2010,** 24, (8), 4116-4122.
25. Nassar, N. N.; Hassan, A.; Luna, G.; Pereira-Almao, P., Comparative study on thermal cracking of Athabasca bitumen. *Journal of thermal analysis and calorimetry* **2013,** 114, (2), 465-472.

26. Hosseinpour, N.; Khodadadi, A. A.; Bahramian, A.; Mortazavi, Y., Asphaltene Adsorption onto Acidic/Basic Metal Oxide Nanoparticles toward in Situ Upgrading of Reservoir Oils by Nanotechnology. *Langmuir* **2013,** 29, (46), 14135-14146.
27. Hosseinpour, N.; Mortazavi, Y.; Bahramian, A.; Khodatars, L.; Khodadadi, A. A., Enhanced pyrolysis and oxidation of asphaltenes adsorbed onto transition metal oxides nanoparticles towards advanced in-situ combustion EOR processes by nanotechnology. *Applied Catalysis A: General* **2014,** 477, 159-171.
28. Cortés, F. B.; Mejía, J. M.; Ruiz, M. A.; Benjumea, P.; Riffel, D. B., Sorption of asphaltenes onto nanoparticles of nickel oxide supported on nanoparticulated silica gel. *Energy & Fuels* **2012,** 26, (3), 1725-1730.
29. Cortés, F. B.; Mejía, J. M.; Ruiz, M. A.; Benjumea, P.; Riffel, D. B., Sorption of Asphaltenes onto Nanoparticles of Nickel Oxide Supported on Nanoparticulated Silica Gel. *Energy & Fuels* **2012,** 26, (3), 1725-1730.
30. Franco, C.; Patiño, E.; Benjumea, P.; Ruiz, M. A.; Cortés, F. B., Kinetic and thermodynamic equilibrium of asphaltenes sorption onto nanoparticles of nickel oxide supported on nanoparticulated alumina. *Fuel* **2013,** 105, (0), 408-414.
31. Franco, C. A.; Nassar, N. N.; Ruiz, M. A.; Pereira-Almao, P.; Cortés, F. B., Nanoparticles for Inhibition of Asphaltenes Damage: Adsorption Study and Displacement Test on Porous Media. *Energy & Fuels* **2013,** 27, (6), 2899-2907.
32. Talu, O.; Meunier, F., Adsorption of associating molecules in micropores and application to water on carbon. *AIChE journal* **1996,** 42, (3), 809-819.
33. Tatiana Montoya, D. C., Camilo Franco, Nashaat Nassar, Farid Cortés, A Novel Solid-Liquid Equilibrium Model for Describing the Adsorption of Associating Asphaltene Molecules onto Non-Porous Surfaces Based on the "Chemical Theory". *Energy & Fuels* **2014**.
34. Smith, J. M.; Van Ness, H. C.; Abbott, M. M., *Introduction to chemical engineering thermodynamics*. Boston: McGraw-Hill; 7th ed.: 2005.
35. Montgomery, D. C.; Runger, G. C., *Applied statistics and probability for engineers*. John Wiley & Sons: 2010.
36. Vyazovkin, S.; Burnham, A. K.; Criado, J. M.; Pérez-Maqueda, L. A.; Popescu, C.; Sbirrazzuoli, N., ICTAC Kinetics Committee recommendations for performing kinetic computations on thermal analysis data. *Thermochimica Acta* **2011,** 520, (1), 1-19.
37. Nassar, N. N.; Hassan, A.; Vitale, G., Comparing kinetics and mechanism of adsorption and thermo-oxidative decomposition of Athabasca asphaltenes onto TiO 2, ZrO 2, and CeO 2 nanoparticles. *Applied Catalysis A: General* **2014,** 484, 161-171.
38. Doyle, C., Synthesis and evaluation of thermally stable polymers. II. *Polymer evaluation. Appl Polym Sci* **1961,** 5, 285-292.
39. Doyle, C. D., Series approximations to the equation of thermogravimetric data. **1965**.
40. Ozawa, T., A new method of analyzing thermogravimetric data. *Bulletin of the chemical society of Japan* **1965,** 38, (11), 1881-1886.
41. Flynn, J. H.; Wall, L. A., A quick, direct method for the determination of activation energy from thermogravimetric data. *Journal of Polymer Science Part B: Polymer Letters* **1966,** 4, (5), 323-328.
42. Opfermann, J.; Kaisersberger, E., An advantageous variant of the Ozawa-Flynn-Wall analysis. *Thermochimica acta* **1992,** 203, 167-175.
43. Flynn, J., The isoconversional method for determination of energy of activation at constant heating rates: corrections for the Doyle approximation. *Journal of Thermal Analysis and Calorimetry* **1983,** 27, (1), 95-102.
44. Rooney, J. J., Eyring transition-state theory and kinetics in catalysis. *Journal of Molecular Catalysis A: Chemical* **1995,** 96, (1), L1-L3.
45. Young, D. A., *Decomposition of solids*. Pergamon: 1966; Vol. 1.
46. Sestak, J., Thermodynamical properties of solids. *Prague: Academia* **1984**.

47. Cortes, F. B.; Rojano, B.; Chejne Janna, F., Advantages and thermodynamic limitations of the experimental sorption isosteric method. *Dyna* **2013,** 80, (182), 155-162.
48. Sing, K.; Sing, K.; Everett, D.; Haul, R.; Moscou, L.; Pierotti, R.; Rouquerol, J.; Siemieniewska, T., Reporting physisorption data for gas/solid systems. *Pure Appl. Chem* **1982,** 54, (11), 2201.
49. Nassar, N. N.; Tatiana Montoya, T.; Franco, C. A.; Cortés, F. B.; Pereira-Almao, P. R., A New Model for Describing the Adsorption of Asphaltenes on Porous Media at a High Pressure and Temperature under Flow Conditions. *Energy & Fuels* **2015**.
50. Alboudwarej, H.; Pole, D.; Svrcek, W. Y.; Yarranton, H. W., Adsorption of asphaltenes on metals. *Industrial & engineering chemistry research* **2005,** 44, (15), 5585-5592.
51. Cortés, F. B.; Chejne, F.; Rojano, B., A new model for predicting sorption isotherm of water in foods. *International Journal of Food Engineering* **2011,** 7, (2).
52. Fenistein, D.; Barré, L.; Broseta, D.; Espinat, D.; Livet, A.; Roux, J.-N.; Scarsella, M., Viscosimetric and neutron scattering study of asphaltene aggregates in mixed toluene/heptane solvents. *Langmuir* **1998,** 14, (5), 1013-1020.
53. Milanova, D.; Kumar, R., Heat transfer behavior of silica nanoparticles in pool boiling experiment. *Journal of Heat Transfer* **2008,** 130, (4), 042401.
54. Dietrich, P.; Lerche, K.-H.; Reusch, J.; Nitzsche, R., The characterization of silica microparticles by electrophoretic mobility measurements. *Chromatographia* **1997,** 44, (7-8), 362-366.
55. Shayan, N. N.; Mirzayi, B., Adsorption and Removal of Asphaltene Using Synthesized Maghemite and Hematite Nanoparticles. *Energy & Fuels* **2015,** 29, (3), 1397-1406.
56. Bailon-Garcia, E.; Carrasco-Marin, F.; Perez-Cadenas, A.; Maldonado-Hodar, F., Microspheres of carbon xerogel: An alternative Pt-support for the selective hydrogenation of citral. *Applied Catalysis A: General* **2014,** 482, 318-326.
57. Xing, C.; Hilts, R.; Shaw, J., Sorption of Athabasca vacuum residue constituents on synthetic mineral and process equipment surfaces from mixtures with pentane. *Energy & Fuels* **2010,** 24, (4), 2500-2513.
58. Adams, J. J., Asphaltene adsorption, a literature review. *Energy & Fuels* **2014,** 28, (5), 2831-2856.
59. Franco, C. A.; Montoya, T.; Nassar, N. N.; Pereira-Almao, P.; Cortés, F. B., Adsorption and Subsequent Oxidation of Colombian Asphaltenes onto Nickel and/or Palladium Oxide Supported on Fumed Silica Nanoparticles. *Energy & Fuels* **2013,** 27, (12), 7336-7347.
60. Contreras, J. L.; Fuentes, G. A., Sintering of Supported Metal Catalysts. *ChemInform* **2013,** 44, (41).
61. Wu, Y.; Wang, D.; Zhao, P.; Niu, Z.; Peng, Q.; Li, Y., Monodispersed Pd− Ni Nanoparticles: Composition Control Synthesis and Catalytic Properties in the Miyaura− Suzuki Reaction. *Inorganic chemistry* **2011,** 50, (6), 2046-2048.
62. Trejo, F.; Rana, M. S.; Ancheyta, J., Thermogravimetric determination of coke from asphaltenes, resins and sediments and coking kinetics of heavy crude asphaltenes. *Catalysis Today* **2010,** 150, (3), 272-278.
63. Savage, P. E.; Klein, M. T.; Kukes, S. G., Asphaltene reaction pathways. 1. Thermolysis. *Industrial & Engineering Chemistry Process Design and Development* **1985,** 24, (4), 1169-1174.
64. Ali, M. F.; Saleem, M., Thermal decomposition of Saudi crude oil asphaltenes. *Fuel science & technology international* **1991,** 9, (4), 461-484.
65. Alshareef, A. H.; Scherer, A.; Tan, X.; Azyat, K.; Stryker, J. M.; Tykwinski, R. R.; Gray, M. R., Formation of archipelago structures during thermal cracking implicates a chemical mechanism for the formation of petroleum asphaltenes. *Energy & Fuels* **2011,** 25, (5), 2130-2136.
66. Habib, F. K.; Diner, C.; Stryker, J. M.; Semagina, N.; Gray, M. R., Suppression of Addition Reactions during Thermal Cracking Using Hydrogen and Sulfided Iron Catalyst. *Energy & Fuels* **2013,** 27, (11), 6637-6645.

67. Sanford, E. C., Molecular approach to understanding residuum conversion. *Industrial & engineering chemistry research* **1994,** 33, (1), 109-117.
68. Gray, M. R.; McCaffrey, W. C., Role of chain reactions and olefin formation in cracking, hydroconversion, and coking of petroleum and bitumen fractions. *Energy & fuels* **2002,** 16, (3), 756-766.
69. Siddiqui, M. N., Catalytic pyrolysis of Arab Heavy residue and effects on the chemistry of asphaltene. *Journal of Analytical and Applied Pyrolysis* **2010,** 89, (2), 278-285.
70. Hamedi Shokrlu, Y.; Babadagli, T., In-Situ Upgrading of Heavy Oil/Bitumen During Steam Injection by Use of Metal Nanoparticles: A Study on In-Situ Catalysis and Catalyst Transportation.
71. Vélez, J. F.; Chejne, F.; Valdés, C. F.; Emery, E. J.; Londoño, C. A., Co-gasification of Colombian coal and biomass in fluidized bed: an experimental study. *Fuel* **2009,** 88, (3), 424-430.
72. Barrio, V.; Arias, P.; Cambra, J.; Güemez, M.; Pawelec, B.; Fierro, J., Aromatics hydrogenation on silica–alumina supported palladium–nickel catalysts. *Applied Catalysis A: General* **2003,** 242, (1), 17-30.
73. Guo, Y.; Zhou, L.; Kameyama, H., Steam reforming reactions over a metal-monolithic anodic alumina-supported Ni catalyst with trace amounts of noble metal. *international journal of hydrogen energy* **2011,** 36, (9), 5321-5333.
74. Inoue, S.; Muto, A.; Kudou, H.; Ono, T., CHARACTERISTICS OF NOVEL TITANIA CATALYST PREPARED BY MULTI-GELATION METHOD IN DEEP-DESULFURIZATION CONDITION. *Prepr. Pap.-Am. Chem. Soc., Div. Fuel Chem* **2003,** 48, (2), 496.
75. Łaniecki, M.; Małecka-Grycz, M.; Domka, F., Water–gas shift reaction over sulfided molybdenum catalysts: I. Alumina, titania and zirconia-supported catalysts. *Applied Catalysis A: General* **2000,** 196, (2), 293-303.

3. Influence of *n*-C_7 asphaltene aggregation on their adsorption and catalytic behavior of nanoparticles

Most of the reported nanoparticles used for adsorption of asphaltenes and subsequent decomposition of the adsorbed asphaltenes were believed to be effective adsorbents and catalysts. However, it is very well accepted that asphaltenes have the ability to self-assemble onto various aggregates and colloids.[1-3] Therefore, the changes in the colloidal state of asphaltenes can impact the catalytic activity of the nanoparticle surfaces after adsorption. However, until now there are no studies in specialized literature that correlates the self-association of asphaltenes with the adsorption affinity or catalytic activity of the nanoparticle surfaces. Although adsorption isotherms for "effective" multilayers of asphaltene have been reported in the literature, there was no evidence about the effect of the size of the adsorbed asphaltene monomers, dimers, *i*-mers or nanoaggregates on the catalytic activity of the nanoparticle surface.

Hence, a study of the impact of asphaltene aggregates on the nanoparticle surface adsorption affinity and catalytic activity is of paramount importance. To this end, Montoya et al.[4] has recently developed a novel three-parameters solid-liquid equilibrium (SLE) model for describing the behavior of the adsorption of self-associating asphaltene molecules onto solid surfaces based on the self-association theory.[4] In addition to predicting the affinity and ability of asphaltenes to be adsorbed onto the nanoparticles surface, this novel SLE model provides, at the macro level, an insight on the extent of the asphaltene aggregates on the nanoparticle surface. Hence, this study continues the line of Chapter 2, aiming to investigate the impact of asphaltenes monomers, dimers, *i*-mers or nanoaggregates on the catalytic activity of the nanoparticles.

Accordingly, CS and nanoparticles of NiO and PdO supported on CS were employed for the adsorption and post-adsorption oxidation of n-C_7 asphaltenes using different ratios of heptol (*n*-heptane and toluene). A correlation between the adsorption affinity, the extent of asphaltene aggregation and catalytic activity is developed using the parameters of SLE model, and the values of effective activation energies are estimated by the isoconversional method.

3.1 Materials, methods and modeling

3.1.1 Materials

Virgin solid *n*-C_7 asphaltenes were extracted from the AK18 crude oil. Crude oil properties and isolation method are described in Chapter 2. *n*-Heptane (99%, Sigma-Aldrich, St. Louis, MO) was used as a precipitant for asphaltene extraction, and in the preparation of the heavy oil model solution with toluene (99.5%, MerkK GaG, Germany). The ratio of *n*-heptane to toluene (heptol) was varied from 0 to 40 %v/v to obtain different sizes of asphaltene nanoaggregates. CS and CSNi1Pd1

nanoparticles were used as adsorbents and catalysts. Nanoparticles properties can be found in Chapter 1.

3.1.2 Preparation of model solutions

Heavy oil model solutions were prepared by exposing *n*-C_7 asphaltenes to a mixture of different ratios of *n*-heptane and toluene (heptol) at 25°C. Three different ratios of *n*-heptane to toluene were considered in this study, namely, 0, 20 and 40 %v/v of *n*-heptane. Before adding the *n*-C_7 asphaltenes, the heptol mixtures were mixed at 300 rpm for 2 h. Then, a specified mass of *n*-C_7 asphaltenes was added to the corresponding solution to obtain a stock solution of 6000 mg/L. The mixture was stirred for 6 h at 300 rpm to ensure that the system was homogenous and the size of the asphaltene aggregate remained constant.[5] As asphaltenes precipitation is time-dependent process,[6] the stability of asphaltene in solution was monitored through the Oliensis Spot Test Number[7, 8] and Polarized Light Microscopy[9] for 72 h and it confirms that no significant precipitation of asphaltenes could be observed for the selected heptol ratios during the time of adsorption experiment.

3.1.3 Evaluation of nanoparticles as adsorbents and catalysts

Batch adsorption experiments were conducted at room temperature 25°C for different initial concentrations of *n*-C_7 asphaltenes from 100 to 6000 mg/L following the procedure described in Section 2.1.2. Nanoparticles containing adsorbed *n*-C_7 asphaltenes were dried overnight in a vacuum oven at 65ºC. Approximately 5 mg of dried nanoparticles with adsorbed asphaltenes was taken for thermogravimetric analysis. Thermogravimetric analyses were performed according to Section 2.1.2 in presence of air.

3.1.4 Modeling

The obtained experimental data of adsorption isotherms were described by the solid-liquid equilibrium model (SLE).[4] The catalytic behavior of the nanoparticles towards *n*-C_7 asphaltenes was described by the isoconversional method of Ozawa−Flyn−Wall (OFW).[10-12] Details of the SLE model and OFW method can be found in Section 2.2.

3.2 Results and discussions

3.2.1 *n*-C_7 asphaltenes adsorption isotherms from toluene and Heptol solutions

Figure 3.1 shows the experimental isotherm data obtained together with the fit of the SLE model for *n*-C_7 asphaltene adsorption from different heptol solutions onto nanoparticles of CS and CSNi1Pd1 at a temperature of 25°C. The estimated SLE model parameters are listed in Table 3.1.

As anticipated, for both cases, the *n*-C_7 asphaltene adsorption increases with an increase in the *n*-heptane to toluene volume ratio. These results are in excellent agreement with previous studies reported in the literature for asphaltene adsorption from oil solutions with different precipitants onto different solid surfaces, such as hydrophilic and hydrophobic silica particles,[13] clay minerals (like kaolinite, illite, montmorillonite and mineral oil reservoir rocks),[14] coated quartz crystals[15] and

metals.[4, 16] It is well known that by adding an asphaltene precipitant to a heavy oil solution, the solubility of asphaltenes will decrease and hence asphaltene aggregation and self-association will be enhanced.[17] Accordingly, asphaltenes will be adsorbed on solid surface as large aggregates. [18, 19] Furthermore, Figure 3.1 also shows that CSNi1Pd1 nanoparticles clearly adsorbed more *n*-C_7 asphaltenes than CS nanoparticles across the entire range of *n*-C_7 asphaltene concentrations; the difference was more significant at higher concentrations (200 mg/L). This indicates that asphaltene adsorption is surface specific and that the induced selectivity of the included metal oxides apparently enhances the adsorption capacity of the nanoparticles. These results are also in agreement with the previous results observed in Chapter 2 on the adsorption of *n*-C_7 asphaltenes onto CS nanoparticles functionalized with NiO and/or PdO.

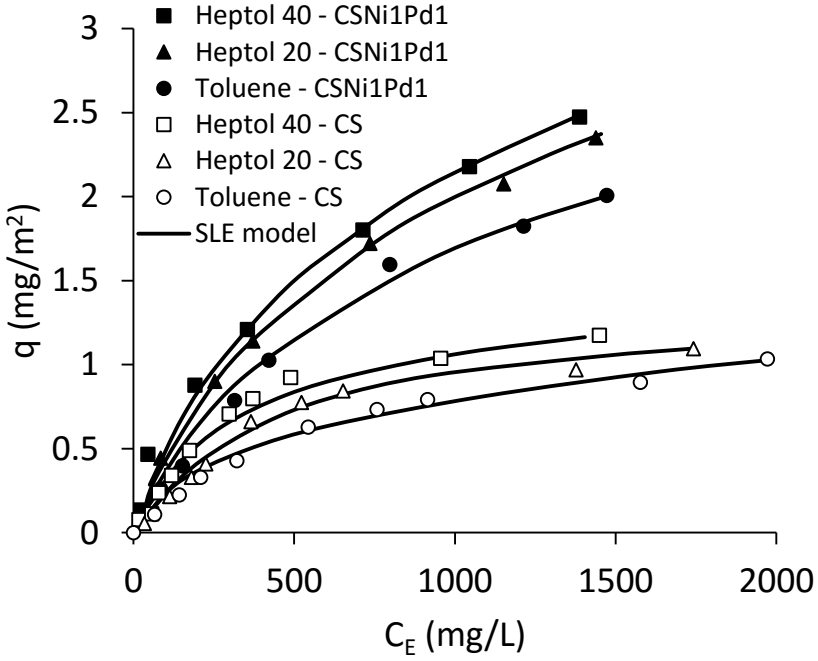

Figure 3.1. Adsorption isotherms of *n*-C_7 asphaltenes onto CS and CSNi1Pd1 nanoparticles at 25°C and different heptol ratios. The symbols are experimental data and the solid lines are from the SLE model.

To further understand this adsorption behavior, the experimental isotherm data are fitted to the SLE model. As seen in Figure 3.1 and indicated by the values of the regression coefficient and *RSME%* in Table 3.1, the SLE model fits the experimental data well. The results in Table 3.1 also show that the adsorption capacity of both nanoparticles, represented by q_m, followed the order heptol 40 > heptol 20 > toluene. A similar trend is obtained for the adsorption affinity, represented by the reciprocal of the *H* parameter of the SLE model. In addition, based on the values of q_m and the reciprocal of *H*, it is very clear that the CSNi1Pd1 nanoparticles have a higher adsorption affinity and capacity than the CS nanoparticles for all Heptol solutions employed. On the other hand, lower *K* values were observed for the CSNi1Pd1 nanoparticles than for CS, indicating that the inclusion of NiO and PdO on the CS surface allows the inhibition of the self-association of the asphaltenes. The differences in ranking the SLE model parameters (i.e., q_m, *H*, and *K*) between the two types of nanoparticles with different volume ratios of *n*-heptane to toluene can be attributed to the different degree of interactions between the nanoparticle surface and the *n*-C_7 asphaltenes molecules or aggregates.

It is noteworthy that the SLE model is based on the assumptions that the adsorption process is mainly divided into three regions, namely:[4] the first region, which corresponds to low uptake, here the adsorption will likely occur in the high-energy sites and asphaltenes molecules would be possibly adsorbed as monomers; the second region is at medium uptake and here the asphaltene will form aggregates around the high-energy sites; and the last region is at high uptake, in this region it is assumed that the finite volume available for adsorption will become crowded with asphaltene molecules, which are expected to be in the form of *i*-mers, nanoaggregates, etc. These findings are interesting, as asphaltene self-association and aggregation can cause formation damage and consequently impact the oil recovery efficiency.[20] In addition, large *n*-C_7 asphaltene aggregates might block some of the active sites of the nanoparticles, and hence they, could impact the catalytic activity in the case of the catalytic decomposition of the adsorbed asphaltenes.[4]

Table 3.1. SLE model parameters of Colombian n-C_7 asphaltenes adsorption from different heptol mixtures onto CS and CSNi1Pd1 nanoparticles at 25°C.

Material	Solvent	H (mg/g)	K (g/g) x 10^{-4}	q_m (mg/m^2)	R^2	*RSME%*
CS	Toluene	2.02	4.51	2.89	0.99	8.72
	Heptol 20	1.59	4.96	2.97	0.99	8.56
	Heptol 40	1.12	5.47	3.15	0.99	9.13
CSNi1Pd1	Toluene	1.77	2.16	6.36	0.99	3.36
	Heptol 20	1.18	2.74	6.40	0.99	5.26
	Heptol 40	1.07	3.29	6.58	0.99	5.21

3.2.2 Effect of *n*-C_7 asphaltenes aggregation and nanoparticle type on the catalytic oxidation

Panels a-c in Figure 3.1 show a) the plot of rate of mass loss, b) the evolution profiles of the production of CO and CO_2 and c) the degree of conversion for asphaltene oxidation from toluene, heptol 20 and heptol 40 in the presence of CS nanoparticles for a fixed amount of asphaltenes adsorbed at 0.67 ± 0.03 mg/m^2. As is shown in Table 3.1, according to the *K* parameter, the degree of asphaltene self-association increases as the amount of *n*-heptane in the solvent increases, indicating that large aggregates can be found over the adsorbent surface.

Figure 3.2a shows two peaks for the three asphaltenes adsorbed onto CS nanoparticles from different solvents. The first peak is found at approximately 359°C for the three systems, and no significant shift was observed. On the other hand, the second peak is observed at 509, 519 and 536°C for toluene, heptol 20 and heptol 40, respectively, confirming a delay in the oxidation of asphaltenes due to an increase in the size of the aggregate. In any case, the first peak for asphaltene oxidation in the presence of CS nanoparticles is lower than for virgin *n*-C_7 asphaltenes (see Chapter 2). However, the second peak is found at a higher temperature than for the virgin asphaltenes. This could be due to the high asphaltene loading that leads to early addition reactions, which probably occur due to the reaction mechanism of free radical chains.[21] After the O_2 stabilizes the radical species, heavier compounds that are more difficult to decompose are expected to be produced by the radial recombination at termination step of the chain reactions.[22] Also, heavier compounds than the starting specie can be produced from addition reactions that occur by the addition of free radicals to olefins,[23]

cross-linking reactions between aromatic clusters[21] or reactions between aromatics joined by alkyl bridges.[24]
As was observed for the virgin asphaltenes, the profile of production of CO_2 is similar to the rate of mass loss plot. Although in the rate of mass loss there was no clear evidence of the temperature shifting for the first peak, for the gas analyses in Panel c in Figure 3.2, it can be observed that there is a delay in the CO_2 peaks as the heptol ratio increases. In the second peak of Figure 3.2b it is observed that the production of CO_2 is shifted to a lower temperature in the order toluene < heptol 20 < heptol 40. In addition, it is observed that the ratio CO/CO_2 increases as the degree of the self-association of asphaltenes decreases. This could be attributed to the fact that the higher asphaltene aggregates tend to hinder some active sites that are then released as asphaltenes are oxidized. Therefore, the CO could be chemisorbed onto the liberated active sites of the nanoparticles to form CO_2; as oxides (like SiO_2) are active catalysts for the oxidation of the CO by its reaction with the subsurface oxygen.[25] Figure 3.2c shows that the conversion of asphaltenes occurs at a lower temperature in the order of toluene < heptol 20 < heptol 40, indicating that as the asphaltene aggregate increases, the temperature needed for the oxidation of asphaltenes increases. For instance, the temperatures at a fixed degree of 50% conversion are 447, 456 and 485°C for toluene, heptol 20 and heptol 40, respectively.

According to the values observed for the *K* parameter of the SLE model (Table 3.1), the degree of asphaltene self-association is lower for the supported nanoparticles than for the CS support; hence, it is expected that the catalytic activity towards asphaltene oxidation will be enhanced by the CSNi1Pd1 nanoparticles. Panels a-c of Figure 3.3 show a) the plot of rate of mass, b) the evolution profiles of production of CO and CO_2 and c) the degree of conversion for asphaltene oxidation from different solvents in presence of CSNi1Pd1 nanoparticles at an amount of adsorbed asphaltenes of 0.67 mg/m^2.

Panels a and b in Figure 3.3 show two peaks for the three samples from different solvents, but at a much lower temperature than for CS nanoparticles (Figure 3.2b-c), confirming the higher catalytic activity of the CSNi1Pd1 nanoparticles. It can be noticed that for the CS support, the second peak for toluene, heptol 20 and heptol 40 were about 27, 29 and 31 % higher than the first peak of each sample, respectively. In the case of CSNi1Pd1 nanoparticles, the second peaks are about 13, 20 and 26% higher than the first peak for toluene, heptol 20 and heptol 40, respectively. These results indicate that for CSNi1Pd1 nanoparticles higher amount of asphaltenes are decomposed in the region where the first peak appears in comparison to the CS support, confirming their higher catalytic activity. In the first peak observed in Figure 3.3a, a small shift can be noticed due to the solvent evaluated at temperatures 332, 341 and 394°C. This could be due to higher adsorbed aggregates of asphaltenes that lead to higher temperatures of oxidation. However, in the second peak, there is no clear shift regarding the heptol ratio, and this could be due to the catalytic effect of the nanoparticles, leading to additional reactions occurring to the same degree for toluene and both systems with heptol. In addition, it is observed that the production of both CO and CO_2 starts earlier with the supported nanoparticles and that the first peak of CO_2 production is found at 344, 367 and 399°C for toluene, heptol 20 and heptol 40, respectively. This again proves that the size of the asphaltene aggregate influences the catalytic activity of the nanoparticles.

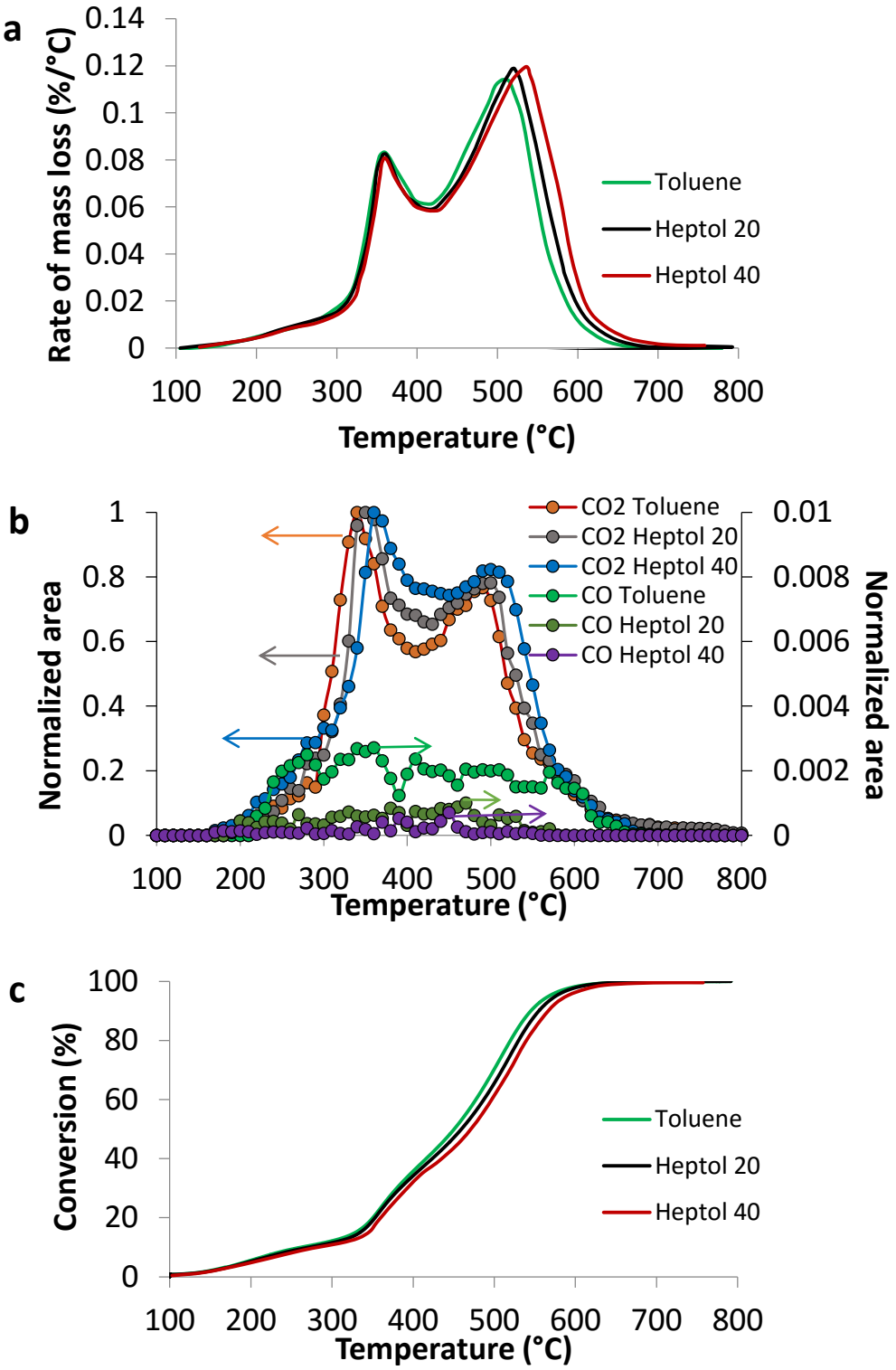

Figure 3.2. a) Plot of rate of mass loss, b) the evolution profiles of the production of CO and CO_2 and c) conversion for oxidation of virgin asphaltenes from different solvents in presence of CS nanoparticles; asphaltenes adsorbed = 0.67 ± 0.03 mg/m^2.

As was seen for the CS nanoparticles, for CSNi1Pd1, higher degrees of conversion are obtained in the order of toluene > heptol 20 > heptol 40. However, for the CSNi1Pd1 samples the asphaltene oxidation occurred much earlier than for the CS support. Figure 3.3c shows that for toluene, heptol 20 and heptol 40 a 50% degree of conversion is reached at 397, 422 and 429 °C, respectively. These temperatures are approximately 50, 34 and 56°C lower than for the CS nanoparticles, indicating that the CSN1Pd1 nanoparticles are able to inhibit the self-association of the asphaltenes on the active sites and hence have better catalytic activity than the CS support.

3.2.3 Effect of *n*-C_7 asphaltenes loading

The effect of the asphaltene loading was also evaluated using CSNi1Pd1 nanoparticles. Panels a-c in Figure 3.4 show a) the plot of the rate of mass loss, b) the evolution profiles of production of CO and CO_2 and c) the degree of conversion for asphaltene oxidation from different solvents in presence of CSNi1Pd1 nanoparticles at a fixed amount of adsorbed asphaltenes of 0.17 ± 0.02 mg/m^2. In contrast to what was observed for a higher amount of adsorbed asphaltenes, in the plot of rate of mass loss in Figure 3.4a, three peaks are observed for the three asphaltenes from different solvents. These were observed over three different temperature ranges, namely, a low-temperature range (LTR) between 200 and 270°C, a mid-temperature (MTR) between 271 and 460°C and a high-temperature range (HTR) between 461 and 800°C. In this case, none of the peaks showed a clear shifting for different heptol ratios, and this observation could be due to both low asphaltenes loading and the catalytic effect of the nanoparticles that would have a higher amount of active sites for the reaction. [26] These facts make the nanoparticles able to oxidize asphaltenes of different sizes at approximately the same temperature. The first peak in Figure 3.4a appeared in the LTR at approximately 240°C for toluene and both systems with heptol and was due to a lower asphaltene loading. This results in less hindering of active sites and a subsequent enhancement of the catalytic activity of the catalyst.

Asphaltenes are adsorbed on the nanoparticle surface via diffusive processes in which smaller asphaltene aggregates or monomers at low concentrations, are adsorbed first, followed by larger asphaltenes. In this order, finding that the first peak in the LTR means that for a lower asphaltene loading the first-adsorbed asphaltenes in the first layer retained a lower degree of self-association and are more easily cracked than those for a larger amount adsorbed. On the other hand, the MTR peak appears at approximately 375°C for the three solvents evaluated, approximately 15°C greater than the peak observed for the CSNi1Pd1 nanoparticles in the same region for an amount adsorbed of 0.67 mg/m^2. This increase in the temperature can be explained because the oxidation of the asphaltenes in the LTR led to the formation of heavier compounds. The same situation is observed for the peak in the HTR, where the peak of asphaltene oxidation is found at a temperature 35°C greater than for the sample with more adsorbed asphaltene.

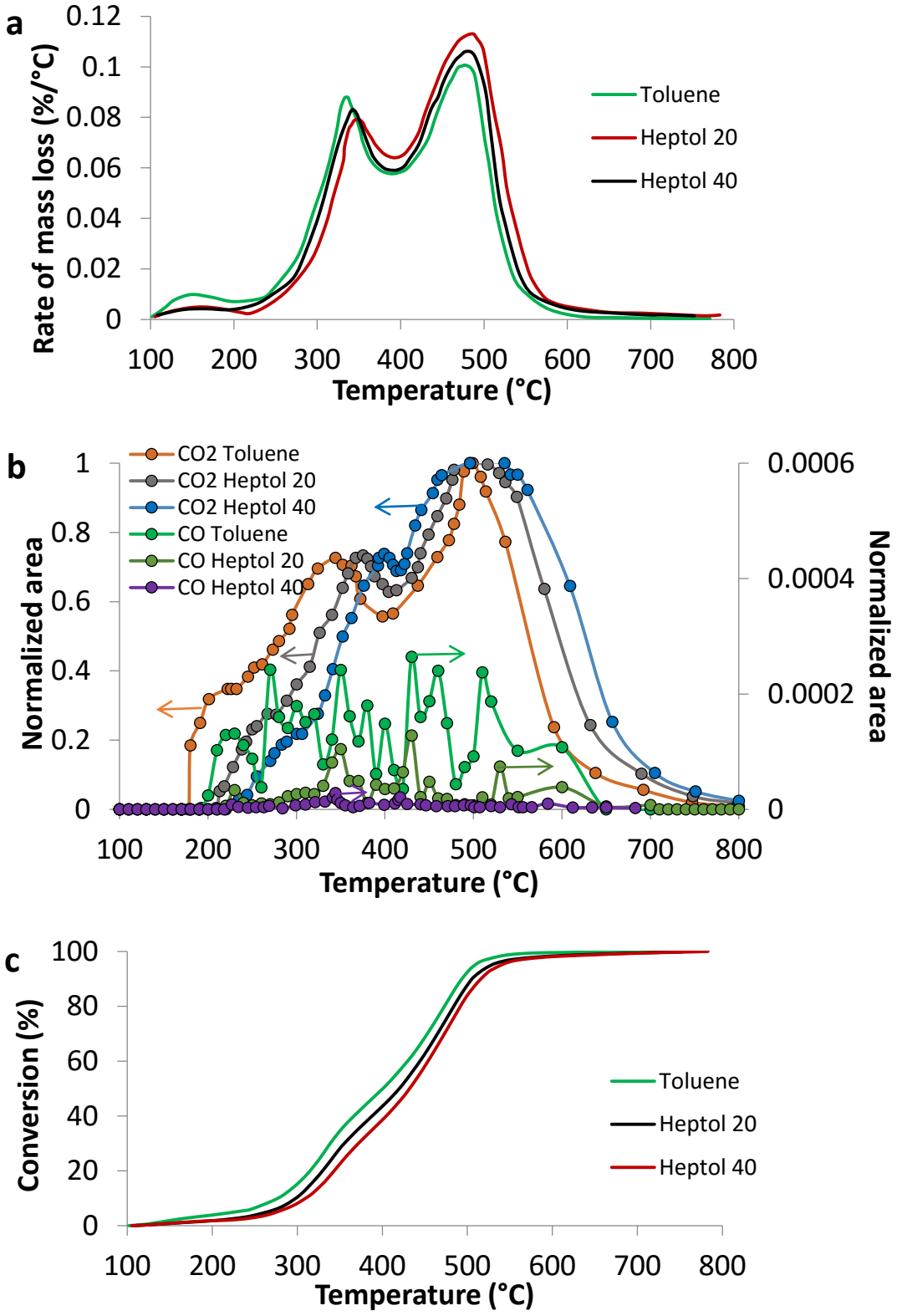

Figure 3.3. a) Plot of rate of mass loss, b) the evolution profiles of the production of CO and CO_2 and c) conversion for oxidation of virgin asphaltenes from different solvents in presence of CSNi1Pd1 nanoparticles; asphaltenes adsorbed = 0.67 ± 0.03 mg/m^2.

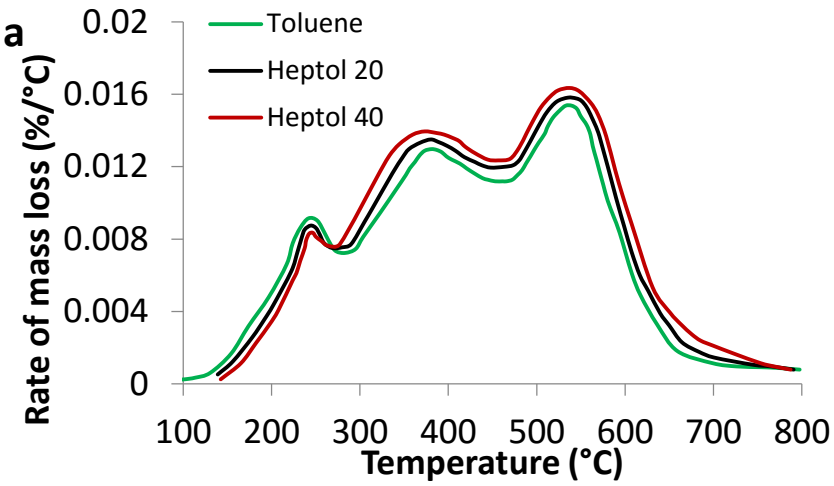
a
Rate of mass loss (%/°C)
0.02
0.016
0.012
0.008
0.004
0
Toluene
Heptol 20
Heptol 40
100 200 300 400 500 600 700 800
Temperature (°C)

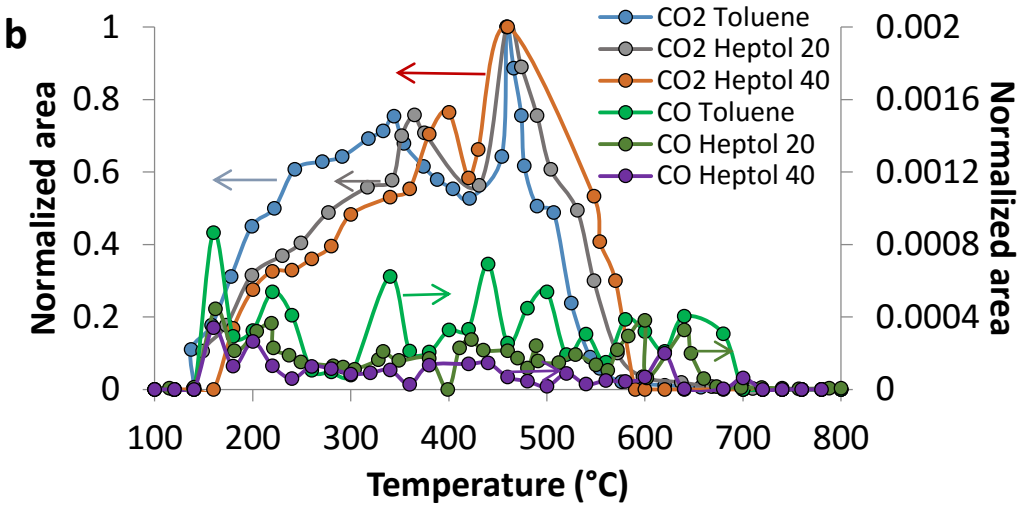
b
Normalized area
1
0.8
0.6
0.4
0.2
0
CO2 Toluene
CO2 Heptol 20
CO2 Heptol 40
CO Toluene
CO Heptol 20
CO Heptol 40
0.002
0.0016
0.0012
0.0008
0.0004
0
Normalized area
100 200 300 400 500 600 700 800
Temperature (°C)

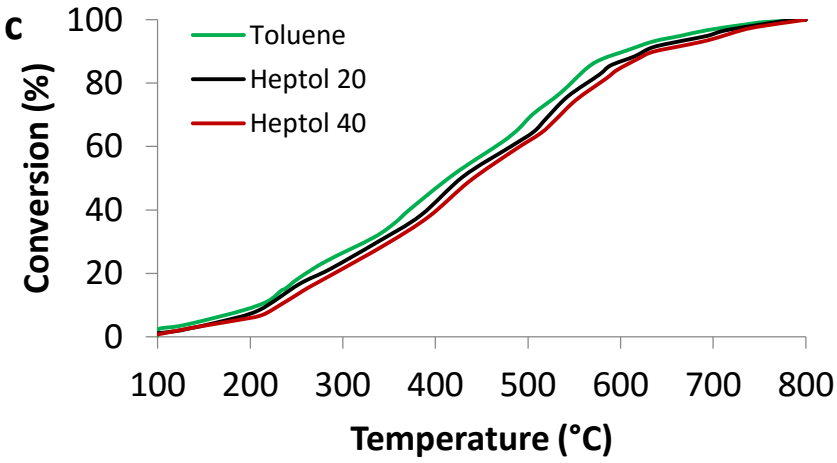
c
Conversion (%)
100
80
60
40
20
0
Toluene
Heptol 20
Heptol 40
100 200 300 400 500 600 700 800
Temperature (°C)

Figure 3.4. a) Plot of rate of mass loss, b) the evolution profiles of the production of CO and CO_2 and c) conversion for oxidation of virgin asphaltenes from different solvents in presence of CSNi1Pd1 nanoparticles; asphaltenes adsorbed = 0.17 ± 0.02 mg/m^2.

The CO and CO_2 evolution in Figure 3.4b confirms that a higher degree of asphaltene self-association leads to lower catalytic activity of the nanoparticles. It is observed that the production of CO_2 starts at lower temperatures as the heptol ratio decreases. A wide first peak is observed for the CO_2 for toluene, heptol 20 and heptol 40 and is due to the oxidation of asphaltenes in the LTR and MTR. In addition, a shift of the peak to the right in the MTR is observed in the order of toluene < heptol 20 < heptol 40, indicating that the catalytic oxidation of asphaltenes occurs earlier for the systems with a lower degree of self-association. Additionally, as seen in Figure 3.4c, higher degrees of conversion are obtained as the amount of *n*-heptane in the solvent decreases.

3.2.4 Estimation of the effective activation energies for the different toluene and heptol systems

Figure 3.5 shows the estimated E_α for virgin asphaltenes and asphaltenes from different solvents in the presence of CS nanoparticles. It is observed that for virgin asphaltenes the effective activation energy ranged between 200 and 125 kJ/mol and decreased as the percentage of conversion increases. For asphaltenes adsorbed on CS nanoparticles, the E_α trend was the opposite of that for virgin asphaltenes; as the percentage of conversion increases, the E_α increased, indicating that the oxidation mechanism is different than for virgin asphaltenes and that different factors, such as addition reactions, steps involved and reaction order.

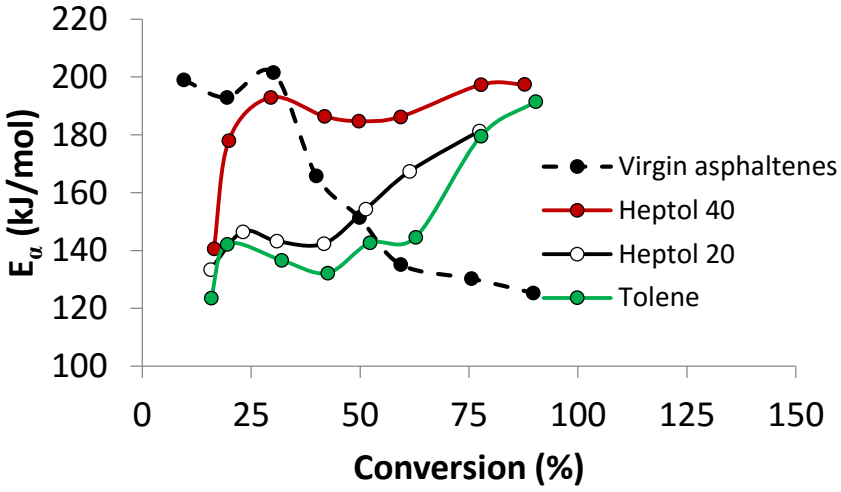

Figure 3.5. Effective activation energies by the OFW method as function of the conversion for CS nanoparticles.

For the three asphaltenes from different solvents, the trend followed by E_α was heptol 40 > heptol 20 > toluene, indicating that for larger asphaltene aggregates, more energy is needed to oxidize the adsorbed asphaltenes. It is also observed that for the three asphaltenes adsorbed, the pathway followed by the E_α is similar with an upward shift as the amount of *n*-heptane increases, suggesting that the mechanisms involved are similar for the three samples.

Figure 3.6 shows the estimated E_α for asphaltenes adsorbed onto CSNi1Pd1 nanoparticles at adsorbed amounts of 0.17 and 0.67 mg/m^2. In the evaluation of these two amounts adsorbed, the trend followed by E_α was also heptol 40 > heptol 20 > toluene, and for the asphaltenes adsorbed at a concentration of 0.67 mg/m^2 from the same solvent, the E_α was always higher than for those at a concentration of 0.17 mg/m^2. These results indicate that the larger asphaltene aggregates can block the active sites and strongly affect the catalytic activity of the nanoparticles. It is worth mentioning that the pathway followed by the E_α for both amounts of asphaltenes adsorbed on CSNi1Pd1 is similar. However, when a comparison is made for different nanoparticles, it is seen that the trend is different and the oxidation mechanism and reaction order is specific to the type of nanoparticle.

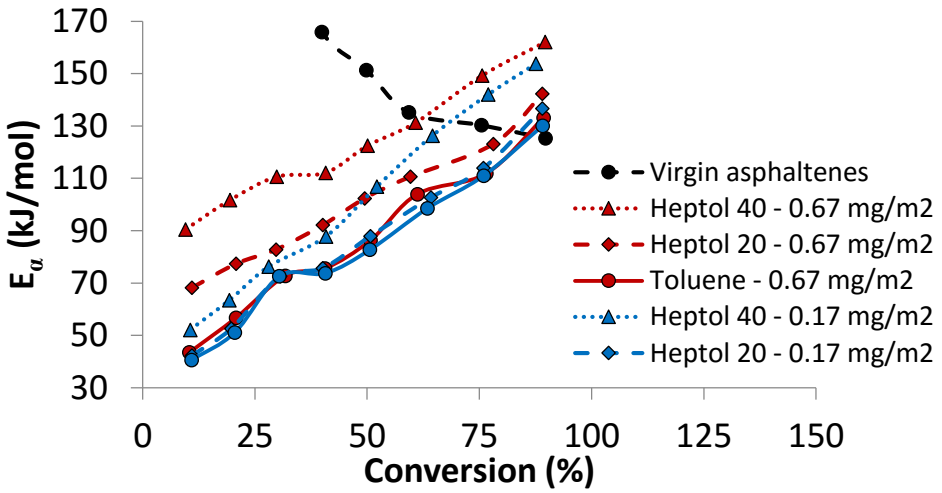

Figure 3.6. Effective activation energies by the OFW method as function of the conversion for CSNi1Pd1 nanoparticles at two different amounts of asphaltenes adsorbed.

The mechanism for the asphaltenes oxidation is highly dependent on the way asphaltenes are adsorbed on the nanoparticles surface. In fact, depending on the nanoparticles chemical nature, selectivity towards asphaltenes adsorption could change from one type of nanoparticle to another. In this order, asphaltenes can be adsorbed in perpendicular or parallel ways depending on the nanoparticles selectivity towards different functional groups in the asphaltenes structure, affecting the degree of asphaltenes self-association. Thus, the synergistic effect of NiO and PdO on the CS surface alters the selectivity towards different species present in the asphaltenes structure and hence, the way asphaltenes are adsorbed. Then, the disposition of asphaltenes over the nanoparticle surface is different and is in agreement with the values of the *K* parameter of the SLE model (Table 3.1). Also, the activated state will be different for the oxidation of asphaltenes in presence of both CS and CSNi1Pd1 nanoparticles, being less disordered for the one presenting lower effective activation energies.[27]

As the application of nanoparticles for asphaltene adsorption and catalytic decomposition has gained interest in the oil industry, a better understanding of the relation of the adsorption behavior and the catalytic activity of the nanoparticles is needed. In this regard, it is proposed a correlation between the SLE model parameters (i.e., *H* and *K)* that give information about the adsorptive behavior of the nanoparticle surface and the E_α estimated by the OFW model that provides the catalytic behavior of the nanoparticle surface. It is worth remembering that the SLE parameters and E_α are obtained for the adsorption isotherms of asphaltenes from different solvents as shown in the previous sections.

Panels a and b in Figure 3.7 show the relation between the H parameter and the effective activation energy for a) CS and b) CSNi1Pd1 nanoparticles at the three different degrees of asphaltene conversion of 20, 50 and 80%. As seen in Figure 3.7 for both nanoparticles, E_α decreases as the H value increases, i.e., as the adsorption affinity decreases. This observed trend is different from the trend obtained in Chapter 2 for asphaltene oxidation, pyrolysis and gasification, where the activation energy decreased as the adsorption affinity increased. Nevertheless, Chapter 2 focused on changing the type of adsorbents for the same asphaltene molecular/aggregate feature, which is different from the current study, where the asphaltene aggregate feature is changing as the heptol ratio changes.

The difference between the correlations can be explained because the different adsorbent surfaces would inhibit the asphaltene self-association over the surface of the nanoparticles, directly affecting the catalytic activity.[4] In addition, one has to keep in mind that the increase in the adsorption affinity as the amount of *n*-heptane increase, is due to the increasing aggregate size and that it could lead to a greater attachment of the asphaltene aggregates that will affect the catalytic activity of the nanoparticles. This finding is in good agreement with the behavior observed in Figure 3.6, where E_α increased with an increase in the heptol ratio, with larger asphaltene aggregates. On the other hand, Figure 3.8a and b show the relation between the constant K from SLE model and the estimated activation energy from the OFW model for asphaltene oxidation in the presence of a) CS and b) CSNi1Pd1 nanoparticles. Clearly, for both CS and CSNi1Pd1 nanoparticles, there is a linear trend between the K parameter and the E_α whereby increasing the degree of asphaltene self-association, the activation energy needed for the asphaltene oxidation increases because the higher aggregates are more prone to have buried or hidden functional groups that could interact with the catalyst surface.[28] Additionally, when different adsorbents are compared using the same asphaltenes from the same solvent, it is observed that E_α decreases as the adsorption affinity increases and as the degree of self-association of the asphaltenes decreases. For example, in the case of asphaltenes adsorbed from toluene onto CSNi1Pd1 nanoparticles the H parameter takes value of 2.02 mg/g and $E_{\alpha=50\%}$ of 42.17 kJ/mol; while for the CS nanoparticles the values of H and $E_{\alpha=50\%}$ are 1.77 mg/g and 86.21 kJ/mol, respectively, indicating that for higher affinities the effective activation energy will decrease. Same observations can be seen for both heptol 20 and heptol 40 mixtures, and effective activation energies at values of α of 20 and 80%. However, the higher affinity of the CSNi1Pd1 nanoparticles towards asphaltenes adsorption from same solvent is related to the synergistic effect of NiO and PdO. That synergistic effect enables different unified selectivities, changing intermolecular forces between heteroatoms and functional groups of asphaltenes, and enhancing the surface electronegativity for a more efficient catalytic process. This trend of the effective activation energies as function of adsorption affinity does agree with results reported in Chapter 2.

For the CS nanoparticles, it is observed that the slope of the trend line is similar for conversions of 20 and 50%, but for 80%, the slope is lower, indicating that at this value of conversion there is probably a switch in the oxidation mechanism. Additionally, when different adsorbents are compared using the same asphaltenes from the same solvent, it is observed that E_α decreases as the adsorption affinity increases and as the degree of self-association of the asphaltenes increases.

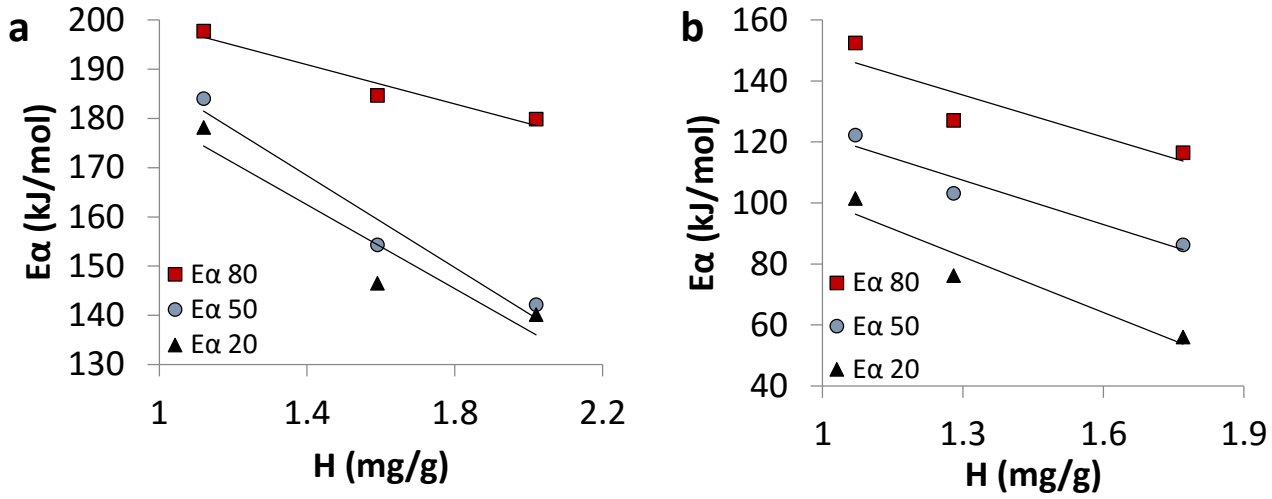

Figure 3.7. Relation between the Henry's law constant from SLE model and the estimated activation energy from the OFW model for asphaltenes thermo oxidation in presence of a) CS and b) CSNi1Pd1 nanoparticles. Degrees of conversion of the activation energy of 20 (■), 50 (●) and 80% (▲).

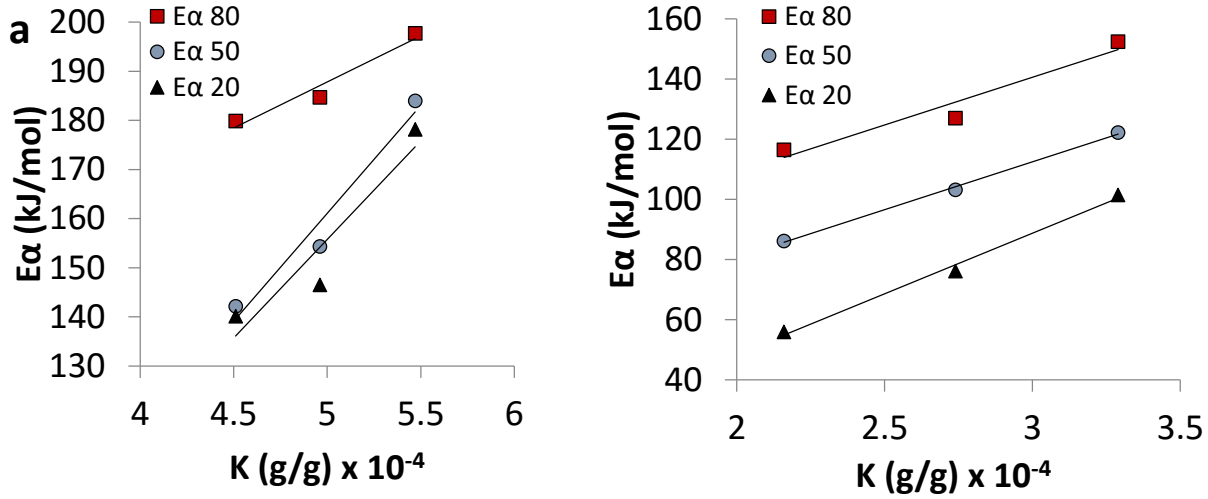

Figure 3.8. Relation between the constant K from SLE model and the estimated activation energy from the OFW model for asphaltenes thermo oxidation in presence of a) CS and b) CSNi1Pd1 nanoparticles. Degrees of conversion of the activation energy of 20 (■), 50 (●) and 80% (▲).

3.3 Partial conclusions

The impact of asphaltene self-association on the adsorption affinity and catalytic activity of CS and CSNi1Pd1 towards the adsorption of *n*-C_7 asphaltenes and their subsequent thermo-oxidative decomposition was investigated. The SLE model was used to fit the adsorption isotherms of

asphaltene from different solvents with different volume ratios of *n*-heptane/toluene. The results showed that the *H* parameter followed the trend of toluene > heptol 20 > heptol 40, indicating that the adsorption affinity increased as the amount of precipitant increased. It was also observed, according to the *K* parameter, that the asphaltene self-association over the adsorbent surface increased in the order heptol 40 > heptol 20 > toluene. In addition, TGA/FTIR tests were performed to investigate the effect of the asphaltene aggregate on the catalytic oxidation and the outcome of CO and CO_2 gases. These TGA/FTIR tests provided useful information and revealed that as the extent of asphaltene aggregation increased, the temperature of asphaltene oxidation increased. The results showed that nanoparticles portray different reaction mechanisms in the catalytic oxidation of asphaltenes and that the pathway followed is specific to the type of nanoparticle. It was observed that the temperature of asphaltene oxidation decreased in the order heptol 40 > heptol 20 > toluene, indicating that for larger aggregates, the catalytic activity of nanoparticles is reduced The OFW model was used to estimate the effective activation energies in the asphaltene oxidation process, and it was found that as the extent of asphaltene aggregate increased, higher E_α are needed. Finally, a correlation between the SLE parameters and the E_α from the OFW model was found. As the parameter *H* decreased, i.e., the affinity increases, the E_α increased. However, it was shown that the E_α greatly decreased as the degree of asphaltene self-association decreased.

3.4 References

1. Groenzin, H.; Mullins, O. C., Molecular Size and Structure of Asphaltenes from Various Sources. *Energy & Fuels* **2000,** 14, (3), 677-684.
2. Mullins, O. C., The Modified Yen Model†. *Energy & Fuels* **2010,** 24, (4), 2179-2207.
3. Mullins, O. C., The asphaltenes. *Annual Review of Analytical Chemistry* **2011,** 4, 393-418.
4. Montoya, T.; Coral, D.; Franco, C. A.; Nassar, N. N.; Cortés, F. B., A Novel Solid-Liquid Equilibrium Model for Describing the Adsorption of Associating Asphaltene Molecules onto Solid Surfaces Based on the "Chemical Theory". *Energy & Fuels* **2014**.
5. Rahmani, N. H.; Masliyah, J. H.; Dabros, T., Characterization of asphaltenes aggregation and fragmentation in a shear field. *AIChE journal* **2003,** 49, (7), 1645-1655.
6. Maqbool, T.; Balgoa, A. T.; Fogler, H. S., Revisiting asphaltene precipitation from crude oils: A case of neglected kinetic effects. *Energy & Fuels* **2009,** 23, (7), 3681-3686.
7. Asomaning, S., Test methods for determining asphaltene stability in crude oils. *Petroleum science and technology* **2003,** 21, (3-4), 581-590.
8. Oliensis, G. In *THE OLIENSIS SPOT TEST--WHAT JUSTIFICATION IS THERE FOR ITS USE?*, Association of Asphalt Paving Technologists Proceedings, 1935; 1935.
9. Mohammadi, M.; Akbari, M.; Fakhroueian, Z.; Bahramian, A.; Azin, R.; Arya, S., Inhibition of asphaltene precipitation by TiO2, SiO2, and ZrO2 nanofluids. *Energy & Fuels* **2011,** 25, (7), 3150-3156.
10. Flynn, J. H.; Wall, L. A., A quick, direct method for the determination of activation energy from thermogravimetric data. *Journal of Polymer Science Part B: Polymer Letters* **1966,** 4, (5), 323-328.
11. Ozawa, T., A new method of analyzing thermogravimetric data. *Bulletin of the chemical society of Japan* **1965,** 38, (11), 1881-1886.
12. Nassar, N.; Hassan, A.; Luna, G.; Pereira-Almao, P., Comparative study on thermal cracking of Athabasca bitumen. *Journal of Thermal Analysis and Calorimetry* **2013,** 114, (2), 465-472.
13. Tu, Y.; Kingston, D.; Kung, J.; Kotlyar, L. S.; Sparks, B. D.; Chung, K. H., Adsorption of pentane insoluble organic matter from oilsands bitumen onto clay surfaces. *Petroleum science and technology* **2006,** 24, (3-4), 327-338.

14. Pernyeszi, T.; Patzko, A.; Berkesi, O.; Dékány, I., Asphaltene adsorption on clays and crude oil reservoir rocks. *Colloids and Surfaces A: Physicochemical and Engineering Aspects* **1998,** 137, (1), 373-384.
15. Bennion, D. B., An overview of formation damage mechanisms causing a reduction in the productivity and injectivity of oil and gas producing formations. *Journal of Canadian Petroleum Technology* **2002,** 41, (11).
16. Alboudwarej, H.; Pole, D.; Svrcek, W. Y.; Yarranton, H. W., *Ind. Eng. Chem. Res.* **2005,** 44, 5585.
17. Nassar, N. N., Asphaltene Adsorption onto Alumina Nanoparticles: Kinetics and Thermodynamic Studies. *Energy & Fuels* **2010,** 24, (8), 4116-4122.
18. Dudášová, D.; Simon, S.; Hemmingsen, P. V.; Sjöblom, J., Study of asphaltenes adsorption onto different minerals and clays: Part 1. Experimental adsorption with UV depletion detection. *Colloids and Surfaces A: Physicochemical and Engineering Aspects* **2008,** 317, (1), 1-9.
19. Zahabi, A.; Gray, M. R.; Dabros, T., Heterogeneity of Asphaltene Deposits on Gold Surfaces in Organic Phase Using Atomic Force Microscopy. *Energy & Fuels* **2012,** 26, (5), 2891-2898.
20. Franco, C. A.; Nassar, N. N.; Ruiz, M. A.; Pereira-Almao, P.; Cortés, F. B., Nanoparticles for Inhibition of Asphaltenes Damage: Adsorption Study and Displacement Test on Porous Media. *Energy & Fuels* **2013,** 27, (6), 2899-2907.
21. Habib, F. K.; Diner, C.; Stryker, J. M.; Semagina, N.; Gray, M. R., Suppression of Addition Reactions during Thermal Cracking Using Hydrogen and Sulfided Iron Catalyst. *Energy & Fuels* **2013,** 27, (11), 6637-6645.
22. Sanford, E. C., Molecular approach to understanding residuum conversion. *Industrial & engineering chemistry research* **1994,** 33, (1), 109-117.
23. Gray, M. R.; McCaffrey, W. C., Role of chain reactions and olefin formation in cracking, hydroconversion, and coking of petroleum and bitumen fractions. *Energy & fuels* **2002,** 16, (3), 756-766.
24. Alshareef, A. H.; Scherer, A.; Tan, X.; Azyat, K.; Stryker, J. M.; Tykwinski, R. R.; Gray, M. R., Formation of archipelago structures during thermal cracking implicates a chemical mechanism for the formation of petroleum asphaltenes. *Energy & Fuels* **2011,** 25, (5), 2130-2136.
25. Guczi, L.; Beck, A.; Horvath, A.; Koppány, Z.; Stefler, G.; Frey, K.; Sajo, I.; Geszti, O.; Bazin, D.; Lynch, J., AuPd bimetallic nanoparticles on TiO 2: XRD, TEM, in situ EXAFS studies and catalytic activity in CO oxidation. *Journal of Molecular Catalysis A: Chemical* **2003,** 204, 545-552.
26. Nassar, N. N.; Hassan, A.; Pereira-Almao, P., Comparative oxidation of adsorbed asphaltenes onto transition metal oxide nanoparticles. *Colloids and Surfaces A: Physicochemical and Engineering Aspects* **2011,** 384, (1), 145-149.
27. Nassar, N. N.; Hassan, A.; Vitale, G., Comparing kinetics and mechanism of adsorption and thermo-oxidative decomposition of Athabasca asphaltenes onto TiO2, ZrO2, and CeO2 nanoparticles. *Applied Catalysis A: General* **2014,** 484, (0), 161-171.
28. Toulhoat, H.; Prayer, C.; Rouquet, G., Characterization by atomic force microscopy of adsorbed asphaltenes. *Colloids and Surfaces A: Physicochemical and Engineering Aspects* **1994,** 91, 267-283.

4. Effect of Resin I on *n*-C_7 asphaltene adsorption onto nanoparticles

Asphaltenes are typically considered a menace in the oil and gas industry for both down- and upstream processes.[1, 2] Because of the chemical nature and complex structure, asphaltenes can self-associate and form aggregates that lead to their precipitation/deposition on porous media and consequently lead to formation damage in the downstream process. Asphaltenes are also a concern for refiners because asphaltenes are significant constituents of the heavy oils that can impact a number of refinery processing streams.[3] Additionally, as asphaltenes are the most polar and surface-active fraction of crude oil,[4] they tend to adsorb over the reservoir formation surface,[5-7] and they may be deposited and accumulated at many places along the production system,[3, 8-10] leading to an increase in production costs and the need for additional treatments to mitigate or remediate these asphaltene-related problems.

It is well documented in the scientific literature[4, 11-13] that resins from crude oil play a significant role in the stability of asphaltenes as the resins can act as peptizing agents that prevent asphaltene-asphaltene interactions and hence the self-association and subsequent aggregation.[11, 13] Resins have intermediate polarity in comparison to asphaltenes, and the chemical structure of resins differs from the chemical structure of the asphaltenes mainly in the reduced aromatic species and the number or length of the alkyl chains, resulting in a higher H/C ratio.[4, 11] According to León et al.,[14] the stabilization of asphaltenes in the presence of resins is due to the help that resins give asphaltenes to diffuse in the oil matrix following four main steps, as follows: i) resins form a layer over the asphaltene aggregate surface, ii) resins penetrate the asphaltenes aggregate microporous structure, iii) resins break the asphaltene aggregate microporous structure and iv) the asphaltene-resin complex diffuses in the oil matrix. Pereira et al.[15] reported that the stability/instability of asphaltenes is directly related to the adsorption capacity of resins over the asphaltene surface. Poor resin-resin interactions with low adsorption on the asphaltene surface favor the asphaltene stabilization with resins acting as peptizing agents. However, higher resin-resin interactions lead to the formation of a "thick and sticky" layer over the asphaltene surface that promotes flocculation.[15] Several studies have focused on the effect of resins on the asphaltene adsorption over large-grain solid surfaces.[16-20] However, none of these studies reported on the adsorption isotherms by family (i.e., asphaltenes and resins). The authors simply reported the interactions of asphaltenes and resins on surfaces like bulk isotherms, but not specifically for resins I and asphaltenes.[21-23] In the adsorbed phase, the asphaltene-asphaltene interactions have been reported to be more important than the interactions of asphaltenes and resins, and resins have been reported to have a "less facile" adsorption than asphaltenes.[4, 16, 19]

Recently, nanoparticles have become of especial interest in the oil industry due to their capacity to adsorb asphaltenes and enhance their stability for the inhibition of formation damage[24-27] and enhanced oil upgrading and recovery applications.[28-36] However, to date, there are no adsorption studies reported in the literature that account for the competitive adsorption of resins and asphaltenes over nanoparticles. Only Nassar et al.[21, 37] indirectly studied the effect of resins on the adsorption of

asphaltenes by evaluating the effect of the maltene fraction of crude oil on the asphaltene adsorption onto γ-alumina nanoparticles[21] and by comparing the adsorption of more resinous asphaltenes such as *n*-C_5 asphaltenes with the adsorption of *n*-C_7 asphaltenes over NiO nanoparticles.[41] Nassar[21] found that the amount adsorbed decreased in the order asphaltenes > bitumen > maltenes, indicating that the coexisting molecules impact the adsorption process of asphaltenes due to changes in the asphaltene arrangement in the adsorbed and bulk phases. In addition, Nassar et al. [41] found that *n*-C_5 asphaltenes were less prone to adsorb over the NiO nanoparticle surface than *n*-C_7 asphaltenes because resins affect the colloidal behavior of asphaltenes and hence, the adsorbate-adsorbent interactions.

Therefore, this chapter aims at explore the respective adsorption isotherms of *n*-C_7 asphaltenes and resins I to provide a better understanding of the effect of the resins on the adsorption of asphaltenes. The adsorption experiments were conducted in the batch mode at different *n*-C_7 asphaltene to resin I ratios (A:R) of 7:3, 1:1 and 3:7 and different concentrations of the asphaltene-resin mixture from 500 to 5000 mg/L. The comparative adsorption studies outlined here were validated and supported by the solid-liquid equilibrium (SLE)[38] isotherm model. Results and discussion are divided into two sections, namely: i) adsorption isotherms of *n*-C_7 asphaltenes and resins I over nanoparticles constructed separately for each compound, and ii) the evaluation of the competitive adsorption between *n*-C_7 asphaltenes and resins I for different mixtures of A:R ratios.

4.1 Experimental

4.1.1 Nanoparticles, asphaltenes and resins

CS nanoparticles were used as adsorbents for this study. Full nanoparticles characterization can be found in Chapter 1. AK9 EHO (See Chapter 2) was used as a source of *n*-C_7 asphaltenes and resins I. The EHO was mixed with *n*-heptane (99%, Sigma-Aldrich) in a ratio of 1 g per each 40 mL of precipitant,[28] sonicated for 2 h and then magnetically stirred for 20 h at 200 rpm. Further, the mixture was centrifuged for 45 min at 4500 rpm using a Z 306 Hermle Universal Centrifuge (Labnet, NJ). Petroleum resins can be divided into resins I and II, the former being more prone to interact with the asphaltenes.[39] In this order, resins II were discarded with the supernatant or deasphalted oil while the precipitate was placed in the chamber of a Soxhlet setup and washed with *n*-heptane for 72 h. Solid *n*-C_7 asphaltenes were obtained from the Soxhlet chamber, and resins I were extracted by distillation from the Soxhlet liquid.[40]

4.1.2 Adsorption experiments

Batch-mode adsorption experiments were conducted at a temperature of 25°C. Adsorption isotherms were constructed for *n*-C_7 asphaltenes (A) and resins I (R) individually and collectively at different A:R weight ratios of 7:3, 1:1 and 3:7. The *n*-C_7 asphaltenes in toluene, resins I in toluene and mixtures of *n*-C_7 asphaltenes + resins I in toluene solutions were prepared at different concentrations from 100 to 5000 mg/L. In the adsorption process, a fixed amount of 100 mg of nanoparticles per each 10 mL of solution was added to the oil model solutions and magnetically stirred for 24 h to ensure the maximum adsorption of *n*-C_7 asphaltenes and/or resins I over the nanoparticle surface. Further, nanoparticles with adsorbed *n*-C_7 asphaltenes and/or resin I were separated from the solution by centrifugation at 4000 rpm for 30 min to guarantee the maximum recovery of nanoparticles.

The competitive adsorption of *n* species over a solid surface is expected to be addressed by *n* degrees of freedom, i.e., following *n* or more measurements.[41] Hence, in this work, $n = 2$ regarding the *n*-C_7

asphaltenes and resins I and the degrees of freedom were satisfied through thermogravimetric analyses (TGA) and softening point (SP) measurements. The amount of *n*-C_7 asphaltenes and/or resin I adsorbed was determined using combined information from the adsorbates in the bulk and the adsorbed phases after adsorption. The amount of *n*-C_7 asphaltenes and/or resin I in the adsorbed phase was measured by TGA using a Q50 thermogravimetric analyzer (TA Instruments, Inc., New Castle, DE). For this purpose, 10.0 ± 0.5 mg of sample (virgin nanoparticles and nanoparticles with *n*-C_7 asphaltenes and/or resin I adsorbed) were placed in a platinum pan and heated in an air atmosphere from 100 to 800°C at a heating rate of 10°C/min. The air flow was fixed at 100 mL/min. The amount of adsorbate on the nanoparticles surface was determined by differences in the mass loss between the virgin nanoparticles and nanoparticles with the adsorbed species. TGA experiments were performed in duplicate.

The *n*-C_7 asphaltenes and/or resins I in the bulk phase were determined by SP measurements that allow the estimation of the wt% of *n*-C_7 asphaltenes and/or resins I in the sample. SP experiments were developed following the ASTM E28-14 method.[42] A calibration curve of laboratory-made mixtures of *n*-C_7 asphaltenes + resins I against SP was constructed for this purpose. Figure 4.1 shows the calibration curve obtained. Hence, after separating the nanoparticles from the solution, the supernatant was recovered, the solvent was evaporated and the SP of the solid obtained was determined.

Finally, knowing the wt% of adsorbate in the adsorbed phase and the respective wt% of *n*-C_7 asphaltenes and resins I in the bulk phase, a mass balance is applied and the amount of *n*-C_7 asphaltenes and resins I adsorbed can be determined. For the individual adsorption of *n*-C_7 asphaltenes and resins I on nanoparticles, the amount adsorbed was determined using TGA only, and results were consistent with the results obtained with the commonly used UV-vis technique.[21, 28]

Valuable information about adsorbate-adsorbate and adsorbate-adsorbent interactions can be obtained from the SLE model.[38] Hence, the SLE model was used for describing the adsorption isotherms of *n*-C_7 asphaltenes and resins I .SLE model equation and details can be found in Chapter 2.

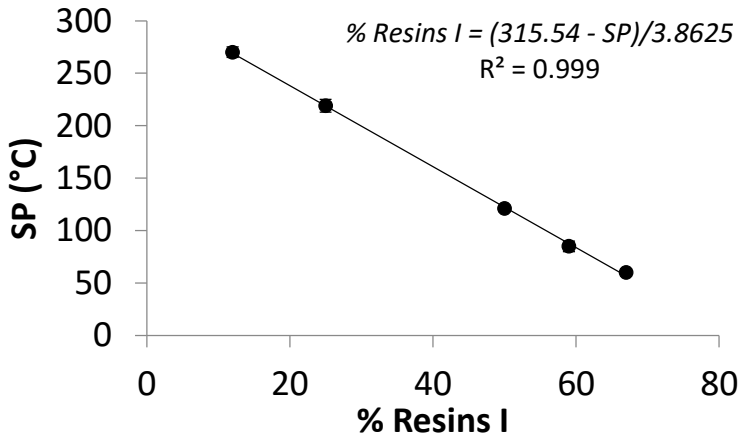

Figure 4.1. Softening point calibration curve.

4.2 Results and discussions

4.2.1 Individual adsorption of *n*-C_7 asphaltenes and resins I

Figure 4.2 shows the individual experimental adsorption isotherms data together with the fit of the SLE model for *n*-C_7 asphaltenes and resins I over CS nanoparticles at 25°C. However, the adsorption isotherms for resins I over CS nanoparticles followed a Type III behavior according to the IUPAC,[43] indicative of a low affinity between the adsorbent–adsorbate leading to multilayer adsorption.[41, 44, 45] This multilayer adsorption is confirmed by the values of the SLE parameters presented in Table 4.1. There is good agreement between the SLE model and the experimental results according to the R^2 and *RSME%* values. Table 4.1 shows that the *H* parameter is higher for the adsorption of resins I than for *n*-C_7 asphaltenes, indicating that the interaction between *n*-C_7 asphaltenes–CS nanoparticles is higher than resins I–CS nanoparticles and that *n*-C_7 asphaltenes are more prone to be in the adsorbed phase than in the bulk phase.[38] Hence, we can infer that the CS nanoparticles are more selective for adsorption of *n*-C_7 asphaltenes than resins I. The *K* parameter is several orders of magnitude greater for resins I than for *n*-C_7 asphaltenes. Although the resin–resin interaction in the bulk phase is low (almost inconsequential),[11, 12] once adsorbed the polar character of the resins may lead to their self-association around the active sites of the adsorbent surface, suggesting that the resin– resin interaction over the solid surface is not negligible and leads to the formation of multilayers.

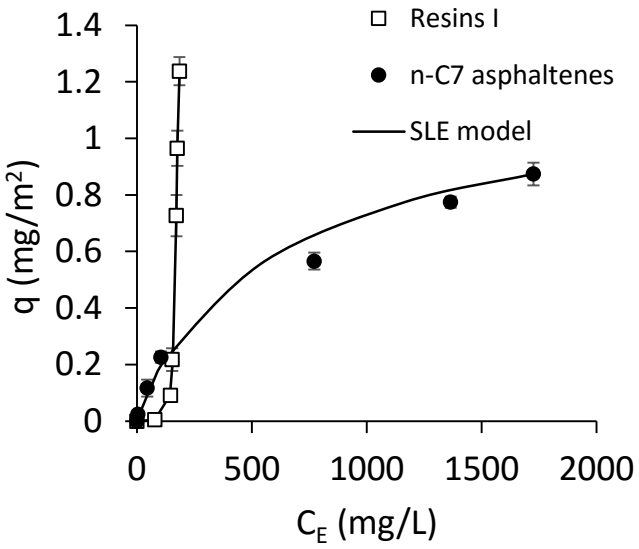

Figure 4.2. Adsorption isotherms of *n*-C_7 asphaltenes and resins I over CS nanoparticles at 25°C constructed separately for each component.

Table 4.1. SLE model estimated parameters for the adsorption of *n*-C_7 asphaltenes and resins I from different A:R ratios.

A:R ratio	*n*-C_7 asphaltenes					Resins I				
	H ***(mg/g)***	***K*** ***(g/g)***	q_m ***(mg/m²)***	R^2	***RSME%***	***H*** ***(mg/g)***	***K*** ***(g/g)***	q_m ***(mg/m²)***	R^2	***RSME%***
Individual components	0.99	4.46×10^{-4}	0.47	0.99	6.69	126.70	637.77	2.01	0.99	2.13
7:3	2.48	4.78×10^{-4}	2.55	0.99	6.42	2.90	4.02×10^{-5}	0.13	0.97	7.14
1:1	10.24	9.98×10^{-4}	392.18	0.99	5.30	21.94	0.10	0.21	0.98	8.82
3:1	18.18	9.29×10^{-4}	378.78	0.99	3.41	41.82	11.31	0.81	0.99	4.13

4.2.2 Competitive adsorption between *n*-C_7 asphaltenes and resins I asphaltenes and resins I

Adsorption isotherms of *n*-C_7 asphaltenes and resins I were constructed simultaneously at different A:R values of 7:3, 1:1 and 3:7 at 25°C. Panels a and b of Figure 4.3 show the experimental adsorption isotherms obtained together with the fit of the SLE model for the competitive adsorption of a) *n*-C_7 asphaltenes and b) resins I over the CS nanoparticles surface. Figure 4.3a shows that the amount of *n*-C_7 asphaltenes adsorbed over the nanoparticle surface decreased as the amount of resins I in the bulk phase increased. For comparison, at C_E = 160 mg/L, the amount of asphaltenes adsorbed decreased from 0.25 mg/m^2 for the *n*-C_7 asphaltenes in absence of resins I to 0.18, 0.08 and 0.03 mg/m^2 for the A:R ratios of 7:3, 1:1 and 3:7, respectively. This decrease could be explained by two main reasons: i) resins I affect the colloidal state of the *n*-C_7 asphaltenes in the bulk phase,[14, 37, 46, 47] resulting in an interrupted colloidal structure of the *n*-C_7 asphaltene molecules and their subsequent adsorption behavior to the adsorbent surface; and ii) the reduction of the number of surface active sites available for adsorption due to the resins I adsorption. For the adsorption of *n*-C_7 asphaltenes for an A:R ratio of 7:3, the shape of the adsorption isotherms follows a clear Type I behavior similar to *n*-C_7 asphaltenes in the absence of resins I, indicating that at a higher amount of *n*-C_7 asphaltenes than resins I in the system, the diminution in the amount adsorbed could be more closely associated with the restrictions in the diffusion from the bulk phase to the S nanoparticles surface. The colloidal state of asphaltenes in the presence of resins changes due to a micelle-type formation of a polar asphaltene core surrounded by resins,[46] peptization[14] or the termination of the asphaltene self-association due to the presence of resins that may act as terminator molecules.[47] When asphaltenes and resins coexist, the interaction asphaltene–resins is more likely to occur than asphaltene–asphaltene or resins–resin interactions.[12] Results are in agreement with those reported by Nassar et al.[37] on the adsorption of *n*-C_5 and *n*-C_7 asphaltenes over NiO nanoparticles. The authors found that although both adsorption isotherms followed a Type I behavior, the adsorption capacity was lower for the more resinous *n*-C_5 asphaltenes than for *n*-C_7 asphaltenes. However, Figure 4.3a shows that for A:R ratios of 1:1 and 3:7, the shape of the adsorption isotherms has a somewhat linear trend, suggesting that the adsorption of *n*-C_7 asphaltenes can be restricted due to the resins I occupation of the active sites and also that the adsorption may occur in a multilayer form. Experimental results were also supported by the SLE parameters obtained (Table 4.1). As Table 4.1 shows, the *H* parameter increased as the amount of resins I in the system increased, i.e., the preference of the asphaltenes for being in the adsorbed phase becomes reduced. With regard to the degree of *n*-C_7

asphaltene self-association over the nanoparticle surface, the *K* parameter is higher for the individual adsorption of *n*-C_7 asphaltenes than for the adsorption of *n*-C_7 asphaltenes with an A:R ratio of 7:3, indicating that the asphaltene-asphaltene interactions become reduced by the presence of resins I on the CS nanoparticle surface. However, a critical ratio of A:R seems to exist, where the asphaltene-asphaltene and/or asphaltene-resin interactions become important to form multilayer adsorption as observed with the increased values of the *K* parameter after the A:R ratio of 1:1. Asphaltene-resin interactions over the adsorbent surface could be a key parameter for the formation of multilayers as long as the asphaltene-resin interactions are supposed to be greater than resins-resin interactions.

Figure 4.3b shows the adsorption isotherms of resins I onto CS nanoparticles for different A:R ratios at 25°C. The shape of the adsorption isotherms is observed to change drastically from a Type III behavior for the system without *n*-C_7 asphaltenes to Type I and Type II isotherms for A:R ratios of 7:3 and 1:1, respectively, possibly because the affinity of the resins I for being in the adsorbed phase is also influenced by the presence of asphaltenes and is supported by the *H* values of the SLE model that decreased drastically for the adsorption of resins I in presence of *n*-C_7 asphaltenes in comparison to the adsorption of the resins I in the absence of *n*-C_7 asphaltenes. However, as the amount of resins I in the system increased, the adsorption affinity decreased, and the trend to form multilayers was favored. This trend to form multilayers is also supported by the *K* parameter that increased for the systems in the presence of *n*-C_7 asphaltenes in the order 7:3 > 1:1 > 3:7.

Nevertheless, when comparing adsorption isotherms from Figure 4.3a with those of Figure 4.3b for the systems with the presence of both *n*-C_7 asphaltenes and resins I at the different A:R ratios evaluated, the amount adsorbed is always higher for *n*-C_7 asphaltenes than for resins I, indicating that the CS nanoparticles can be used effectively in the design of special treatments that aim to select *n*-C_7 asphaltenes instead of resins I.

4.2.3 Prediction of the amount of *n*-C_7 asphaltenes adsorbed

For a better understanding of the role of resins I in the adsorption of *n*-C_7 asphaltenes over CS nanoparticles, the adsorbed amount of individual *n*-C_7 asphaltenes and *n*-C_7 asphaltenes in the presence of resins I for A:R ratios of 7:3 and 1:1 was predicted from the amount of *n*-C_7 asphaltenes adsorbed at an A:R ratio of 3:7. If resins I affect the colloidal state of *n*-C_7 asphaltenes in the bulk solution at different degrees according to the amount of resins I in the system, the adsorption of *n*-C_7 asphaltenes would be affected in different degrees accordingly to the A:R ratio evaluated. Nevertheless, if resins I similarly affect the colloidal state of *n*-C_7 asphaltenes, independent of the amount of resins in the system, the adsorption of *n*-C_7 asphaltenes would be similar for all of the A:R ratios evaluated and controlled by the *n*-C_7 asphaltene concentration and the occupation of the respective nanoparticle active sites by resins I.
Prediction of the amount of *n*-C_7 asphaltenes adsorbed was performed, assuming that at a fixed A:R ratio, the amount of *n*-C_7 asphaltenes adsorbed would correspond to a fraction of the amount of individual *n*-C_7 asphaltenes adsorbed and vice versa. For instance, the amount of *n*-C_7 asphaltenes adsorbed at an A:R ratio of 3:7 would correspond to 30% of the amount adsorbed of individual *n*-C_7 asphaltenes. A good prediction is expected to result in a linear plot of the amount adsorbed predicted ($q_{predicted}$) against the experimentally observed amount adsorbed ($q_{experimental}$). If the $q_{predicted}$ agrees with $q_{experimental}$, it would imply that the slope (m) and the intercept (b) of the equation of a straight line (Eq. 4.1) should be equal to 1.0 and 0.0, respectively, with a linear correlation coefficient R^2 = 1.0.

$$q_{predicted} = m \cdot q_{experimental} + b \tag{4.1}$$

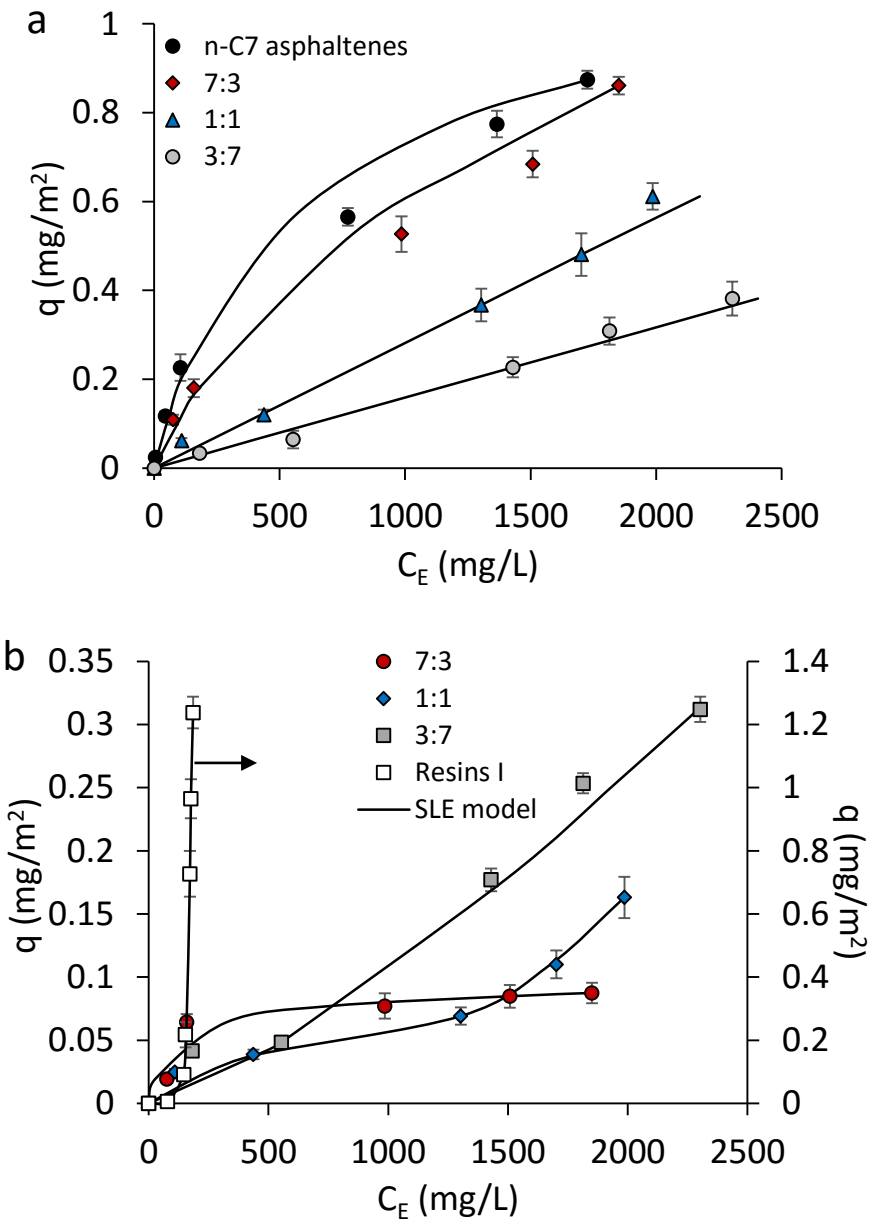

Figure 4.3. Adsorption isotherms of a) *n*-C_7 asphaltenes and b) resins I over CS nanoparticles at 25°C constructed simultaneously for different *n*-C_7 asphaltenes to resins I ratios of 7:3, 1:1 and 3:7.

Figure 4.4 shows the $q_{predicted}$ against $q_{experimental}$ linear plots for the prediction of the amount of *n*-C_7 asphaltenes adsorbed over CS nanoparticles in absence of resins I and for the different A:R ratios. Additionally, Table 4.2 shows the estimated slope and intercept of the straight-line equation associated with the respective equation of a straight line together with the corresponding values of R^2 and *RSME%*. As Figure 4.4 shows, there is an excellent prediction of the amount adsorbed for the

systems with A:R ratios of 7:3 and 1:1. Additionally, Table 4.2 shows that the values for *m* and *b* are less than the 6% expected for a perfect prediction. Results suggest that the colloidal state of the *n*-C_7 asphaltenes is affected to similar degrees independent of the amount of resins I in the system. Hence, the reduction of the amount of *n*-C_7 asphaltenes in the presence of resins I would be more controlled by the concentration of *n*-C_7 asphaltenes in the system and the ability of resins I to occupy the active sites on the adsorbent surface.

Figure 4.4 and Table 4.2 show that prediction of the amount of individual *n*-C_7 asphaltenes adsorbed over CS nanoparticles was not successful over the whole range of $q_{experimental}$ evaluated. In this order, the plot of $q_{predicted}$ versus $q_{experimental}$ was divided in two sections, namely: i) C_i < 3000 mg/L, and ii) $C_i \geq$ 3000 mg/L. For the section with C_i < 3000 mg/L, the amount adsorbed was successfully predicted with values of *m* and *b* close to the expected values for a perfect prediction and with R^2 and *RSME%* value of 0.98, respectively. However, for the section with $C_i \geq 3000$ mg/L, the values of $q_{predicted}$ differ from those of $q_{experimental}$ by more than 25%, corroborated by the large values *m* and *b*.

For the case of 1:1 over CS nanoparticles at 25°C, prediction was made from adsorption at an A:R ratio of 3:7. The results indicate that for $C_i \geq 3000$ mg/L, the colloidal state of the *n*-C_7 asphaltenes in the absence of resins I varies significantly from the colloidal state in the presence of resins I and implies that the way *n*-C_7 asphaltenes diffuse from the bulk phase to the adsorbent surface indeed changes due to the presence of resins I in the system. However, for C_i < 3000 mg/L, the colloidal state of the *n*-C_7 asphaltenes does not change drastically and hence, resins I will not considerably affect the way the *n*-C_7 asphaltenes diffuse through the oil matrix. According to Mullins,[48, 49] as of 2010, it was well accepted that the concentration of asphaltene cluster formation is between 2000 and 5000 mg/L, suggesting that in the case of C_i close to 3000 mg/L, the cluster formation would occur to different degrees in the presence and the absence of resins I, which would directly affect the adsorption over the CS nanoparticles.

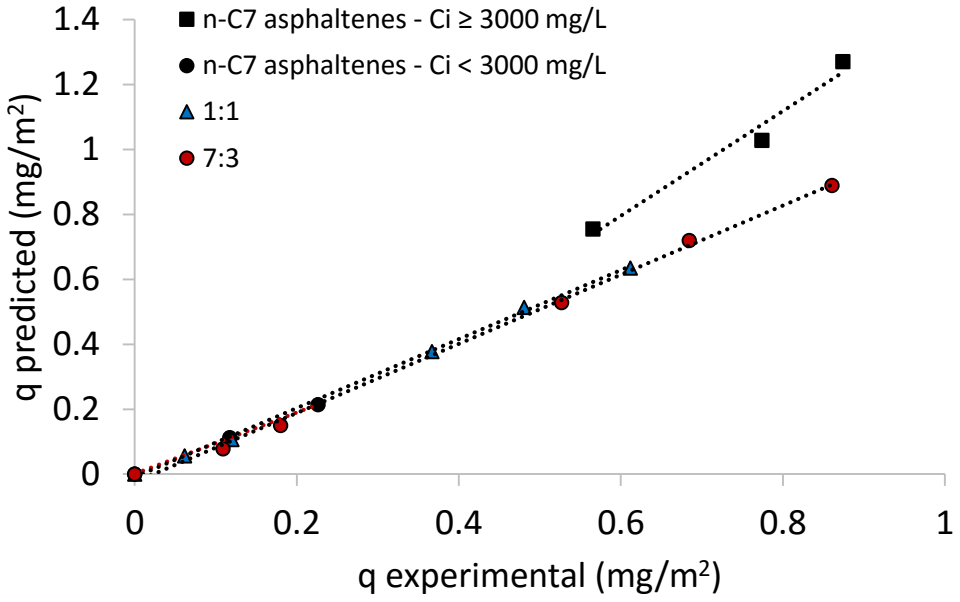

Figure 4. $q_{predicted}$ against $q_{experimental}$ linear plots for the individual adsorption of *n*-C_7 asphaltenes and *n*-C_7 asphaltenes in presence of resins I and for different A:R ratios.

Table 2. Estimated slope and intercept of the $q_{predicted}$ against $q_{experimental}$ linear plots for the prediction of the amount of n-C_7 asphaltenes adsorbed in the absence and the presence of resins I

Material	A:R ratio		*m*	*b*	R^2	*RSME%*
S	Individual *n*-C_7 asphaltenes	C_i < 3000 mg/L	0.94	0.0238	0.99	0.98
		$C_i \geq$ 3000 mg/L	1.61	-0.1728	0.97	11.24
	7:3		1.05	-0.0006	0.99	4.11
	1:1		0.94	0.0084	0.99	2.88

4.3 Partial conclusions

The competitive adsorption of *n*-C_7 asphaltenes and resins I on CS nanoparticles was described successfully through the simultaneous construction of the respective adsorption isotherms at 25°C. The amounts of *n*-C_7 asphaltenes and resins I adsorbed were obtained through a novel method based on TGA and SP measurements. Results showed that although the amount of *n*-C_7 asphaltenes adsorbed becomes reduced as the amount of resins I in the system increase, the adsorption is always higher for *n*-C_7 asphaltenes than for resins I for the different asphaltene to resin ratios evaluated. Adsorption isotherms were successfully described by the SLE model.

In addition, following a simple rule of three, the amount of *n*-C_7 asphaltenes adsorbed in presence of resins I was predicted successfully from the known amount of *n*-C_7 asphaltenes adsorbed at a defined A:R ratio, which discard any specific interactions between asphaltenes and resins either in the bulk at the surface. Results also suggest that CS nanoparticles are promising for the treatment of asphaltene-related problems. For the different *n*-C_7 asphaltene to resins I ratios employed, the nanoparticles were always more selective to adsorb asphaltenes than resins I. However, for high amounts of resins in the system, it is recommended the design of a more *n*-C_7 asphaltene-selective nanoparticle that enhances the *n*-C_7 asphaltene adsorption.

4.4 References

1. Franco, C. A.; Nassar, N. N.; Ruiz, M. A.; Pereira-Almao, P.; Cortés, F. B., Nanoparticles for inhibition of asphaltenes damage: adsorption study and displacement test on porous media. *Energy & Fuels* **2013,** 27, (6), 2899-2907.

2. Kokal, S. L.; Sayegh, S. G. In *Asphaltenes: The cholesterol of petroleum*, Middle East Oil Show, 1995; Society of Petroleum Engineers: 1995.

3. Akbarzadeh, K.; Hammami, A.; Kharrat, A.; Zhang, D.; Allenson, S.; Creek, J.; Kabir, S.; Jamaluddin, A.; Marshall, A. G.; Rodgers, R. P., Asphaltenes—problematic but rich in potential. *Oilfield Review* **2007,** 19, (2), 22-43.

4. Adams, J. J., Asphaltene Adsorption, a Literature Review. *Energy & Fuels* **2014,** 28, (5), 2831-2856.

5. de la Cruz, J. L. M.; Castellanos-Ramírez, I. V.; Ortiz-Tapia, A.; Buenrostro-González, E.; Durán-Valencia, C. d. l. A.; López-Ramírez, S., Study of monolayer to multilayer adsorption of asphaltenes on reservoir rock minerals. *Colloids and Surfaces A: Physicochemical and Engineering Aspects* **2009,** 340, (1), 149-154.

6. Piro, G.; Canonico, L. B.; Galbariggi, G.; Bertero, L.; Carniani, C., Asphaltene adsorption onto formation rock: An approach to asphaltene formation damage prevention. *SPE Production & Facilities* **1996,** 11, (03), 156-160.
7. Jienian, Y.; Plancher, H.; Morrow, N., Wettability changes induced by adsorption of asphaltenes. *Oceanographic Literature Review* **1998,** 3, (45), 587-588.
8. Leontaritis, K.; Mansoori, G. In *Asphaltene flocculation during oil production and processing: A thermodynamic collodial model*, SPE International Symposium on Oilfield Chemistry, 1987; Society of Petroleum Engineers: 1987.
9. Alboudwarej, H.; Pole, D.; Svrcek, W. Y.; Yarranton, H. W., Adsorption of asphaltenes on metals. *Industrial & engineering chemistry research* **2005,** 44, (15), 5585-5592.
10. Gawel, I.; Bociarska, D.; Biskupski, P., Effect of asphaltenes on hydroprocessing of heavy oils and residua. *Applied Catalysis A: General* **2005,** 295, (1), 89-94.
11. Speight, J., Petroleum Asphaltenes-Part 1: Asphaltenes, resins and the structure of petroleum. *Oil & gas science and technology* **2004,** 59, (5), 467-477.
12. Andersen, S. I.; Speight, J. G., Petroleum resins: separation, character, and role in petroleum. *Petroleum science and technology* **2001,** 19, (1-2), 1-34.
13. Murgich, J.; Rodríguez, J.; Aray, Y., Molecular recognition and molecular mechanics of micelles of some model asphaltenes and resins. *Energy & Fuels* **1996,** 10, (1), 68-76.
14. León, O.; Contreras, E.; Rogel, E.; Dambakli, G.; Acevedo, S.; Carbognani, L.; Espidel, J., Adsorption of native resins on asphaltene particles: a correlation between adsorption and activity. *Langmuir* **2002,** 18, (13), 5106-5112.
15. Pereira, J. C.; López, I.; Salas, R.; Silva, F.; Fernández, C.; Urbina, C.; López, J. C., Resins: the molecules responsible for the stability/instability phenomena of asphaltenes. *Energy & fuels* **2007,** 21, (3), 1317-1321.
16. TU, Y.; WOODS, J.; KUNG, J.; MCCRACKEN, T.; KOTLYAR, L.; SPARKS, B.; DONG, M., Adsorption of SARA Fractions from Heavy Oil and Bitumen on Kaolinite. *Clay Science* **2006,** 12, (Supplement2), 183-187.
17. Acevedo, S.; Castillo, J.; Fernández, A.; Goncalves, S.; Ranaudo, M. A., A study of multilayer adsorption of asphaltenes on glass surfaces by photothermal surface deformation. Relation of this adsorption to aggregate formation in solution. *Energy & fuels* **1998,** 12, (2), 386-390.
18. Czarnecka, E.; Gillott, J., Formation and characterization of clay complexes with bitumen from Athabasca oil sand. *Clays and Clay minerals* **1980,** 28, (3), 197-203.
19. Acevedo, S.; Ranaudo, M. A.; Escobar, G.; Gutiérrez, L.; Ortega, P., Adsorption of asphaltenes and resins on organic and inorganic substrates and their correlation with precipitation problems in production well tubing. *Fuel* **1995,** 74, (4), 595-598.
20. Zahabi, A.; Gray, M. R.; Dabros, T., Kinetics and properties of asphaltene adsorption on surfaces. *Energy & Fuels* **2012,** 26, (2), 1009-1018.
21. Nassar, N. N., Asphaltene Adsorption onto Alumina Nanoparticles: Kinetics and Thermodynamic Studies. *Energy & Fuels* **2010,** 24, (8), 4116-4122.
22. Hannisdal, A.; Ese, M.-H.; Hemmingsen, P. V.; Sjöblom, J., Particle-stabilized emulsions: effect of heavy crude oil components pre-adsorbed onto stabilizing solids. *Colloids and Surfaces A: Physicochemical and Engineering Aspects* **2006,** 276, (1), 45-58.
23. Labrador, H.; Fernández, Y.; Tovar, J.; Munoz, R.; Pereira, J. C., Ellipsometry study of the adsorption of asphaltene films on a glass surface. *Energy & fuels* **2007,** 21, (3), 1226-1230.
24. Zabala, R.; Mora, E.; Botero, O.; Cespedes, C.; Guarin, L.; Franco, C.; Cortes, F.; Patino, J.; Ospina, N. In *Nano-Technology for Asphaltenes Inhibition in Cupiagua South Wells*, IPTC 2014: International Petroleum Technology Conference, 2014; 2014.
25. Mohammadi, M.; Akbari, M.; Fakhroueian, Z.; Bahramian, A.; Azin, R.; Arya, S., Inhibition of asphaltene precipitation by TiO2, SiO2, and ZrO2 nanofluids. *Energy & Fuels* **2011,** 25, (7), 3150-3156.

26. Hashemi, S. I.; Fazelabdolabadi, B.; Moradi, S.; Rashidi, A. M.; Shahrabadi, A.; Bagherzadeh, H., On the application of NiO nanoparticles to mitigate in situ asphaltene deposition in carbonate porous matrix. *Applied Nanoscience* **2015**, 1-11.
27. Kazemzadeh, Y.; Malayeri, M.; Riazi, M.; Parsaei, R., Impact of Fe 3 O 4 nanoparticles on asphaltene precipitation during CO 2 injection. *Journal of Natural Gas Science and Engineering* **2015,** 22, 227-234.
28. Franco, C.; Patiño, E.; Benjumea, P.; Ruiz, M. A.; Cortés, F. B., Kinetic and thermodynamic equilibrium of asphaltenes sorption onto nanoparticles of nickel oxide supported on nanoparticulated alumina. *Fuel* **2013,** 105, 408-414.
29. Nassar, N. N.; Hassan, A.; Vitale, G., Comparing kinetics and mechanism of adsorption and thermo-oxidative decomposition of Athabasca asphaltenes onto TiO 2, ZrO 2, and CeO 2 nanoparticles. *Applied Catalysis A: General* **2014,** 484, 161-171.
30. Nassar, N. N.; Hassan, A.; Pereira-Almao, P., Application of nanotechnology for heavy oil upgrading: Catalytic steam gasification/cracking of asphaltenes. *Energy & Fuels* **2011,** 25, (4), 1566-1570.
31. Nassar, N. N.; Hassan, A.; Carbognani, L.; Lopez-Linares, F.; Pereira-Almao, P., Iron oxide nanoparticles for rapid adsorption and enhanced catalytic oxidation of thermally cracked asphaltenes. *Fuel* **2012,** 95, 257-262.
32. Hashemi, R.; Nassar, N. N.; Pereira-Almao, P., Transport behavior of multimetallic ultradispersed nanoparticles in an oil-sands-packed bed column at a high temperature and pressure. *Energy & Fuels* **2012,** 26, (3), 1645-1655.
33. Hashemi, R.; Nassar, N. N.; Pereira Almao, P., In situ upgrading of athabasca bitumen using multimetallic ultradispersed nanocatalysts in an oil sands packed-bed column: Part 2. Solid analysis and gaseous product distribution. *Energy & Fuels* **2014,** 28, (2), 1351-1361.
34. Hashemi, R.; Nassar, N. N.; Pereira Almao, P., Enhanced heavy oil recovery by in situ prepared ultradispersed multimetallic nanoparticles: A study of hot fluid flooding for Athabasca bitumen recovery. *Energy & Fuels* **2013,** 27, (4), 2194-2201.
35. Hashemi, R.; Nassar, N. N.; Pereira Almao, P., In situ upgrading of athabasca bitumen using multimetallic ultradispersed nanocatalysts in an oil sands packed-bed column: Part 1. Produced liquid quality enhancement. *Energy & Fuels* **2013,** 28, (2), 1338-1350.
36. Hashemi, R.; Nassar, N. N.; Almao, P. P., Nanoparticle technology for heavy oil in-situ upgrading and recovery enhancement: Opportunities and challenges. *Applied Energy* **2014,** 133, 374-387.
37. Nassar, N. N.; Hassan, A.; Pereira-Almao, P., Metal oxide nanoparticles for asphaltene adsorption and oxidation. *Energy & Fuels* **2011,** 25, (3), 1017-1023.
38. Montoya, T.; Coral, D.; Franco, C. A.; Nassar, N. N.; Cortés, F. B., A Novel Solid–Liquid Equilibrium Model for Describing the Adsorption of Associating Asphaltene Molecules onto Solid Surfaces Based on the "Chemical Theory". *Energy & Fuels* **2014,** 28, (8), 4963-4975.
39. Navarro, L.; Álvarez, M.; Grosso, J.-L.; Navarro, U., Separación y caracterización de resinas y asfaltenos provenientes del crudo Castilla. Evaluación de su interacción molecular. *CT&F-Ciencia, Tecnología y Futuro* **2004,** 2, (5), 53-67.
40. Carnahan, N. F.; Salager, J.-L.; Antón, R.; Dávila, A., Properties of resins extracted from Boscan crude oil and their effect on the stability of asphaltenes in Boscan and Hamaca crude oils. *Energy & Fuels* **1999,** 13, (2), 309-314.
41. Franco, C. A.; Nassar, N. N.; Cortés, F. B., Removal of oil from oil-in-saltwater emulsions by adsorption onto nano-alumina functionalized with petroleum vacuum residue. *Journal of colloid and interface science* **2014,** 433, 58-67.
42. ASTM E28-14, Standard Test Methods for Softening Point of Resins Derived from Pine Chemicals and Hydrocarbons, by Ring-and-Ball Apparatus. *ASTM International, West Conshohocken, PA* **2014**.

43. Ssing, K.; Everett, D.; Haul, R.; Moscou, L.; Pierotti, R.; Rouquerol, J.; Siemieniewsks, T., Reporting physisorption data for gas/solid system. *Pure and Applied Chemistry* **1985,** 57, (4), 603-619.
44. Franco, C. A.; Cortés, F. B.; Nassar, N. N., Adsorptive removal of oil spill from oil-in-fresh water emulsions by hydrophobic alumina nanoparticles functionalized with petroleum vacuum residue. *Journal of colloid and interface science* **2014,** 425, 168-177.
45. Franco, C. A.; Martínez, M.; Benjumea, P.; Patiño, E.; Cortés, F. B., Water Remediation Based on Oil Adsorption Using Nanosilicates Functionalized with a Petroleum Vacuum Residue. *Adsorption Science & Technology* **2014,** 32, (2), 197-208.
46. Mullins, O. C.; Sheu, E. Y.; Hammami, A.; Marshall, A. G., *Asphaltenes, heavy oils, and petroleomics*. Springer Science & Business Media: 2007.
47. Gray, M. R.; Tykwinski, R. R.; Stryker, J. M.; Tan, X., Supramolecular assembly model for aggregation of petroleum asphaltenes. *Energy & Fuels* **2011,** 25, (7), 3125-3134.
48. Mullins, O. C., The Modified Yen Model†. *Energy & Fuels* **2010,** 24, (4), 2179-2207.
49. Mullins, O. C., The asphaltenes. *Annual Review of Analytical Chemistry* **2011,** 4, 393-418.

5. Influence of shear and nanoparticles on the aggregation and fragmentation of asphaltene aggregates

The production of conventional and unconventional crude oil can be affected by several sources of damage under subsurface and surface conditions that can affect oil production.[1] Formation damage may occur during different stages of oil and/or gas production such as production, drilling, hydraulic fracturing, and workover operations.[2] According to Bennion,[1] formation damage is technically defined as *"any process that causes a reduction in the natural inherent productivity of an oil or gas producing formation, or a reduction in the injectivity of a water or gas injection well".* Heavy compounds in crude oil, such as asphaltenes, are a source of damage in light,[3] medium and heavy oils.[4] Although the source of the damage is the same, the type of damage is dependent on the crude oil quality and origin. In light crude oils with low contents of asphaltenes, the damage is induced by the precipitation, deposition and adsorption of asphaltenes on the porous media and the entire production system.[3] On the other hand, in crude oils with high asphaltene content, the damage is associated with high viscosities that reduce the oil mobility and lead to fingering problems, [5, 6] resulting in the production of large amounts of water that negatively affect the environment. In addition, nanoaggregates, formed at low concentrations tend to self-assemble at higher concentrations leading to large aggregates that subsequently increase the heavy oil (HO) viscosity.[4, 7] The asphaltene self-association occurs as their concentration in the system increases, hence promoting the formation of nanoaggregates (2 nm) and clusters (5 nm) with aggregation numbers lower than 10.[8, 9] Due to these characteristics of asphaltenes and the consequent problems in the production and transportation of crude oil, several mathematical models have been developed and reported in the literature to understand the phenomena associated with the aggregation of asphaltenes. [10-22]

Boek et.al. [16] used a slot capillary experiment and the dynamics of stochastic rotation (SRD) to study the potential interaction of asphaltenes under flow conditions and its effect on the asphaltene deposition process. The authors indicated that at a certain flow rate (5 μL/min), the pressure drop across the capillary increased slowly. However, by increasing the flow rate (10 μL/min) the aggregation and subsequent precipitation/deposition occurred earlier; however, the asphaltene deposits were later dragged by the flow. The simulation showed that for slow and fast flow rates, permanent and transient blocking occurred, respectively. The colloidal interaction potential was identified as a key parameter in the flocculation and deposition of asphaltenes under flow conditions and could be modified by including co-precipitated elements.[16]

In this regards, a number of population balance equations have been proposed for describing the asphaltenes growth.[13, 14, 19-23] Khoshandam and Alamdari[19] used mass and population balance equations for modeling the growth of asphaltenes particles in Heptol solutions. The proposed model employed four fitting parameters including the coefficient of growth rate and the agglomeration coefficient; supersaturation as driving force was quantitatively related to the agglomeration and

growth mechanisms. These authors reported a good fitting of the model towards the experimental observations made by dynamic light scattering with a relative deviation of 10%.[19] Maqbool et al.[21] developed a geometric population balance model that includes the Smoluchowski kernel for the simulation of the asphaltenes aggregates growth in presence of a precipitant such as *n*-heptane. The model fitted well the experimental observations regarding the asphaltenes aggregates size distribution and is useful in the prediction of the precipitation onset time of asphaltenes at low precipitant concentrations. Additionally, the authors found that the velocity at which asphaltenes aggregate in larger particles increase as the concentration of precipitant increases due to higher driving forces for asphaltenes aggregation. Rahimi and Solaimany-Nazar[20, 22] build up a fractal population balance model for the prediction of fractal aggregates size distribution of Iranian crude oil asphaltene solutions in Heptol mixtures in presence of shear. They reported that the fractal dimension of the aggregates is dependent on the shear and a time-dependent function can be used for it's description. Additionally, the number average diameter curves showed a maximum and further decreases until a steady state was reached. That trend was attributed to that after the maximum average size time, the breakage rate overcome that of aggregation, resulting in smaller aggregates.[20] Eskin et al.[23] simulated the particle size evolution of asphaltenes in pipeline under turbulent flows employing a population balance method. They estimated the collision efficiency, particle critical size and particle-wall sticking by fitting with the experimental observations obtained with a Couette device. Rahmani et al.[13, 14] studied asphaltene size distribution in organic solvents under a shear rate. Additionally, Rahmani et al. employed a mathematical model based on a population balance to analyze the experimental data pertaining to the aggregate size distribution of asphaltenes under certain shear rates, solvents and asphaltene loadings. The model and experimental data described the asphaltene aggregation as two-process phenomena involving the aggregation and fragmentation of asphaltenes induced by the presence of a shear rate until reaching a steady-state aggregate size. [13, 14] Generally, by increasing the shear rate, the rate of breakage of the asphaltene aggregates increases, leading to the formation of smaller aggregate sizes. In addition, as the asphaltene loading or the amount of precipitant increases, the rate of asphaltene aggregation growth is increased. [13, 14]

Montoya et al. [17, 18] developed two models to describe adsorption isotherms that accounts for the asphaltene self-association on the solid surface at reservoir[18] and surface[17] conditions. These solid−liquid equilibrium (SLE) and solid−liquid equilibrium at reservoir conditions (SLE−RC) models were based on the chemical theory and provide valuable information about the adsorption affinity of certain adsorbents towards asphaltenes and the method by which the asphaltenes self-associate over the solid surface at equilibrium conditions.[17, 18] The effects of the types of adsorbent, asphaltene chemical nature and the temperature were successfully described by the SLE and SLE-RC models. In addition, the SLE model provides accurate information about the thermodynamic properties of adsorption.[17]

Nanoparticles have become an interesting field of study regarding the inhibition or prevention of asphaltene damage at the laboratory[24-27] and oil field scales.[28] Although it is well known that the adsorption of asphaltenes on the nanoparticle surface would reduce the capacity of these asphaltic compounds to interact with each other, limited studies have been performed regarding the processes and the mechanisms associated with the effect of nanoparticles on the inhibition of the formation damage due to asphaltenes. To better understand this phenomenon from a mathematical approach, a population balance model (PBM) is proposed to describe the kinetics of asphaltene flocculation-fragmentation in the presence of nanoparticles. The model assumes that asphaltenes in the presence of a shear rate are related to the aggregation and fragmentation phenomena and includes a term related to the asphaltene adsorption on nanoparticles. An adsorption kinetic term was introduced into the model using the double exponential model. Experimental data of the kinetics of asphaltene aggregation were obtained by Dynamic Light Scattering (DLS) measurements at a fixed initial asphaltene concentration of 1000 mg/L and with different Heptol mixtures. In this study, CS, CM

and CAl nanoparticles were used as adsorbents to study the effect of the chemical nature of the nanoparticles on the inhibition of the asphaltene growth and for model validation. Additionally, to demonstrate the versatility of the proposed model, the effect of asphaltene was also evaluated. The obtained results from the proposed population balance model agree well with the experimental data, within an $RSME\% < 9\%$. The mathematics and other details of the model are described below.

5.1 Experimental

5.1.1 Materials

CS, CAl and CM nanoparticles were used as adsorbents for this study. Physicochemical properties of the selected nanoparticles can be found in Chapter 1. AK18 *n*-C_7 asphaltenes were also employed for the study. Some properties of the EHO and procedure for *n*-C_7 asphaltenes isolation are presented in Chapter 2. *n*-Heptane (99%, Sigma-Aldrich, St. Louis, MO) was used as received for asphaltene isolation and for the preparation of heavy oil model solutions. Toluene (99.5%, Merck KGaA, Germany) was also used for heavy oil solutions preparation.

5.1.2 Methods

- **Asphaltene aggregation kinetics**

It is well known that when a flocculation solvent, such as *n*-heptane, is added to an asphaltene solution under shearing, a steady state will be reached after the particle aggregation and fragmentation processes are equilibrated.[14] Therefore, a desired amount of *n*-C_7 asphaltenes is added to toluene and magnetically stirred for 1 h at 300 rpm. Then, *n*-heptane in the proportions of 20 v/v% (Heptol 20) and 40 v/v% (Heptol 40) is added to the heavy oil model solutions to complete a fixed concentration of 1000 mg/L *n*-C_7 asphaltenes. It is expected that the asphaltene size will increase as the amount of *n*-heptane increases.[29] Immediately, the solutions are magnetically stirred at a fixed shear rate of 300 rpm, and aliquots are taken to obtain the mean asphaltene aggregate size at a desired time. DLS measurements for the experiments on asphaltene aggregation kinetics were performed using a nanoplus-3 from Micromeritics (Norcross, ATL) set at a desired temperature and equipped with a 0.9 mL glass cell. [29-31] It is noteworthy that no asphaltene precipitation was observed for the employed Heptol solutions, as verified by the Oliensis Spot Test Number [32, 33] and Polarized Light Microscopy.[25] The asphaltene mean particle size was measured until a steady state was reached. The scattering angle varies according to the solvent used to optimize the intensity of the flocculation of scattering light. The mean aggregate diameter of asphaltenes d_{asp} (hydrodynamic diameter) is obtained from the Stokes-Einstein equation, as follows: [34]

$$d_{asp} = \frac{k_B T}{3\pi\eta D_a} \tag{5.1}$$

where k_B (1.38 x 10^{-23} $m^2 kg \cdot s^{-2} K^{-1}$) is the Boltzmann constant , T (K) is temperature, η [35] is the viscosity of the medium, and D_a ($m^2 \cdot s^{-1}$) is the diffusion coefficient of the particles. In addition, to evaluate the inhibition of the asphaltene aggregation using nanoparticles, the procedure was repeated in the presence of the selected nanomaterials with dose of 10 g/L of solution. The nanoparticle dose

was selected to allow the supernatant decantation for accurate measurements of asphaltene aggregation by minimizing the risk of noise due to suspended nanoparticles.

- **Adsorption kinetics experiments**

Batch-mode adsorption experiments were performed at a ratio of 1:10 (L:g) model heavy oil solution/mass of the nanoparticles following a procedure described in previous works.[36, 37] In brief, the adsorption of asphaltene in the experiments was monitored for 100 min at a fixed asphaltene initial concentration of 1000 mg/L, similar to the concentration used for the aggregation kinetics tests, and the solution temperature was 20°C. Samples were selected at predetermined time intervals and analyzed for asphaltene concentration using a Genesys 10S UV-vis spectrophotometer (Thermo Scientific, Waltham, MA). The adsorbed amount of n-C_7 asphaltenes relative to the mass of nanoparticles, q (mg/g), was estimated following the mass balance $q_t = (C_i - C_t)/M$, where q_t (mg/g) and C_t (mg/L) are the concentration of asphaltenes in the solution at a desired time t (min), and M (g/L) is the ratio of dry mass nanoparticles to solution volume.

5.2 Aggregation and inhibition model of asphaltene growth

5.2.1 General population balance equation

To model the kinetics of aggregation and inhibition, a PBM that accounts for the adsorption of asphaltene moieties onto nanoparticles is proposed. The model assumes that asphaltene aggregation in the presence of a shear rate is related to the aggregation and fragmentation phenomena. Rahmani et al.[14] proposed a PBM that describes the kinetics of aggregation and fragmentation of asphaltene particles following the expression developed by Austin 1971[38] and Friedlander 1977[39] for the change rate of the particle size of a given size due to the processes of aggregation and fragmentation. This model is based on the theory that at the initial stages of the aggregation/fragmentation process, the asphaltene aggregate size grows rapidly, i.e., aggregation is promoted. The fragmentation phenomena gains importance as the aggregation increases and as the hydrodynamic stresses equalize to cause stress of the aggregates.[38, 40] Therefore, the asphaltene aggregate size is dependent on the dominant phenomena in a specific moment. In this study, a modification of the model employed by Rahmani et al. [14] is proposed to account for the effect of nanoparticles in solution. It could be said that the presence of nanoparticles will affect the kinetics of asphaltene aggregation/fragmentation; hence, a new term representing aggregate inhibition provided by nanoparticles through the adsorption process is included in the new version of the PBM model, as described in equation 5.2:

$$\frac{dn_i}{dt} = B - D - \frac{dq}{dt} \tag{5.2}$$

where,

- $\frac{dn_i}{dt}$ is the rate number concentration (asphaltene particles per volume with size *i*,

- B and D are general terms regarding the appearance and disappearance of asphaltene particles of size *i*, respectively, and
- $\frac{dq}{dt}$ is the term related to the rate of adsorption of asphaltene particles on nanoparticles.

A detailed expression of the inhibition model of asphaltene aggregations is shown in equation 5.3,[14, 39, 41] after considering the adsorption on nanoparticles

$$\frac{dn_i}{dt} = \frac{1}{2}\sum_{j+k=i} \alpha\beta_{jk}(\mathrm{V}_j, \mathrm{V}_k) n_j n_k - n_i \sum_{k=1}^{n_{\max}} \alpha\beta_{ki}(V_k, V_i) n_k - B_i n_i + \sum_{j=i+1}^{n_{\max}} \gamma_{i,j} B_j n_j - \frac{dq}{dt} \tag{5.3}$$

where, n_i is the number concentration of aggregates with size *i* that contains *i* primary particles, and $n_{\max}$ is the maximum size of the particles that will form fragments of size i before fragmentation. In equation 5.3 from right to left, the first term defines the adsorption kinetic on nanoparticle, the second and fifth terms define the formation of *i*-sized particles, and the third and fourth terms account for the disappearance of particles of size *i*. β_{jk} is the collision frequency between particles of volume V_j and V_k due to Brownian motion and fluid shear, as expressed in equation 5.4: [14, 42, 43]

$$B_{jk} = \frac{2}{3}\frac{K_B T}{\mu}\left(\frac{d_i - d_j}{d_i d_j}\right)^2 + \frac{G}{6}(d_i + d_j)^3 \tag{5.4}$$

where, μ (Pa·s) is the solution viscosity, and G (1/s) is the shear rate. The volume of a particle of size *i* is expressed as a function of the volume in the previous step, as follows:

$$V_i = \frac{fV_{i-1}}{1-\varepsilon} \tag{5.5}$$

where, f is the sectional spacing, which is equal to 2, [14, 40, 44, 45] and ε is the aggregate porosity that is assumed constant for aggregate formation from primary particles and is used as a fitting parameter.

The collision efficiency, α, i.e., the fraction of collisions that results in aggregations, is assumed equal to 1.0 because large aggregates have fractal and porous structures.[44-46] Nevertheless, the collision efficiency is a function of the surface properties of the particles, the structure of the aggregates, the diameter of the aggregates,[14] the prevailing colloidal force and hydrodynamic effects.[47, 48] Additionally, $\gamma_{i,j}$ represents the volume fraction of aggregates of size *i* originating from aggregates of size *j* expressed as $\gamma_{i,j} = V_j / V_i$, and B_i is the fragmentation or breakup rate of aggregates of size i, given as a function of particle volume, as follows: [49-51]

$$B_i = bV_i^{0.33} \tag{5.6}$$

where, b is the breakup rate coefficient for shear-induced fragmentation.[14] In this work, b is assumed as a fitting parameter to correlate the experimental and simulation results.

5.2.2 Accounting for the kinetics of asphaltene adsorption onto nanoparticles

The inhibition term of asphaltene aggregation was introduced into the model using adsorption kinetics of asphaltenes onto the nanoparticles. Asphaltenes are first found in the bulk solution as large aggregates, and as nanoparticles gradually interact with the medium, the adsorption forces become greater than the aggregation forces, and disaggregation of asphaltene begins. Then, asphaltenes migrate from the bulk solution to the nanoparticle surface depending on the adsorption potential induced by the adsorbent. In a determined time, the nanoparticles adsorb a certain mass of asphaltenes that would not be able to interact in the process of asphaltene aggregation; therefore, the volume of asphaltenes available for growth decreases.

The double exponential model[52, 53] is used to determine the adsorption rate. Equation 5.7 describes the double exponential model used to fit the kinetic adsorption experimental data, respectively: [52, 53]

$$q_t = q_m - \frac{D_f}{M}\exp(-k_f t) - \frac{D_s}{M}\exp(-k_s t) \tag{5.7}$$

The double exponential model describes in two steps the kinetics of adsorption, namely, a fast and a slow step.[54] Therefore, k_f (min^{-1}) and k_s (min^{-1}), as well as D_f (mg/L) and D_s (mg/L) are the rate constants and adsorption coefficients of the fast and slow steps of the double exponential model, respectively, and q_m (mg/g) is the maximum amount of adsorbed asphaltenes.

Thus, the formation of large asphaltene aggregates in solution is inhibited in the presence of nanoparticles, as the adsorption on the nanoparticle hinders or changes the growth of asphaltene aggregate. Therefore, considering the adsorption kinetics of the nanoparticles, the free asphaltene primary particles are re-calculated each time, and this population is used in the model to find the aggregate size at a determined time. As described earlier, the free asphaltene primary particle is defined as the smallest particle distribution detected by means of the observation method employed (see next section). Eq. 5.8 describes the final form for calculating C_t as function of the parameters of the double exponential model:

$$C_t = C_i - \left(\frac{q_m}{M} + D_f \exp(-k_f t) + D_s \exp(-k_s t) \right) \tag{5.8}$$

Hence, the size and number concentration of asphaltene particles is re-calculated according to the value of C_t obtained by following the procedure described in Section 5.2.3.

5.2.3 Simulation characteristics

- **Size and number concentration of primary asphaltene particles**

The initial size distribution and the initial number concentration of the asphaltene particles were determined using experimental data. The volume of the primary particles was calculated according to the particle diameter obtained from DLS experiments assuming asphaltenes aggregates as spherical particles.[14] Then, at the initial state, the suspension is assumed homogeneous, and the

distribution of the primary particles is calculated using the mass and density of asphaltenes assumed as 1200 kg/m^3, as reported in the literature.[13, 14, 55]

- **Simulation conditions**

The developed model of aggregation and inhibition of asphaltenes considered in this study has the following characteristics and restrictions:

i. It is a grey-box model in which the structure is given by the equation of the population balance of asphaltenes, and the parameters were determined by constitutive equations.

ii. It is on the macroscopic scale and discrete because the growth of aggregates occurs over a wide size range; thus, a continuous model of flocculation may require excessive computation time.

iii. Although the asphaltene aggregation is typically described by probability distributions, the developed model has deterministic characteristics to obtain a practical model for the inhibition process in the presence of nanoparticles.

iv. It has dynamic characteristics because the size of the asphaltene aggregates change over time.

v. It has distributed parameters because each "family" of asphaltenes has their own values.

vi. Considering these characteristics, the model was solved numerically by a finite difference scheme using the Quasi-Newton Method.[56, 57]

The model parameters are obtained by minimizing the root mean square error (*RMSE%*,) between the theoretical and experimental data points using an implemented routine in the program code.

5.3 Results and discussions

The PBM proposed in this work describes the kinetics of asphaltene aggregation-fragmentation in systems with different conditions in the absence and presence of nanoparticles. The results and analyses are divided into two main sections: (i) kinetics of asphaltene adsorption on the selected nanoparticles and (ii) kinetics of asphaltene aggregation-fragmentation in the absence and presence of nanoparticles. The effects of the amount of precipitant in the solution, the system temperature and the nanoparticles' chemical nature and dosage were evaluated to demonstrate the PBM versatility.

5.3.1 Kinetics of *n*-C_7 asphaltene adsorption on the selected nanoparticles

- **Effect of the nanoparticles' chemical nature**

Panels a and b from Figure 5.1 show the adsorption kinetics of asphaltenes on the selected nanoparticles together with the double exponential adsorption kinetic model fit at different *n*-heptane concentrations of a) Heptol 20 and b) Heptol 40 at a fixed temperature of 20°C and a particles dosage of 10 g/L. For all of the cases, it was observed that asphaltene adsorption onto nanoparticles is a fast process requiring times less than 70 min to reach saturation. Note that at the beginning of the

adsorption process in the CM nanoparticles case and for Heptol 40, 93% of the total amount adsorbed is reached in 10 min and is likely to be due to the non-porous characteristics of the nanoparticles that favor a rapid first step of asphaltene adsorption just over the nanoparticles surface.[36, 37] From Figure 5.1, it is also observed that for the three nanoparticles evaluated, the amount adsorbed increases as the amount of *n*-heptane in the solutions increases. This reflects the increase of asphaltene aggregates in solution and the subsequent decrease in asphaltene solubility. The results are in good agreement with the trend observed in Chapter 3 for the adsorption of *n*-C_7 asphaltenes from different Heptol solutions over CS and functionalized CS nanoparticles where it was obtained higher asphaltene uptake as the amount of *n*-heptane increased.

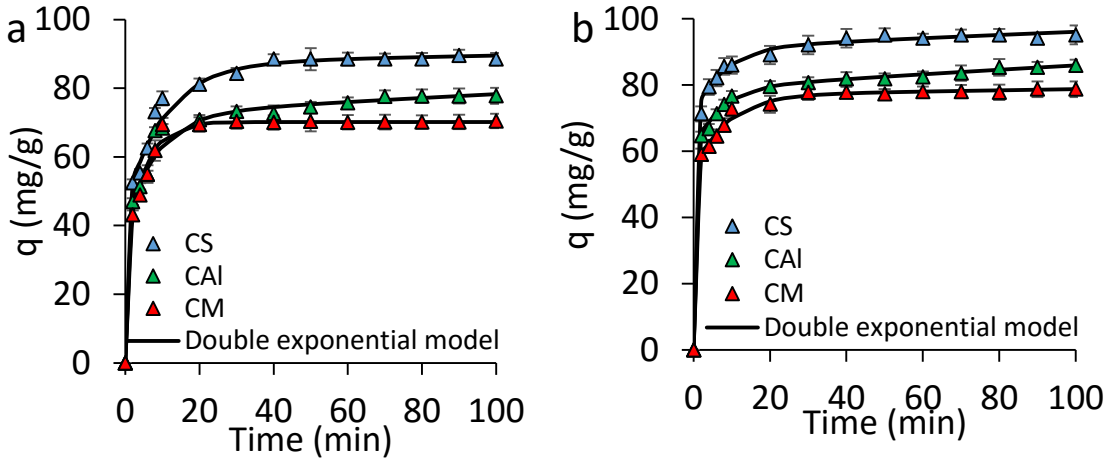

Figure 5.1. Adsorption kinetics for AK18 *n*-C_7 asphaltenes onto the selected nanoparticles from solutions of a) Heptol 20 and b) Heptol 40.

The double exponential model was used to describe the adsorption kinetics of AK18 n-C_7 asphaltenes onto the three employed nanoparticles. Table 5.1 shows the estimated parameters for the model used, the respective correlation coefficient and the root square mean error. As shown in Table 5.1, the double exponential model showed an excellent correlation towards the experimental data with $RSME\% < 4.10\%$. This means that due to van der Waals and electrostatic attraction forces, a first and rapid initial kinetic mechanism occurred where the adsorbate diffuses toward the adsorbent.[54, 58, 59] Values higher than 0.0 for the parameters k_s and D_s indicate that the fast step is followed by a gradual or slow adsorption of the asphaltenes over the nanoparticle surface by complexation.[58-60] These findings are in good agreement with the studies reported by Nassar [36] and Franco et al.[37] Regarding the adsorption efficiency in the fast step (k_f), for the Heptol 20 solutions, it can be observed that they tend to decrease in the order of CM > CAl > CS, indicating that as the surface area increases, longer times are required to reach the maximum capacity of adsorption. However, the results of the double exponential model indicate that there is not a second step for CM nanoparticles, and the rate of adsorption is higher for CAl than for CS nanoparticles. On the other hand, for Heptol 40, the trend followed by both k_f and k_s is CAl > CS > CM. In the case of CM nanoparticles in Heptol 40, the dosage of nanoparticles was duplicated to 20 g/L, resulting in a decreasing in the amount adsorbed in units of mg/g. However, when amount adsorbed is not normalized by dry mass of nanoparticles, an increase in the *n*-C_7 asphaltenes is observed when comparing with the results at 10 g/L and could be due to a larger amount of active sites available for adsorption. More details of the effect of the nanoparticles dosage can be found in the Appendix D.

- **Effect of the system temperature on the *n*-C_7 asphaltenes adsorption**

Figure 5.2 shows the comparison of AK18 *n*-C_7 asphaltenes adsorption kinetics onto CM nanoparticles at the two temperatures of 20 and 30°C. It can be observed from Figure 5.2 that the amount adsorbed decreases as the system temperature increases. This behavior is because the colloidal state of asphaltenes is affected by temperature, and their adsorption over the nanoparticle surfaces is an exothermic process. The results are in excellent agreement with those observed by Nassar [36] who evaluated the temperature effect on the Athabasca and with results obtained in Chapter 2 for *n*-C_7 asphaltenes adsorption over different type of nanoparticles.
In this case, the double exponential model also had excellent fitting towards the experimental results R^2 and $RSME\%$ of 0.99 and 5.82, respectively. Values of k_s and D_s of the double exponential model were equal to 0.00. This indicates that the adsorption mechanisms change from a two-step process to a one-step process by altering the system temperature. The q_m of the double exponential model was estimated as 88.95 mg/g. Values of k_f and D_f were estimated as 0.65 (min^{-1}) and 440.42 mg/L, respectively.

Table 5.1. Estimated parameters for the double exponential model for n-C_7 asphaltene obtained from Ak18

Heptol Ratio	**Sample**	$q_{m,exp}$ **(mg/g)**	q_m **(mg/g)**	D_f **(mg/L)**	k_f **(min^{-1})**	D_s **(mg/L)**	$k_s \times 10^{-3}$ **(min^{-1})**	R^2	$RSME\%$
20	CM	70.46	106.60	420.30	0.09	194.14	1.29	0.99	3.39
	CAl	77.80	104.58	325.04	0.12	323.70	2.09	0.98	4.10
	CS	88.49	70.17	401.18	0.20	0.00	0.00	0.99	1.30
40	CM	78.73	119.69	211.95	0.14	287.66	1.97	0.99	1.59
	CAl	85.93	113.71	194.78	0.16	350.32	2.32	0.99	0.91
	CS	95.14	93.72	235.76	0.12	168.59	1.19	0.99	1.32

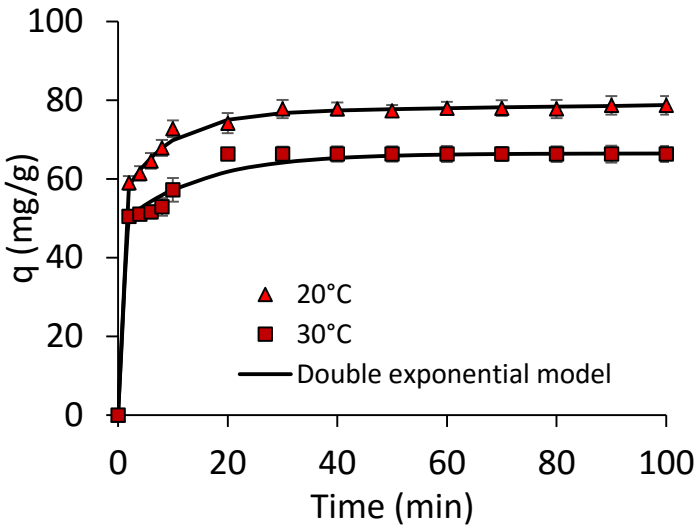

Figure 5.2. Adsorption kinetics for AK18 n-C_7 asphaltenes from Heptol 40 onto CM nanoparticles at temperatures of 20 and 30°C.

5.3.2 Asphaltene aggregation-fragmentation kinetics

The proposed PBM model was validated through series of DLS measurements for the mean aggregate particle size of asphaltenes under different conditions of temperature, Heptol solution and nanoparticle chemical nature. Different adsorption kinetic models were used to account for the asphaltene adsorption on the selected nanoparticles and their effect on the inhibition of the asphaltene growth. For each system, the kinetic adsorption double exponential model was used for describing the *n*-C_7 asphaltenes adsorption over the nanoparticles.

- **Effect of the nanoparticles' chemical nature on *n*-C_7 asphaltene aggregation-fragmentation**

It is expected that the presence of nanoparticles in a solution of asphaltene aggregates would create an adsorption potential that would promote the *n*-C_7 asphaltenes adsorption over the nanoparticles. Once the potential is induced, the interaction nanoparticle-*n*-C_7 asphaltenes overcome that of *n*-C_7 asphaltene- *n*-C_7 asphaltenes and hence, the asphaltene aggregate tends to disaggregate itself to migrate as molecules or smaller aggregates from the bulk solution to the adsorbent surface. This means that as *n*-C_7 asphaltenes adsorb on the nanoparticles surface, the asphaltene particles available in the aggregation system decrease. As the amount of asphaltenes adsorbed increases, the adsorption potential decreases, and gradually, the nanoparticle- *n*-C_7 asphaltenes interactions decrease until the maximum amount adsorbed is reached. Then, the asphaltene aggregates are re-organized but with a smaller aggregate size than prior to introducing the nanoparticles.

Figure 5.3 shows the evolution of the virgin *n*-C_7 asphaltene aggregate size as a function of time for asphaltenes in Heptol 20 and Heptol 40 along with the PBM fit. As observed, when the amount of *n*-heptane increases, the average size of the asphaltene aggregates at any time also increases. For example, in the Heptol 40 system, the asphaltene aggregates reach a maximum size of 1086 nm, while in the Heptol 20 system, the maximum size observed was 842 nm, which are found at 190 and 236 min, respectively. This is in agreement with the results reported by Maqbool et al.,[21] who reported that as the amount of *n*-heptane increased, the speed at which asphaltenes self-associate to

form larger aggregates increased due to the to higher driving forces. This, of course, is expected in view of the much lower solubility parameter of n-heptane when compared to toluene.[61, 62] In addition, the ratio of polar/nonpolar moieties in the asphaltene structure defines the polarity [62, 63] and leads to either a less or more favorable self-association phenomena.[17]

It is also observed that for both of the cases, the asphaltene size increases until a maximum and then decreases. This is due to the kinetics of asphaltene growth in the presence of a shear that involves both aggregation and fragmentation due to the asphaltene aggregates collision.[14] Table 5.2 shows the obtained parameters for the PBM fitting for kinetic aggregation-fragmentation of asphaltenes in the absence and presence of nanoparticles. As shown in Figure 5.3 and according to the obtained values of R^2 and $RSME\%$ of 0.97 and 5.47, respectively, the model has a good fit to the experimental results. The parameters ε and b varied depending on the system evaluated. For virgin asphaltenes, ε has values of 0.31 and 0.46 for Heptol 20 and Heptol 40 solutions, respectively, indicating a dependence on solvent composition (Heptol). This is because by increasing the amount of *n*-heptane in the Heptol solutions, the solubility of the asphaltenes decreases, leading to the formation of larger aggregates, hence increasing the porosity. The values of the porosity of the aggregates are in agreement with the findings by Rahmani and Masliyah.[14] For the breakup coefficient, b, the values had a weak dependence on the solvent composition for experiments with virgin AK18 *n*-C_7 asphaltenes with a value of 4.26 ± 0.01 for the Heptol 20 and Heptol 40 systems.

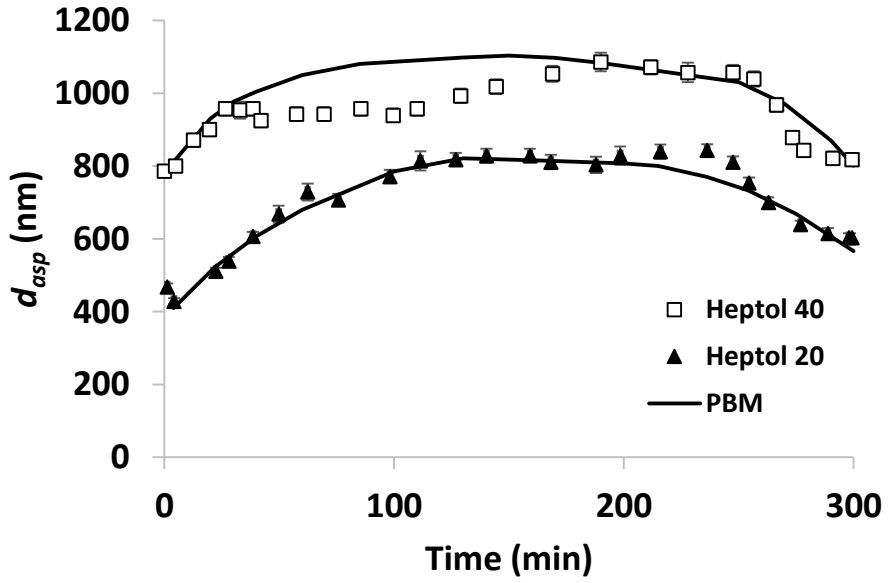

Figure 5.3. Kinetics of virgin *n*-C_7 asphaltenes aggregation-fragmentation at a temperature of 20°C in Heptol 20 and Heptol 40 solutions.

Figure 5.4 a and b shows the *n*-C_7 asphaltene growth kinetics in the presence of the selected nanoparticles for solutions of a) Heptol 20 and b) Heptol 40. Using DLS experiments, the kinetic of asphaltene aggregation-fragmentation in the presence of CS nanoparticles in Heptol 20 solutions could not be determined due to the low signal/noise ratio. Probably this is due to the size of particles being lower that the detection limit of the DLS technique used.[64] This is coherent with the results observed in Figure 5.4b for *n*-C_7 asphaltenes growth in the presence of CS nanoparticles in Heptol 40 that showed the lowest asphaltene aggregates among the evaluated nanoparticles. For the other materials, smaller aggregates were found in the order of CAL < CM < virgin *n*-C_7 asphaltenes, which was true for both Heptol 20 and Heptol 40 solutions. Although the effect of nanoparticles in terms

of affinity cannot be compared due to the differences in the chemical nature of the materials, the adsorption process can be a key factor in understanding the effect of the nanoparticles in the inhibition of the asphaltene self-association in the oil matrix. The observed trend corresponds to the results obtained for the adsorption kinetics that revealed a higher adsorption capacity for CAl than for CM nanoparticles. Due to the magnetic characteristics of CM nanoparticles, they tend to aggregate due to anisotropic dipolar attraction and form clusters,[65] hence reducing the surface area available for asphaltene adsorption. Thus, higher adsorption capacities will result in higher asphaltene adsorption and then will result in a reduction of the asphaltenes available in the solution for the aggregation-fragmentation process. The size of nanoparticles is another factor to be considered (see Chapter 1); in fact, nanoparticles size and capacity to reduced aggregate size are in line with each other. It can be suggested that this is related to the easy diffusion of the nanoparticles into the solution. This allows for a more effective scavenging of the dissolved *n*-C_7 asphaltene material.

The proposed PBM also showed a good fit to the experimental results for *n*-C_7 asphaltenes in the presence of nanoparticles and was confirmed by values of $R^2 > 0.94$ and *RMSE%* < 8.7. The ε parameter decreased in the order of virgin *n*-C_7 asphaltenes > CM > CAl > CS, indicating that smaller aggregates result from the addition of nanoparticles to the system, which is in agreement with the experimental results in Figure 5.4. On the other hand, the b parameter did not follow a clear trend, according to the kinetics of asphaltenes aggregation-fragmentation; this may be because the breakup coefficient would change as a function of the resultant asphaltene concentration and could also be affected by the presence of nanoparticles, their particle size and morphology. For example, CM nanoparticles that have a more squared shape than CAl nanoparticles would generate a different field of adsorption, thus directly affecting the rate of breakup of asphaltene aggregates. In addition, this may be because the breakup rate coefficient depends on not only the flocculants type and concentration but also the properties that are strongly influenced by the presence of the nanoparticles, such as the primary particles, flock structure and suspension of the medium. Also, when applying a higher dosage of CM nanoparticles of 20 g/L in Heptol 40 solutions, it was found that the asphaltene aggregates show a greater decrease as the amount of nanoparticles may significantly alter the asphaltene aggregate size in solution because more active sites will be available for adsorption. More information of nanoparticles dosage can be found in the Appendix D.

Table 5.2. Estimated parameters of the population balance model (PBM).

Heptol Ratio	Sample	ε	$b \times 10^5$	R^2	*RMSE%*
20	Virgin *n*-C_7 asphaltenes	0.31	4.27	0.97	5.47
	CM	0.24	3.59	0.94	8.43
	CAl	0.20	5.57	0.94	8.68
	CS	-	-	-	-
40	Virgin *n*-C_7 asphaltenes	0.46	4.25	0.98	4.73
	CM	0.41	6.03	0.98	4.28
	CAl	0.37	4.69	0.95	4.58
	CS	0.22	3.96	0.97	8.40

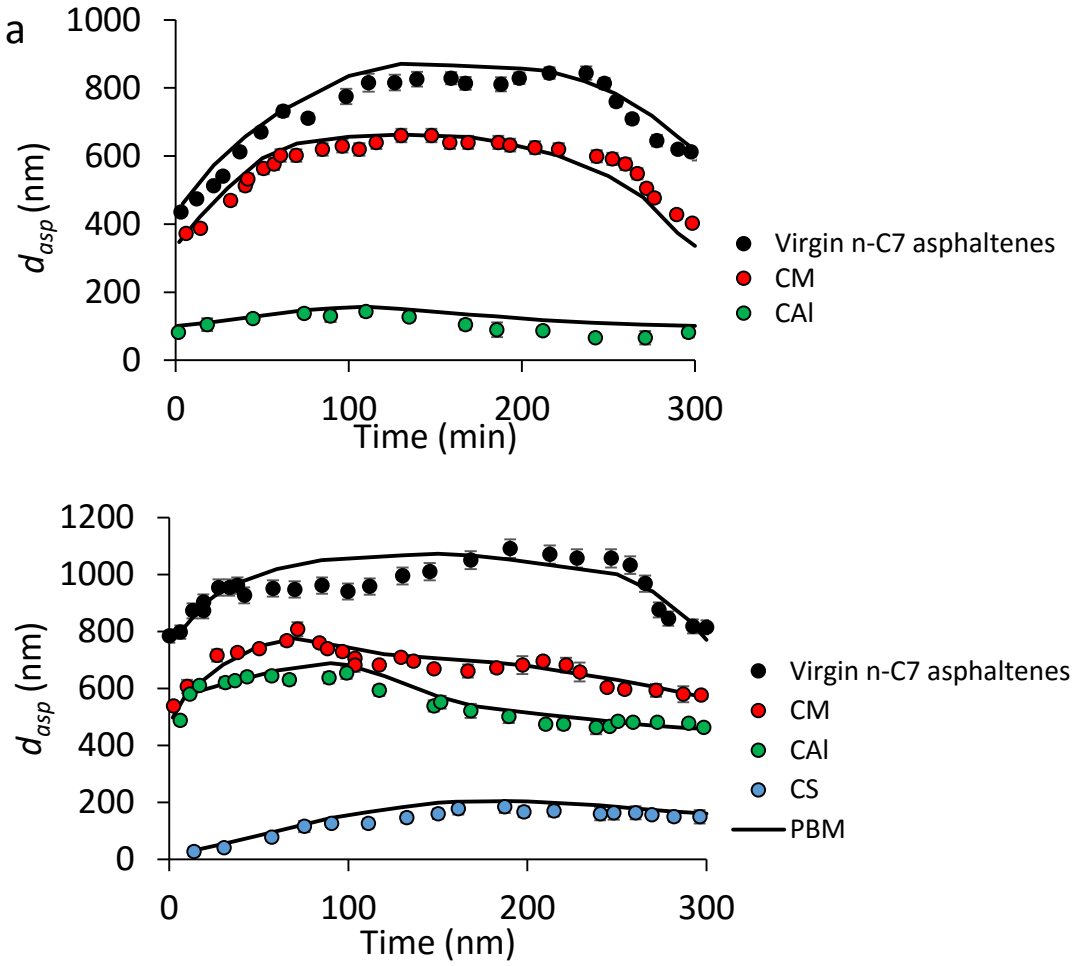

Figure 5.4. Kinetics of asphaltenes aggregation-fragmentation in the presence of nanoparticles for a) Heptol 20 and b) Heptol 40 at 20°C.

- **Effect of the system temperature on *n*-C_7 asphaltene aggregation-fragmentation**

Fragmentation of large aggregates by shear means that corresponding fragmentation energy is small and comparable to the available thermal energy; thus, relative small changes in temperature leads to significant changes in the aggregate size distribution.

It is expected that as the temperature increases, the asphaltene aggregate size decreases.[15, 66, 67] In this set of experiments, the effect of the system temperature in the aggregation-fragmentation of asphaltenes in the presence and absence of nanoparticles was evaluated at 20 and 30°C for a fixed Heptol solution (Heptol 40) with CM nanoparticles. Figure 5.5 shows the kinetics of virgin *n*-C_7 asphaltenes at the temperatures of 20 and 30°C. It is observed that at the equilibrium between the aggregation and fragmentation processes, the asphaltene aggregate is approximately 59% lower at 30°C. In addition, it is observed that the fragmentation processes overcomes that of aggregation earlier at 30°C than at 20°C. The PBM showed a good fit with R^2 = 0.98 and *RMSE%* = 3.18. The values of 0.35 and 7.93 × 10^{-5} were obtained for the parameters $\mathcal{E}$ and b. This confirms the formation of smaller aggregates and an increase in the breakup rate as the temperature increases compared with the values at 20°C (Table 5.2). The phenomenon can be explained because as forces

between molecules change with an increase in temperature due to the increased collision frequency, the asphaltene molecules will be more excited. Thus, intermolecular interactions, induction forces and electrostatic forces, will decrease, leading to a reduction in the degree of asphaltene self-association. In addition, according to Rassamdana and Sahimi,[67] the temperature increases the rotational motion of the aggregates, resulting in smaller sizes. Therefore, according to Pacheco-Sánchez et al.,[15] the concentration of asphaltene *n*-mers (i.e., asphaltene aggregates formed by "*n*" asphaltene molecules) decreases as the temperature increases, leading to an augmentation of aggregates composed of less than *n* asphaltene molecules.

Figure 5.5 shows the kinetics of asphaltene aggregation-fragmentation of *n*-C_7 asphaltenes in the absence and presence of CM nanoparticles at 30°C. It is observed that the fragmentation process in the presence of nanoparticles overcomes the aggregation in the first 50 min, which is earlier than at 20°C and is in agreement with the observed values for virgin asphaltenes. Additionally, the PBM fit with R^2 = 0.99 and *RMSE%* = 1.95 revealed values of ξ and b of 0.27 and 5.29×10^{-5}, respectively, that when compared with the values for the same system at 20°C (Table 5.2), indicated that the asphaltene aggregates are smaller, and the breakup rate of asphaltenes is higher. However, as from the adsorption kinetics at both temperatures, the amount adsorbed decreased as the temperature increased; hence, one can anticipate that the effect of temperature is higher in the inhibition of the asphaltene growth than the effect of nanoparticles. Nevertheless, both the temperature effect and the nanoparticles' adsorptive capacity have a synergistic effect in the reduction of the asphaltene aggregate size.

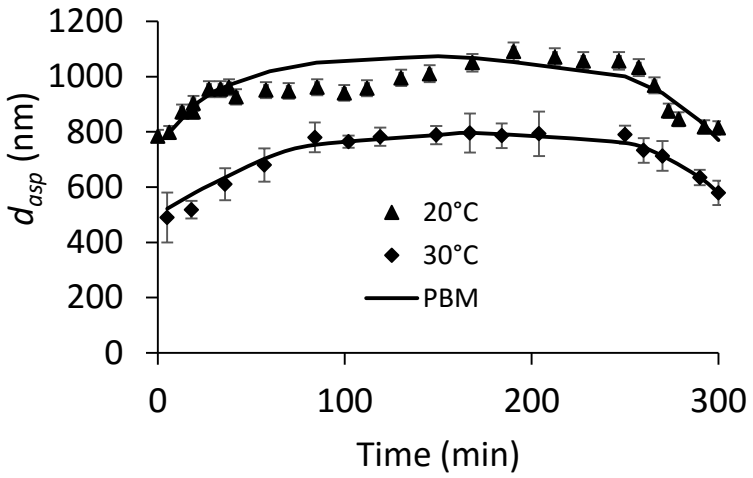

Figure 5.5. Kinetics for virgin *n*-C_7 asphaltene aggregation-fragmentation at the temperatures of 20 and 30°C in a Heptol 40 solution.

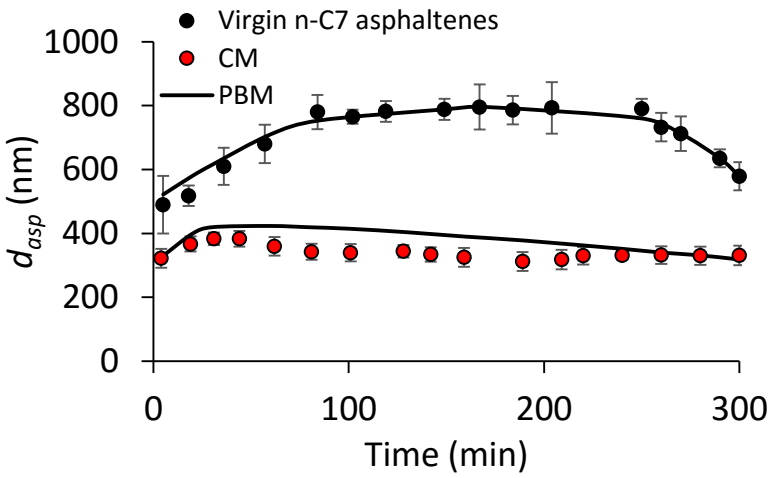

Figure 5.6. Kinetics for *n*-C_7 asphaltene aggregation-fragmentation in the presence of CM nanoparticles at a temperature of 30°C in a Heptol 40 solution.

5.4 Partial conclusions

A model to describe the asphaltene aggregation-fragmentation in the absence and presence of different metal oxide nanoparticles that accounts for the adsorption process was successfully developed. The model validity was sustained in population balance equations, and the adsorption term was introduced by employing the double kinetic exponential model. Under the different conditions examined all nanoparticles in different degrees reduce the hydrodynamic radii of large aggregates in solution as a result of adsorption. The effect of the nanoparticles' chemical nature, Heptol solution and temperature was successfully evaluated through DLS measurements. In general, the population balance model had a good fit towards the experimental results with $RSME\% < 9$. For all of the systems evaluated, the double exponential model showed a high affinity; therefore, it was incorporated into the PBM. In addition, the estimated PBM parameters ξ and b were in agreement with the behavior of the experimental curves of asphaltene aggregation-fragmentation.

5.5 References

1. Bennion, D. B., An overview of formation damage mechanisms causing a reduction in the productivity and injectivity of oil and gas producing formations. *Journal of Canadian Petroleum Technology* **2002,** 41, (11), 29-36.
2. Civan, F., *Reservoir formation damage*. Gulf Professional Publishing: 2011.
3. Adams, J. J., Asphaltene adsorption, a literature review. *Energy & Fuels* **2014,** 28, (5), 2831-2856.
4. Leontaritis, K.; Amaefule, J.; Charles, R., A systematic approach for the prevention and treatment of formation damage caused by asphaltene deposition. *SPE Production & Facilities* **1994,** 9, (03), 157-164.
5. Slobod, R.; Thomas, R., Effect of transverse diffusion on fingering in miscible-phase displacement. *Society of Petroleum Engineers Journal* **1963,** 3, (01), 9-13.
6. Homsy, G. M., Viscous fingering in porous media. *Annual review of fluid mechanics* **1987,** 19, (1), 271-311.

7. Ghanavati, M.; Shojaei, M.-J.; SA, A. R., Effects of asphaltene content and temperature on viscosity of Iranian heavy crude oil: experimental and modeling study. *Energy & Fuels* **2013,** 27, (12), 7217-7232.
8. Mullins, O. C., The asphaltenes. *Annual Review of Analytical Chemistry* **2011,** 4, 393-418.
9. Mullins, O. C., The Modified Yen Model†. *Energy & Fuels* **2010,** 24, (4), 2179-2207.
10. Rogel, E., Studies on asphaltene aggregation via computational chemistry. *Colloids and Surfaces A: Physicochemical and Engineering Aspects* **1995,** 104, (1), 85-93.
11. Rogel, E., Thermodynamic modeling of asphaltene aggregation. *Langmuir* **2004,** 20, (3), 1003-1012.
12. Murgich, J., Molecular simulation and the aggregation of the heavy fractions in crude oils. *Molecular Simulation* **2003,** 29, (6-7), 451-461.
13. Rahmani, N. H.; Dabros, T.; Masliyah, J. H., Evolution of asphaltene floc size distribution in organic solvents under shear. *Chemical engineering science* **2004,** 59, (3), 685-697.
14. Rahmani, N. H.; Masliyah, J. H.; Dabros, T., Characterization of asphaltenes aggregation and fragmentation in a shear field. *AIChE journal* **2003,** 49, (7), 1645-1655.
15. Pacheco-Sánchez, J.; Zaragoza, I.; Martínez-Magadán, J., Asphaltene aggregation under vacuum at different temperatures by molecular dynamics. *Energy & fuels* **2003,** 17, (5), 1346-1355.
16. Boek, E. S.; Ladva, H. K.; Crawshaw, J. P.; Padding, J. T., Deposition of Colloidal Asphaltene in Capillary Flow: Experiments and Mesoscopic Simulation†. *Energy & Fuels* **2008,** 22, (2), 805-813.
17. Montoya, T.; Coral, D.; Franco, C. A.; Nassar, N. N.; Cortés, F. B., A Novel Solid–Liquid Equilibrium Model for Describing the Adsorption of Associating Asphaltene Molecules onto Solid Surfaces Based on the "Chemical Theory". *Energy & Fuels* **2014,** 28, (8), 4963-4975.
18. Nassar, N. N.; Tatiana Montoya, T.; Franco, C. A.; Cortés, F. B.; Pereira-Almao, P. R., A New Model for Describing the Adsorption of Asphaltenes on Porous Media at a High Pressure and Temperature under Flow Conditions. *Energy & Fuels* **2015**.
19. Khoshandam, A.; Alamdari, A., Kinetics of asphaltene precipitation in a heptane− toluene mixture. *Energy & Fuels* **2010,** 24, (3), 1917-1924.
20. Rahimi, H.; Solaimany Nazar, A. R., Asphaltene aggregates fractal restructuring model, a population balance approach. *Energy & Fuels* **2009,** 24, (2), 1088-1093.
21. Maqbool, T.; Raha, S.; Hoepfner, M. P.; Fogler, H. S., Modeling the aggregation of asphaltene nanoaggregates in crude oil− precipitant systems. *Energy & Fuels* **2011,** 25, (4), 1585-1596.
22. Solaimany-Nazar, A. R.; Rahimi, H., Dynamic determination of asphaltene aggregate size distribution in shear induced organic solvents. *Energy & Fuels* **2008,** 22, (5), 3435-3442.
23. Eskin, D.; Ratulowski, J.; Akbarzadeh, K.; Pan, S., Modelling asphaltene deposition in turbulent pipeline flows. *The Canadian Journal of Chemical Engineering* **2011,** 89, (3), 421-441.
24. Franco, C. A.; Nassar, N. N.; Ruiz, M. A.; Pereira-Almao, P.; Cortés, F. B., Nanoparticles for inhibition of asphaltenes damage: adsorption study and displacement test on porous media. *Energy & Fuels* **2013,** 27, (6), 2899-2907.
25. Mohammadi, M.; Akbari, M.; Fakhroueian, Z.; Bahramian, A.; Azin, R.; Arya, S., Inhibition of asphaltene precipitation by TiO2, SiO2, and ZrO2 nanofluids. *Energy & Fuels* **2011,** 25, (7), 3150-3156.
26. Hashemi, S. I.; Fazelabdolabadi, B.; Moradi, S.; Rashidi, A. M.; Shahrabadi, A.; Bagherzadeh, H., On the application of NiO nanoparticles to mitigate in situ asphaltene deposition in carbonate porous matrix. *Applied Nanoscience* **2015**, 1-11.
27. Kazemzadeh, Y.; Malayeri, M.; Riazi, M.; Parsaei, R., Impact of Fe 3 O 4 nanoparticles on asphaltene precipitation during CO 2 injection. *Journal of Natural Gas Science and Engineering* **2015,** 22, 227-234.

28. Zabala, R.; Mora, E.; Botero, O.; Cespedes, C.; Guarin, L.; Franco, C.; Cortes, F.; Patino, J.; Ospina, N. In *Nano-Technology for Asphaltenes Inhibition in Cupiagua South Wells*, IPTC 2014: International Petroleum Technology Conference, 2014; 2014.
29. Ramalho, J. B. V.; Lechuga, F. C.; Lucas, E. F., Effect of the structure of commercial poly (ethylene oxide-b-propylene oxide) demulsifier bases on the demulsification of water-in-crude oil emulsions: elucidation of the demulsification mechanism. *Química Nova* **2010,** 33, (8), 1664-1670.
30. Yudin, I. K.; Anisimov, M. A., Dynamic light scattering monitoring of asphaltene aggregation in crude oils and hydrocarbon solutions. In *Asphaltenes, Heavy Oils, and Petroleomics*, Springer: 2007; pp 439-468.
31. Rane, J. P.; Harbottle, D.; Pauchard, V.; Couzis, A.; Banerjee, S., Adsorption kinetics of asphaltenes at the oil–water interface and nanoaggregation in the bulk. *Langmuir* **2012,** 28, (26), 9986-9995.
32. Asomaning, S., Test methods for determining asphaltene stability in crude oils. *Petroleum science and technology* **2003,** 21, (3-4), 581-590.
33. Oliensis, G. In *THE OLIENSIS SPOT TEST--WHAT JUSTIFICATION IS THERE FOR ITS USE?*, Association of Asphalt Paving Technologists Proceedings, 1935; 1935.
34. Bern, B.; Pecora, R., Dynamic Light scattering with Applications to Chemistry. *Biology and Physics (Wiley, New York, 1976). JJ Fisz et al./Two-photon-excitation fluorescence depolarization in solutions* 207.
35. Cross, K. M.; LU, Y.; Zheng, T.; Zhan, J.; McPherson, G.; John, V., Water Decontamination Using Iron and Iron Oxide Nanoparticles. In *Nanotechnology Applications for Clean Water*, Diallo, M.; Duncan, J.; Savage, N.; Street, A.; Sustich, R., Eds. William Andrew Inc.: Norwich, 2009; pp 347-364.
36. Nassar, N. N., Asphaltene adsorption onto alumina nanoparticles: kinetics and thermodynamic studies. *Energy & Fuels* **2010,** 24, (8), 4116-4122.
37. Franco, C.; Patiño, E.; Benjumea, P.; Ruiz, M. A.; Cortés, F. B., Kinetic and thermodynamic equilibrium of asphaltenes sorption onto nanoparticles of nickel oxide supported on nanoparticulated alumina. *Fuel* **2013,** 105, 408-414.
38. Austin, L. G., Introduction to the mathematical description of grinding as a rate process. *Powder Technology* **1971,** 5, (1), 1-17.
39. Friedlander, S. K., Smoke, dust and haze: Fundamentals of aerosol behavior. *New York, Wiley-Interscience, 1977. 333 p.* **1977,** 1.
40. Hounslow, M.; Ryall, R.; Marshall, V., A discretized population balance for nucleation, growth, and aggregation. *AIChE Journal* **1988,** 34, (11), 1821-1832.
41. Jindal, P.; Austin, L., A review introduction to the mathematical description of grinding as a rate process. *Powder Tech* **1976,** 5, 1-17.
42. Elimelech, M.; Jia, X.; Gregory, J.; Williams, R., *Particle deposition & aggregation: measurement, modelling and simulation*. Butterworth-Heinemann: 1998.
43. Smoluchowski, M., Versuch einer mathematischen Theorie der Koagulationskinetik kolloider Lösungen. **1917**.
44. Kusters, K. A.; Pratsinis, S. E.; Thoma, S. G.; Smith, D. M., Ultrasonic fragmentation of agglomerate powders. *Chemical engineering science* **1993,** 48, (24), 4119-4127.
45. Spicer, P. T.; Pratsinis, S. E., Coagulation and fragmentation: Universal steady-state particle-size distribution. *AIChE Journal* **1996,** 42, (6), 1612-1620.
46. Serra, T.; Casamitjana, X., Effect of the shear and volume fraction on the aggregation and breakup of particles. *AIChE journal* **1998,** 44, (8), 1724-1730.
47. Higashitani, K.; Iimura, K.; Sanda, H., Simulation of deformation and breakup of large aggregates in flows of viscous fluids. *Chemical Engineering Science* **2001,** 56, (9), 2927-2938.
48. Burban, P. Y.; Lick, W.; Lick, J., The flocculation of fine-grained sediments in estuarine waters. *Journal of Geophysical Research: Oceans (1978–2012)* **1989,** 94, (C6), 8323-8330.

49. Boadway, J. D., Dynamics of growth and breakage of alum floc in presence of fluid shear. *Journal of the Environmental Engineering Division* **1978,** 104, (5), 901-915.
50. Kapur, P., Self-preserving size spectra of comminuted particles. *Chemical Engineering Science* **1972,** 27, (2), 425-431.
51. Pandya, J.; Spielman, L., Floc breakage in agitated suspensions: effect of agitation rate. *Chemical engineering science* **1983,** 38, (12).
52. Wilczak, A.; Keinath, T. M., Kinetics of sorption and desorption of copper (II) and lead (II) on activated carbon. *Water Environment Research* **1993,** 65, (3), 238-244.
53. Chiron, N.; Guilet, R.; Deydier, E., Adsorption of Cu (II) and Pb (II) onto a grafted silica: isotherms and kinetic models. *Water Research* **2003,** 37, (13), 3079-3086.
54. Shayan, N. N.; Mirzayi, B., Adsorption and Removal of Asphaltene Using Synthesized Maghemite and Hematite Nanoparticles. *Energy & Fuels* **2015,** 29, (3), 1397-1406.
55. Vananton, H. W., Asphaltene Solubility and Asphaltene Stabilized Water-in-Oil Emulsions. **1997**.
56. Dennis, J., John E; Moré, J. J., Quasi-Newton methods, motivation and theory. *SIAM review* **1977,** 19, (1), 46-89.
57. Cameron, I. T.; Hangos, K., *Process modelling and model analysis*. Academic Press: 2001; Vol. 4.
58. Franco, C. A.; Cortés, F. B.; Nassar, N. N., Adsorptive removal of oil spill from oil-in-fresh water emulsions by hydrophobic alumina nanoparticles functionalized with petroleum vacuum residue. *Journal of colloid and interface science* **2014,** 425, 168-177.
59. Franco, C. A.; Nassar, N. N.; Cortés, F. B., Removal of oil from oil-in-saltwater emulsions by adsorption onto nano-alumina functionalized with petroleum vacuum residue. *Journal of colloid and interface science* **2014,** 433, 58-67.
60. Nassar, N. N., Kinetics, equilibrium and thermodynamic studies on the adsorptive removal of nickel, cadmium and cobalt from wastewater by superparamagnetic iron oxide nanoadsorbents. *The Canadian Journal of Chemical Engineering* **2012,** 90, (5), 1231-1238.
61. Spiecker, P. M.; Gawrys, K. L.; Trail, C. B.; Kilpatrick, P. K., Effects of petroleum resins on asphaltene aggregation and water-in-oil emulsion formation. *Colloids and surfaces A: Physicochemical and engineering aspects* **2003,** 220, (1), 9-27.
62. Spiecker, P. M.; Gawrys, K. L.; Kilpatrick, P. K., Aggregation and solubility behavior of asphaltenes and their subfractions. *Journal of colloid and interface science* **2003,** 267, (1), 178-193.
63. Pernyeszi, T.; Patzko, A.; Berkesi, O.; Dékány, I., Asphaltene adsorption on clays and crude oil reservoir rocks. *Colloids and Surfaces A: Physicochemical and Engineering Aspects* **1998,** 137, (1), 373-384.
64. Anisimov, M. A.; Ganeeva, Y. M.; Gorodetskii, E.; Deshabo, V.; Kosov, V.; Kuryakov, V.; Yudin, D.; Yudin, I., Effects of Resins on Aggregation and Stability of Asphaltenes. *Energy & Fuels* **2014,** 28, (10), 6200-6209.
65. Lu, Y.; Yin, Y.; Mayers, B. T.; Xia, Y., Modifying the surface properties of superparamagnetic iron oxide nanoparticles through a sol-gel approach. *Nano letters* **2002,** 2, (3), 183-186.
66. Espinat, D.; Fenistein, D.; Barre, L.; Frot, D.; Briolant, Y., Effects of temperature and pressure on asphaltenes agglomeration in toluene. A light, X-ray, and neutron scattering investigation. *Energy & fuels* **2004,** 18, (5), 1243-1249.
67. Rassamdana, H.; Sahimi, M., Asphalt flocculation and deposition: II. Formation and growth of fractal aggregates. *AIChE journal* **1996,** 42, (12), 3318-3332.

6. Heavy oil upgrading and enhance recovery in a continuous steam injection process assisted by nanoparticulated catalysts

The production of heavy and extra–heavy oil in Colombia is adverse due the rheological properties that the crude oil present because its high asphaltene content. Also, the upgrading of these unconventional oils needs large amounts of energy that lead to low cost-effective processes either at surface or sub-surface conditions. As of today fossil fuels supply about 82% of the world's energy demand.[1] Hence, the growing demand for crude oil worldwide has led to the need to exploit deposits of heavy and extra heavy crude oils, which are approximately of the same order to those of conventional crude oil according to the International Energy Agency.[2, 3] In fact, in the scenario 2014-2035 about the 9% of the cumulative investment upstream is necessary for developing heavy and extra heavy oil resources.[4] For the case of Colombia for instance, heavy and extra-heavy crude oils represent about the 45% of the total local oil production and it is expected to increase up to 60% by 2018.[5]

Accordingly, several in-situ techniques have been employed for enhancing HO and EHO recovery with objective of upgrading the oil and improving its viscosity and mobility. These techniques include thermal process, like steam assisted gravity drainage (SAGD) [6-14] and cold techniques, like treatments using diluents such as natural gas condensate.[15-19] The latter (i.e., cold process) is used to improve the crude oil by dilution or destabilization and deposition of asphaltene components in the reservoir by injecting solvents that have a direct impact on viscosity reduction.[18, 19] The more frequently employed thermal techniques for heavy oil upgrading deal with breaking the heavier compounds of oil using combustion process,[6, 7] low-temperature oxidation,[20, 21] aquathermolysis,[12-14] and pyrolysis, also called thermal cracking or thermolysis.[9, 11, 22, 23] However, most of these techniques do not exceed the 20-25% of oil recovery and the 50% in the case of the steam assisted gravity drainage (SAGD) process.[24-26] According to the Agencia Nacional de Hidrocarburos (National Hydrocarbons Agency), by the end of 2014 there were approved 25 enhanced oil recovery projects, from which 14 correspond to water injection and the others to vapor and gas injection.[27] Nevertheless, due the need of increase the efficiency in recovery of the aforementioned techniques, new technologies need to be developed. In this order, nanoparticle technology has emerged as an alternative with a great potential to enhance the aforementioned techniques and increase the oil recovery.[28] Catalyst nanoparticles may be used for in-situ heavy oil upgrading, leading to an economic expense by reducing negative environmental impact and increasing the oil recovery.[29-31] Galarraga and Pereira-Almao[30] studied the effect of NiWMo submicronic ultradispersed catalysts for Athabasca bitumen upgrading simulating near in-reservoir conditions. The authors reported that the catalyst enhanced the bitumen upgrading by increasing the H/C ratio, reducing both oil viscosity and coke formation. A more recent study, Hashemi et al.[29] used in-situ prepared ultra-dispersed multi-metallic nano-catalysts of Ni-W-Mo within a vacuum gas oil matrix for enhancing Athabasca bitumen upgrading and recovery at a typical SAGD temperature and pressure conditions. The authors

found that nanoparticles enhanced bitumen upgrading and recovery by increasing the API gravity and reducing the oil viscosity by hydrogenation reactions. Also, the microcarbon residue, the sulfur and nitrogen content were reduced.

Hamedi et al.[31] compared the effect of nickel nanoparticles against an industrial micro-sized Raney nickel catalyst during steam-injection for heavy oil upgrading. Tests were carried out in presence and absence of a porous media. The authors reported that in mass base, the catalytic activity of nickel nanoparticles was greater than that for Raney nickel catalyst. Further, the authors found that the catalytic process was enhanced in the presence of the porous media due to the fact that the sand grains behave as support for the nickel nanoparticles. In addition, the authors found that the reactivity and particle distribution are greatly influenced by the viscosity of the nanoparticle suspension, the injection rate and direction.

However, until now there are not studies that report the evaluation of nanoparticled catalysts in stemaflooding processes. Hence, this chapter aims at investigate the effect of catalytic active nanoparticles in the improvement of the efficiency in recovery of a continuous steam injection process. Oil recovery was evaluated using a slim tube filled with a non-confined sand pack in steam injection scenarios in absence and presence of a water-based nanofluid. Changes in physicochemical properties of crude oil were evaluated trough *n*-C_7 asphaltene content and simulated distillation (SimDis) measurements.

6.1 Experimental

6.1.1 Materials

Bimetallic nanoparticles were used as catalyst in the steam flooding process. Deionized water (conductivity of 3 μS/cm) was used for steam generation and for brine and nanofluid preparation. A synthetic brine as 2000 mg/L of NaCl (≥99.5%, Merck KGaA, Germany) was also used for injection into the porous media and for nanofluid preparation. Commercial surfactant Tween 80 (Panreac, Spain) was employed for nanoparticles dispersion. AK9 EHO with a viscosity of 1385 cP at 85°C was used for the displacement test. Additional properties of the employed crude oil can be found in Table 2.1 of Chapter 2. Clean silica sand (Ottawa sand, US sieves 30−40 mesh) was purchased from Minercol S.A., Colombia and was used as porous media. In addition, toluene, methanol (99.8%, Panreac, Spain) and HCl (37%, Panreac, Spain) were used for porous media cleaning.

Porous media: Before use, the prepared porous bed was initially cleaned with a solution 1:1 of toluene and methanol at 10 mL per 5 g of sand. The sand then was washed with excess deionized water and HCl at 10% v/wt to remove any dust or surface impurities. Further, the sand was placed in a vacuum oven at 120°C for 12 h to evaporate any remaining solvent. Then, approximately 100 g of the sand was transferred to a stainless steel slim tube. The porous medial has an absolute permeability of 8.3 Darcy and porosity of 38%. It is worth to mention that high value of absolute permeability is due to there was no any confining step in the porous media preparation and that all test were conducted without overburden pressure. The slim tube has an inside diameter of 1.12 cm and length of 100 cm. The absolute permeability of the porous media was measured by injecting brine after sand packing. Brine was injected inside the porous media at a defined rate (0.5 mL/min), and two pressure transducers were used to record the pressure values at the injection and production points. Accordingly, the porous media permeability was estimated following Darcy's law.

Preparation of Nanofluid: The nanofluid was prepared by mixing 1 wt% of tween 80 with distilled water and dispersing 500 mg/L of bimetallic nanoparticles. The nanofluid was magnetically stirred

at 300 rpm at room temperature for 6 h and then sonicated for 24 h at the same temperature before injection into the porous media.[32] The size of bimetallic nanoparticles in the aqueous solution was about 61 nm, as measured by DLS technique as explained in Chapter 1.

6.1.2 Methods

- **Fluid injection test**

Figure 1 shows a schematic representation of the experimental setup. The setup consists mainly of a tank containing the nanofluid, a cylinder containing water for steam generation, an oil-containing cylinder, a positive displacement pump (DB Robinson Group, Canada), a tubular furnance (Thermo scientific, USA), manometers, a thermocouple, valves, fraction collectors and a stainless steel slim tube. Nanofluid mixtures were injected into the porous media from the production point by positive displacement pump. The surrounding slim tube environment was maintained at a constant temperature of 85°C for all steps of the displacement test using an oven. A leak test was performed by pressurizing the packed bed reactor with pure nitrogen up to 1000 psi. A 1% change in pressure per hour was considered to be the maximum allowable pressure reduction during the leak test. The main objective of this displacement test was to evaluate the effectiveness of the nanoparticles in changing the physicochemical properties of the employed EHO and in enhancing a process of oil recovery with continuous vapor injection. The displacement test was carried out by (1) constructing the base curves, (2) estimating the oil recovery by the continuous injection of vapor in absence of nanofluid and (3) identifying the influence of the nanoparticles in the enhanced recovery of oil. For construction of the base curves, 10 pore volumes (PV) of water were injected to measure the absolute permeability at 85°C. Then, at the same temperature, and under the saturation condition of residual water (Swr), the crude oil was injected until the pressure no longer changed. Finally, 20 PV of water were injected for estimating the water effective permeability (Kw) at Sor conditions. Before step (2), system was saturated with oil until similar state of Swr than that before Kw determination. For step (2), the steam was introduced into the porous media by passing the water through the coil line from the water cylinder and monitoring the pressure and temperature in the injection point. The water was displaced at a flow ranging between 3.0 and 8.0 mL/min in order to avoid condensation after the coil line and for maintaining the injection pressure and temperature at 200 psi and 300°C. Injection temperature was stablished according to the results obtained in previous Chapters. As observed in Chapter 2, it is expected that for a temperature of 300°C in presence of nanoparticles a high *n*-C_7 asphaltene conversion would be achieved. At stablished injection conditions it is ensured a vapor quality of 100%. Vapor was introduced to the system until no oil production was observed. Then, the system was saturated with oil until same conditions of Swr than before vapor injection were obtained. In step (3), 0.5 pore volumes (PV) of nanofluid were injected at 0.5 mL/min by the production inlet. Increases in the system ΔP were recorded with the transducer in order to determine if the additional recovery of oil was induced to the energy won after the nanofluid injection. It is worth to mention that in step (2) as blank 0.5 PV of a mixture of water + 1 wt% tween 80 + 2000 mg/L NaCl was injected in the same conditions than the nanofluid. Porous media was soaked with the nanofluid for 24 h. Finally, vapor was injected at the same conditions than that of step (2) until there was not oil production.

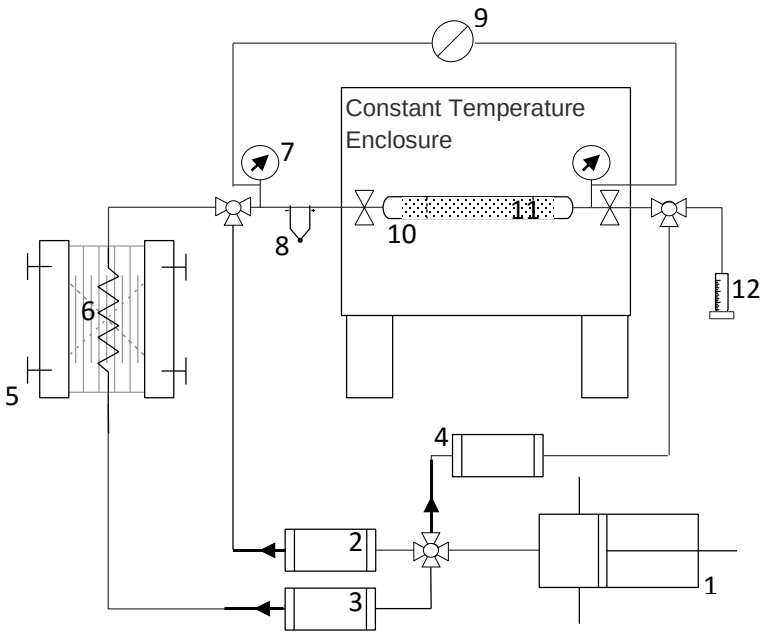

Figure 6.1. Schematic representation of the experimental setup. Legend: 1) the displacement positive pump the core holder, 2) the oil-containing displacement cylinder, 3) the water-containing displacement cylinder, 4) the nanofluid-containing displacement cylinder, 5) the tubular furnace 6) the coil line 7) the manometers, 8) the thermocouple, 9) the pressure transducer, 10) the slim tube, 11) the sand packed bed and 12) sample output.

- **Analytical methods**

n-C_7 asphaltene and residue content were determined in order to determine the effect of the nanoparticles in the EHO upgrading before and after recovery with vapor injection. Oil sample for analytical test was the one taken before each step of the displacement test ended. *n*-C_7 asphaltene content was estimated according to the procedure explained in Chapter 2. Residue content (620°C+) was estimated using high-temperature simulated distillation (HTSD) following ASTM D-7169 procedure using an Agilent 7890 chromatographer. Results are presented as residue conversion (*R%*) as follows:[29]

$$R\% = \frac{R_{virginEHO} - R_{treatment}}{R_{virginEHO}} \times 100 \qquad (6.1)$$

where $R_{virginEHO}$ and $R_{treatment}$ represent the residue of the virgin EHO and the oil after production in presence of nanoparticles, respectively.

6.2 Results and discussions

Displacement testes were carried out in three steps namely (1) construction of base curves, (2) oil recovery with vapor continuous injection and (3) oil recovery with vapor continuous injection assisted by catalytic nanoparticles. After step (1) the measured absolute permeability, Ko and Kw values were estimated as 8.3, 92.0 and 9.4 Darcy, respectively. High Ko value could be due to two

the high viscosity of the EHO employed that increase the permeability value according to the Darcy's equation. After step (1) system was saturated with the employed EHO and then 0.5 PV of a brine + Tween 80 mixture was injected and left to soaking for 24 h and a ΔP of 0.23 psi was observed. Figure 6.2 shows the oil recovery curves with continuous vapor injection with and without the nanoparticles assistance. As observed in Figure 6.2, the oil recovery with the injection of vapor without nanoparticles stopped after approximately 12000 pore volumes injected of vapor (Vapor PVI), reaching a recovery of 34% and after 43000 PVI the recovery was 36%. Oil recovery is enhanced by vapor injection due to volatilization of light hydrocarbons, viscosity reduction, thermal expansion, variation of the relative permeability and capillary pressure and gravitational segregation.[33] An increase in the oil recovery due to the inclusion of nanoparticles is clearly seen in Figure 6.2. Similar percentages of recovery than that in absence of nanoparticles are achieved with less vapor PVI. As comparison, after 4100 vapor PVI a recovery of 34% was obtained. However, at 43000 vapor PVI the 82% of the oil in the slim tube was recovered, representing a 46% more that in absence of nanoparticles. It is worth to mention that ΔP at the nanofluid soaking stage the ΔP was 0.19 psi and as this value is lower than the soaking stage in step (2), it can be said that additional oil production was not due to additional energy obtained in the nanofluid injection.

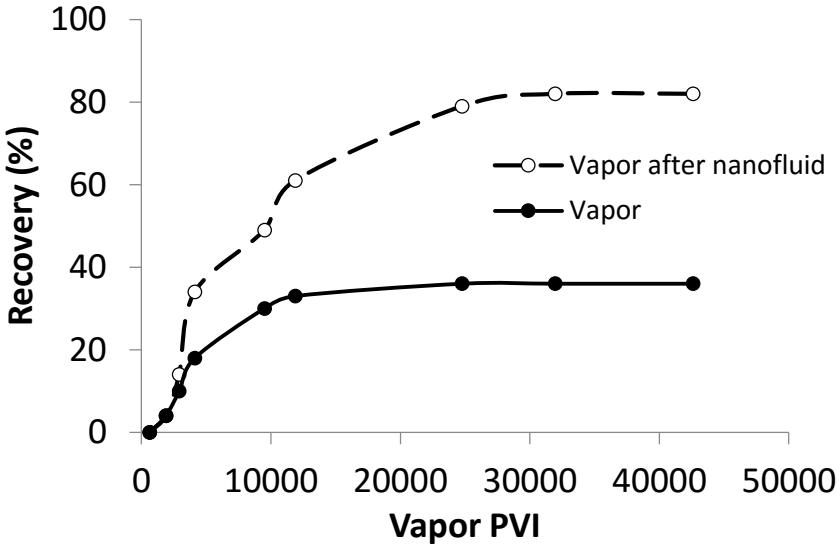

Figure 6.2. Oil recovery curves for vapor injection with and without nanoparticles.

Table 6.1. Estimated values for saturation of water residual (*Swr*) and saturation of oil residual (*Sor*) at different stages.

Stage	***Swr***	***Sor***	
		Initial	***Final***
(1)	20%	80%	48%
(2)	22%	78%	43%
(3)	25%	75%	24%

Three main reasons are responsible for the enhanced recovery of oil using vapor assisted with nanoparticles in comparison with the system without nanoparticles. As nanoparticles entry the porous media, they may alter the system wettability to a strong water-wet condition generating a sort of decoration of the rock that enhance its preference for water.[34] Giraldo et al.[34] shown trough Contact angle measurements, imbibition tests and core displacement test at reservoir conditions that alumina-based nanofluids are able to change the system wettability from strongly oil-wet to strongly water-wet condition. In this case, wettability changes are corroborated by the states of saturations at each stage as listed in Table 6.1.

In addition to wettability changes, asphaltene adsorption over the injected nanoparticles also lead to increase in oil recovery. Once nanoparticles interact with crude oil asphaltenes feel more attracted for being adsorbed than in the oil matrix. As the asphaltene-asphaltene interactions are lower than those of asphaltene-nanoparticle, asphaltenes would be removed from the aggregation system in the oil matrix and diffuse trough the bulk phase to the nanoparticles surface until maximum adsorption capacity is reached; asphaltenes remaining in the bulk phase would "reorganize" and form smaller aggregates (please refer to Chapter 5 of this document). Reduction in the asphaltene aggregate directly leads to diminution of the crude oil viscosity. Although resins may also be adsorbed over the nanoparticles surface, it was demonstrated in Chapter 4 that it does not have significant interference in the adsorption process of asphaltenes.

Once asphaltenes are adsorbed over the nanoparticles surface, they can be converted in lighter products at determined conditions of temperature, asphaltene loading, degree of self-association around nanoparticles active sites, chemical nature of the nanoparticulated catalyst, chemical nature of the asphaltene molecule, etc. (please see Chapters 2 and 3 for further information). The formation of lighter products will change the chemical composition of crude oil and enhance the aforementioned processes that affect the oil recovery with vapor such as volatilization of light hydrocarbons, viscosity reduction, thermal expansion, variation of the relative permeability and capillary pressure and gravitational segregation. In this order, Table 6.2 shows the values of *n*-C_7 asphaltene content and R% for virgin crude oil, crude oil obtained after vapor injection and crude oil produced after vapor injection assisted by nanoparticles. As observed, physicochemical properties of crude oil changed in both scenarios with and without nanoparticles. However, a higher upgrading was obtained in presence of nanoparticles as revealed by the *n*-C_7 asphaltene content and the values of *R%*. This is not surprising as the presence of nanoparticles reduce the temperature of asphaltene decomposition, lead to a decrease in the effective activation energy and generate different reaction pathways in the asphaltene decomposition in agreement with results obtained in Chapters 2 and 3.

Table 6.2. Estimated values for *R%* and *n*-C_7 asphaltene content for virgin crude oil, crude oil obtained after vapor injection and crude oil produced after vapor injection assisted by nanoparticles.

Property	**Sample**		
	Virgin EHO	**Crude oil after vapor injection**	**Crude oil after vapor injection assisted by nanoparticles**
n-C_7 asphaltene (wt%)	13.1	11.8	7.9
R%	0	13	47

6.3 Partial conclusions

Successfully a methodology for evaluating the effect of nanoparticulated catalyst in processes of continuous vapor injection was developed. Displacement test were carried out by injecting vapor in presence and absence of the selected nanoparticles. It was observed that the oil recovery increased up to 46% for the system assisted by nanoparticles in comparison with the vapor injection without the nanocatalyst. Additionally, trough *n*-C_7 asphaltene and residue content it was demonstrated that nanoparticles are an excellent alternative for HO and EHO upgrading in processes involving vapor injection. *n*-C_7 asphaltene content decreased a 5.2% after vapor injection in presence of nanoparticles in comparison with the virgin EHO. Also, the residue content (620°C+) decreased a 47%. Enhanced oil recovery due to nanoparticles injection could be attributed to three main reasons: i) wettability alteration of the porous media, ii) viscosity reduction due to reduction of the asphaltene aggregate and iii) crude oil upgrading. This study should generate a better landscape about the use of catalytic nanoparticles in the improvement of enhanced oil recovery processes and its application in local and international scenarios.

6.4 References

1. Ghannam, M. T.; Hasan, S. W.; Abu-Jdayil, B.; Esmail, N., Rheological properties of heavy & light crude oil mixtures for improving flowability. *Journal of Petroleum Science and Engineering* **2012,** 81, 122-128.
2. Tedeschi, M. n. In *[13] RESERVES AND PRODUCTION OF HEAVY CRUDE OIL AND NATURAL BITUMEN*, 13th World Petroleum Congress, 1991; World Petroleum Congress: 1991.
3. IEA, Resources to reserves 2013. **2013**.
4. IEA, World Energy Investment Outlook. **2014**.
5. Energía, C. Crudos pesados, la gran apuesta del sector. (10-08-2015),
6. Cavallaro, A.; Galliano, G.; Moore, R.; Mehta, S.; Ursenbach, M.; Zalewski, E.; Pereira, P., In situ upgrading of Llancanelo heavy oil using in situ combustion and a downhole catalyst bed. *Journal of Canadian Petroleum Technology* **2008,** 47, (9), 23-31.
7. Moore, R.; Laureshen, C.; Mehta, S.; Ursenbach, M.; Belgrave, J.; Weissman, J.; Kessler, R., A downhole catalytic upgrading process for heavy oil using in situ combustion. *Journal of Canadian Petroleum Technology* **1999,** 38, (13).
8. Greaves, M.; Saghr, A.; Xia, T.; Turtar, A.; Ayasse, C., THAI-new air injection technology for heavy oil recovery and in situ upgrading. *Journal of Canadian Petroleum Technology* **2001,** 40, (03).
9. Kumar, J.; Fusetti, L.; Corre, B. In *Modeling In-Situ Upgrading of Extraheavy Oils/Tar Sands by Subsurface Pyrolysis*, Canadian Unconventional Resources Conference, 2011; Society of Petroleum Engineers: 2011.
10. Kapadia, P. R.; Kallos, M.; Gates, I. D. In *A Comprehensive Kinetic Theory to Model Thermolysis Aquathermolysis Gasification Combustion and Oxidation of Athabasca Bitumen*, SPE Improved Oil Recovery Symposium, 2010; Society of Petroleum Engineers: 2010.
11. Speight, J., Thermal cracking of Athabasca bitumen, Athabasca asphaltenes, and Athabasca deasphalted heavy oil. *Fuel* **1970,** 49, (2), 134-145.
12. Jiang, S.; Liu, X.; Liu, Y.; Zhong, L. In *In situ upgrading heavy oil by aquathermolytic treatment under steam injection conditions*, SPE International Symposium on Oilfield Chemistry, 2005; Society of petroleum engineers: 2005.
13. Fan, H.; Zhang, Y.; Lin, Y., The catalytic effects of minerals on aquathermolysis of heavy oils. *Fuel* **2004,** 83, (14), 2035-2039.

14. Maity, S.; Ancheyta, J.; Marroquín, G., Catalytic aquathermolysis used for viscosity reduction of heavy crude oils: A review. *Energy & Fuels* **2010,** 24, (5), 2809-2816.
15. Luo, P.; Yang, C.; Gu, Y., Enhanced solvent dissolution into in-situ upgraded heavy oil under different pressures. *Fluid phase equilibria* **2007,** 252, (1), 143-151.
16. James, L.; Rezaei, N.; Chatzis, I., VAPEX, warm VAPEX and hybrid VAPEX: the state of enhanced oil recovery for in situ heavy oils in Canada. *Journal of Canadian Petroleum Technology* **2008,** 47, (4), 12-18.
17. Castro, L. V.; Flores, E. A.; Vazquez, F., Terpolymers as Flow Improvers for Mexican Crude Oils†. *Energy & Fuels* **2011,** 25, (2), 539-544.
18. Luo, P.; Yang, C.; Tharanivasan, A.; Gu, Y., In situ upgrading of heavy oil in a solvent-based heavy oil recovery process. *Journal of Canadian Petroleum Technology* **2007,** 46, (9), 37-43.
19. Cavallaro, A.; Galliano, G.; Sim, S.; Singhal, A.; Fisher, D. In *Laboratory investigation of an innovative solvent based enhanced recovery and in situ upgrading technique*, Canadian International Petroleum Conference, 2005; Petroleum Society of Canada: 2005.
20. Xu, H. H.; Okazawa, N.; Moore, R.; Mehta, S.; Laureshen, C.; Ursenbach, M.; Mallory, D. In *In situ upgrading of heavy oil*, Canadian International Petroleum Conference, 2000; Petroleum Society of Canada: 2000.
21. Wichert, G.; Okazawa, N.; Moore, R.; Belgrave, J. In *In-situ upgrading of heavy oils by low-temperature oxidation in the presence of caustic additives*, International heavy oil symposium, 1995; 1995; pp 529-536.
22. Monin, J.; Audibert, A., Thermal cracking of heavy-oil/mineral matrix systems. *SPE reservoir engineering* **1988,** 3, (04), 1,243-1,250.
23. Nassar, N. N.; Hassan, A.; Luna, G.; Pereira-Almao, P., Comparative study on thermal cracking of Athabasca bitumen. *Journal of thermal analysis and calorimetry* **2013,** 114, (2), 465-472.
24. Butler, R., SAGD comes of age! *Journal of Canadian Petroleum Technology* **1998,** 37, (07).
25. Nasr, T.; Beaulieu, G.; Golbeck, H.; Heck, G., Novel expanding solvent-SAGD process ES-SAGD. *Journal of Canadian Petroleum Technology* **2003,** 42, (1), 13-16.
26. Hashemi, R.; Nassar, N. N.; Pereira Almao, P., Enhanced heavy oil recovery by in situ prepared ultradispersed multimetallic nanoparticles: A study of hot fluid flooding for Athabasca bitumen recovery. *Energy & Fuels* **2013,** 27, (4), 2194-2201.
27. Proyectos de recobro, salvavidas de producción petrolera. *Portafolio* 2014.
28. Hashemi, R.; Nassar, N. N.; Almao, P. P., Nanoparticle technology for heavy oil in-situ upgrading and recovery enhancement: Opportunities and challenges. *Applied Energy* **2014,** 133, 374-387.
29. Hashemi, R.; Nassar, N. N.; Pereira-Almao, P., *Energy Fuels* **2012,** 26, (3), 1645.
30. Galarraga, C. E.; Pereira-Almao, P., Hydrocracking of Athabasca bitumen using submicronic multimetallic catalysts at near in-reservoir conditions. *Energy & Fuels* **2010,** 24, (4), 2383-2389.
31. Hamedi Shokrlu, Y.; Babadagli, T., In-Situ Upgrading of Heavy Oil/Bitumen During Steam Injection by Use of Metal Nanoparticles: A Study on In-Situ Catalysis and Catalyst Transportation.
32. Franco, C. A.; Nassar, N. N.; Ruiz, M. A.; Pereira-Almao, P.; Cortés, F. B., Nanoparticles for inhibition of asphaltenes damage: adsorption study and displacement test on porous media. *Energy & Fuels* **2013,** 27, (6), 2899-2907.
33. Wu, C. H. In *A critical review of steamflood mechanisms*, SPE California Regional Meeting, 1977; Society of Petroleum Engineers: 1977.
34. Giraldo, J.; Benjumea, P.; Lopera, S.; Cortés, F. B.; Ruiz, M. A., Wettability alteration of sandstone cores by alumina-based nanofluids. *Energy & Fuels* **2013,** 27, (7), 3659-3665.

7. Conclusions y recommendations

7.1 Conclusions

This study provides an important insight about nano-sized catalysts in the *n*-C_7 asphaltenes decomposition. Different supports such silica, alumina and titania were employed for the synthesis of SHS nanoparticles by the inclusion of NiO and/or PdO nanocrystals on its surface. Additionaly, synthesized silica nanoparticles and carbon nanospheres were employed for the adsorption ad subsequent catalytic oxidation of *n*-C_7 asphaltenes from different sources. Trough thermogravimetric experiments the catalytic activity of the selected nanoparticles was proved. All nanoparticles resulted in the lowering of effective activation energies, mainly at degrees of conversion lower than 50%; all functionalized materials behaved better than the support. The monometallic SHS with PdO showed better results than the nanoparticles functionalized with NiO. Bimetallic SHS showed highest catalytic activity for asphaltene adsorption and post catalytic thermal decomposition by reducing the cracking temperature, inhibiting the degree of asphaltenes self-association and suppressing addition reactions and coke formation. The great behavior of the bimetallic SHS is linked to the synergistic effect of NiO and PdO on the silica surface that leads to higher selectivity than the independent effect for the monometallic SHS. In addition, the catalytic effect of the bimetallic SHS was corroborated by the estimated thermodynamic properties of the transition state functions. The kinetic equations for the thermal decomposition of asphaltenes in presence and absence of the selected nanoparticles were obtained. Also, it was demonstrated that the asphaltene aggregate size over the nanoparticles surface has impact on the catalytic activity of the nanoparticles and a correlation between the adsorption affinity and the degree of asphaltenes-self association with the effective activation energies estimated trough the OFW method was encountered. Also, it was observed that resins adsorption do not affect significantly the adsorption process of asphaltenes. Additionally, a population balance model was proposed to describe the kinetics of asphaltene flocculation-fragmentation in the presence of nanoparticles. The model assumes that asphaltenes in the presence of a shear rate are related to the aggregation and fragmentation phenomena and includes a term related to the asphaltene adsorption on nanoparticles. An adsorption kinetic term was introduced into the model using the double exponential model. Finally, using an in-house designed setup it was proved that nanoparticles are able to enhance the oil recovery in vapor injection processes and upgrade the oil recovered. This works should provide a new insight of the use of nanoparticles for inhibition of formation damage and *in-situ* heavy and extra-heavy oil upgrading and the effect of the adsorption process on the efficiency of the catalytic activity of the nanoparticles.

7.2 Recommendations and future works

According to the results obtained, the following recommendations are proposed:

- To explore other supports such as ceria, zirconia, etc. and functionalizing materials such as Mo, Fe, Pt, etc. for the adsorption and subsequent catalytic decomposition of asphaltenes.
- To evaluate the effect of resins in the catalytic activity of nanoparticles.
- To develop optimization of the synthesized materials using another response variables such as maximum adsorption capacity, effective activation energy, etc.
- To include high catalytic agents to carbon nanospheres for the adsorption and subsequent catalytic decomposition of asphaltenes.
- To study the effect of resins in the aggregation/fragmentation of asphaltenes in presence of nanoparticles for inhibition of formation damage.
- To evaluate the effect of catalytic nanoparticles in different enhanced oil recovery processes such as cyclic steam stimulation, *in-situ* combustion, etc.
- To develop a more extensive study about the influence of temperature in the aggregation/fragmentation of asphaltenes.
- To determine the selectivity of nanoparticles towards different chemical characteristics of asphaltenes such as chemical architecture, heteroatoms content, aromaticity, etc.
- To evaluate the effect of other co-existing molecules in crude oil in the adsorption and decomposition of asphaltenes in presence of nanoparticles.
- To corroborate the effect of resins I in the adsorption of *n*-C_7 asphaltenes using nanoparticles with different chemical nature.
- To determine the desorption capacity of asphaltenes from the adsorbed phase.
- To evaluate the effect of particle size in the inhibition of the asphaltene aggregation.

8. Publications and awards

As scientific contribution of this Ph.D. thesis, the following documents have been published:

8.1 Scientific papers and book chapter

- Adsorption and Subsequent Oxidation of Colombian Asphaltenes onto Nickel and/or Palladium Oxide Supported on Fumed Silica Nanoparticles. ***Energy & Fuels, 2013***, 27(12), 7336-7347.
- **Book Chapter:** NiO and PdO Supported on Fumed Silica Nanoparticles for Adsorption and Catalytic Steam Gasification of Colombian C7 Asphaltenes. ***Handbook on Oil Production Research, 2014.***
- Influence of asphaltene aggregation on the adsorption and catalytic behavior of nanoparticles. ***Energy & Fuels, 2015***, 29(3), 1610-1621.
- Effect of oxide support on Ni–Pd bimetallic nanocatalysts for steam gasification of *n*-C_7 asphaltenes***. Fuel, 2015***, 156, 110-120.
- Development of a Population Balance Model to Describe the Influence of Shear and Nanoparticles on the Aggregation and Fragmentation of Asphaltene Aggregates. ***Industrial & Engineering Chemistry Research., 2015***, 54 (33), 8201–8211.
- ***In review:*** Kinetics and mechanisms of catalytic thermal cracking of adsorbed asphaltenes onto supported nanoparticles. Journal of Petroleum Science and Engineering, 2015.

8.2 Oral presentations

- Mejoramiento de crudo pesado mediante la inyección de vapor de agua asistido por catalizadores nanoparticulados, III Escuela de verano – Tecnologías aplicadas al recobro de crudo, May 13-15, 2014, Medellín, Colombia.
- Nanopartículas de sílice funcionalizadas con compuestos monometálicos, bimetálicos y trimetálicos de óxidos de Ni, Fe y/o Mo para adsorción selective de asfaltenos y subsecuente

craqueo catalítico. 2nd Iberoamerican symposium of adsorption. April 26-30. Cartagena, Colombia.

- Nanotecnología aplicada a la industria petrolera, II Escuela de verano – Tópicos avanzados de daño de formación, October 1-3, 2014, Medellín, Colombia.
- Nanoparticle technology for inhibition of asphaltene damage at reservoir conditions and enhancing oil recovery, Heavy Oil Latin America HOLA 2014, October 15-17 Isla Margarita, Venezuela.
- Adsorption and subsequent thermal cracking of asphaltenes in presence of fumed silica nanoparticles: effect of the surface basicity and acidity. Heavy Oil Latin America HOLA 2014, October 15-17 Isla Margarita, Venezuela.
- Carbon Nanospheres (CNS) for heavy oil in situ upgrading under inert and oxidative atmospheres. XVI Congreso colombiano del petróleo y gas, August 26-28, 2015, Bogotá, Colombia.

8.3 Poster presentations

- Supported hygroscopic salts for adsorption and post catalytic pyrolysis of Colombian asphaltenes. 2nd Iberoamerican symposium of adsorption. April 26-30. Cartagena, Colombia.
- Effect of the particle size synthesized silica gel nanoparticles on the inhibition of the asphaltene precipitation. 2nd Iberoamerican symposium of adsorption. April 26-30. Cartagena, Colombia.

8.4 Awards

- **ACIPET price to innovation:** Uso de nanopartículas funcionalizadas para inhibir el daño de formación por asfaltenos y aumentar el factor de recobro. 2014.
- **GIORGIO ZGRABLICH 1st Price** Poster modality: *Supported hygroscopic salts for adsorption and post catalytic pyrolysis of Colombian asphaltenes*. 2015.

A. Appendix: Simplex−Centroid Mixture Design

Simplex−centroid mixture design (SCMD), performed with the STATGRAPHICS Centurion XVI software (StatPoint Technologies Inc.), was used to determine the optimal mixture of palladium, nickel, and CS nanoparticles to minimize the oxidation temperature of the asphaltenes. Normally, SCMD is used to study the relationships between the proportions of different variables and responses.[1] The fractions of each component must meet the following constraints:[2]

$$\sum_{i=1}^{\theta} x_i = x_1 + x_2 + \ldots + x_\theta = 1, \quad x_i \geq 0 \tag{A.1}$$

where x_i and θ are the proportions of each component and the number of components in the mixture, respectively. In this study, θ was 3 when x_1 = CS, x_2 = Pd, and x_3 = Ni. The amount of Pd and/or Ni oxides was restricted up to 2% in the design. Consequently, the limits of each compound are the following:

$$0.98 \leq CS \leq 1.00 \tag{A.2}$$

$$0 \leq Pd \leq 0.02 \tag{A.3}$$

$$0 \leq Ni \leq 0.02 \tag{A.4}$$

Using a three-component SCMD evaluates seven points at different concentrations of each component to adjust the response variable for the design and the desired model. In this case, each component was evaluated at the maximum allowable fraction at an intermediate and the centroid points of the mixture, as displayed in Figure 1.2 (see Chapter 1). The regression model for the oxidation temperature was established using a special cubic regression fitting. The regression model equations were as follows:

$$N_j = \sum_{i=1}^{\theta} \beta_i x_i^{'} + \sum_{i<j} \beta_{ij} x_i^{'} x_j^{'} + \sum_{i<j<k} \beta_{ijk} x_i^{'} x_j^{'} x_k^{'} \tag{A.5}$$

$$x_i^{'} = \frac{x_i - L_i}{1 - L} \tag{A.6}$$

where N_j is the oxidation temperature for a desired amount of asphaltenes adsorbed onto the adsorbent surface, β_i are the coefficients of the linear terms of the components, β_{ij} are the components of the binary mixtures of the nonadditive components, and β_{ijk} is the component of the nonadditive ternary mixture. Equation A.6 is a pseudocomponent of x_i (fraction) and is used because of the restrictions mentioned in eqs A2-A4. In these equations, L_i is the lower limit of each component, and L is the sum of the lower boundaries.

References

1. Scheffe, H. J. R. Stat. Soc., B **1963**, 25, 235−263..
2. Cornell, J. A. Experiments with Mixtures. Designs, Models, and the Analysis of Mixture Data, 3rd ed.; John Wiley & Sons, Inc.: New York, 2002.

B. Appendix: Thermodynamic parameters of the transition state functions for *n*-C_7 asphaltenes catalytic thermal cracking and steam gasification

The kinetic parameters and thermodynamic properties of the transition state functions for the oxidation of *n*-C_7 asphaltenes in presence and absence of the selected nanoparticles were estimated following the procedure described in Section 2.2.2 and are presented in Tables B1 and B2 for catalytic thermal cracking and steam gasification, respectively. As seen, the values of n ranged from 1.5 to 10 with values of the slope between -1.07 and -0.97 for R^2 =0.99 in the case of thermal cracking. For steam gasification, n ranged from 3 to 16 with values of the slope between -1.04 and -0.99 for R^2 =0.99 However, it is worth to mention that values of n > 4 lack of chemical significance and were only used as fitting parameters for the description of the kinetic equation and the estimation of the thermodynamic properties. This is due as the chemical composition and structure of *n*-C_7 asphaltenes is very complex and could result in a series of unidentified simultaneous reactions. Also, different values of n imply that the thermal cracking or steam gasification of *n*-C_7 asphaltenes in presence or absence of the selected nanoparticles is not a single-mechanism process and that it is highly dependent on the nanoparticles chemical nature. From Tables B1 and B2 it can be also observed that the trend of the change of the enthalpy of activation follows the order of virgin *n*-C_7 asphaltenes > CS > CSNi2 > CSP2 > CSNi1Pd1, indicating that the highest catalytic effect was obtained for the bimetallic SHS as the reduction in $\Delta H^{\ddagger}$ was highest among the system evaluated; same observations can be made for $\Delta G^{\ddagger}$**.** In addition, according to the negative values of $\Delta S^{\ddagger}$ it can be inferred that the entropy of the activated stated is lower than that of the initial state.

Table B.1. Kinetic parameters and thermodynamic properties of the transition state functions for the catalytic thermal cracking of *n*-C_7 asphaltenes in presence and absence of SHS for a fixed value of α =50%.

Material	n	**slope**	R^2	A **(x10^5 s^{-1})**	**Kinetic equation**	$\Delta S^{\ddagger}$ **(J/mol·K)**	$\Delta H^{\ddagger}$ **(kJ/mol)**	$\Delta G^{\ddagger}$ **(kJ/mol)**
Virgin *n*-C_7 asphaltenes	1.5	-1.00	0.99	1.76	$\frac{d\alpha}{dt} = 2A_{\alpha}\exp\left(-\frac{E_{\alpha}}{RT}\right)(1-\alpha)^{3/2}$	-160.22	179.99	115.86
CS	5	-1.07	0.99	28.05	$\frac{d\alpha}{dt} = \frac{A_{\alpha}}{5}\exp\left(-\frac{E_{\alpha}}{RT}\right)(1-\alpha)^{6}$	-137.00	176.09	97.45
CSNi2	7	-1.01	0.99	39.84	$\frac{d\alpha}{dt} = \frac{A_{\alpha}}{7}\exp\left(-\frac{E_{\alpha}}{RT}\right)(1-\alpha)^{8}$	-133.65	143.39	90.22
CSPd2	9	-1.02	0.99	26.47	$\frac{d\alpha}{dt} = \frac{A_{\alpha}}{9}\exp\left(-\frac{E_{\alpha}}{RT}\right)(1-\alpha)^{10}$	-136.05	129.03	81.49
CSNi1Pd1	10	-0.97	0.99	5.91	$\frac{d\alpha}{dt} = \frac{A_{\alpha}}{10}\exp\left(-\frac{E_{\alpha}}{RT}\right)(1-\alpha)^{11}$	-147.91	130.59	78.31

Table B.2. Kinetic parameters and thermodynamic properties of the transition state functions for the catalytic steam gasification of *n*-C_7 asphaltenes in presence and absence of SHS for a fixed value of α =50%.

Material	n	**slope**	R^2	A **(x10^3 s^{-1})**	**Kinetic equation**	$\Delta S^{\ddagger}$ **(J/mol·K)**	$\Delta H^{\ddagger}$ **(kJ/mol)**	$\Delta G^{\ddagger}$ **(kJ/mol)**
Virgin *n*-C_7 asphaltenes	4	-1.04	0.99	0.79	$\frac{d\alpha}{dt}=\frac{A_\alpha}{4}\exp\left(-\frac{E_\alpha}{RT}\right)(1-\alpha)^5$	-160.22	179.99	115.86
CS	3	-1.08	0.99	1.08	$\frac{d\alpha}{dt}=\frac{A_\alpha}{3}\exp\left(-\frac{E_\alpha}{RT}\right)(1-\alpha)^4$	-137.00	176.09	97.45
CSNi2	9	-1.00	0.99	29.49	$\frac{d\alpha}{dt}=\frac{A_\alpha}{9}\exp\left(-\frac{E_\alpha}{RT}\right)(1-\alpha)^{10}$	-133.65	143.39	90.22
CSPd2	14	-1.02	0.99	968.05	$\frac{d\alpha}{dt}=\frac{A_\alpha}{14}\exp\left(-\frac{E_\alpha}{RT}\right)(1-\alpha)^{15}$	-136.05	129.03	81.49
CSNi1Pd1	16	-0.99	0.99	5558.32	$\frac{d\alpha}{dt}=\frac{A_\alpha}{16}\exp\left(-\frac{E_\alpha}{RT}\right)(1-\alpha)^{17}$	-147.91	130.59	78.31

C. Appendix: *n*-C_7 asphaltenes adsorption over CTi- and CAl- supported nanoparticles

According to surface area values for the CTi support and the functionalized CTi nanoparticles, it can be inferred that the inclusion of the PdO and/or NiO on the particle surface does not affect strongly the available area for asphaltenes adsorption. However, in the case of CAl support and CAl-functionalized nanoparticles the values of the measured S_{BET} follow the trend **C**Al > CAlNi2 > CAlPd2 > CAlNi1Pd1, indicating that some of the small pores of the support could be blocked by the NiO and/or PdO nano-crystals on their surface. The obtained values of S_{BET} of the nanoparticles are listed in Table C.1.

Table C.1. Estimated surface area and particle size of the CTi- and CAl-supported nanoparticles.

Material	**S_{BET} m^2/g**
CTi	54
CTiNi2	50
CTiPd2	50
CTiNi1Pd1	48
CAl	223
CAlNi2	176
CAlPd2	143
CAlNi1Pd1	133

Figure C.1 shows the experimental adsorption isotherms of *n*-C_7 asphaltenes onto nanoparticles of TiO_2 and TiO_2 with the corresponding mono and bimetallic loading at 25°C along with the solid-liquid-equilibrium (SLE) model. As shown in Figure C.1, the functionalized nanoparticles have higher adsorptive capacities than the TiO_2 support; this is expected because NiO and/or PdO showed higher affinities than TiO_2 towards compounds such as pyridine, benzoic acid, phenol and pyrrole.[1] This suggests that the observed increase in asphaltene uptake for the functionalized nanoparticles could be associated with the presence of nitrogen and oxygen in the asphaltene molecules, which favored the interaction with the nanoparticle surface.[1] NiO and PdO supported on the TiO_2 nanoparticles alone showed similar adsorption behavior. Metal coverage on the Ti surface could be highly influenced by the oxidation temperature used in the material synthesis and could influence

the amount of active sites available for asphaltene adsorption. This suggests that in addition to individual selectivities of Pd and Ni towards different functional groups of the asphaltene molecule, the type and strength of the bond between Ni and Pd with the Ti support produces different orientations of the asphaltene molecules after adsorption on the nanoparticle surface. Hence, similar degrees of selectivity are found to be independent of the preferred species; however, bimetallic nanoparticles showed higher uptakes than monometallic nanoparticles, particularly for equilibrium concentrations above 80 mg/L. This could be due to the high dispersion of metal oxide on the support and the subsequent synergistic effect of PdO and NiO that lead to different unified selectivities, intermolecular forces between the functional groups and heteroatoms of asphaltenes. These findings are in excellent agreement with studies on Capella n-C_7 asphaltenes adsorption onto CS nanoparticles functionalized with NiO and PdO presented in Chapter 2, where it was observed that higher uptake was obtained for bimetallic nanoparticles than for monometallic nanoparticles.

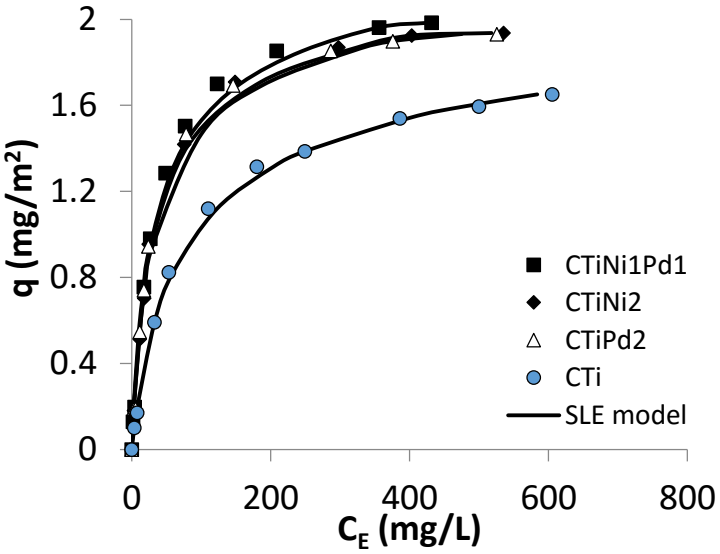

Figure C.1. *n*-C_7 Asphaltene adsorption isotherms onto CTi, CTiNi2, CTiPd2 and CTiNi1Pd1 nanoparticles at 25°C.

Figure C2 shows the adsorption isotherms of *n*-C_7 asphaltenes onto CAl, CAlNi2, CAlPd2 and CAlNi1Pd1 nanoparticles at 25°C with the SLE model. Again, the adsorption capacity is shown to be enhanced after functionalizing the support nanoparticles with higher uptakes obtained in the order CAlNi1Pd1 > CAlPd2 > CAlNi2 > CAl. However, the amount adsorbed of asphaltenes on Al nanoparticles is lower than for CTi nanoparticles; also, Ni-Pd/γ-Al_2O_3 nanoparticles showed a lower adsorption capacity than Ni-Pd/TiO_2. This could be attributed to different metal-support interactions and the geometric and electronic effects on the adsorbent surface that influence the selectivity for different functional groups or heteroatoms in *n*-C_7 asphaltene molecules.

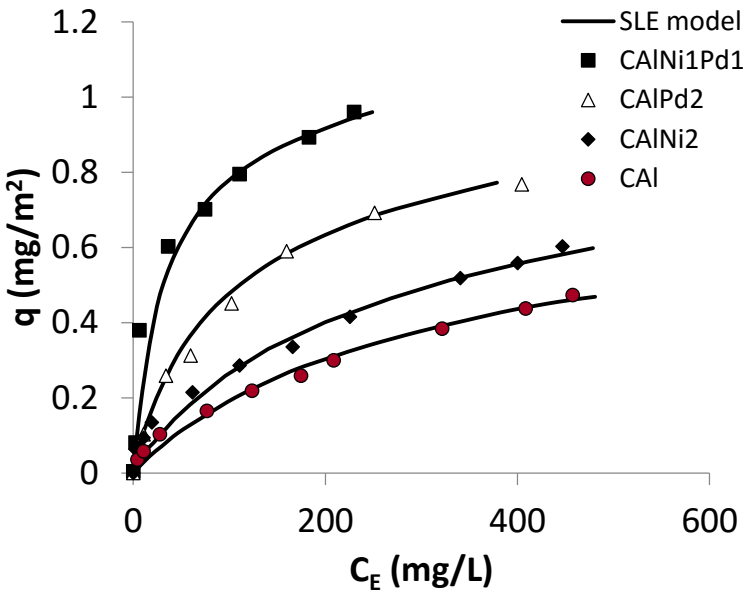

Figure C.2. *n*-C_7 Asphaltene adsorption isotherms onto CAl, CAlNi2, CAlPd2 and CAlNi1Pd1 nanoparticles at 25°C.

Table C.2 lists the estimated values of the SLE model parameters. As shown for all cases, the SLE model produces an excellent fit to the experimental data, which is indicated by the low values of *RSME%*. Additionally, the adsorption affinity, represented by the reciprocal of *H* value, increases in the order bimetallic > monometallic > support. Similar trends can be observed for the q_m parameter. Conversely, the degree of asphaltene self-association on active sites, which is represented by *K*, is higher for the support than for the functionalized nanoparticles. Owing to their complex structure, the asphaltenes can self-associate and form aggregates on the nanoparticles surface. It is expected that at low uptake the asphaltenes will be adsorbed in the high energy sites of the adsorbent as monomers. However, by increasing the concentration at medium and high uptake, asphaltenes molecules will form aggregates around the high-energy sites until the volume available for adsorption is crowded. In this order, and depending on the adsorbent chemical structure, asphaltenes may be adsorbed in perpendicular, parallel or flat ways subject to the selectivity of the surface towards the aromatic part of the asphaltenes or heteroatoms present in their structure. Due to by functionalizing the nanoparticles different selectivities are induced, this led the asphaltenes being in different degrees of self-association around the high-energy sites available for adsorption. The trends of the SLE parameters agree well with the experimental adsorption isotherms as q_m could be seeing as a control parameter for the model fitting and follows the same trend than the observed experimental results.

Table C.2. Estimated parameters of the SLE model

Material	H **± 0.02 (mg/g)**	K **± 0.08 (g/g) x 10^{-4}**	q_m **± 0.01 (mg/m^2)**	R^2	***RSME%***
CTi	0.69	4.67	2.78	0.99	0.77
CTiNi2	0.37	4.11	3.01	0.98	2.96
CTiPd2	0.33	3.48	3.02	0.99	2.02
CTiNi1Pd1	0.30	2.98	3.11	0.99	1.55
CAl	1.89	3.82	1.30	0.99	1.84
CAlNi2	1.62	3.56	1.51	0.99	2.13
CAlPd2	0.73	2.58	1.55	0.99	0.70
CAlNi1Pd1	0.25	2.38	1.67	0.99	1.13

References

1. Zimmer, A. K.; Becker, C.; Chambliss, C. K., Exploiting Metal Oxide Nanoparticle Selectivity in Asphaltenes for Identification of Pyridyl-Containing Molecules. Energy & Fuels ***2013***, 27, (8), 4574-4580.

D. Appendix: Effect of nanoparticle dosage and system temperature on *n*-C_7 asphaltene aggregation-fragmentation

Two different nanoparticle dosages of 10 and 20 g/L were selected to evaluate its effect on the *n*-C_7 asphaltenes uptake. Figure D.1 shows the adsorption kinetics of AK18 *n*-C_7 asphaltenes onto CM nanoparticles for the selected dosages. The amount of asphaltenes adsorbed decreased by increasing the amount of nanoparticles. Following the mass balance $q_t = (C_i - C_t)/M$ employed for the calculation of the amount adsorbed, it can be seen that as increasing the dosage of nanoparticles M in the denominator will result in an intrinsic decrease of the value of q_t. This behavior can be explained by the reduction of the surface area caused by interactions between the nanoparticles caused by their aggregation at higher concentrations,[1-3] which reduces the surface area available for adsorption. Therefore, this change in the surface area reduces the probability of the asphaltene aggregates contacting the available nanoparticle surfaces.

In this case, the double exponential model also had a good fit with values of 0.99 and 0.74 for the R^2 and $RSME\%$, respectively. Accordingly, the results of the double exponential model fitting also showed that the adsorption process is governed by one fast step with values of k_s and D_s of 0.00. The obtained values of the q_m, k_f and D_f parameters were 44.5 mg/g, 0.09 min^{-1} and 177.3 mg/L, respectively.

However, if a control volume of 10 mL is assumed and the amount adsorbed is not normalized by the dry mass of nanoparticles, the mass balance changes as shown in Eq. D.1:

$$q_t = (C_i - C_t) \cdot V \tag{D.1}$$

where V (L) is the solution volume.

Hence, the trend of the amount adsorbed would be the opposite as shown in Figure D.1. This is expected as by increasing the number of nanoparticles in the system, there would be a larger amount of active sites available for adsorption. Although one could also expect that the amount adsorbed without mass normalization would be higher by a factor of 2 in presence of 20 g/L than that of 10 g/L, this does not occur due to the inherent aggregation behavior of the nanoparticles and limitations in the asphaltene diffusion trough the bulk of the solution.

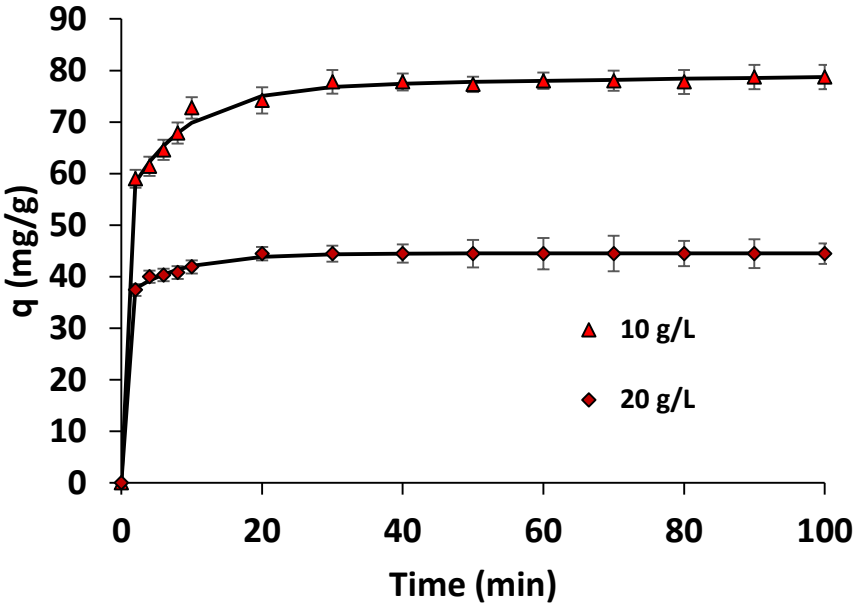

Figure D.1. Amount of asphaltenes adsorbed from Heptol 40 onto CM nanoparticles at dosages of 10 g/L and 20 g/L in units of mg/g.

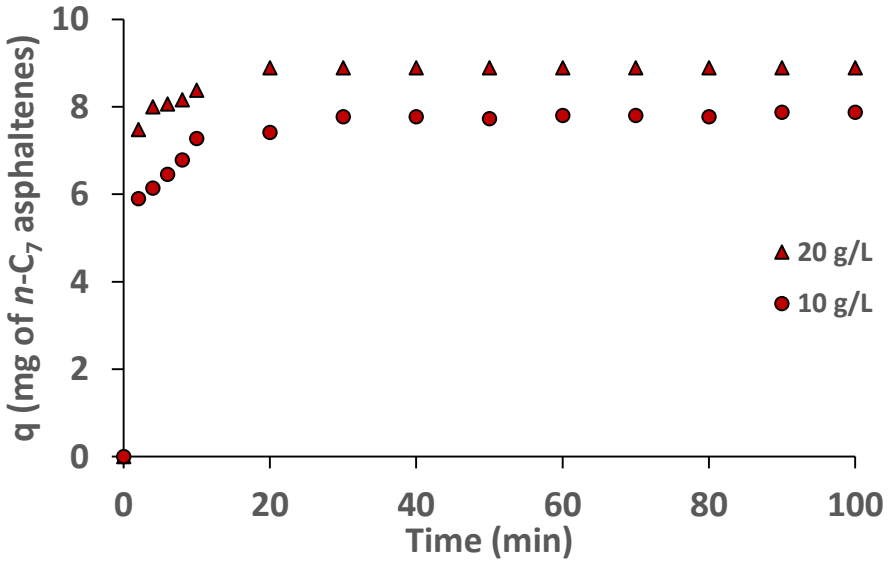

Figure D.2. Mass of AK18 asphaltenes adsorbed from Heptol 40 onto magnetite nanoparticles at dosages of 10 g/L and 20 g/L.

The amount of nanoparticles may significantly alter the asphaltene aggregate size in solution because more active sites will be available for adsorption. Heptol 40 solutions of AK18 *n*-C_7 asphaltenes at 20°C and CM nanoparticles at two different dosages of 10 and 20 g/L were used to study the effect of nanoparticles dose. Figure D.3 shows the results obtained from DLS measurements for the kinetics of asphaltene growth in the absence and presence of CM nanoparticles at both of the dosages used.

As expected, the asphaltene aggregates show a greater decrease in the presence of 20 g/L of magnetite nanoparticles. In this case, the PBM also adjusted well towards the experimental results with R^2 = 0.94 and *RMSE%* = 6.27. A value of 0.29 was obtained for the ξ parameter, indicating that lower porosities are obtained as the nanoparticle dosage increases. On the other hand, the b parameter has a value of 6.09×10^{-5}, indicating that there is no significant difference in the breakup rate by changing the amount of nanoparticles and that the inhibition of the asphaltene growth is more dependent on the adsorption process. Note that at the equilibrium of the fragmentation and aggregation processes, the aggregate is 29.1 and a 61.1 % lower than for the virgin AK18 n-C7 asphaltenes for nanoparticle dosages of 10 and 20 g/L, respectively.

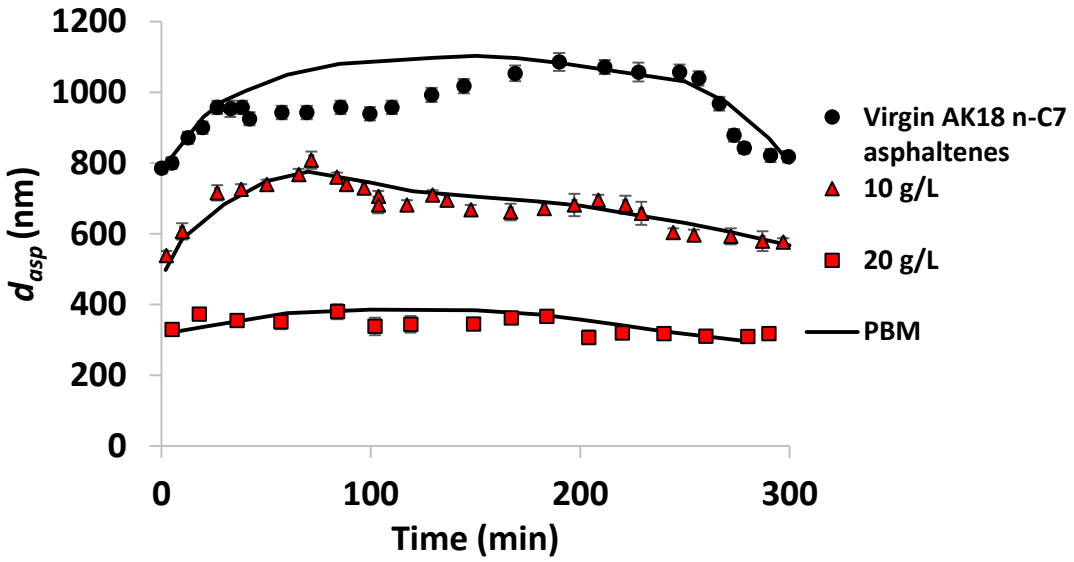

Figure D.3. Kinetics for AK18 asphaltenes aggregation-fragmentation in the presence of 10 g/L and 20 g/L of magnetite nanoparticles at 25°C in Heptol 40 solutions.

References

1. Keller, A. A.; Wang, H.; Zhou, D.; Lenihan, H. S.; Cherr, G.; Cardinale, B. J.; Miller, R.; Ji, Z. Stability and Aggregation of Metal Oxide Nanoparticles in Natural Aqueous Matrices. Environ. Sci. Technol. **2010**, 44, (6), 1962.

2 Baalousha, M. Aggregation and Disaggregation of Iron Oxide Nanoparticles: Influence of Particle Concentration, Ph and Natural Organic Matter. Sci. Total Environ. **2009**, 407, (6), 2093.

3 Hakim, L. F.; Portman, J. L.; Casper, M. D.; Weimer, A. W. Aggregation Behavior of Nanoparticles in Fluidized Beds. Powder Technol. **2005,** 160, (3), 149.